University of Strathclyde

Department of Naval Architecture, Ocean and Marine Engineering

Assessing the performance of an Oscillating Water Column type wave energy device

Saishuai Dai

A thesis submitted in fulfilment of the
requirements for the degree of

Doctor of Philosophy

May 2016

Statement of Originality

This thesis is the result of the author's original research. It has been composed by the author and has not been previously submitted for examination which has led to the award of a degree. The copyright of this thesis belongs to the author under the terms of the United Kingdom Copyright Acts as qualified by University of Strathclyde Regulation 3.50. Due acknowledgement must always be made of the use of any material contained in, or derived from, this thesis.

Signed:
Date:

Abstract

To meet the need of clean energy, a variety of renewable energy technologies have been developed. Among those, wave energy stands out for its' outstanding merits. For instance, wave energy is clean, renewable, has high energy intensity and long resource available time et.al. However, due to the short development history of wave energy technologies, the cost of wave energy is too high compared with the other renewable energy technologies.

As well as lack of cost effective Wave Energy Converters (WECs) scenarios, another reason that keeps the cost of wave energy high is that the performance of a WECs may not be accurately assessed during its' design and development stage. This leads to error in estimating the cost of energy produced by the full scale device. Therefore, this study aims to drive the cost of WECs down by investigate several major aspects that will bias the assessing the performance of a WEC during the design and development stage.

Literature review suggested the uncertainty in the measurement, the tank width effect (in tank testing.), the performance of the simulated simple Power Take Off (PTO) and the scale effect are major aspects that bias the assessment. By tank testing and Computational Fluid Dynamic (CFD) simulation, the above three aspects were investigated.

It is found that the uncertainty in the measurement leads to an uncertainty in the power captured at model scale about 5% around the peak output. The appearance of the tank wall will over estimate the performance of a single unit depends on the width of the tank. A $1:150^{th}$ scaled (of the full scale.) device may under estimate the performance of the device by about 34% compared with a $1:16.67^{th}$ scaled device, while a $1:50^{th}$ scaled device under estimate the performance of a $1:16.67^{th}$ scaled device by 6.6%.

The CFD simulation demonstrated it's advantage over the tank testing when scaling and tank width effect is concerned. Therefore, to better

estimate the performance, the assessment shall be carried out by both experiment and numerical simulation.

Based on the study carried out, recommendation and guide line for tank testing of a FSCOWC device was given at the end of the thesis.

Contents

Abstract **iii**

Contents **v**

1 Introduction **1**

1.1 Background 1
1.2 Renewable energy resources 2
1.3 Wave energy 3
1.4 Aim and plan of the thesis 5
1.5 Chapter summary 6

2 Literature review **7**

2.1 Wave energy technologies 7
2.2 OWC technology development 14
2.3 Current status and prospects 21
2.4 A cost effective scenario 22
2.5 Existing numerical assessment methods 25
2.6 Areas for study 26
2.7 Research objectives and thesis structure 32

3 OWC theory **34**

3.1 Chapter overview 34
3.2 Theory of pressure distribution 34
3.3 Result of the proposed FSCOWC WEC 38
3.4 Chapter summary 39

4 Experiment on a moderate scale FSCOWC **41**

4.1 Chapter overview 41
4.2 Facilities 41
4.3 FSCOWC models and configuration 42
4.4 Instruments 45

4.5 Uncertainties . . . 47
4.6 Testing procedures . . . 52
4.7 Data processing . . . 55
4.8 Estimation of uncertainties in current test . . . 58
4.9 Results and discussion . . . 61
4.10 Chapter summary . . . 76

5 Experiment on a small scale FSCOWC **79**
5.1 Chapter overview . . . 79
5.2 Scaling law . . . 79
5.3 Facilities . . . 80
5.4 FSCOWC models and configuration . . . 81
5.5 Instruments . . . 82
5.6 Testing procedures . . . 83
5.7 Data processing . . . 84
5.8 Results presentation . . . 85
5.9 Chapter summary . . . 93

6 Reflection-free Numerical Wave Tank **95**
6.1 Chapter overview . . . 95
6.2 Methodology . . . 95
6.3 Wave generation and absorption in CFD approaches . . . 98
6.4 Results presentation . . . 109
6.5 Chapter summary . . . 115

7 RANS simulation of the moderate scale FSCOWC **116**
7.1 Chapter overview . . . 116
7.2 Geometry of the FSCOWC device . . . 116
7.3 Domain and boundary conditions . . . 117
7.4 Mesh distribution . . . 118
7.5 Results presentation . . . 120
7.6 Chapter summary . . . 129

8 RANS simulation of the small scale FSCOWC **130**
8.1 Chapter overview . . . 130
8.2 Scaling of the small scale simulation . . . 130
8.3 Results presentation . . . 132
8.4 Chapter summary . . . 139

9 CFD study of simulated PTO characteristics **141**
9.1 Chapter overview 141
9.2 Characteristics of the PTO system 141
9.3 Chapter summary 147

10 Conclusion and future works **149**
10.1 Conclusion 149
10.2 Future works 153

References **162**

Abbreviations and Nomenclature **162**

Appendix A Pressure transducer calibration **166**

Appendix B Determination of hydrodynamic coefficients **170**

Appendix C Further results for tank width effect **178**

Appendix D RANS simulation uncertainty **181**

Appendix E Simulation of the orifice plate **184**

Appendix F Recommendation for tank testing **187**

List of Figures **200**

List of Tables **201**

Acknowledgements **203**

Chapter 1

Introduction

1.1 Background

The Deep water Horizon oil spill (also referred to as the BP oil spill) happened on 20^{th} April 2010 in the Gulf of Mexico. Claimed eleven lives directly, discharged around 4.9 million barrels oil which polluted 6500 to $180000km^2$ sea area. As well as extensive damage to marine and wildlife habitats, fishing and tourism industries are also affected. Moreover, human health problems have continued through 2013.

The Fukushima Daiichi nuclear plant exploded on 11st March 2011 caused by tsunamis. This disaster released an estimated 10 to 30% of the radiation of the Chernobyl accident. More than 2 years after, on 22nd July 2013, radioactive water is still found leaking into the Pacific Ocean from Fukushima Daiichi nuclear plant. This causes hidden danger in human health as nuclear radiation can be deadly.

These two worldwide well known disasters happened recently mentioned above made us aware of the pollution may be cause by fossil fuel and nuclear power in the extracting or generation process. Further more, fossil fuel resource will run out in the next several decades. Energy crisis will arrive if we human being can't find an alternative energy resource. Renewable energy is developed to solve those problems talked above. For its environmental friendly, renewable (or we may say inexhaustible) and last but not least, economic reasons, renewable energy has been studied extensively worldwide in recent years.

1.2 Renewable energy resources

As stated by Twidell and Weir (2006), renewable energy can be defined as 'energy obtained from the continuous or repetitive currents of energy recurring in the natural environment'. Figure 1.1 presents the source and magnitudes of the renewable energy available to earth. Apart from tidal and geothermal energy, all the other renewable energy is the production of solar radiation.

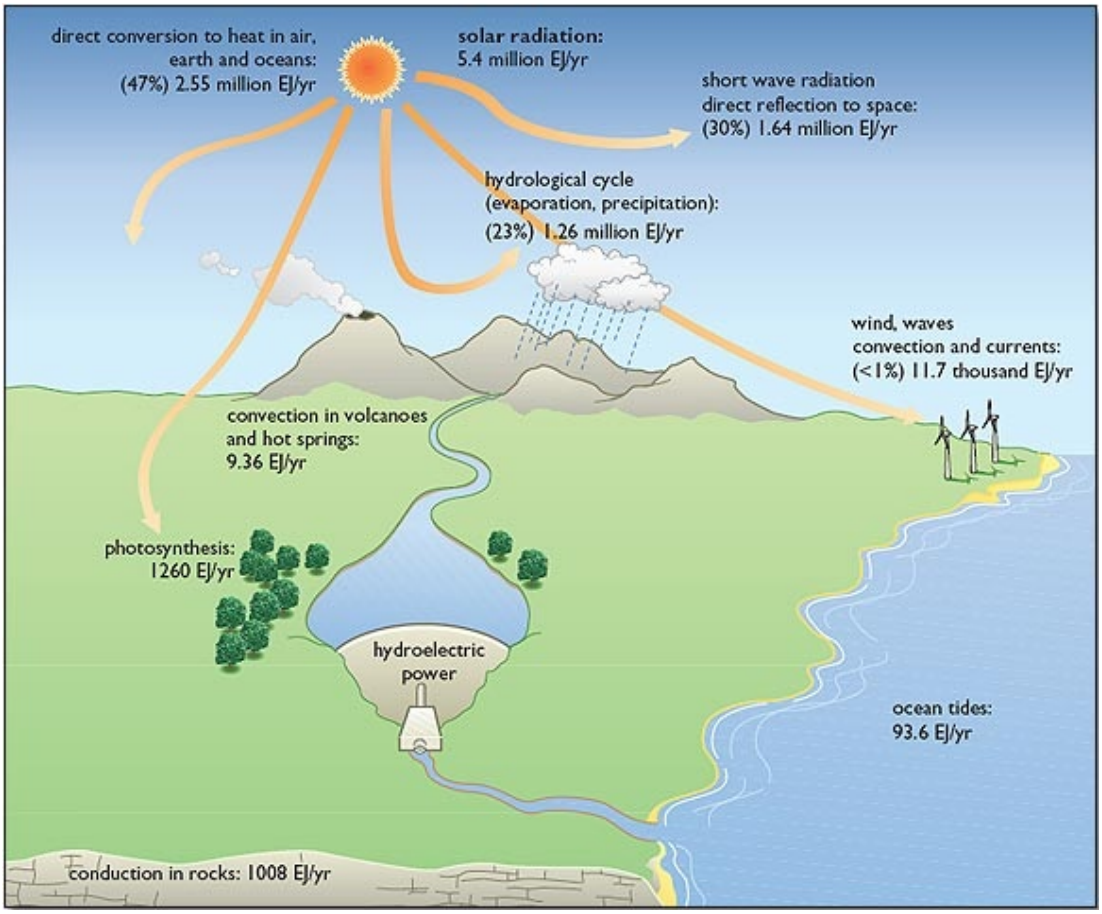

Figure 1.1: Renewable energy resources, where Photosynthesis stands for biomass. Figure is taken from Twidell and Weir (2006).

Existing renewable energy extracting technology can utilise almost all the renewable energy listed in Figure 1.1. For instance, the solar radiation can be absorbed and transformed into electricity by solar photovoltaic, wind energy can be extracted by means of wind turbine, and hydro power can be harvested by hydro turbine.

1.3 Wave energy

Ocean wave energy originally caught us human being's sight possibly because of its destructive effect. As indicated by Figure 1.1, wave energy is concentrated form of solar energy: the sun produces temperature differences across the globe, causing winds that blow over the ocean surface. These cause ripples, which grow into swells.

1.3.1 Wave energy resources

World Energy Council estimated the total worldwide wave resource is $2TW$ or 17500 $TWh/year$ (Thorpe, 1999) which is of the same order of magnitude as world electricity consumption. Figure 1.2 demonstrates the calculated global annual mean wave power density and annual mean best direction (Gunn and Stock-Williams, 2012).

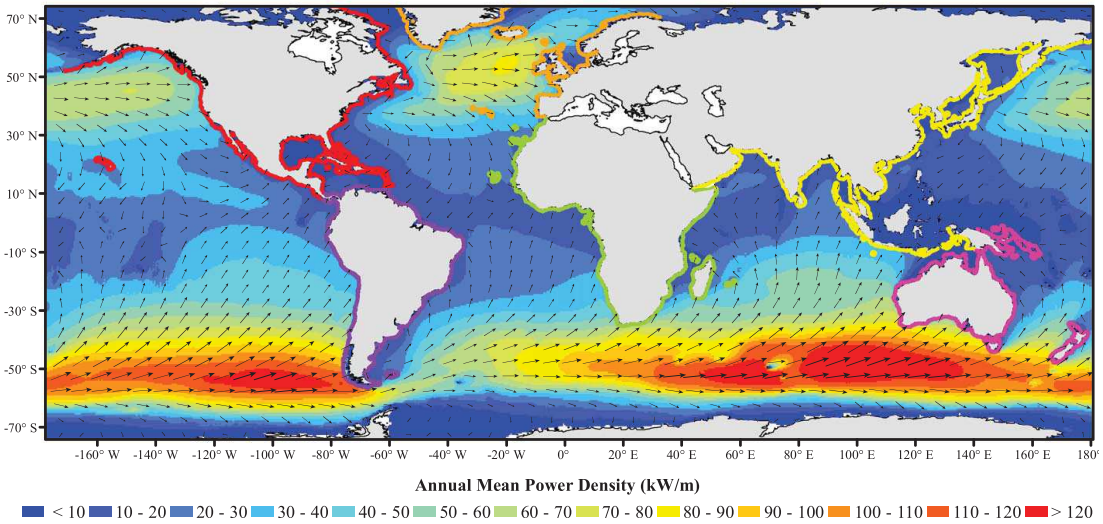

Figure 1.2: Global annual mean wave power density and mean best direction (shown as arrows). Figure is taken from Gunn and Stock-Williams (2012).

This, however, is the theoretical total wave energy resource. The theoretical wave energy resource is the overall wave energy available to wave energy devices estimated based on wave information (wave height, periods and location). To address the effect of wave energy devices' performance, technical energy resource is introduced. The technical energy resource estimate the energy resource by considering the devices' performance, site coverage and electrical efficiency. Practical resource is then further introduced to include social, economic and

environmental constrains. Normally, practical energy resource is far smaller than the theoretical resource. For example, the theoretical wave energy for UK is $146TWh/y$ for offshore and $133TWh/y$ for near-shore and reduced to $70TWh/y$ and $5.7TWh/y$, respectively, when practical resource is considered (Richard, 2012). It should be noted that most of the exploitable energy lies near the coast simply because those offshore site with high energy density is not approachable due to current technique limitation.

More detailed wave energy resources can be found in several reviews, for instance Falnes (2007), Drew et al. (2009) and Thorpe (1999).

1.3.2 Merits and drawbacks of wave energy

Why do we bother to extract wave energy rather than wind or solar energy directly since the wave energy comes from wind? This is in fact one of the most important reasons why researchers are interested in developing WEC. When solar energy is transformed to wind energy, the time averaged power flow is spatially concentrated from an intensity of typically 0.1-0.3 kW/m^2 horizontal surface of the earth to $0.5kW/m^2$ envisaged area perpendicular to wind direction. When wind energy is converted to wave energy, further spatial concentration takes place. The average power flow intensity is typically 2-3 kW/m^2 of envisaged area perpendicular to the direction of wave propagation (Falnes, 2007). This means that, given the same working area, the available energy of waves is several times larger than wind or solar energy. As well as the high power intensity, wave energy has following major advantages:

- Free and renewable resources
- Longer available time: wave energy can offer power up to 90% of the time. (20-30% for wind and solar)(Drew et al., 2009)
- Environmentally friendly: Unlike fossil fuels and biomass, wave power utilization will not involving combustion thus no harmful gas will be released to the air. Since wave energy devices are installed near-shore or offshore, there will be little visual impact and noise will be generally lower than the noise of wave breaking. Unlike some devices, generally wave energy device will not require impounding reservoirs or dams thus there is no worry about flooding. With some specific technology, for example oscillating water column wave energy converter incorporate with breakwater, wave energy

devices, can even provide coastal protection.

Considering disadvantages, the wave energy intensity varied with seasons is one of the shortcomings. Fortunately, the variability follows the electricity demand in temperate climates (Clément et al., 2002)

Another draw back is that the installed capacity of wave energy device is usually less than 1 Megawatt (MG) based on the "small is beautiful" rule (Falnes, 1994) while the capacity of wind turbine can reach typically 5-7 MW. However, this can be solved by constructing wave energy devices array (farm) which consists of several MW capacity devices.

the high cost of generated electricity could be the most eye-catching drawback of wave energy utilization. According to Max Carcas, External Liaison for EMEC, the current cost of electricity produced by wave energy device is about 25-30 p/kWh (EMEC, 2013). This cost is relatively high compared to wind energy (onshore wind 10 p/kWh, offshore wind $15-17p/kWh$, standard price provided by ScottishPower Ltd is $13.84p/kWh$ from 2015.). However, wave energy utilization has a relatively short development history (15-20 years behind wind energy technology). Therefore, it is anticipated that the price will drop further in the near future.

1.4 Aim and plan of the thesis

1.4.1 Aim of the thesis

Inspired by the reasons discussed above (and the current status and prospects that will be discussed in literature review), the main aim of this thesis is to assist on driving the wave energy extraction cost down by better understanding of the aspects that will bias the assessment of a particular WEC during its design and development stage. For detailed impact of assessment on driving the cost of WEC down, see literature review.

1.4.2 Plan of the thesis

A review of the wave energy extraction technologies will be first carried out to evaluate different type of WECs, followed by an investigation into the aspects

needing further research. Different methods for assessing the performance of a WEC will be reviewed.

Assessment on the performance of the selected device will be carried out by using the methods selected based on the literature review. The main difficulties lies in assessing the performance of a WEC will also be investigated by the selected methods.

Conclusion and recommendation will be drawn on how to predict the performance of a WEC better at the end of this thesis.

The detailed structure of this thesis can be found at the end of the literature review.

1.5 Chapter summary

This chapter introduced the background of this project and briefly described the benefit of wave energy compared with the other renewable energy resources. Having such a predominant wave energy resource, the UK government are keen to develop the wave energy industry. However, due to the high cost of the technology commercial success is some way off..

To drive the cost down, it is inevitable to have a better understanding of the performance of wave energy technology, especially on assessment of the performance of the WECs during their design and development stage (see literature review for detail).

Thesis plan is given in this chapter after defined the aim of current study.

Chapter 2

Literature review

2.1 Wave energy technologies

Wave energy technologies is reviewed in this section in order to evaluate different technologies.

2.1.1 Brief history of uk wave energy development

Comparing with some other renewable energy technology, wave energy converting technology has a relative short history. Although the first wave energy device invented can be traced back to 1799 by French father and son named Girard, the modern wave energy technology started around 1965 with the commercialization of a navigation buoy powered by wave energy in Japan. That navigation buoy (was named as oscillating water column (OWC) later) was developed by the father of modern wave energy technology Yoshio Masuda. After that, a much larger device: Kaimei was promoted by Masuda, however, since the knowledge of wave energy absorption was in its infancy, Kaimei was not a great success.

Wave energy was not a popular research topic until the explosion of oil crisis in 1973. Publication of "Wave power" in the journal of Nature by Salter (1974) brought wave energy to the attention of the international scientific community. Since then research into the wave energy technology flourished.

Before early 1990s, the activity remained mainly at academic level due to considerable theoretical difficulty. The most visible achievement in 1990s in European was the commissioning of the LIMPET power station in Islay Scotland

(2000). This is the world's first commercial onshore wave power device connected to the United Kingdom's National Grid. Since then several full scale size devices has been installed. Including the Archimedes Wave Swing (AWS), and the Pelamis which is the world's first commercial scale wave energy converter to generate electricity to a national grid from offshore waves.

Due to a lot of reasons, several promising wave energy developer ceased their company. In 2013, Voith Hydro decided to shut down WaveGen who developed the LIMPET power station. One year later, the Pelamis went burst. The Aquamarine Ltd which developed the Oyster device stopped their business in November 2015. In spite of the above sad news, the wave energy industry is still vigorous. Several existing and new company are developing and testing their wave energy devices under the support from the Wave Energy Scotland organization(WES). Table 2.1 listed some active promising UK developers and their devices.

Table 2.1: Some promising UK wave energy technology developers and their device.

Developer	Country base	Device name	website
AlbaTERN	UK	WaveNET (Squid)	http://albatern.co.uk
Mocean Energy Ltd	UK	Mocean Wave Energy Converter	http://www.moceanenergy.com
Zyba Limited	UK	CCell	http://www.ccell.co.uk
AWS OCEAN ENERGY	UK	Advanced Archimedes Waveswing	http://awsocean.com
Checkmate Seaenergy Ltd.	UK	Anaconda	http://www.checkmateukseaenergy.com
SeaPower	UK/Ireland	SeaPower Platform	http://www.seapower.ie

2.1.2 Classification of wave energy converters

Unlike wind energy utilization which is mainly based on wind turbines, there are several varieties of wave energy technologies. Thus several methods has been proposed to classify wave energy systems by researchers. For example, WECs can be classified into on-shore, near-shore and off-shore in the forms of installation position. Alternatively devices can be distinguished as motion-dependent and motion independent device if we look into the behaviour of WECs, see Figure 2.1 for example. A further popular classification is based on their basic working principal (Drew et al., 2009), where WECs can be classified into three predominant types as following.

Attenuator

Attenuators lie parallel to the predominant wave direction and 'ride' the waves. The world's first offshore WEC-Pelamis that generates electricity into grid is a

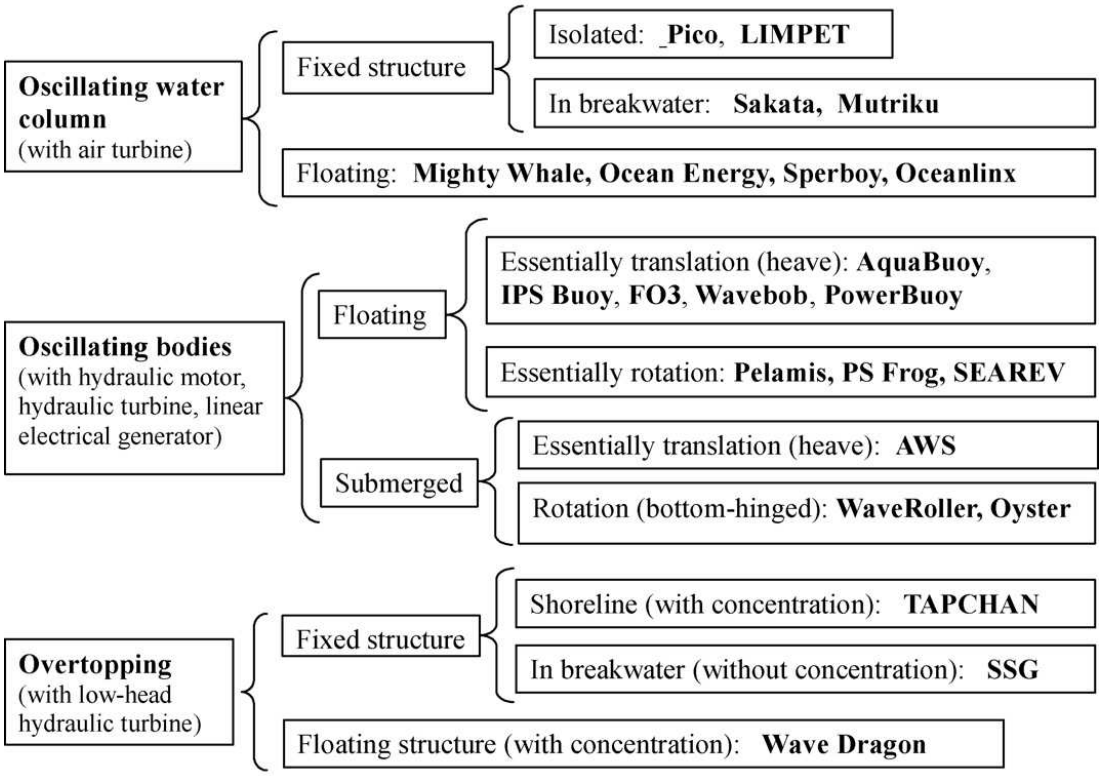

Figure 2.1: Classification of WECs proposed by Antonio (2010).

typical example as shown in Figure 2.2. The Pelamis WEC has a overall power conversion efficiency ranges from around 70% at low power levels to over 80% at full capacity.

Figure 2.2: Pelamis wave power machine. Figure is taken from Drew et al. (2009).

Checkmate sea energy's Anaconda (Anaconda, 2014) is another example, see Figure 2.3. This type of WECs usually has a relatively long and slender structure. Wave energy absorbed decreased along the structure length direction due to the fact that wave energy has been partially absorbed by heading part. Moreover,

since attenuator's power extraction relies on motion of device or relative motion between different parts of device, thus attenuator has less possibility to be an onshore device.

Figure 2.3: Anaconda WEC. Figure is taken from (Anaconda, 2014).

Terminator

As the name implies, terminator physically intercept waves. Their principal axis parallel to the wave front. Salter's Duck can be the most representative example as illustrated in Figure 2.4. As indicated by Salter, Duck device can convert wave energy at an amazing efficiency about 80%.

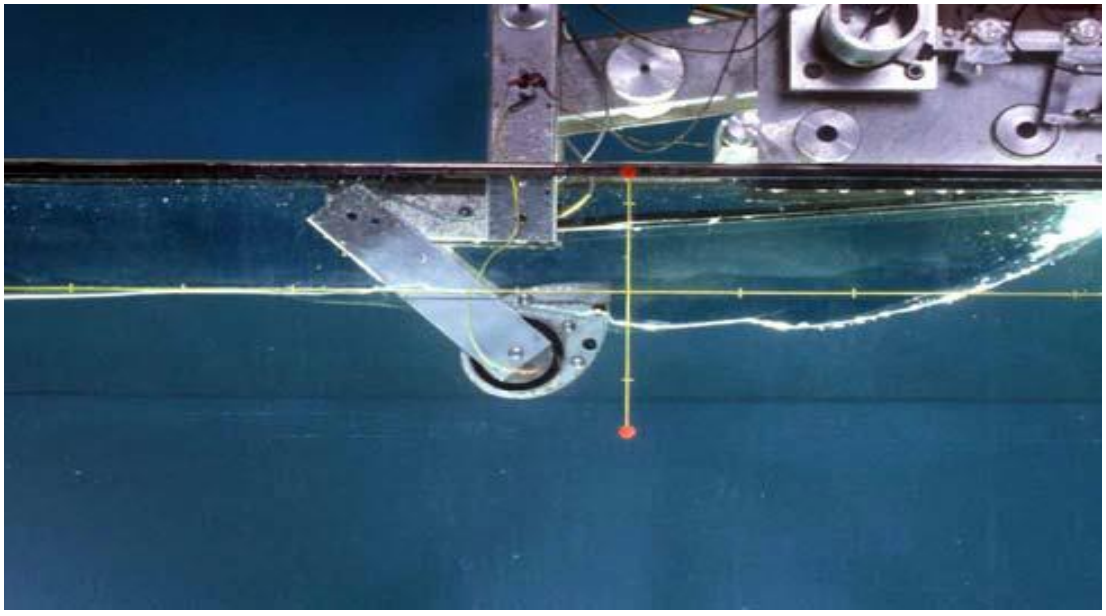

Figure 2.4: Salter's Duck. Figure is taken from Drew et al. (2009).

Due to the mechanics of terminators, the performance of most of the devices is quite directional sensitive. Moreover, for Oyster, it can only be installed near shore since it needs to be installed on the seabed-though this means that waves are mostly normal to device.

Point absorber

Point absorber can be floating devices that heave up and down on the water surface under wave excitation, for instance the OPT Powerbuoy (power technologies, 2014) shown in Figure 2.5. Alternatively they it can be a installed under water, utilizing the pressure difference caused by wave crests and troughs, for example, the Archimedes Wave Swing as shown in Figure 2.6. In either case, the point absorber has a relatively small dimension compared to the incident wavelength. Due to the axisymmetric structure design, point absorbers are usually not directionally sensitive.

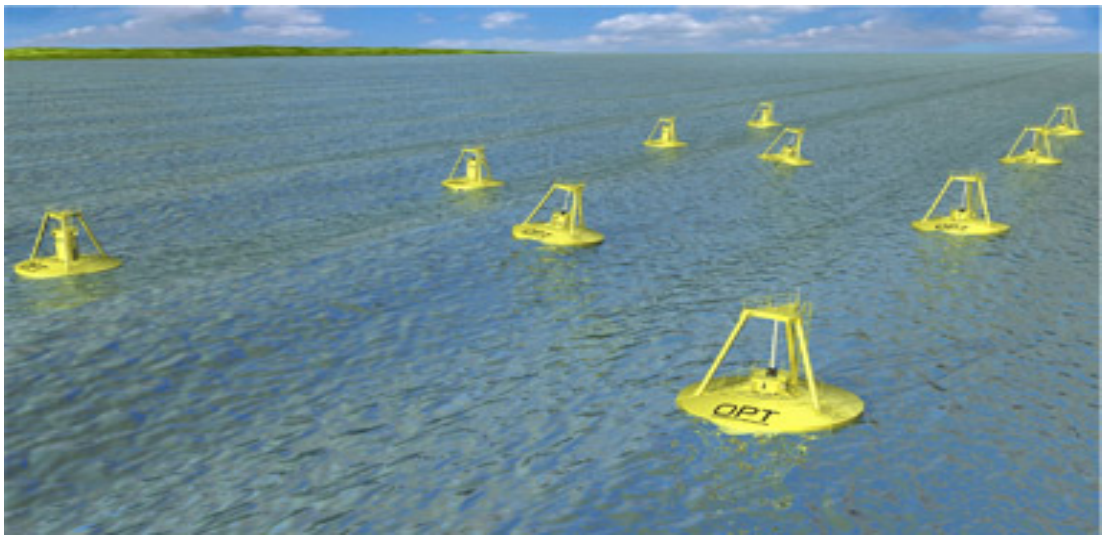

Figure 2.5: Floating absorber, the OPT buoy. Figure is taken from Drew et al. (2009).

2.1.3 Oscillating water column device

Although most WECs fall into one of the three categories discussed above, the Oscillating Water Column (OWC) device can be a terminator or a point absorber depending on different design configurations.

The OWC device is probably the only technology where a key part of the system can be seen as naturally occurring structure in the form of blow holes Heath

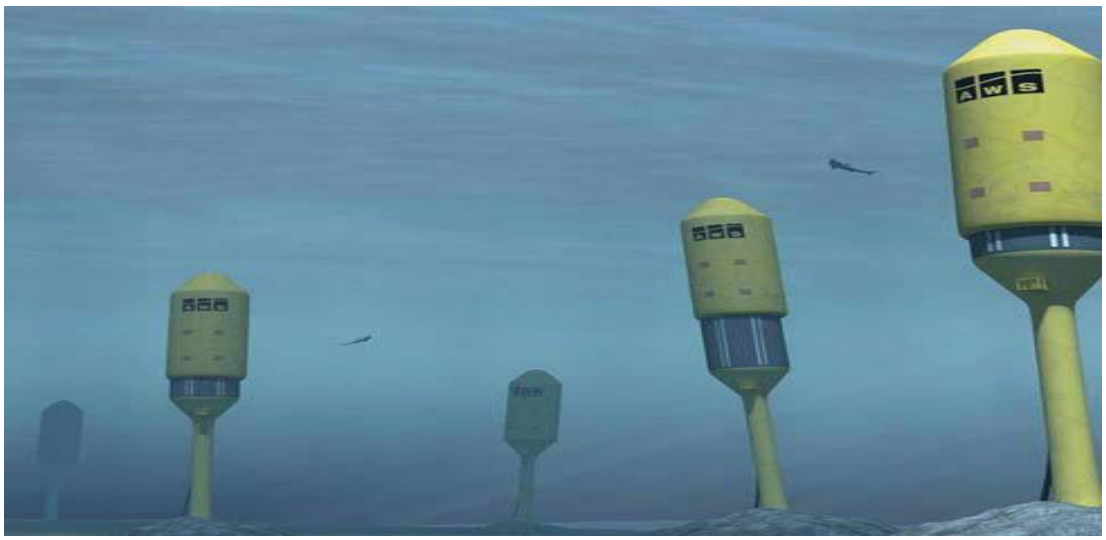

Figure 2.6: submerged pressure differential device: the Archimedes Wave Swing. Figure is taken from Drew et al. (2009).

(2012). These are common in limestone cliffs as shown in Figure 2.7.

Figure 2.7: Blowhole at Quobba Western Australia. Figure is taken from Heath (2012).

An OWC WEC usually comprises two main parts: an air chamber which acts as the first stage energy collector that transfers the wave energy into pneumatic power, and a power take off (PTO) system which converts the pneumatic power into electricity or some other form of energy. As illustrated in Figure 2.8, when the OWC device encounters waves, air inside the chamber is compressed and forced to pass throught the PTO system when the water column rises. When the water column falls, the reduced pressure will suck in air outside the chamber. Again, when the air passes PTO system, power will be generated. Usually, a self-rectifying turbine such as a Wells turbine or radial impulse turbine is chosen

to be the PTO system so that turbine will be driven in the same direction when water column rises and falls.

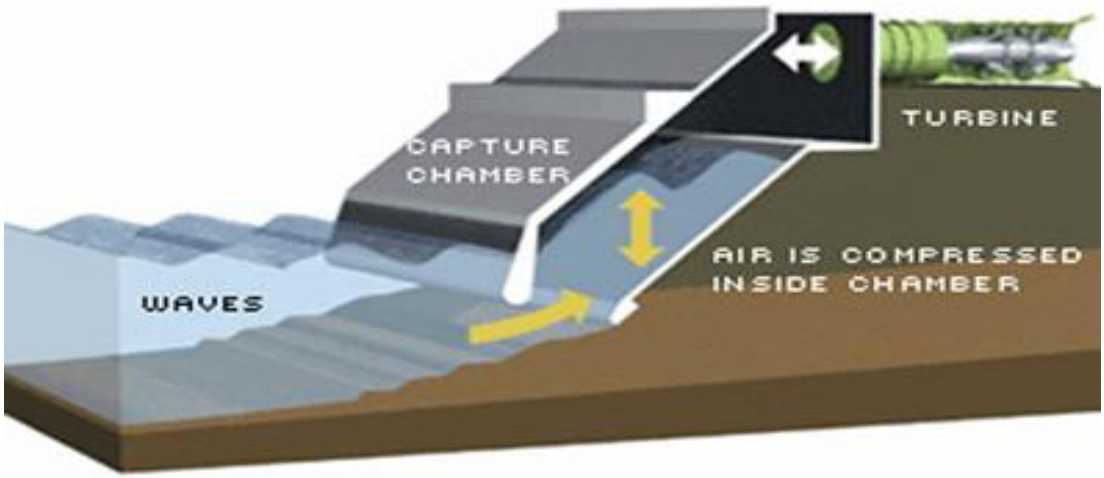

Figure 2.8: Shoreline OWC. Figure is taken from Poullikkas (2014).

A shoreline OWC device (Figure 2.8) is a typical representative application of this kind of technology and can be classified as a terminator while the floating OWC sparbuoy Figure 2.9(left) captures energy as a point absorber. Different designs make the OWC technology suit both onshore, near shore andoffshore applications.

Figure 2.9: Sparbuoy OWC (left); Mutriku power plant during a storm (right). Figure is taken from TETHYS (2012)

In addition to the flexible choice of working location, OWC is one of the few WECs which can embedded into some other facilities. For instance the Mutriku

wave power plant (TETHYS, 2012) (Figure 2.9(right)) located in Bay of Biscay in Spain extracts wave energy and provides coastal protection at the same time. Another possible application is sea water desalination. Oceanlinx limited claimed on 11^{st} November 2013 that their 'greenWAVE' device can produce fresh water from sea water by attaching a desalination unit.

Moreover, unlike most of the other WECs whose energy extraction depends mostly on the motion of the structure, OWC can maintain good energy converting efficiency even when the main structure is fixed in position. This feature makes OWC devices to be more suitable to combine with other renewable energy devices like offshore floating or fixed type wind turbine since the fact of relative motion between the two devices will reduce the risk of crashing each other under extreme weather condition. For instance, Bayoumi (2013) proposed a renewable energy converting platform consist of four OWC devices which are used as floaters of a wind turbine. It is pointed out that OWC devices and wind turbine can share the electrical cable and power transfer equipment to export the electricity to shore. In addition to the cable and power transfer equipment, combined OWC devices and offshore wind turbine can also share the mooring system which could further reduce the capital cost.

Last but not least, OWC devices has the most attractive characteristic that is its robustness which make it one of the most popular WECs from the beginning of wave energy technology.

For the above reasons, the OWC technology is selected to be investigated in the present study.

2.2 OWC technology development

2.2.1 Industrial development

OWC technologies were not used as WECs in the first instance. The earliest recorded application was a whistling buoy (Figure 2.10) serving as a navigation aid patented by J.M.Courtney. It was reported in Scientific American that 34 operating whistling buoys were installed along the coast of the USA in 1885 (Heath, 2012).

It was over half a century later when Masuda designed and installed the first OWC driving navigation light buoy (Figure 2.11) in Japan in 1947. Although the

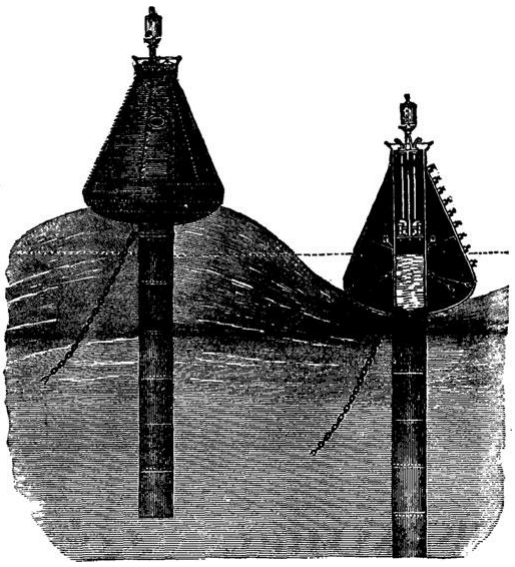

Figure 2.10: Whistling buoy. Figure is taken from Heath (2012).

output of each unit is low (about 70-500W), this device still represents the first successful case of converting wave energy into electricity (Antonio, 2010; Masuda, 1971). Thirty years later, Masuda promoted a larger floating device Kaimei in 1976, however, the desing output power is not achieved because of the fact that the theoretical knowledge of wave energy absorption was in its infancy.

Figure 2.11: Navigation buoy in Tokyo Bay. Figure is taken from Heath (2012).

During the 1980s and 1990s, several shoreline and shore-connected OWCs were built and tested in Japan, India, China, Norway, Portugal and Britain (Antonio, 2010). Including the small 75kW rated OWC shoreline prototype (Figure 2.12) at island of Islay developed by Queen's University (Whittaker et al., 1993), and a 60kW converter integrated into a break-water at the port of Sakata, Japan

(Ohneda et al., 1991).

Figure 2.12: Queen's University Belfast 75kW demonstrator on Islay. Figure is taken from Heath (2012).

In late 2000, the LIMPET (Figure 2.13) plant (Heath et al., 2000) designed by Wavegen and Queen's university team was commissioned. It was originally rated at $500kw$ and was later downgraded to $250kW$ due to miscalculation. Even though its performance was not as powerful as intended, the LIMPET is a milestone in the development history of OWC devices since it is the first commercial wave power device connected to the United Kingdom's National Grid. In the same year, Japan Marine Science and Technology Center developed another floating OWC named Mighty Whale and tested near the mouth of Gokasho Bay, in Mie Perfecture, Japan (Washio et al., 2000).

During the past decade, more devices have come to open sea tests or commercial stages, including both fixed and floating type devices. For instance:

The first multiple oscillating water column (MOWC) plant offering the opportunity for studying the interaction of the units and the complexities of multiple control was commissioned in spring 2011 at Mutriku in the Pais Vasco of northern Spain (Heath, 2012).

A $1/4^{th}$ scaled model of Backward Bent Duct Buoy (BBDB Figure 2.14) has been tested in the sheltered sea waters of Galway Bay (western Ireland) since the end of 2006 (OceanEnergy, 2014).

Compared with fixed type OWC WECs, the floating type OWC WECs have the advantage of higher power capture efficiency and capture bandwidth since they are designed to have multiple resonance (resonance of the OWC itself and

Figure 2.13: Wavegen LIMPET OWC plant. Figure is taken from Heath (2012).

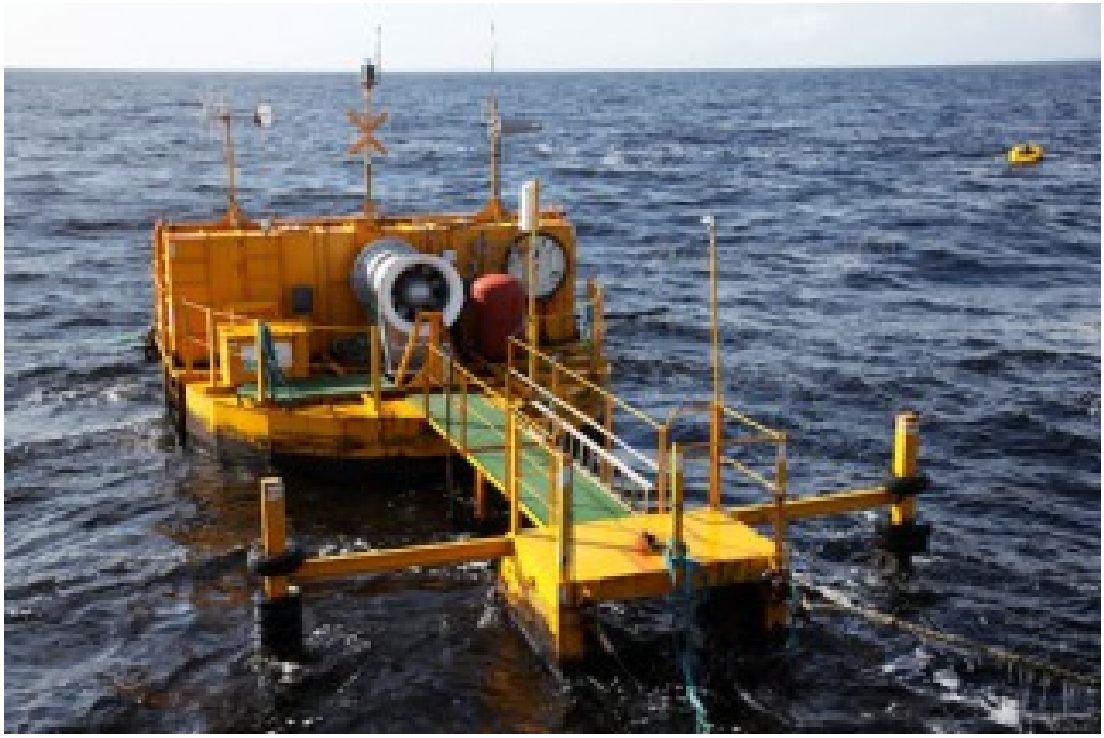

Figure 2.14: Backward Bent Duct Buoy (BBDB). Figure is taken from OffshoreWind.biz (2012).

resonance due to the floater.). However, they are yet not cost effective because their design and construction is more technically difficult. In addition to requiring additional structure cost for the floater, floating type OWC WECs requirea proper mooring system. Especially for the BBDB type OWC devices, as well as anchoring the device, the mooring system is required to be designed in such a way so that the device will be facing the incoming wave itself to maximise the performance. Maintenance would be another drawback of the floating type device since the

maintenance usually could not be done on site and required towing back to a dock. Therefore only fixed type OWC WEC will be considered in the remaining part of this thesis.

2.2.2 Research development

To provide theoretical support, research activities were carried out in full swing since the publication of "Wave power".

In the second half of the 1970s, several distinguished mathematicians published several papers to solve the wave energy absorption which is a hydrodynamic process of considerable theoretical difficulty. For instance, Evans (1978) derived the theoretical maximum efficiency for a 2D symmetric OWC device by assuming the OWC moves like a rigid piston. It was concluded that for a 2D axis-symmetry OWC device (Figure 2.15 (a)), the maximum power capture efficiency (defined as the ratio between the captured power and the available power in the incident wave. can not exceed 50% and the maximum capture width (defined as the ratio between the efficiency and the width of the device. can no be larger than $1/k$ for a 3D axis-symmetry tube. Here the k is the wave number of a linear wave.

Since the piston model can not account for the spatial variation of the OWC, Evans (1982) extended Stoker (1957)'s work and applied the pressure distribution to describe OWC. Results showed that the same maximum efficiency and capture width ratio for a 2D symmetrical rectangular OWC and a 3D tube can be achieved as those calculated based on rigid piston model.

It is pointed out that pressure distribution model can describe the physical situation more accurately than the piston model (Sarmento and Falcao, 1985). Moreover, such pressure distribution model also has the advantage of producing simpler boundary value problems to be solved.

Using the pressure distribution theory, Sarmento and Falcao (1985) analysed the effects of finite water depth, air compressibility and the turbine character. It was noted that for smaller relative depths (defined as the ratio between the water depth and wave length) the air compressibility affects the efficiency. It is suggested that for a scaled model test, the volume of the air inside the air chamber should be equal to the corresponding full-scale value. Besides, it was noted that linearising the spring like air compressibility can provide a satisfactory approximation to results obtained by using non-linear isentropic pressure-density

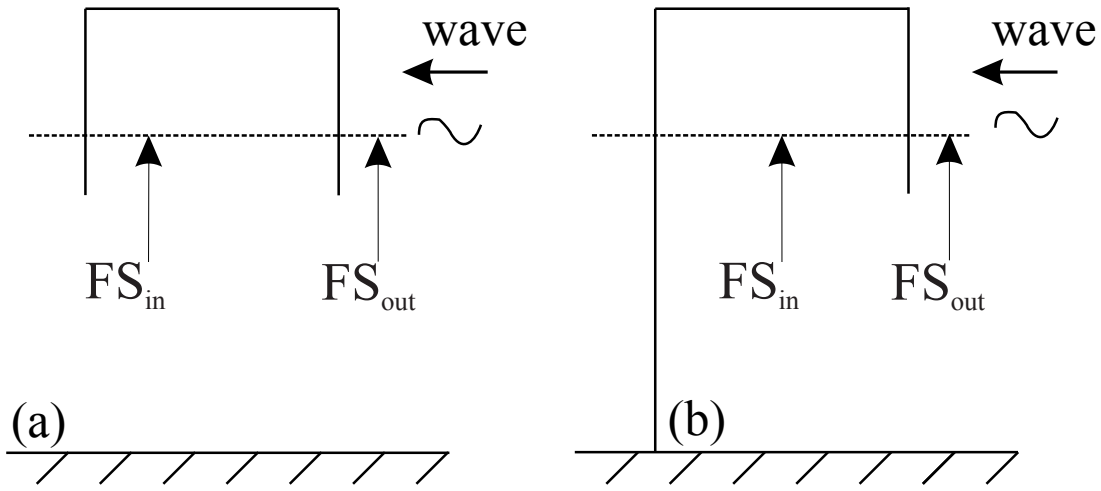

Figure 2.15: Illustration of symmetrical and Asymmetrical OWC devices: (a) symmetrical device,(b) asymmetrical device. Where FS_{in} and FS_{out} is free surface inside and outside the chamber respectively

relation. Another remarkable outcome from this paper is that it was found that applying a vertical reflecting wall at the back of the device extending to the sea bottom will prevent energy loses due to transmission of wave. Theoretically, unity capture efficiency can be achieved by the present of such a reflecting wall when the reflected wave from the reflecting wall cancel the radiated wave from the chamber. Hereafter, this type devices are referred as axis asymmetry device as illustrated in Figure 2.15 (b)). Moreover, it was found that even if the device is equipped with a strongly non-linear PTO system, unity efficiency could still be reached. Namely, the maximum efficiency that the device can reach is independent of the PTO form (linear or non-linear). However, the efficiency became dependent on the incident wave amplitude and wavelength while efficiency of linear PTO only depends on the wavelength.

Seven years later, Sarmento (1992) carried out a tank width wide OWC experiment investigated both symmetrical and asymmetrical OWC WECs to validate his pressure distribution theory, in which the energy extraction is calculated by subtracting the transmitted and reflected energy from the incident wave energy (Knott and Flower, 1979). Due to the method he adopted to calculate the power captured, the energy loss due to air-water interaction and PTO mechanics cannot be included in the final pneumatic power. This leads to the calculated efficiency being slightly higher than that actually should be. Two different types of PTO systems were simulated in this experiment. A porous filter represented linear PTO simulating a Wells turbine while a non-linear PTO representing a unidirectional turbine with a system of valves was simulated by circular orifice plate. It is

concluded that the maximum efficiency achieved by a non-linear PTO system is almost the same as that of linear one. Furthermore, effect of the immersion of the front wall was also investigated. Results showed that increasing of the immersion of the front wall shifts the resonant point to lower frequencies and induces narrower efficiency curves, however, the maximum efficiency is independent of the immersion depth. The increasing of the immersion of the front wall leads to growth of the inertia of the OWC inside the chamber, therefore natural frequency is decreased. It is once again predicted that the maximum efficiency equal to unity is expected whenever the radiated and the reflected waves cancel each other which requires the same wave amplitude for both waves and a phase shift of $\pi/2$.

Whittaker and Stewart (1993) checked the effect of a channel or 'harbour' in front of the entrance to the water column. They found that a rectangular harbour can widen the frequency bandwidth of OWC, however, maximum power output is not improved. When the same OWC device is embedded in a fully reflecting coastline, the maximum power output is improved by a factor of 2. Furthermore, by using a tapered harbour with a length similar to that of the rectangular harbour, the maximum capture factor is almost 3 times than that of an OWC device without a harbour.

Koola et al. (1995) investigated a harbour like OWC device in a 3D model. The influence of the length of the device, lip thickness and sidewall thickness were studied. It is concluded that thicker walls with rounded edges enhance absorption capability.

Evans and Porter (1995) proposed an efficient calculation method to study a 2D asymmetrical shoreline OWC. Different parameters including draft and the length of the front wall were studied. Using the same method, Evans and Porter (1997) extend the work to a 3D Fixed type axis Symmetry Cylindrical OWC (FSCOWC) device. He concluded that these devices do not appear very attractive for long-term development as part of commercial wave-power plants. Which indeed was the declaration of death for the FSCOWC device.

Probably due to the theoretical performance of an asymmetric type OWC is better than that of an axis symmetry type OWC WEC, researchers started to study asymmetric type OWC WEC extensively aiming to further improve the performance of the device:

Wang et al. (2002) performed an analytical and experimental study on the hydrodynamic performance of an onshore OWC device. The effect of bottom slop

was examined. It is found that when the slope of the bottom increases, the peaks of the capture-width ratios will shift to lower frequency.

Morris-Thomas et al. (2007) found that the front wall geometry has a minor effect on the maximum performance of the OWC device, however, it tends to affect the overall shape and bandwidth of the hydrodynamic efficiency curve. It is also pointed out that the increase in front wall submergence and thickness appears to reduce the hydrodynamic efficiency in short waves. Their result showed a good agreement with inviscid 2D theory in overall trends. The large difference in magnitude is caused by the reason that inviscid ideal fluid cannot model the viscous energy loses and the theory is performed with optimum PTO damping.

More recently researches found that the performance of asymmetric device is quite sensitive to the incident wave direction (Jin et al., 2012; Ikoma et al., 2013), due to the reason that the available energy received by the device is less than the case that the encounter with wave orthogonally). In fact it is not difficult to imagine that for a 2D asymmetric device, if the wave comes from the opposite direction, all the incident wave will be reflected leading no power captured at all.

Latest review of the OWC wave energy technologies include both fixed and floating type devices can be found in Falcão and Henriques (2016).

2.3 Current status and prospects

Although OWC technology is now much more mature than before, there has not been a greater uptake for commercial deployment. As pointed out by Heath (2012) that it is still not cost effective because:

- Projects are small so that project costs are disproportionately high.
- Small volumes mean high equipment cost.
- Poor grid infrastructure at suitable coastal sites mean high connection charges.

To resolve this cost effective problem, it is first required to reduce the total costs in the whole project. As well as the three aspects already mentioned above, the structure cost (including the devices itself and anchoring system.), installation and maintenance cost also need consideration.

The second crux would be make the device itself more effective. That requires the designed device to produce the output predicted by the designer. In particular, it is critical to assess the performance of the device accurately during their design and development stage.

2.4 A cost effective scenario

To propose a cost effective scenario, it is worthwhile to look into the reason why the conventional fixed OWC devices has not been not a great success.

With decades' research on improving the efficiency of the fixed type asymmetric OWC WECs, the actual extracted power of this type of OWC WEC is not as amazing as the theoretical conversion efficiency (Maximum 100%) mainly due to:

- This type of OWC WECs are usually installed at the shoreline where the available incident wave power is lower than that of near shore and offshore devices due to friction of seabed and wave breaking etc.
- When the water depth is small while the wave length is relative large, the shallow water changes the fundamental hydrodynamics of the waves and the fluid motion is dominated by horizontal velocity. This produces substantial wave run-up on the front wall and leads to sloshing of the water column inside the chamber. Both of these two phenomenons further dissipate energy.

As indicated by Folley and Whittaker (2009), compared with the net wave power density with deep water (where water depth equals to $50m$), the net wave power density reduced by 40% to 70% at water depth of $5m$ depending on the seabed slop (Figure 2.16). Here net wave power density is directionally resolved power density that is propagating orthogonally to the seabed contours. The asymmetric type OWC WEC will effectively receive that amount of available energy only when the WEC device is aligned with the seabed contours and the opening of the device is orthogonal to the incident wave direction.

The incident power loss problem can be compensated by moving the device to near shore or even offshore site. However, as well as the substantial structure capital and installation cost increase with water depth, transportation of the device and installation will be another issue. For instance, Oceanlinx Ltd developed a $1MW$ rated reinforced concrete OWC WEC 'GreenWave' (Figure 2.18) which will be placed at a water depth around $10m$. The device was designed to sit on the seabed

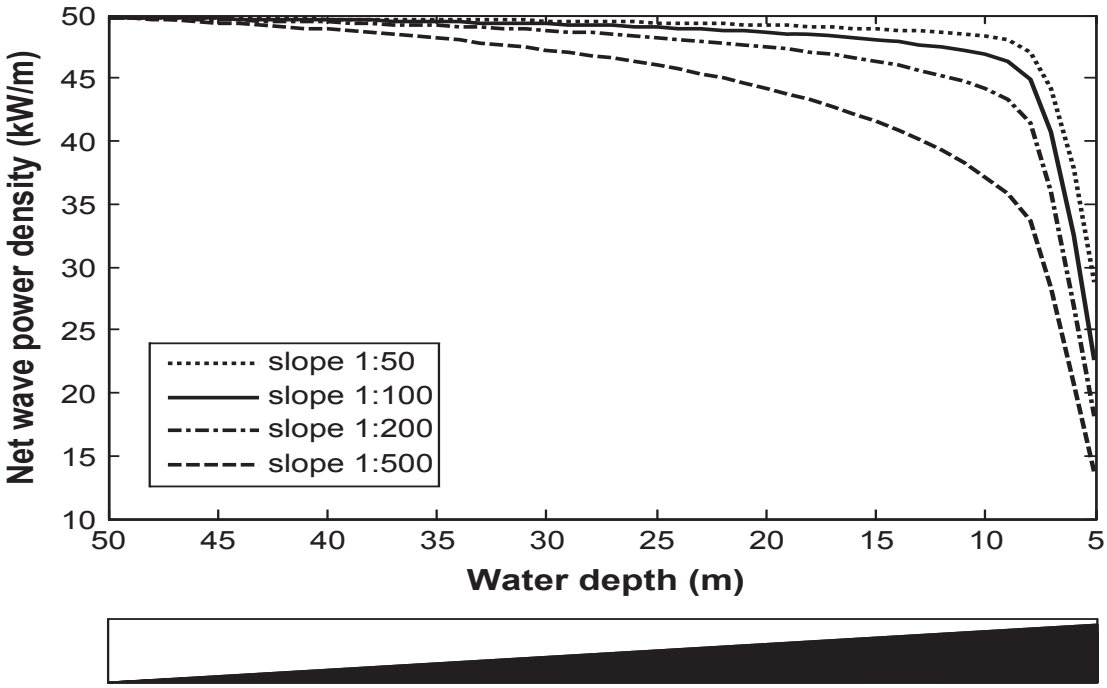

Figure 2.16: Shoaling of a 10s energy period wave propagating orthogonal to depth contours for different seabed slopes. Figure is taken from Folley and Whittaker (2009).

by its own weight. Due to the failure of providing enough buoyancy by the air bags, the 3000 tonnes monster sank and was damaged beyond repair under tow to the specified site. Oceanlinx Ltd went into administration with the failure of the £7 million device.

On the other hand, symmetric type OWC device do not need to be extended to the seabed which will dramatically decrease the civil and structure cost. The drawback of symmetric type OWC device, as known, is that the maximum efficiency of a symmetric device is half of the asymmetric type device. However, the output power could be at least similar (or even greater) to a shoreline asymmetry device by moving the device to near shore/offshore. Having a much lower investment while at the same time produce similar power, symmetric type OWC device will be more cost effective than asymmetric type device.

Since wave propagating is not unidirectional at near shore/offshore site, cylindrical symmetry structures would be an appropriate design to avoid reduction in power capturing performance due to incident wave direction.

The only question is how to anchor the device with as less investment as possible. Attaching the device to some existing near shore/offshore structure seems being able to resolve this issue. As addressed by Pérez-Collazo et al. (2015), combining WECs to wind turbine can reduce substantial operational cost by sharing operation

Figure 2.17: Reinforced concrete Greenwave device under construction

and maintenance costs of wind turbine while wind turbine can reduce the energy cost by sharing the grid connection, the logistics and common infrastructures.

Except for economics, one more benefit of combining WECs and wind turbines is that this combination can secure the maintenance ship by providing a relatively calm environment behind the WEC device since the WEC will absorb part of the incoming wave energy.

Take all the factors talked above into consideration, a Fixed Symmetry Cylindrical OWC (FSCOWC) device is proposed with the anchoring problem solved as shown in Figure 2.18, where the connection is a connection bridge that provide access to the FSCOWC device for maintenance.

This type of FSCOWC device is of particular benefit for research. I.e. the simplicity of the main structure itself (basically a hollow tube.) makes it easy to be built and reproduced at different scale. By using orifice plates to represent the PTO system, there appears no moving part apart from the OWC itself, hence, the power loss due to mechanical friction can be ignored. This will provide the opportunity of addressing the air-water two phase interaction problem without unrealistic idealisation.

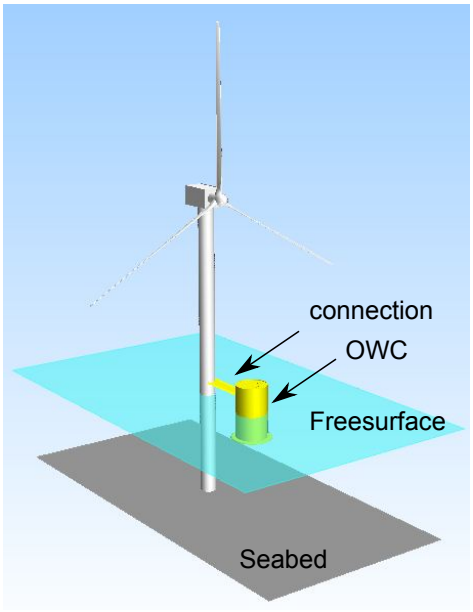

Figure 2.18: Sketch of a combined wind and wave power system

Current study aim to assess the performance a FSCOWC rated capacity of about 1 megawatt at full scale (only hydrodynamic power is considered in current study, that is, the power loss due to PTO efficiency and electricity transmission is omitted.).

Having proposed a cost effective scenario, the rest of this thesis will focus on the second key aspect discussed in the prospects section. That is to develop a methodology and procedures to assess the performance of the proposed FSCOWC device.

2.5 Existing numerical assessment methods

Assessing the performance of the WECs by experiment is generally a good and accurate method since it can reproduce the behaviour of full scale device by proper scaling. However, for the OWC type device the situation is slightly different. As said by Cruz (2007), "A major difficulty is that experimental studies on OWCs are not easy to perform: the hydrodynamic and pneumatic flows require different model scales and the influence of vortex shedding and viscous effects is difficult to infer from small-scale experiments. This makes mathematical and numerical modelling a particularly valuable tool in the development valuable tool in the development of OWCs."

It is noted that early numerical researches are mainly carried out by using potential

theory, namely only inviscid, irrotational and linear problem are investigated. With the development of computer science, it is now possible to study the wave structure interaction problem with some more advance methods like boundary integral equation methods (BIEM) and Computational Fluid Dynamics (CFD). Li and Yu (2012) summarized and compared the advantage and disadvantage of current numerical methods that are popular in the wave energy sector (Table 2.2).

Table 2.2: Features for different numerical scheme

Feature \ Methods	Analytical	Morison	Frequency domain BIEM	Time domain BIEM	CFD
Viscous Effect	No(but can be input)	Yes (Empirical)	No (but can be input)	No (but can be input)	Yes
Wave body interaction	Linear	body has no effect on the waves	Weakly nonlinear	Fully nonlinear	Fully nonlinear
Wave breaking	N/A	N/A	N/A	N/A	Free surface can be modelled by VOF
General accuracy	Acceptable	Acceptable for mooring line	Good	Good	Very good
Accuracy around resonance	Barely acceptable	Acceptable with modified hydrodynamic coefficients	Barely Acceptable (high order scheme)	Acceptable	Very good

Typically, the exact value of response at resonance is not important for ship and offshore platform study since the resonance frequency will be avoided during the design process to maximize the survivability of the structure. This is why some simple and fast numerical methods are popular in these areas. On the contrary, the accuracy at resonance is rather important for wave energy devices since the maximum power output is usually at resonance frequency. Therefore, Reynold Averaged Navier-Stokes Equation Method (RANSEM, also known as CFD) is selected for further study.

2.6 Areas for study

2.6.1 Experiment

2.6.1.1 Available reliable experiment data

Probably due to its' low efficiency, there are not many experimental researches about FSCOWC devices. Most researchers did some FSCOWC experiment to be their first step towards a spar floating type OWC. For instance, Sykes et al. (2008) investigated the hydrodynamic performance of a FSCOWC device using a boundary element model WAMIT without considering the damping effect induced by the PTO system. Results in the software were validated against physical testing. Good agreement was achieved except for the resonant region due to the limitation of potential theory.

Sheng et al. (2012) compared the primary conversion efficiency of different OWC devices from model tests database. Results revealed that FSCOWC device's performance is much lower than the other types of OWC devices. However, since the scale of the FSCOWC device is much smaller than the other type of OWC devices, the efficiency of the FSCOWC device may be significantly underestimated due to scale effect.

Therefore, carrying out an experiment of a moderate size FSCOWC device is the first task.

2.6.1.2 Assessing the incident wave power

To accurately predicate the performance of a WEC, precisely evaluating the incident wave power is critical. In practice, the power in waves from a physical wave maker is not as precise as wave theory suggests since wave theory neglected some practical aspects (e.g. viscosity of water). Hence, the generated wave is usually different from the target value in wave height but identical in wave frequency. As known, the incident wave power is, according to linear wave theory, directly proportional to square of the wave amplitude, therefore, slight difference in wave heigh may lead to a relative large difference in power calculation. The simplest way to measure the incident wave amplitude (hence the power) is to use a wave probe in front of the WEC device and measure the incoming wave before it will reached the WEC device. For example,Koola et al. (1995), Wang et al. (2002) and Bayoumi (2013) all used this method to determine the incident wave amplitude. However, this method has several drawbacks:

- The position of the wave probe which is used to monitor the incident wave is critical. It should be located at a place where is free of evanescent wave due to wave maker (Dalrymple and Dean, 1991) and at the same time away from the WEC device in order to avoid the reflection, radiation and diffraction from the device. This is critical especially for long wave which travels at high phase velocity.
- Since the incident wave amplitude is measured away from the device, wave decay due to viscosity along propagating direction can not be captured which will leads to a slightly overestimated incident wave power than the device actually received hence underestimated the capture efficiency or capture factor.

Another method to monitor the incident wave amplitude is to use two or more wave probes in front of the device (usually not very far from the device), neglect the reflection and other disturbance at testing stage. Once finished testing, incident wave can be separated from the total wave field by the method described in Knott and Flower (1979). For example, He and Huang (2014) and López et al. (2014) used this method.

Both methods mentioned above neglected the spatial variation of the tank (Lamont-Kane et al., 2013) which means even if the wave probe is free from evanescent waves (evanescent waves are standing waves which decay away from the wave maker, and being virtually negligible typically after 2-3 times the water depth away from the wave maker. For details of evanescent waves, see Dalrymple and Dean (1991)) and other disturbances it may be still different from that the device actually received. Thus, a proper method of estimating the incident wave power should be developed.

2.6.1.3 Scale effect

The main purpose of a small scale tank testing of a WEC is to represent the full scale device by a model scale model. This requires scaling the model according to the full scale device correctly so that the geometry, kinematics and dynamics are scaled properly.

A lot of effort have been expended on the theoretical scaling aspect for WECs, for instance, Sheng et al. (2014) and Falcão and Henriques (2014). There are only a few researches published on experiment aspect. For example, Forestier et al. (2007) studied three different scaled OE buoy (The BBDB floating OWC device shown in Figure 2.19.) and concluded that the inital trials at small scale give reasonable representative results even with lots of simplifications. The simplifications made in their test include neglecting the air compressibility scaling, tank size scaling etc. To accurately assess the performance of a WECs, this simplification should be avoided.

2.6.1.4 Tank width effect

Another aspect need consideration is the impact of wave blockage (tank width) effect. Existing guidance for structures like offshore platforms which are generally designed in such a way so that the interaction with waves is small, may not

Figure 2.19: Two different scale models used in Forestier's experiment. (1:15 left and 1:50 scale right.) Figure is taken from Forestier et al. (2007).

suit WECs which are designed to maximise the interaction with wave. Several researchers have studied this wave blockage effect by numerical simulation, for instance,

Ersdal and Moe (2013) talked about the tank width effect by treating the wall as a mirror. Extra devices were placed beside their device to mimic the reflected wave from the side wall. Gomes et al. (2015) investigated this problem using the BEM package WAMIT and result indicated that the presence of the side wall may have significant impact on assessing the performance of the device.

2.6.1.5 Uncertainties in the measurement

It is noted that most researches about OWC did not include an uncertainty analysis of their experiment. As pointed out by Lamont-Kane et al. (2013), physical experiments suffer from errors compared to the true value of the quantity of interest due to the fact that physical experiments and measurements may not be completely repeatable and reproducible. Without considering the uncertainties, one may get different results from each testing even with the same facilities and

model. Although there are several guidelines for estimate the uncertainties in tank testing of resistance and sea keeping, there is no guidelines on estimating the uncertainty in the WECs testing. To make the assessing more meaningful, it is necessary to develop a procedures to estimate the uncertainties in the proposed FSCOWC device.

2.6.2 RANS simulation

2.6.2.1 3D fully nonlinear coupled simulation

Early CFD works on OWC devices neglected the wave structure interaction and assume that the response of the internal free surface is known. For example, El Marjani et al. (2008) modelled a 3D air chamber with a rigid piston that was given a specified harmonic motion.

Later on, Şentürk et al. (2011) studied an 2D OWC device using the commercial software FLUENT by decouple the problem into two parts. They first recorded the internal water elevation in a 2D numerical wave tank. After that, the recorded free surface elevation was applied to a piston that drove the air in a 3D air chamber. This again separated the OWC and PTO into two uncoupled problem.

Zhang et al. (2012) included the wave and air coupling effect in his 2D simulation by using the level set method. The PTO system was represented by an orifice. Results were compared with experiment carried out by Morris-Thomas et al. (2007). Agreement between CFD result and experiment result was not good, probably because the thickness of the orifice was not modelled correct since there was no detail about that in Morris-Thomas et al. (2007).

Kamath et al. (2014) compared the CFD results of a fixed type asymmetric type OWC from 2D and 3D simulation. Results between each simulation were almost identical. The reason is that the 3D model used was indeed a 2D case extend in device width direction, that is the tank width equals to the width of the OWC device. Therefore wave diffraction were not modelled and the radiation problem was only modelled in the wave incoming direction.

For a cylindrical device, 2D simulation will not model the water column correctly, and thus will not be able to predict the performance of the device accurately. Which require the CFD methodology being capable of simulating the proposed device in 3D model.

2.6.2.2 Reflection free numerical wave tank

One common challenge in simulating the OWC problem is usually neglected by some researchers. That is the reflection from the numerical wave maker. For instance, both Luo et al. (2014) and Zaoui et al. (2014) did not consider that aspect.

Later on, López et al. (2014) proposed a wave maker based on mass source term (Lin and Liu, 1999) that will not interact with the reflected wave and placed a wave beach behind the wave maker to absorb the reflected wave. Due to the nature of this wave generation (only specifying the mass and neglected the momentum., the wave generated is quite sensitive to the location of the mass source and hence require trial and error to get desired wave property.

Later on, Kamath et al. (2015) studied the PTO damping in an OWC device using a reflection free numerical wave tank based on the relaxation methods proposed by Larsen and Dancy (1983). The configuration of their numerical wave tank is shown in Figure 2.20. Here the relaxation zone 1 is wave generation zone and the relaxation zone 2 will compute the difference between the analytical solution and the numerical solution. By adding a source term into the momentum equation, the wave will be kept to be the same as analytical one.

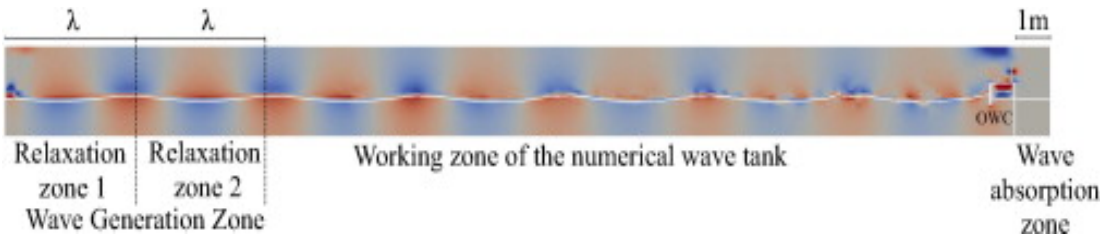

Figure 2.20: Kamath's reflection free numerical wave tank configuration.

As can be seen from Figure 2.20, this method require at least 2 additional wavelengths added to the domain length to achieve the reflection free condition. This is acceptable for two dimensional simulation while on the other hand, when extending to three dimensional simulation this will lead to considerable increment in mesh number (due to dense mesh in wavelength direction.) and hence require additional computing resource. Therefore, to develop a reflection free three dimensional numerical wave tank with reasonable mesh number is one of the key requirement of current work.

Since most of the previous work addressed shoreline devices and no waves are allowed to pass the device, there is no need to adopt a wave beach like absorption

technique to prevent reflection from the end of the tank. In the present study, the wave will pass the device and encounter the outlet of the wave tank, hence, wave absorption at the end of the tank is also need in current numerical wave tank.

2.7 Research objectives and thesis structure

According to literature review, the main objectives to achieve the aim proposed in Chapter 1 along with the structure of this thesis are listed as following:

- Introduction to the backgrounds, the motivation, the aim and the plan of current study is given in Chapter 1.
- Review of the wave energy technology is given in Chapter 2. By comparing the merit and drawback of each different type WECs, the OWC type WECs was selected to be the object of study. A cost effective FSCOWC WEC was proposed in this chapter as well. Areas for study were also discussed.
- The basic FSCOWC theory described the pressure distribution theory is introduced in Chapter 3.
- Experiment of a moderate scale FSCOWC device ($1:50^{th}$ of a full scale FSCOWC device) is designed and executed in Chapter 4 to obtain a reliable tank testing data. A methodology and procedures on how to estimate the uncertainty will be established. A method of more accurately assessing the power in the incident wave will be proposed.
- In order to investigate the tank width and scale effect on the assessment of the performance of the FSCOWC device, a small scale FSCOWC experiment is carried out in Chapter 5.
- A reflection free numerical wave tank that is suitable for FSCOWC device simulation is designed and investigated in Chapter 6.
- RANS simulation for the large scale FSCOWC device is studied in Chapter 7.
- The small scale FSCOWC device is simulated by using RANS method in Chapter 8. Simulation of the open sea condition will be provided in this chapter to investigate the device's performance without the impact of tank wall. A further scaled up FSCOWC device ($1:16.67^{th}$ of a full scale

FSCOWC device) simulation will be carried out to investigate the scale effect.

- Individual investigation of the simulated PTO system (orifice plate) will be given in Chapter 9.
- Conclusion and discussion will be drawn in Chapter 10.

Chapter 3

OWC theory

3.1 Chapter overview

As discussed in the literature review, analytical methods based on potential theory do not perform as well as RANS simulation. However, studying the problem using analytical method can provide a better insight into the physics of the problem. Hence, in this chapter Evans and Porter (1997)'s pressure distribution theory will be adopted to study the proposed OWC device. Basic notations and equations on how to calculate the capture factor etc. are presented.

3.2 Theory of pressure distribution

For the proposed OWC device (Figure 3.1), it is expected that the internal free surface FS_{in} is subjected to a time varying pressure $P(t)$ which has the same frequency (ω) as the incident wave plus the atmosphere pressure P_a. It is assumed that the pressure will be acting on the internal free surface vertically only, namely the horizontal pressure will be neglected. The water depth h is constant and in this case equals to $2.1m$. The atmosphere pressure is the only force acting on the external free surface FS_{out}. Using the coordinates system as illustrated in Figure 3.1 and assuming linear wave theory, the velocity potential $\Phi(x, y, z, t)$ satisfies the well known Laplace equation and solid boundary conditions:

$$\nabla^2\Phi = 0, \text{in the fluid} \tag{3.1}$$

$$\Phi_n = 0, \text{on solid boundaries} \tag{3.2}$$

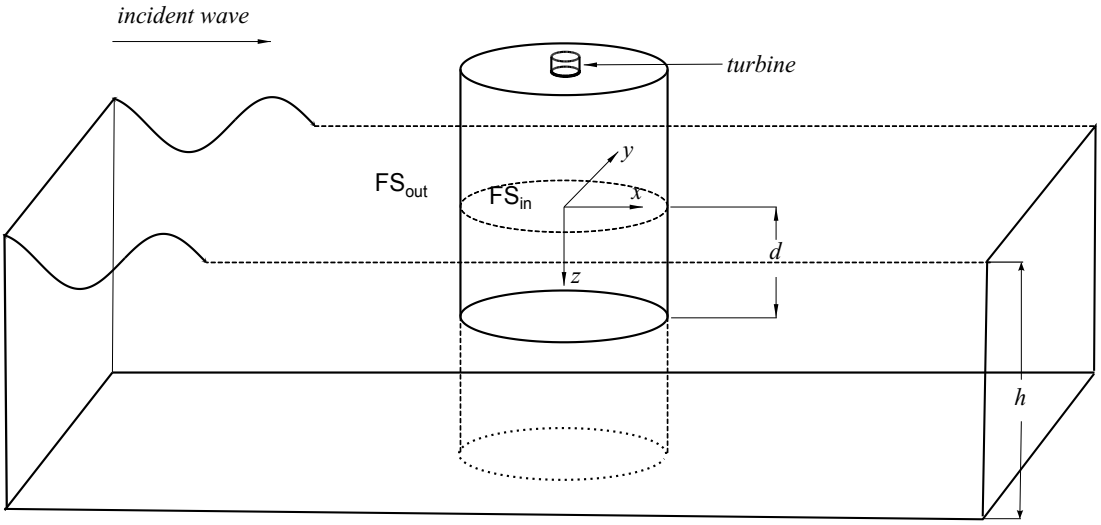

Figure 3.1: Sketch of the proposed OWC device

Here the suffix n is the surface normal and the linearised free surface condition becomes

$$g\eta - \frac{\partial \eta}{\partial t} = \begin{cases} (P_a + P(t))/\rho, & \text{on } FS_{in} \\ P_a/\rho, & \text{on } FS_{out} \end{cases} \tag{3.3}$$

Where ρ is the density of the fluid and $\eta x, y, t$ is the time varying free surface elevation. η is related to the velocity potential by

$$\frac{\partial \eta}{\partial t} = \frac{\partial \Phi}{\partial z}, \text{on z=0} \tag{3.4}$$

All the quantities Φ, P and η can be coverted into a time-independent form Falnes (2002) by using complex potential as

$$\Phi(x, y, z, t) = Re\{\phi(x, y, z)e^{-i\omega t}\} \tag{3.5}$$

$$P(t) = Re\{pe^{-i\omega t}\} \tag{3.6}$$

$$\eta(x, y) = Re\{\eta(x, y)e^{-i\omega t}\} \tag{3.7}$$

Replacing Equation 3.1-3.3 into a time-independent form we have

$$\nabla^2 \phi = 0, \qquad \text{in the fluid} \tag{3.8}$$

$$\phi_n = 0, \qquad \text{on solid boundaries} \tag{3.9}$$

With the free surface conditions

$$K\phi + \frac{\partial \phi}{\partial z} = \begin{cases} -i\omega p/\rho g, & \text{on } FS_{in} \\ 0, & \text{on } FS_{out} \end{cases} \tag{3.10}$$

where $K = \omega^2/g$. Following Evans (1982), the velocity potential can be decomposed into a scattering potential and a radiation potential

$$\phi = \phi^S - \frac{i\omega p}{\rho g}\phi^R \tag{3.11}$$

Here, ϕ^R satisfies Equation 3.7 to 3.8 with Equation 3.9 replaced by

$$K\phi^R + \frac{\partial \phi^R}{\partial z} = \begin{cases} 1, & \text{on } FS_{in} \\ 0, & \text{on } FS_{out} \end{cases} \tag{3.12}$$

The mean available power W that the device can absorb is the time average of the pressure which distributed on FS_{in} and the volume flux induced by the internal free surface over a period of oscillation. First introduce the time independent volume flux q which relates to the time dependent $Q(t)$ by $Q(t) = Re\{qe^{-i\omega t}\}$. Using the same decomposition method as the velocity potential, and choosing the positive flux as measured vertically upwards, the volume flux can be decomposed as

$$q = -\int_{FS_{in}} \frac{\partial \phi}{\partial z} d(FS) = q^S - \frac{i\omega p}{\rho g} q^R \tag{3.13}$$

Where q^S,q^R are the volume fluxes induced by scattering and radiation, respectively, and are defined by

$$q^{S,R} = -\int_{FS_{in}} \frac{\partial \phi^{S,R}}{\partial z} d(FS) \tag{3.14}$$

The volume flux due to the radiation potential can be further decompose into

$$-\frac{i\omega p}{\rho g} q^R = -(\tilde{B} - i\tilde{A})p \tag{3.15}$$

Where $\tilde{A}$ and $\tilde{B}$ are real and analogous to the added mass and radiation damping coefficients in a mass-spring-damper system. Clearly

$$\tilde{A} = -\frac{\omega}{\rho g} Re\{q^R\} \tag{3.16}$$

$$\tilde{B} = -\frac{\omega}{\rho g} Im\{q^R\} \tag{3.17}$$

Now recall the definition of the mean captured power, in the time domain is written as:

$$W = \frac{1}{T}\int_0^T P(t)Q(t)dt \tag{3.18}$$

Where T is the period of the oscillation. Converting Equation 3.18 into a time

independent form by using Equation 3.13 to 3.16 we have:

$$\begin{aligned} W &= \frac{1}{2} Re\{\bar{p}q\} \\ &= \frac{1}{2} Re\{\bar{p}q^S\} - \frac{1}{2}|p|^2\tilde{B} \\ &= \frac{|q^S|^2}{8\tilde{B}} - \frac{\tilde{B}}{2}|p - \frac{q^S}{2\tilde{B}}|^2 \end{aligned} \tag{3.19}$$

Clearly, when

$$p = \frac{|q^S|^2}{8\tilde{B}} \tag{3.20}$$

Equation 3.19 takes the maximum value of

$$W_{max} = \frac{|q^S|^2}{8\tilde{B}} \tag{3.21}$$

One important criteria to assess a WEC is the capture width defined to be the ratio between the captured power and the available power per unit crest length of the incident wave as

$$l = \frac{W}{P_w} \tag{3.22}$$

Where P_w is the mean energy flux per unit length across a vertical plane that is normal to the wave direction when water depth equals to h and is given by Equation 3.22 when the incident wave takes the form $asin(\omega t + \varphi)$ in time domain Mei et al. (2005)

$$P_w = \frac{1}{4}\rho g a^2 \frac{\omega}{k}(1 + \frac{2kh}{sinh(2kh)}) \tag{3.23}$$

Where a is the incident wave amplitude and φ is the phase, and the term in brackets is the so called group velocity V_g. Equation 3.22 becomes the following when the incident wave is described by time independent form $\phi_{inc}(x,z) = e^{\pm ikz}\psi_0$

$$P_w = \rho g K kh/2\omega \tag{3.24}$$

To include the PTO system's effect, it is assumed that the pressure and the volume flow rate are linearly related. (The assumption is reasonable since Wells turbine exhibits this linear characteristic (Raghunathan, 1995).) Assume a real positive control parameter $\wedge$ and neglecting the phase lag between the pressure and the volume flow rate, we have

$$q = \wedge p \tag{3.25}$$

Combining Equation 3.13 and 3.15, we have $[\wedge + (\tilde{B} - i\tilde{A})]p = q^S$, and so

$$W = \frac{|q^S|^2}{8\tilde{B}}\left\{1 - \frac{|\wedge - (\tilde{B} + i\tilde{A})|^2}{|\wedge + (\tilde{B} - i\tilde{A})|^2}\right\} \tag{3.26}$$

Which takes the maximum of

$$W_{max} = \frac{|q^S|^2}{8\tilde{B}}\left\{1 - \frac{\wedge_{opt} - \tilde{B}}{\wedge_{opt} + \tilde{B}}\right\} \tag{3.27}$$

When $\wedge = \wedge_{opt} = (\tilde{B}^2 + \tilde{A}^2)^{1/2}$. Therefore, the maximum capture width can be derived as

$$l_{max} = \frac{|q^S|^2}{4P_w} \cdot \frac{1}{\wedge_{opt} + \tilde{B}} \tag{3.28}$$

More detailed derivation of the foregoing theory can be found in Evans (1982). To evaluate the performance of a WECs and take the size of the WECs into account, one more important parameter, capture factor, is introduced. It is simply defined as the ratio between the capture width and the characteristic dimension of the device. For the proposed OWC device, the characteristic dimension is the diameter of the OWC device.

$$Cf = \frac{l}{D} \tag{3.29}$$

3.3 Result of the proposed FSCOWC WEC

As indicated by Equation 3.13, 3.15 to 3.17 and Equation 3.28, the major task of calculating the power can be absorbed by the OWC WEC is to solve the volume flux induced by scattering and radiation potential. Hence, the problem becomes a hydrodynamic problem solving the scattering and radiation potential. The hydrodynamic problem is solved by dividing the problem (as illustrated in Figure 3.1) into inner and outer regions (inside and outside the OWC device), writing potentials induced by scattering and radiation and then matching them at the region below the OWC device. Finally, the capture factor can be calculated by utilizing a Galerkin approximation. For detailed solution procedures, see Evans and Porter (1997). Capture factor are presented in Figure 3.2 for the proposed device.

Although the current method includes the pressure variation of the internal free surface, namely, included the variation of internal free surface elevation, the result (Figure 3.2) resembles to a single mass-spring-damper case. The plot start from

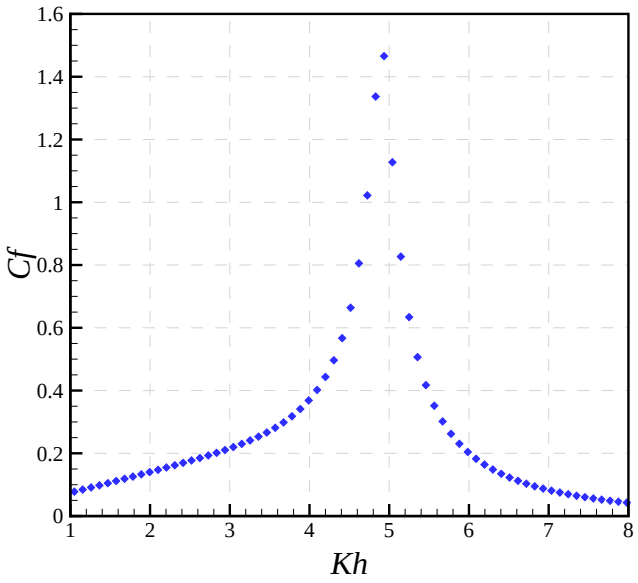

Figure 3.2: Maximum capture factor for the proposed OWC device

non zero at low frequency, reaches the maxima at resonance frequency and tends to zero when approaching higher frequency.

3.4 Chapter summary

The theory of a FSCOWC WEC is introduced based on the pressure distribution theory in this chapter. Equations for capture width and capture factor are given. The theoretical capture factor of the proposed device is calculated. Although this method provides a rapid solution (typically several minutes), it should be noted that current model has several limitations as listed below

- The current result is calculated based on inviscid, irrotational potential theory. Hence, any energy loss due to viscosity are not included. For instance, any scale will returns the same result.
- The damping effect induced by the PTO is an optimised value rather than a real damping effect that is introduced by a certain type of PTO system.
- The spring like air compressibility is neglected.
- Details of the device are not modelled, for example the thickness of the device walls.

Hence, to accurate simulate and predicate the performance of an OWC device, above idealisation must be addressed.

Chapter 4

Experiment on a moderate scale FSCOWC

4.1 Chapter overview

A moderate scale (about 1:50 full scale)FSCOWC device (for simplicity, compared with the small scale experiment, this scale device will be referred as large scale device hereafter.) was designed and tested. The PTO system was represented by an orifice plate for simplicity. The effect of three different PTOs on the performance of the FSCOWC device was investigated. Results and procedures of executing the experiment are introduced and discussed in this chapter.

4.2 Facilities

The large scale experiment was carried out at the Kelvin Hydrodynamics Tank (Figure 4.1) of the University of Strathclyde which has become one of the leading providers of testing services to the UK tidal and wave energy industry in recent years. The tank has a dimension of $76m \times 4.6m \times 2.5m$ and is equipped with a highly repeatable four-flap type absorbing wave maker (Figure 4.2) which absorbs the reflected, radiated wave from the device and makes sure the generated wave is consistent during a single test. A high quality variable slope beach is installed at the end of the tank to absorb the wave and prevent reflection to the testing objects with reflection coefficient typically smaller than 5%. Besides, the tank is equipped with wall-mounted heater to minimize the temperature variation. Data

acquisition is achieved by PC based modular data acquisition system.

Figure 4.1: The Kelvin Hydrodynamic Lab

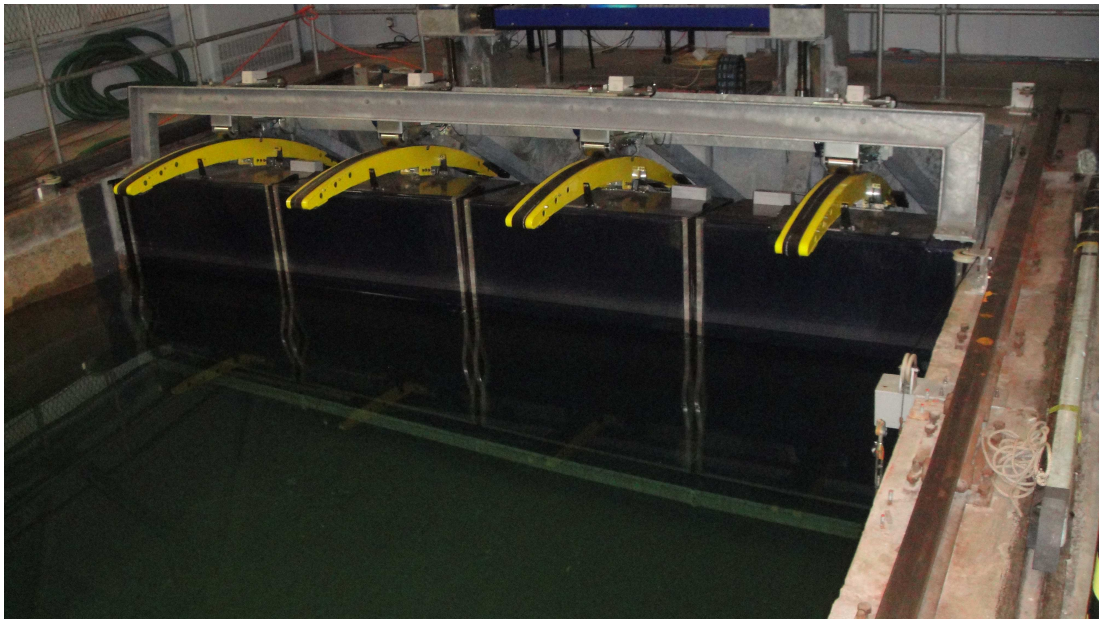

Figure 4.2: The absorbing wave maker

4.3 FSCOWC models and configuration

The OWC chamber and orifice plate is made of acrylic. A filleted plastic ring is installed at the end of the OWC chamber in order to provide a smooth entrance

since the entrance may cause vortices that lead to energy loss (Zhang et al., 2012). Water depth is set to $2.10 \pm 0.01m$ where the $\pm 0.01m$ is the uncertainty lies in the measurement and will be discussed further in section 4.5. The model is fixed in the middle of the tank by a wooden frame as shown in Figure 4.3, $34m$ away from the wave maker. Designed and measured geometry details can be found in Figure 4.4 and Table 4.1, respectively. Note that the large relative uncertainty (2.86%) in the draft is caused by the difficulty in aligning the OWC with the designed water line inside the chamber due to the thickness of the draft line ($2.0 \pm 0.1mm$) and meniscus effect. Besides, aligning is carried out at the same level of the top of the OWC device. Therefore, visual effects also contribute to the uncertainty; For instance, the refraction effect of the transparent acrylic tube. The influence of the uncertainty in draft on results will be discussed later.

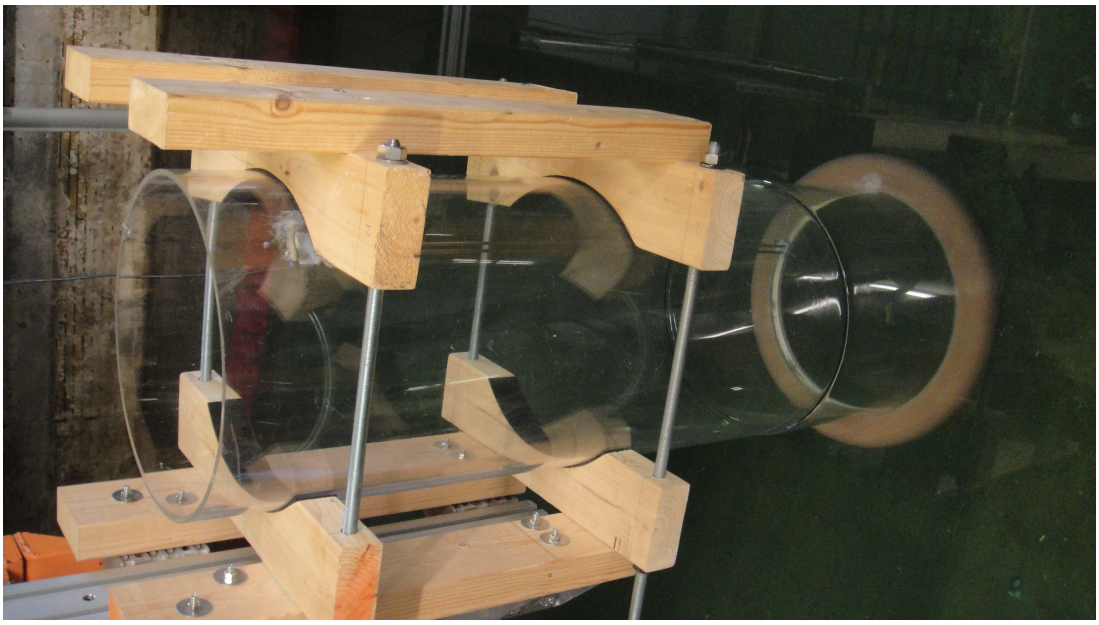

Figure 4.3: FSOWC model fixed in the middle of the tank by a wooden rack

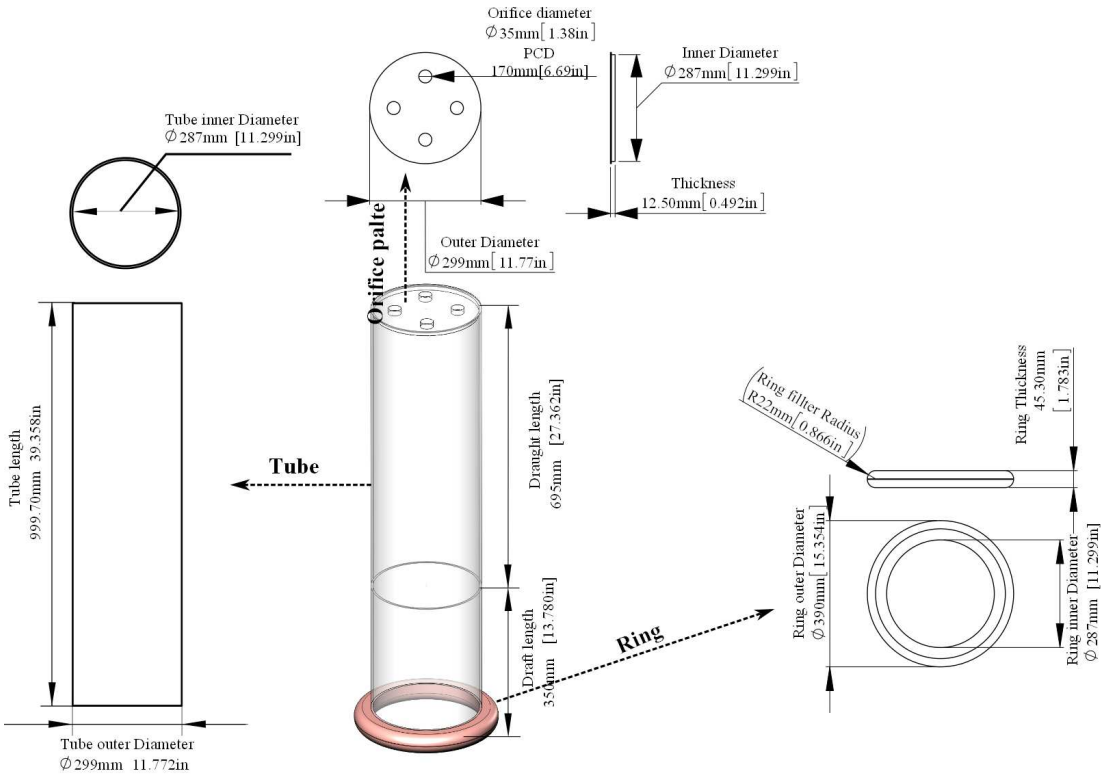

Figure 4.4: Scale drawing of the designed moderate scale FSCOWC.

Table 4.1: Geometry details of the FSOWC where PCD is pitch circle diameter. Here, the relative large uncertainty in the geometry origins from the measurement. It is not the uncertainty in the manufacturing.

Component	Parameters (mm)	EFD
OWC model	total length	1045.0 ± 0.5
	draft	350.0 ± 5.0
Orifice plate	Plate Diameter	299.0 ± 0.5
	Thickness	12.5 ± 0.2
	Orifices Diameter	35.0 ± 0.2
	Orifices position (PCD)	170 ± 0.2
Tube	Outer Diameter	299.0 ± 0.5
	Inner Diameter	287.0 ± 0.5
Ring	Inner Diameter	299.3 ± 0.5
	Outer Diameter	390.0 ± 0.5
	Thickness	45.3 ± 0.2
	Fillet radius	22.0 ± 0.2

4.4 Instruments

As indicated by Equation 3.18, the evaluation of the performance of an OWC device requires investigating the instantaneous pressure and instantaneous vertical component of the air volume flow rate. Hence, the experiment should be designed to be able to measure the two variables.

Due to the difficulty in measuring the volume flow directly, the volume flow rate is obtained implicitly by time derivative of the internal free surface elevation that measured by a point wave probe,hence $Q(t) = \dot{\eta}_{owc}(t) \cdot A_w$ where A_w is the water plane area of the device and $\dot{\eta}_{owc}(t)$ is the instantaneous vertical component of the derivative of the instantaneous internal free surface elevation η_{owc}. Hence, it requires the assumption that the free surface acts like a rigid flat piston, thus the spatial variation is neglected. In present experiment, two different types of wave probe are used to measure the elevation of the OWC.

The first type of wave probe is the self manufactured resistance type wave probe (Figure 4.5 (A)) which is a surface piercing sensor with two parallel stainless steel wires partially submerged into water. The resistance induced by the water between the two parallel wires will vary accordingly, when the submergence of the wave probe changes. Therefore, the output of the resistance type wave probe can be a voltage linearly proportional to the immersed length when supplying a constant current to the probe. As the resistance of the probes is sensitive to fluid properties like temperature, it is essential to calibrate the probe each time when it is used (This will be discussed in detail later). When monitoring waves, the wave probe is fixed in space and the instantaneous output is recorded. This kind of wave probe can provide high resolution data at more than hundreds of cycles per second and therefore be capable of capturing extremely small time variation of the wave. hence, it will not loss much information even when the wave is highly non-linear. However, since this kind of wave probe is surface piercing, the output can be affected by the relevant effect like meniscus between the two parallel wires.

Another type of wave probe used in present study is the Ultrasonic liquid level sensor (Figure 4.5 (B)) which measures the wave by continuously sending high frequency sound waves to the target object (in this case the water surface.) and measuring the time interval between sending the sound waves and receiving the echo from the target object. Hence the distance between the sensor and the target object can be calculated based on the propagating speed of sound. Unlike the resistance type probe, this kind of sensor is non intrusive, and therefore will not

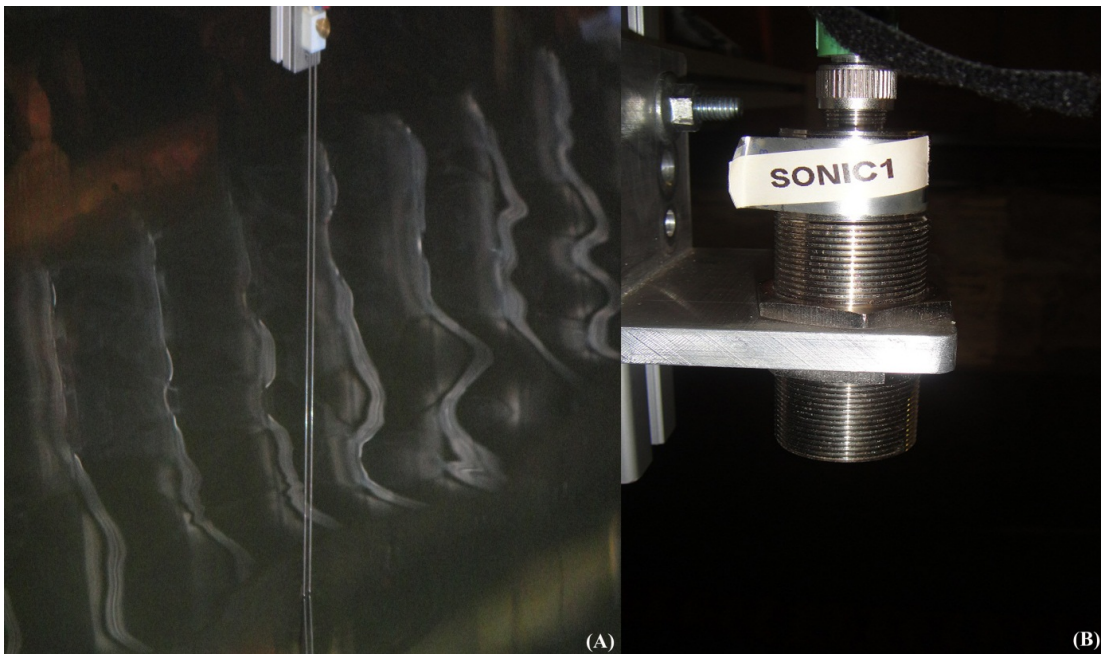

Figure 4.5: Wave probes: A)resistance type wave probe B)Ultra sonic wave probe

interact with free surface. Besides, since the ultrasonic wave probe measure the wave profile mainly rely on the propagating speed of the sound wave in air, which is quite constant especially indoor where the air temperature is relatively constant with the help of the heaters. Thus, the ultrasonic wave probe usually does not require calibration once calibrated by manufactures. However, the output update frequency of the ultrasonic wave is relatively lower than that of a resistance type probe, which is typically below 100 Hz. Besides, the Ultrasonic wave probe can not measure a steep wave since the sound will not be reflected back to receiver when the wave slop is high. Moreover, the ultrasonic probe has a blind area within which the probe will fail to monitor the wave elevation correctly. Hence, sufficient distance between the probe and the water surface should be guaranteed before testing. This may introduce a minor phase lag (typically about $15ms$) which will not affect the monitoring of the wave elevation, however, the phase lag will affect the power calculation. The way to eliminate the phase lag will be discussed later. $UltraLab$® USS20130 ultrasonic wave probe is selected to measure the water level (including the incident wave amplitude and OWC elevation) in this work. The technical resolution of the wave probe is $0.18mm$, and the beam angle is less than 3 degree (leading to a sampling area less than $9cm^2$) . More technical details can be found at GeneralAcoustics (2014).

The pressure is measured by $Honeywell$® 163PC0D75 low pressure differential transducer. This pressure sensor measures the pressure by using the piezoresistive

effect of strain gauges. The resistance of built-in strain gauges will vary linearly with applied pressure hence produce a output voltage that is linearly proportion to the applied pressure. The sensor has two ports as shown in Figure 4.7 and one of the port is connected to the OWC air chamber during testing while the other one is left open to atmosphere and thus the pressure difference can be measured directly. The pressure sensor can measure a pressure ranging from -622.27pa to +622.72pa (Honeywell, 2014).

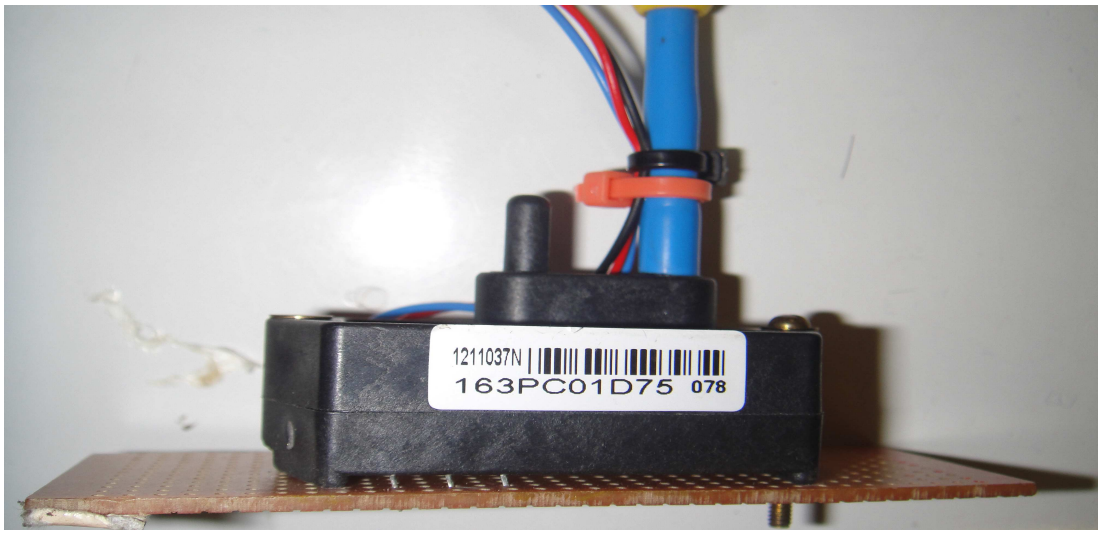

Figure 4.6: Honeywell® 163PC0D75 pressure sensor

All the instruments are connected to an amplifier to get a proper resolution. The signals from the amplifier is then transferred to a PC through the data acquisition interface as shown in Figure 4.8. Finally, the data is visualised with the aid of the Spike2 data acquisition software.

4.5 Uncertainties

In practice, physical experiments may not obtain the true value of the quantity of interest due to lack of knowledge. Therefore, it is more meaningful to give a range that contains the measured result and say the true value will fall into that range instead of giving a single value. The qualitative and quantitative analysis of the range caused by lack of knowledge is called uncertainty analysis.

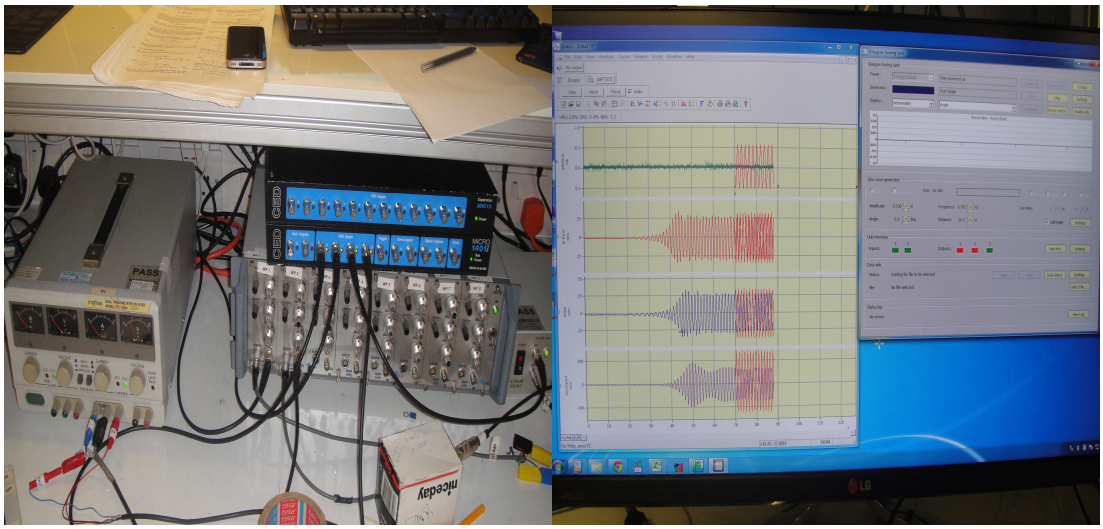

Figure 4.7: data acquisition system: left) the power supplier, amplifier and data acquisition interface, right) Spike software collecting data.

4.5.1 Expression of uncertainties

Following ITTC (2008a), the final measured value of all parameters should be documented as shown in Equation 4.1 (In order to be consistent with the International Organization for Standardization's (ISO) standardized definition(GUM, 2008), all the notations in this section is kept the same as ISO GUM. There maybe notation conflicts against the other contents in this work. Hence, unless specified all the conflicted notions only valid in this section.)

$$Y = y \pm U \tag{4.1}$$

Where the Y is the measurand, that is the value of the particular quantity to be measured. The y in Equation 4.1 is the estimated value of the measurand and the U is the expanded uncertainty and is defined as

$$U = ku_c(y) \tag{4.2}$$

Where the k is the coverage factor decided by the level of confidence needed. The $u_c(y)$ is the combined standard uncertainty which is calculated based on standard uncertainty u. Judging by the two components in Equation 4.2, the expanded uncertainty can be interpreted as a combined standard uncertainty with a level of confidence. Hence, Equation 4.1 can be explained as (assuming the level of confidence is 95% here) there is 95% chance that the measurand Y is $y - u_c \ll Y \gg y + u_c$.

4.5.2 Standard uncertainty

The uncertainty components are categorized as "random" and "systematic" and are associated with errors arising from random effects and known systematic effects in some publication, for instance,Dieck et al. (2005). However, such categorization of components of uncertainty can be ambiguous. For example, a "random" component of uncertainty in one measurement may become a "systematic" component of uncertainty in another measurement in which the result of the first measurement is used as an input datum. Hence, to avoid such ambiguity, as per GUM (2008) the uncertainty is divided into following two types based on the way that the uncertainty is evaluated.

Type A standard uncertainty

Type A evaluation of component of standard uncertainty is a method of evaluation of uncertainty by the statistical analysis of series repeated observations. For a measurand Y that is measured by N independent repeated observations y_k, the best estimated value is the arithmetic mean of the N observations:

$$\bar{y} = \frac{1}{N} \sum_{k=1}^{N} y_k \tag{4.3}$$

The variance of the observations is given by

$$s^2(y_k) = \frac{1}{N-1} \sum_{j=1}^{N} (y_j - \bar{y})^2 \tag{4.4}$$

And the variance of the mean is given by

$$s^2(\bar{y}) = \frac{s^2(y_k)}{N} \tag{4.5}$$

The type A standard uncertainty is simply the positive square root of the variance of the mean and is expressed as

$$u(y) = s(\bar{y}) \tag{4.6}$$

Type B standard uncertainty

Uncertainty component obtained by means other than statistical analysis of series independent repeated observations is denoted as a type B standard uncertainty. This type of component of standard uncertainty is usually obtained by:

- Previous measurement data.

- Experience with or general knowledge of the behaviour and properties of relevant materials and instruments.
- Manufacturer's specifications.
- Data provided in calibration and other certificates.
- Uncertainties assigned to reference data taken from handbooks.

4.5.3 Combined standard uncertainty

In most situation, the measurand of interest is not measured directly, but is determined from N other quantities $X_1, X_2 \cdots X_N$ through a function f as:

$$Y = f(X_1, X_2, \cdot, X_N) \tag{4.7}$$

Where X_i itself is a measurand with estimate value of x_i. Hence, to report the measurand Y with a meaningful indicator, standard uncertainties from each component measurand are combined through the uncertainty propagating law:

$$u_c(y) = \sqrt{\sum_{i=1}^{N} \left(\frac{\partial f}{\partial x_i}\right)^2 u^2(x_i) + 2 \sum_{i=1}^{N-1} \sum_{j=i+1}^{N} \frac{\partial f}{\partial x_i} \frac{\partial f}{\partial x_j} u(x_i, x_j)} \tag{4.8}$$

The partial derivatives of f with respect to x_i and x_j are called sensitivity coefficients c_i and c_j:

$$c_i = \partial f / \partial x_i \tag{4.9}$$

$$c_j = \partial f / \partial x_j \tag{4.10}$$

Equation 4.8 is the general form that applies to both dependent and independent estimated values (x_i,x_j). If the estimated values are correlated or dependent, their degree of correlation is determined by the correlation coefficient $r(x_i, x_j)$:

$$r(x_i, x_j) = \frac{u(x_i, x_j)}{u(x_i)u(x_j)} \tag{4.11}$$

The correlation coefficient's values are symmetric ($r(x_i, x_j) = r(x_j, x_i)$) and range from -1 to +1 (the correlation coefficient equals to 0 when x_j and x_i are independent). The $u(x_i, x_j)$ is the estimated covariance associated with x_i and x_j

and equals to the covariance of x_i and x_j estimated by

$$u(x_i, x_j) = \frac{\sum_{i=1}^{N}(x_i - \bar{x}_i)(x_j - \bar{x}_j)}{N(N-1)} \tag{4.12}$$

Combining Equation 4.8 to 4.11, the $u_c(y)$ can be rewritten as

$$u_c(y) = \sqrt{\sum_{i=1}^{N} c_i^2 u^2(x_i) + 2\sum_{i=1}^{N-1}\sum_{j=i+1}^{N} c_i c_j u(x_i, x_j)} \tag{4.13}$$

4.5.4 Expanded standard uncertainty

As indicated by Equation 4.2, the expanded uncertainty is simply the combined standard uncertainty times the coverage factor k. The value of k is decided by level of confidence required and the assumed distribution of uncertainty. For instance, for a normal distributed uncertainty, the k approximately equals to 2 when the number of sample is larger than 30. Detailed information on the value of the k can be found in several reference, for instance, GUM (2008).

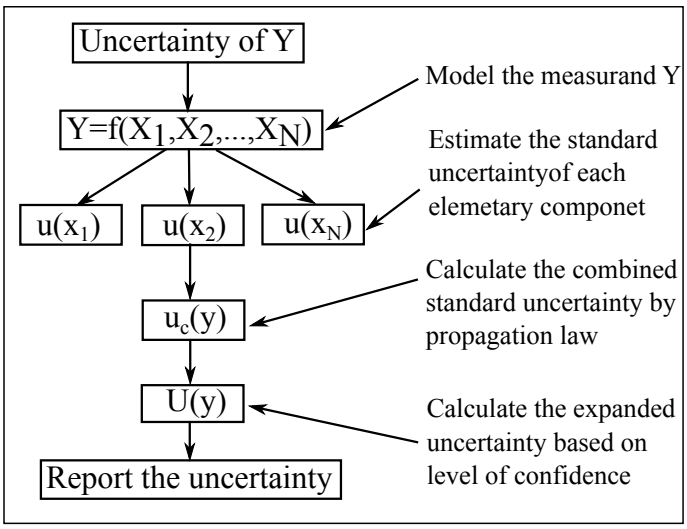

Figure 4.8: Uncertainty Analysis flow chart

The procedures of uncertainty analysis of a measurand Y is summarised as shown in Figure 4.8. The analysis of the uncertainties in the quantities of interest will be discussed in detail later.

4.6 Testing procedures

1. **Instruments calibration procedures**

   Instruments' calibrations were carried out first to obtain the transfer function between the physical quantities and the output signal from the instruments so that the signal data can be converted into a physical data directly.

   Although the ultrasonic wave probe was calibrated by the manufacture, it was recalibrated to quantify the uncertainty. Calibration of the wave probes was achieved by fixing the wave probes on a graduated scaled calibration plate and move up and down accordingly to get different submergence (distance) as shown in Figure 4.9. To ensure the two wave probes were calibrated under a same condition, the two wave probes were calibrated at the same time.

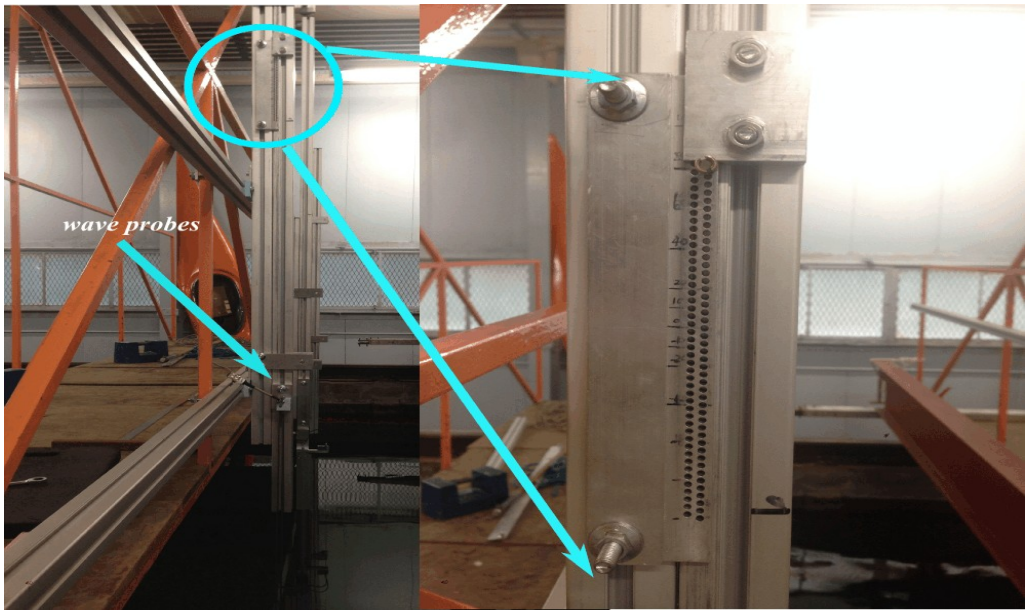

Figure 4.9: Wave probe calibration system

   To get an accurate transfer function and to better estimate the uncertainty, it is recommended to calibrate the wave probes over approximately 10 equal increments and the calibration range should cover the maximum span of the measurement (ITTC, 2008b). However, this criterion was not met in current test due to the maximum range of the calibration plate is $100mm$. At each data point for the calibration, it is recommended to obtain at least 100 samples so that the uncertainty introduced by selecting different range of data will be minimized. Result of the wave probe calibration and uncertainty

estimation will be presented in the result section.

The calibration factor and the uncertainty of the pressure transducer was taken directly from the specification provided by the manufacture (Honeywell, 2014). It should be noted here the uncertainty taken from the data sheet is 2% of the span. Although not specified, it is treated as uncertainty at 95% level of confidence as suggested by GUM (2008). Therefore, care must be paid to the calculation of the expanded uncertainty in power when applying coverage factor using Equation 4.2. The uncertainty in the pressure sensor obtained from the specification need to be converted to standard uncertainty prior to calculation of the combined uncertainty.

2. **Incident wave calibration**

   As explained in the literature review, existing methods of monitoring the incident wave amplitude may lead to less accurate incident wave power estimation. Therefore, in current test the incident wave amplitude was measured prior to any testing by locating a wave probe where the device will be installed so that the influence of spatial variation of wave in the tank can be minimized.

   In addition to the wave probe used to measure the wave at the place where the device will be deployed. Another wave probe (refereed as reference probe hereafter.) was located $15m$ away from the wave maker and $16m$ away from the site the FSCOWC device. This position provided sufficient long distance to avoid the disturbance of the evanescent wave caused by the wave maker and at the same time provide enough time to evaluate the incident wave before the radiated and reflected wave from the FSCOWC starts to superpose with the incident wave. When calibrating the incident wave, both probes' data were recorded and compared. The reference probe was fixed in position through the whole testing. When the device was tested, the incident wave amplitude measured at by the reference probe was compared with the data obtained during the calibration stage to ensure the incident wave is repeatable.

   The wave height of any incident wave was first calibrated and modified so that the difference between the measured and target value do not exceed 1.5% of the target wave height. This is to minimize the nonlinear effect on the OWC response induced by different incident wave height.

   A set of repeat tests of the incident wave was carried out to quantify the

repeatability of the incident wave.

3. **Regular wave test**

   The instruments were connected to the FSCOWC as shown in Figure 4.10. A plastic tube was used to connect the device and the pressure sensor to ensure the pressure sensor stayed away from the orifices to avoid any interaction between the out flow from the orifices and the reference port of the pressure sensor. Otherwise the pressure drop won't be measured correctly. The resistance wave probe was attached to the FSOWC device after calibration as shown in Figure 4.3.

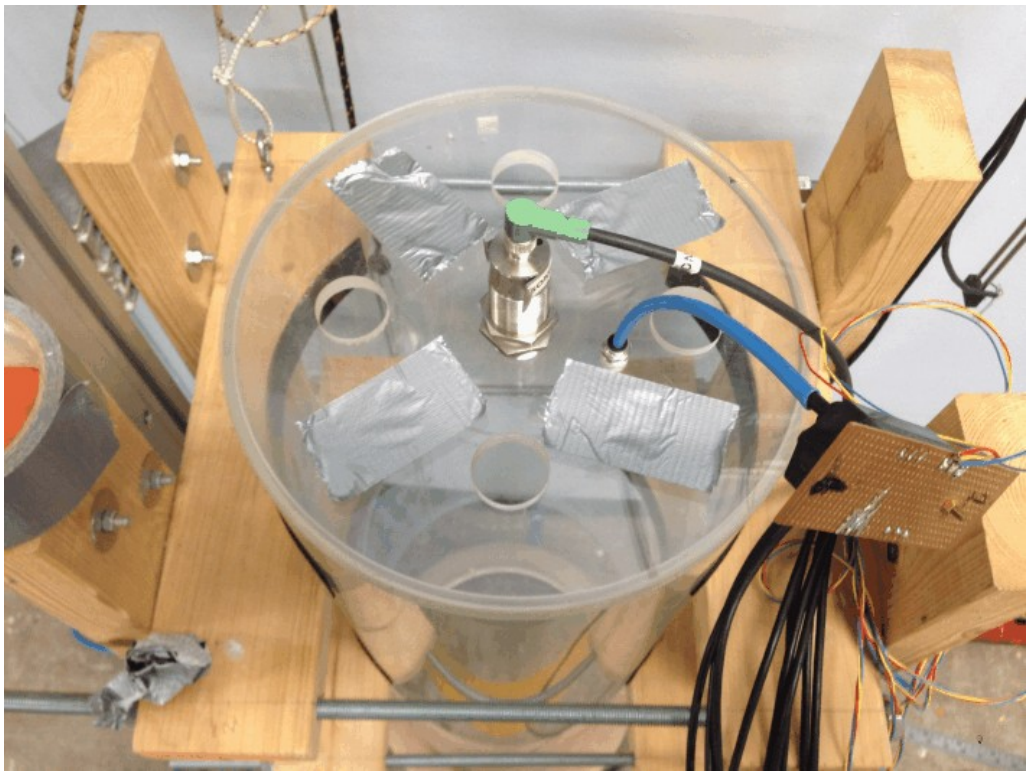

Figure 4.10: Connection between the FSCOWC device and instruments

Waves corresponding to Kh from 2 to 8 unequally spaced in frequency were tested for the FSCOWC device without orifice plate, with 4 orifices open to atmosphere and only one orifice open to atmosphere respectively. Which representing the cases without PTO damping, with moderate PTO damping and strong PTO damping. All data were sampled at a sampling frequency of $137Hz$.

Repeat tests were carried out alternately during the test. Temperature of the water was monitored by a thermometer during the test. The water temperature was relatively constant varied between 18.1°C and 18.5°C.

4.7 Data processing

Typical raw data obtained from data acquisition system for four orifices case at $Kh = 5.1$ is shown in Figure 4.11.

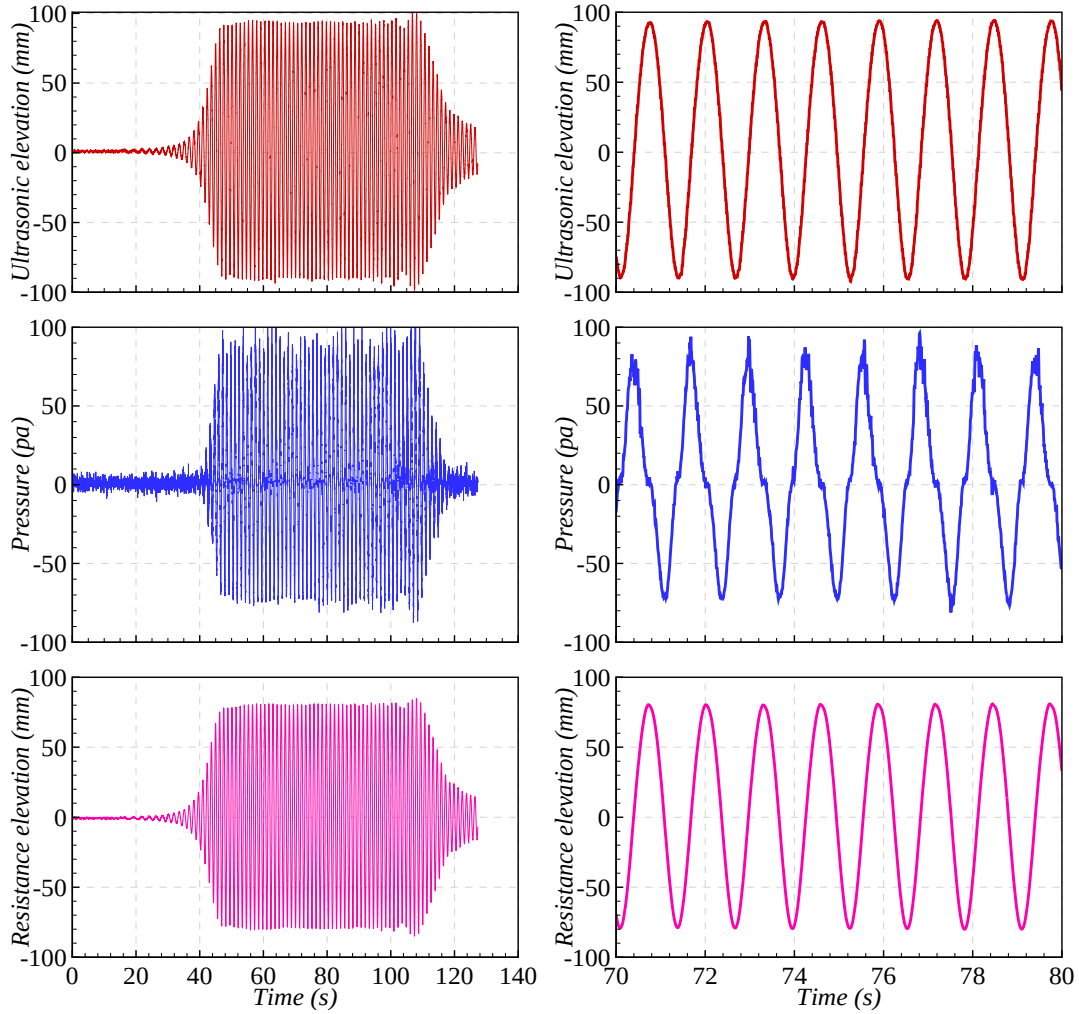

Figure 4.11: Typical raw data obtained from tests (Four orifices case when $Kh = 5.1$). Where from top to bottom are the FSCOWC elevation measured by the ultrasonic wave probe, the pressure difference and the FSCOWC elevation measured by the resistance wave probe, respectively. Data in right hand side is an enlarge view for time equals to 70 seconds to 80 seconds.

Clearly, the pressure suffered from noise introduced by environment (for instance, the main electric noise at $50Hz$.). To minimize the error caused by the noise during data analysing stage, the raw data was first filtered by using a Finite Impulse Response (FIR) low pass data filter provided by the Spike2 software. Care must be drawn on the cut-off frequency used in the filter since improper cut-off frequency can filter the real data. A good rule of thumb is that always

set the cut-off frequency at at least 10 times higher than the frequency of the incident wave frequency. Filtered data should be compared with the raw data to check whether the data is over filtered. The raw and filtered pressure are shown in Figure 4.12 for comparison. As indicated by the filtered pressure signal, there exists some low frequencies components in the pressure signal when the pressure reached the peak, however, that is not experienced in the lowest pressure part. Investigation of the OWC elevation as shown in Figure 4.11 suggests that this is not caused by difference in the OWC motion. This phenomenon may be caused by sloshing of the OWC surface.

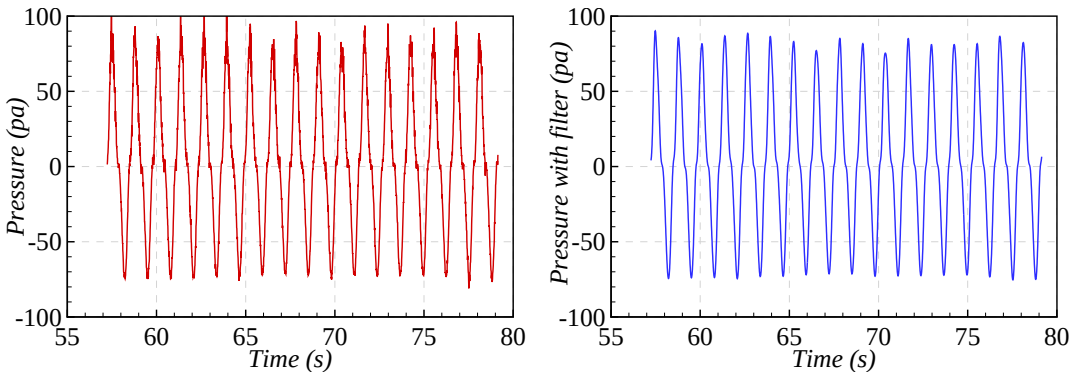

Figure 4.12: Raw pressure and pressure with low pass filter

As illustrated by Figure 4.11, the OWC inside the device first experienced a transient excitation due to arrival of the wave, then it builds up to the maximum elevation and keep relative constant periodic response until the wave stops. Unlike the case where the incident wave frequency is near the OWC natural frequency, cases experiencing a lower or higher incident wave frequency exhibits more complicate response as shown in Figure 4.13 for $Kh = 2$ and $Kh = 8$, respectively.

The OWC oscillated at a larger amplitude due to the first wave encountered and then slowly decay to a relative constant motion. Obviously, it takes a longer time for cases at those incident wave frequencies to reach a stable condition. Therefore, care must be taken on selection of effective data since the reflection from the beach may have affected the motion by the time stable condition is achieved, however, we have said that the beach is very good. To avoid any uncertainty due to the impact of the reflected wave from the beach, it is desirable to select the data before the reflection arrived at the device. This was achieved by estimating the time needed for the reflection wave to reach the device and selecting the data before the reflection happened. The time needed for the reflection wave to reach the device is simply estimated by dividing the distance from the beach

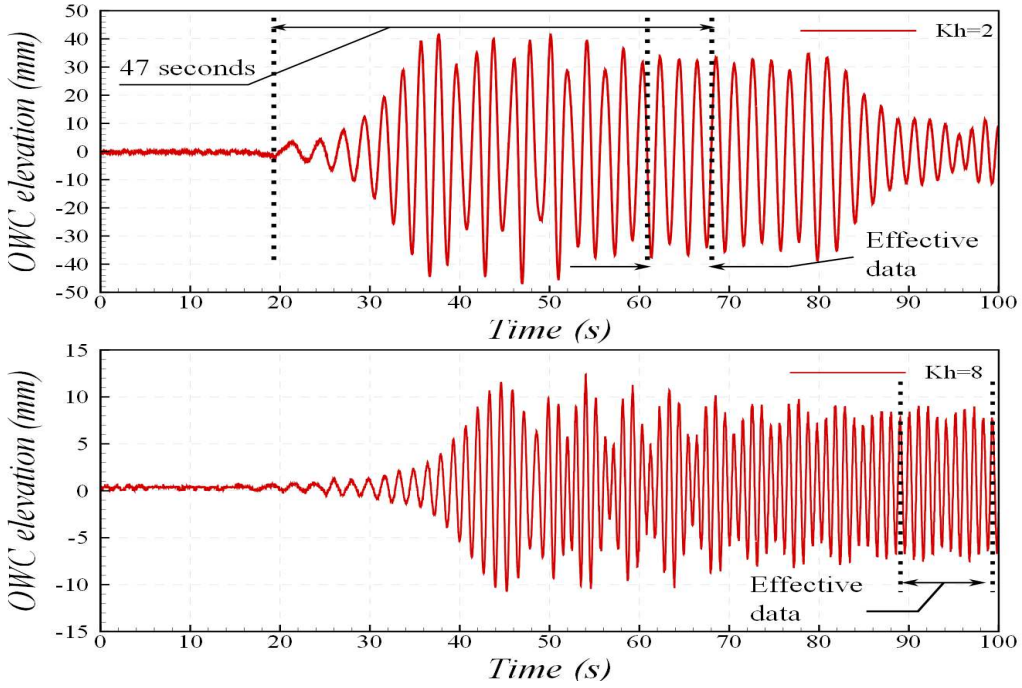

Figure 4.13: OWC elevation for four orifice when $Kh = 2$ and $Kh = 8$.

to the device by the group velocity of the incident wave. To minimize sampling effect, at least 10 cycles of data (typically more than 1000 samples.) was selected for post processing except for cases at low incident wave frequency where the reflection from the beach happened too fast. (The selection of the effective data is illustrated in Figure 4.13 for the lowest (Kh=2) and highest (Kh=8) incident wave frequencies. For Kh=2, time interval between the incident wave arrived the device and reflection reached the device was first calculated, relatively stable data was then selected for post processing. In this case, only 3 cycles of oscillation was selected, however, the effective data still provides around 1000 samples. Selection of effective data for Kh=8 is straight forward since reflection happens about 90 seconds after the first incident wave reaches the device, corresponding to around 110 seconds in Figure 4.13. Hence, it only requires to select the relative stable data (as many as possible.) for post processing.

After noise reduction and selecting valid range of data, the phase lag of the OWC elevation measured by the Ultra sonic wave probe was corrected by referencing to the resistance wave probe and shifted the time accordingly typically around 15ms. The velocity of the OWC surface was calculated by Equation 4.14, where the subscript t denotes the time and δt is the time interval.

$$V_t = \frac{\eta_{owc_{t-\delta t}} - \eta_{owc_{t+\delta t}}}{2\delta t} \tag{4.14}$$

The pressure amplitude and the OWC elevation amplitude were obtained by sine data fitting. Due to the hysteresis caused by the orifice, the pressure amplitude obtained here is only the first order harmonic component of the pressure as shown in Figure 4.14. The impact of using first order harmonic component of the pressure to calculate the power will be discussed later.

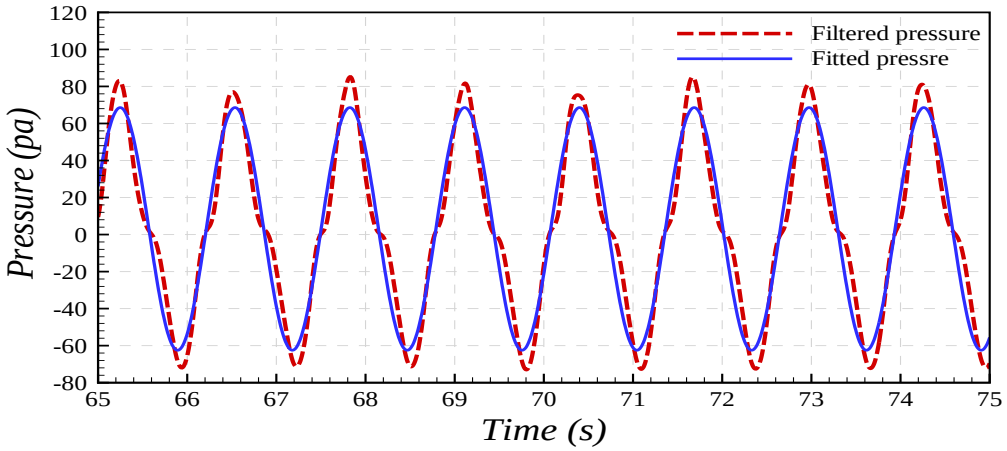

Figure 4.14: Comparison between the filtered and the fitted pressure

4.8 Estimation of uncertainties in current test

Following Figure 4.8, the estimation of uncertainties in the current test starts from modelling the quantities of interest. The quantities of interest in present work are the so called response amplitude operator (RAO), defined as the ratio between the amplitude of the OWC motion and the amplitude of the incident wave, and the mean power, the capture width and the capture factor. To estimate the uncertainties in the above quantities, following Figure 4.8, those quantities were first modelled by their elementary components as:

$$RAO = \frac{\eta_{owc}}{a} \tag{4.15}$$

$$W = \frac{\int_0^T P(t) \cdot Q(t) dt}{T} = \frac{\int_0^T P(t) \cdot \dot{\eta}_{owc}(t) dt \cdot A_w dt}{T} \tag{4.16}$$

$$l = \frac{W}{\frac{1}{2}\rho g \cdot a^2 \cdot \frac{\omega}{k}(1 + \frac{2kh}{sinh(2kh)})} \tag{4.17}$$

Where k and a in Equation 4.17 are the wave number and the incident wave amplitude as defined in Chapter 3 The W and l are the captured power and

capture width, respectively.

Substituting Equation 4.15 into Equation 4.13 we have

$$u_c(RAO) = \sqrt{\left(\frac{u(\eta_{owc})}{a}\right)^2 + \left(\frac{-u(a)\cdot\eta_{owc}}{a^2}\right)^2 - 2\frac{\eta_{owc}}{a^3}\cdot u(\eta_{owc}, a)} \tag{4.18}$$

Since the η_{owc} and the a were measured by two different wave probes, it is reasonable to assume that they are independent quantities. Hence the third term in the equation simply equals to 0. It is now clear that to estimate the combined uncertainty in the RAO, one only needs to know the uncertainty in the measurement of the η_{owc} and the a.

To estimate the uncertainty in the mean power captured based on Equation 4.16 requires the instantaneous standard uncertainty in pressure and OWC elevation which is complex and difficult to convert into a mean standard uncertainty in the W. Therefore, the mean power captured is estimated by assuming the pressure and volume flow rate are all sinusoidal and can be calculated based on time independent pressure and time independent volume flow rate by

$$W = \frac{1}{2}p\cdot\dot{\eta}_{owc}\cdot A_w = \frac{1}{2}p\cdot\omega\cdot\eta_{owc}\cdot A_w \tag{4.19}$$

Substituting 4.19 into Equation 4.13 we have

$$u_c(W) = \sqrt{c_p^2\cdot u(p)^2 + c_{n_{owc}}^2\cdot u(\eta_{owc})^2 + c_{A_w}^2\cdot u(A_w)^2 + Cov(\eta_{owc}, p)} \tag{4.20}$$

Where $c_p = 0.5\cdot\omega\cdot\eta_{owc}\cdot A_w$, $c_{n_{owc}} = 0.5\cdot p\cdot\omega\cdot A_w$, $C_{Aw} = 0.5\cdot p\cdot\omega\cdot\eta_{owc}$ and the covariance term $Cov(\eta_{owc}, p) = 2c_p\cdot c_{\eta_{owc}}\cdot u(\eta_{owc}, p)$. Again the covariance can be neglected due to the η_{owc} and the p are independent quantities.

The mean power captured calculated by Equation 4.19 neglected the non-linear effect in the pressure and the volume flow rate. The feasibility of estimating the uncertainty by current method will be discussed in the result section.

Assuming the density, wave circular frequency and wave number are known and constant. For deep water wave (defined here as water depth is greater than half of the wave length. In present work, only deep wave is investigated.) the group velocity trends to half of the phase velocity. This results in the term including the water depth h in Equation 4.17 becoming negligible. Therefore, it is reasonable to assume that the uncertainty in the capture factor induced by uncertainty in

the water depth is negligible. Use $u(\eta_{owc}$,$u(a)$,$u(p)$ and $u(A_w)$ to represent the standard uncertainty in η_{owc},a,p and $u(A_w)$,respectively. Consider the W as a entire input component of the capture factor, the combined uncertainty in l is

$$u_c(l) = \sqrt{\left(\frac{\xi}{0.5\rho g a^2}\right)^2 \cdot u(W)^2 + \left(-\frac{\xi W}{0.5\rho g 2a^3}\right)^2 \cdot u(a)^2 - \frac{4\xi^2 W}{\rho^2 g^2 a^5} \cdot Cov(W,a)} \tag{4.21}$$

Where $\xi = 1/(\frac{1}{2}\rho g \frac{\omega}{k}(1 + \frac{2kh}{sinh(2kh)}))$. Hence according to Equation 3.29, the combined uncertainty of the capture factor is simply

$$u_c(Cf) = \sqrt{\left(\frac{(u(l)}{D}\right)^2 + \left(\frac{-l \cdot u(D)}{D^2}\right)^2} \tag{4.22}$$

When calculating the combined uncertainty, one shall make sure that each components in Equation 4.8 have the same level of confidence. Otherwise the expanded uncertainty may be under estimated or over estimated. For example, when calculating the uncertainty in the mean power captured, the uncertainty in the pressure measurement obtained by the specification gives a uncertainty at the 95% level of confidence. The coverage factor roughly equals to 2 if a normal distribution is assumed. On the other hand, the uncertainty in the OWC elevation was determined by calibration and 5 repeat tests and the uncertainty is at 68% level of confidence. Hence, to calculate the combined uncertainty, one shall first convert the uncertainty in the pressure from 95% level of confidence to 68% level of confidence first.

The same problem exists when calculating the expanded uncertainty by Equation 4.20 since different components may have different coverage factor. Therefore, the expanded uncertainty calculation in current study was found by expanding the standard uncertainty to 95% level of confidence and then combining together through Equation 4.13 so that the combined uncertainty has a level of confidence equals to 95%.

Results of uncertainty analysis will be given along with the results of quantity of interest in Section 4.9.

Among all the uncertainty components that exist in the present test, some can be linked to the expanded uncertainty directly through uncertainty modelling as shown above. On the other hand, some of the uncertainties in the measurement do not appear in the modelling, for example the draft. The influence of the uncertainty in the draft on results was estimated by assuming the OWC is a rigid

body so that the natural frequency can be estimated by Equation 4.23 where the second term in the denominator is the empirical equation for estimating the frequency independent vertical added mass for a disk, see Bayoumi (2013) for details on estimating the natural frequency of the OWC.

$$\omega_n = \sqrt{\frac{\rho \cdot g \cdot A_w}{\rho \cdot d \cdot A_w + \frac{4}{3}\rho(\frac{D}{2})^3}} \tag{4.23}$$

Substituting the maximum and minimum draft into the equation gives a natural frequency range as listed in Table 4.2.

Table 4.2: Nature frequency for different draft calculated based on rigid body theory

Draft (m)	nature frequency $(radian/s)$	Kh
0.34	4.84	5.02
0.35	4.79	4.91
0.36	4.73	4.80

It is now clear that $\pm 10mm$ uncertainty in the draft will lead to about ± 0.1 in the non-dimensionlized natural frequency Kh.

4.9 Results and discussion

Following the methodology and procedures discussed above, results are presented in this section.

4.9.1 Calibration and uncertainty estimation

The result of calibration of the ultrasonic wave probes used in the test are presented in Figure 4.15 for illustration of the calibration and uncertainty estimation. Calibration result of the resistance wave probe is omitted here since ultimately only the ultrasonic wave probe measurements were used. The reason will be discussed later.

The uncertainty estimation was carried out by following ITTC (2008b). The standard error estimator shown in Figure is defined by

$$SEE = \sqrt{SS_R/(n-2)} \tag{4.24}$$

Where the SS_R in Equation 4.24 is the sum of the squared residuals and the residuals is simply defined by

$$Residual = y_i - a_{intercept} - b_{slope}x_i \tag{4.25}$$

The y_i in Equation 4.25 is the ith reference value, the x_i is the ith measured voltage and the $a_{intercept}$ and the b_{slope} are the intercept and the slope of the linear regression, respectively.

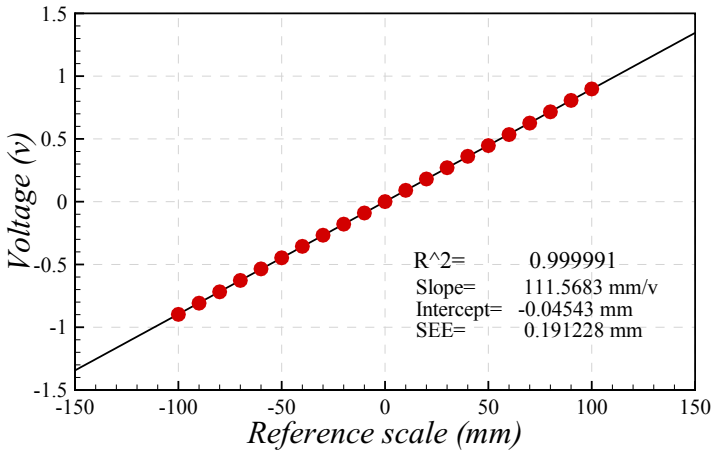

Figure 4.15: Calibration result of the ultrasonic wave probe

The residuals are plotted in Figure 4.16 with prediction limit at 95% confidence calculated based on linear regression theory and calibration theory. Here, the linear regression predication limit is simply the SEE and was expanded to 95% confidence by multiple a coverage factor equals to 2.09. The coverage factor was calculated based on the Student's t-distribution with a degree of freedom equal to 20. The prediction limit at 95% confidence calculated by calibration theory yields 3 times SEE. Detailed information on how to calculate the predication limit based on the calibration theory can be found in ITTC (2008b).

Although the calibration theory seems to over predicated the predication limit as indicated by Figure , 3 times SEE was chosen to be the uncertainty at 95% confidence as recommended by ITTC (2008b). The standard uncertainty (the SEE) obtained in current study is $\pm 0.1912mm$ which is only slightly larger than that technical resolution stated by the manufacture ($\pm 0.18mm$). It is noted that the calibration factor is slightly different from the one provided by the manufacture (111.11 mm/v), this may be caused by several reasons (e.g. the manufacture calibrated the probe in a different environment that may affect the propagating speed of sound.). Of which, using a different data acquisition system

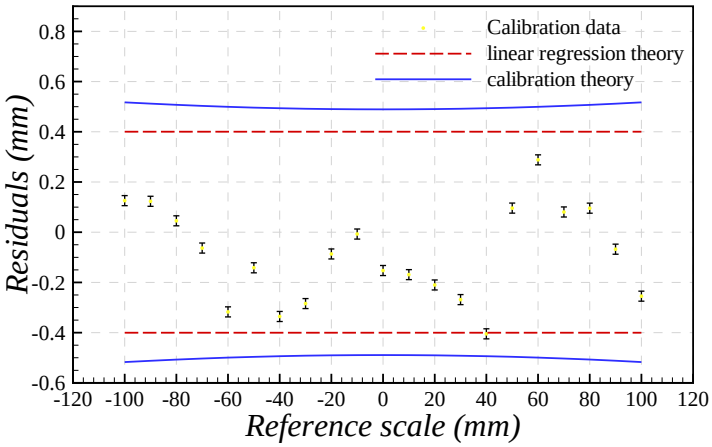

Figure 4.16: Residuals and 95% confidence predication limit for the ultrasonic wave probe calculated based on linear regression theory (dashed line) and calibration theory (solid line). where the small error bar is the uncertainty with 95% confidence in the reference scale

and connections between the probe and data acquisition system is one of the major factor.

Another uncertainty source will rise in the ultrasonic wave probe measurement if the manufacture calibration value is used. I.g. the A/D conversion uncertainty which can be estimated by

$$u(AD) = \frac{1}{2}\frac{Total\,Voltage\,Range}{A/D\,bits} \cdot calibration\,Factor \tag{4.26}$$

Since the data acquisition interface adopted has a 16-bit resolution, with $10V$ total voltage range the standard uncertainty in the A/D conversion is $\pm 0.0085mm$.

The uncertainty introduced by the A/D converter is not included in the uncertainty estimation for all the instruments calibration since all the calibrations were carried out in an End to End manner, i.g. the uncertainty induced by the A/D converter was included in the calibration.. The final uncertainty in the wave probe yields $\pm 0.5743mm$ at 95% confidence. Obviously, the uncertainty induced by the linear regression is the major source of uncertainty with a contribution of 99% to the total uncertainty.

Result of calibration of the incident wave along with 95% confidence interval is shown in Figure 4.17. Although the maximum difference between the measured incident wave amplitude and the target wave amplitude was kept below 1.5%, the uncertainty from the wave probe enlarged the difference to 3.5% when 95% confidence is considered.

Five repeat tests for the incident wave field were carried out at $Kh = 5.0$ in

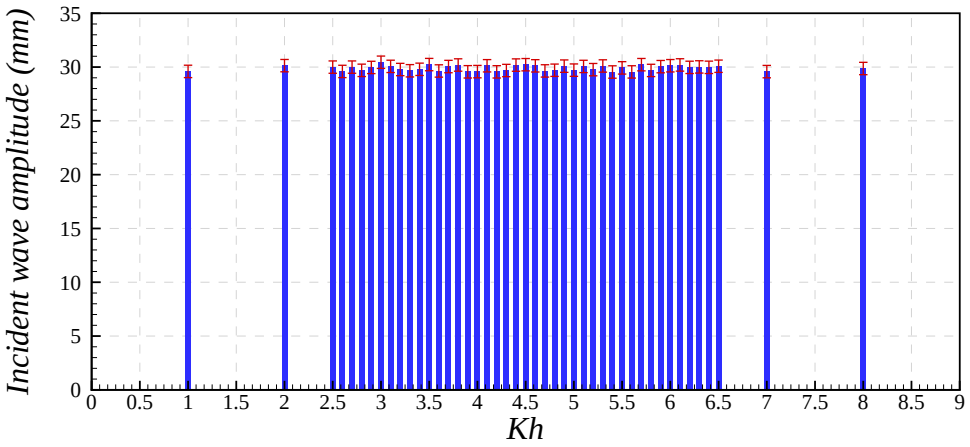

Figure 4.17: Calibration of wave field

order to quantify the repeatability in the incident wave. Ideally, all the frequency should be repeated to check whether there is any random events that is related to the wave frequency. However, it is usually not economic to do so due to tank availability and cost. Hence, it is recommended to carry out the repeat tests at a frequency near the resonance of the model for the reason that usually the power output achieves its maxima at the resonant frequency.

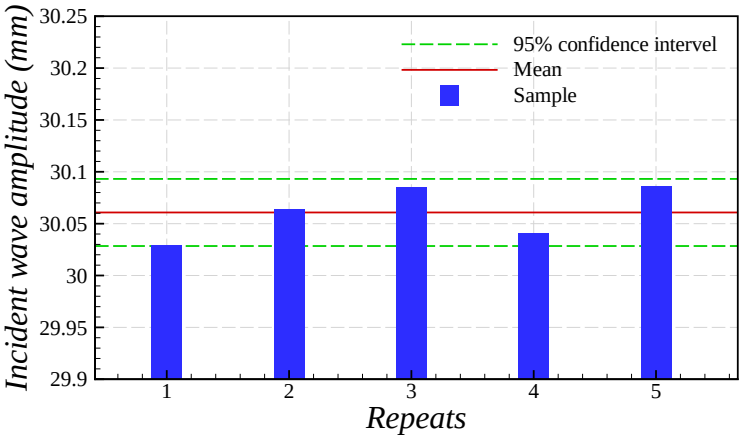

Figure 4.18: wave field repeatability of the KHL tank

As indicated by Figure 4.18, the KHL wave tank is highly repeatable giving a repeatability just about 0.12% of the mean measured wave amplitude at 95% confidence level calculated based on Students' t-distribution (with 4 degrees of freedom) with coverage factor equals to 2.78. Combining the type B uncertainty obtained from the calibration and the type A uncertainty from the repeat test, the total uncertainty in the incident wave amplitude is around 1.92% (at 95% confidence level) of the target incident wave amplitude due to wave decay along its propagation.

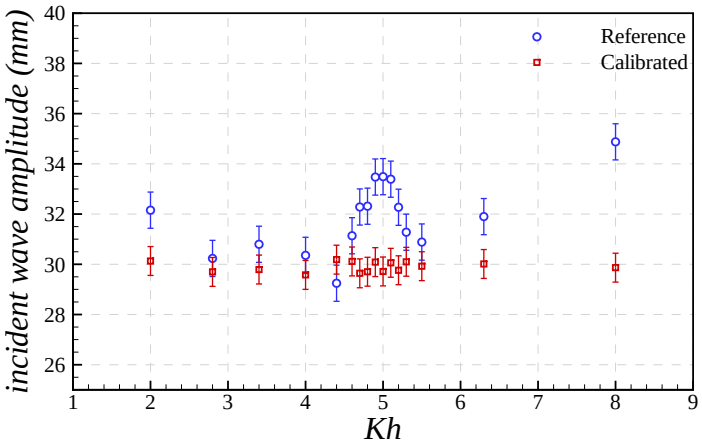

Figure 4.19: Comparison between the wave amplitude measured by the wave probe located at the place the FSCOWC device will be and that measured by the wave probe located at the reference point.

Figure 4.19 illustrated the wave amplitudes measured at the place the FSCOWC device will be and at the reference location. The wave amplitudes were measured in the same run during calibration. Clearly, there is significant difference in the amplitude measured at two different place. Overall, the wave amplitude measured at the reference place is larger than that at the place that the device is going to be placed. The disagreement between the overall trend of the wave amplitude measured by different wave probes suggests the wave amplitude spatial variation in the tank.

4.9.2 Open tube result

Although the open tube case provides no power, it gives an insight into the hydrodynamic problem without the effect from the PTO system. The RAO in frequency domain is shown in Figure 4.20. Where the solid and dashed line are the trend lines.The error bars indicate the uncertainty for RAO at 95% level of confidence where the horizontal bar is the uncertainty induced by the uncertainty in the draft. Due to tank availability, the estimation of type A uncertainty which requires repeat test is only carried out for $Kh = 5.0$ and assume that the uncertainty at any other frequency is not larger than that at the resonant frequency.

As indicated, the RAO calculated based on different wave probes do not agree with each other even considering the uncertainty. Calibration data indicated a 95% confidence uncertainty of $\pm 0.709mm$ in the resistance wave probe. Except for the larger uncertainty, since the resistance wave probe was calibrated individually

(That is the resistance wave probe was calibrated in open water condition instead of calibrated inside the device. This is simply because of the large size and weight of the FSCOWC, it is not realistic to calibrate the resistance wave probe together with the FSCOWC device.). Hence, the effect induced by putting the resistance wave probe close to the device solid surface was not included in the calibration value.

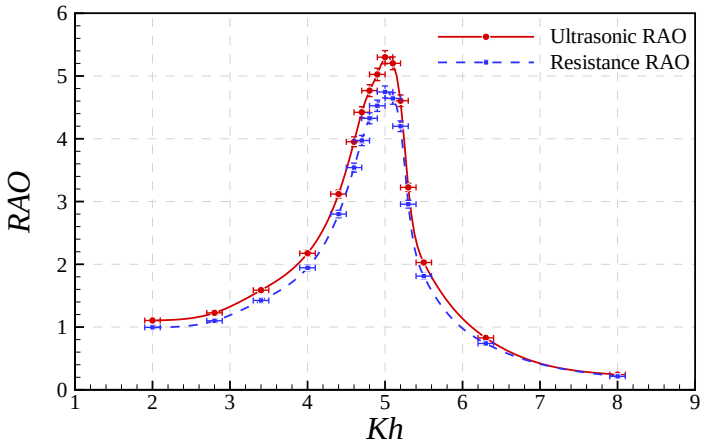

Figure 4.20: Response Amplitude Operator for open tube case calculated based on the data obtained by different wave probes where the error bars indicate the 95% uncertainty with vertical error representing the uncertainty in RAO and horizontal error bar indicating the uncertainty in Kh.

As suggested by Figure 4.20, the result obtained by the resistance wave probe seems to be consistently smaller than that gained by the ultrasonic probe. Hence, the ratio between the peak RAO of each wave probe is calculated which equals to 1.1167. Multiply the ratio with the RAO gained by the resistance wave probe yields almost identical result compared with the RAO calculated based on the ultrasonic probe as shown in Figure 4.21.

To identify whether the difference between the two result is caused by bad calibration of the resistance wave probe, the resistance wave probe was calibrated right after the test. Calibration result suggested almost identical result against the previous calibration result. Which indicating the difference is caused by either spatial variation of the OWC inside the device or sensitivity of the calibration factor of the resistance probe when approaching the solid wall of the device.

Due to the additional uncertainty introduced by the meniscus or the spatial variation to the resistance wave probe, it was decided that the OWC elevation magnitude was monitored by the ultrasonic wave probe and the latency in the ultrasonic wave probe was corrected by referencing the resistance wave probe.

The effect of calculating the RAO based on the calibrated wave amplitude and

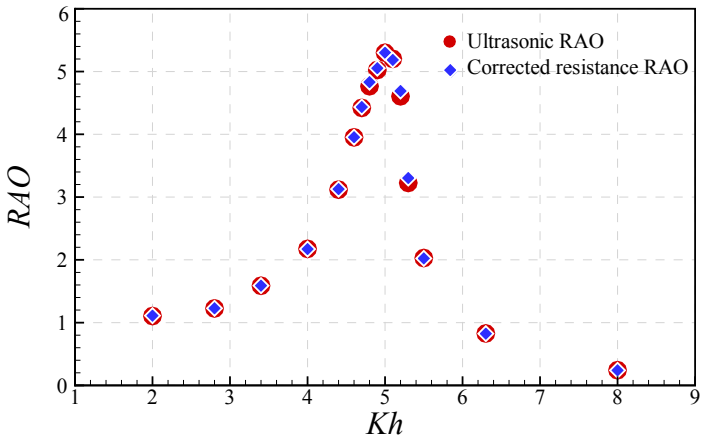

Figure 4.21: Comparison between the corrected RAO obtained by resistance wave probe and the RAO obtained by the ultrasonic wave probe

the reference wave amplitude is checked and result is illustrated by Figure 4.22. It can be seen that the RAO is under estimated especially around the resonance frequency. The incident wave amplitude measured by the reference wave probe during the calibration and during tests are compared. Results (Figure 4.23) suggests that the incident wave is highly repeatable, the difference are all within the uncertainty of measurement.

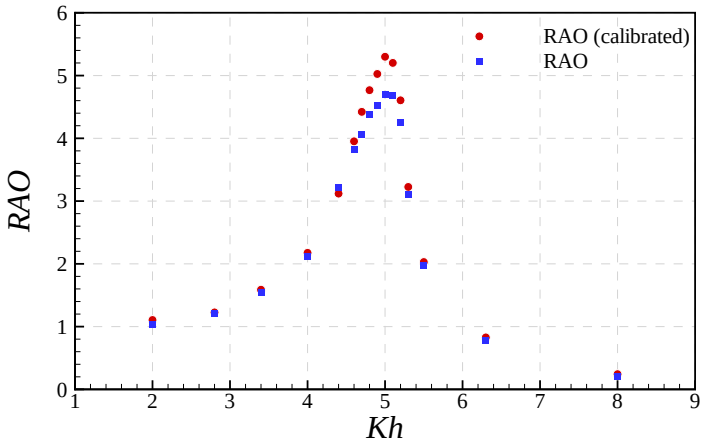

Figure 4.22: RAO calculated based on the calibrated incident wave amplitude and based on the wave amplitude measured by the reference wave probe, where RAO (calibrated) denotes the RAO calculated based on the the wave amplitude measured by the reference probe during the test.

If estimating the incident wave power based on the wave amplitude measured by the reference probe, the situation could become even worse. As can be seen in Figure 4.24, estimation of the incident wave power based on the reference wave probe can over estimate the incident power up to 40%. This will under estimate the performance of the device when calculate the capture width and capture factor about 30%. Therefore, it is critical to calibrate the incident wave at where the

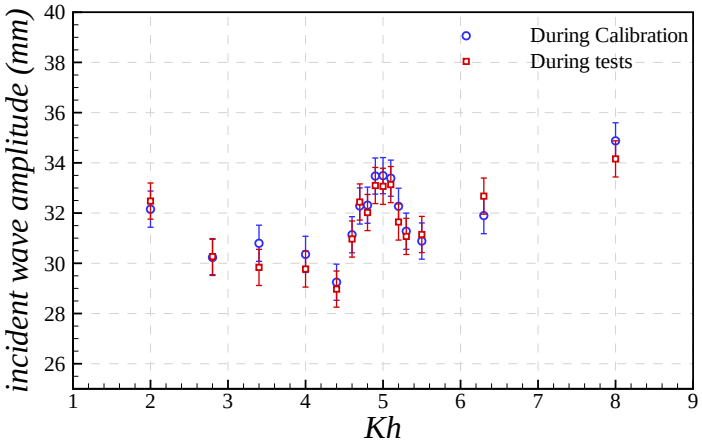

Figure 4.23: Incident wave amplitude measured by the reference wave probe during calibration and during testing.

device is going to be test before testing.

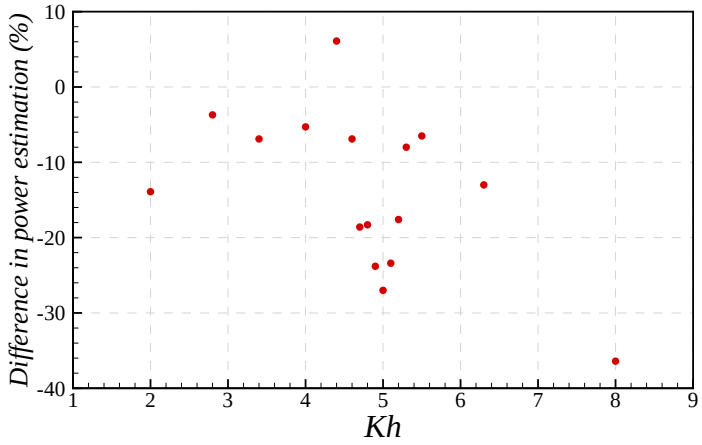

Figure 4.24: Percentage difference of incident wave power estimation based on wave amplitude measured from calibration and wave amplitude from reference probe.

4.9.3 With PTO results

4.9.3.1 Four orifice FSCOWC result

As expected, due to the presence of the orifice plate the RAO of the FSCOWC is damped as shown in Figure 4.25 for four orifice FSCOWC.

The first order harmonic term of the pressure amplitude along with the uncertainty at 95% level of confidence is illustrated in Figure 4.26.The Type A uncertainty in the pressure measurement was decided by repeat test and the Type B uncertainty was obtained from the specification (Honeywell, 2014) which is 2% of the span (equals to 12.4 *pa.*). It is clear that the uncertainty was over estimated as suggested

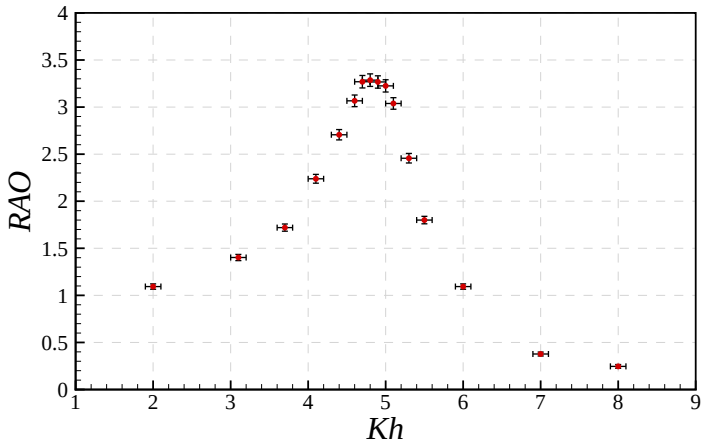

Figure 4.25: RAO of four orifice FSCOWC with uncertainty at 95% level of confidence expanded uncertainty.

by those pressure amplitude smaller than $10pa$ since the pressure amplitude can not be smaller than 0.

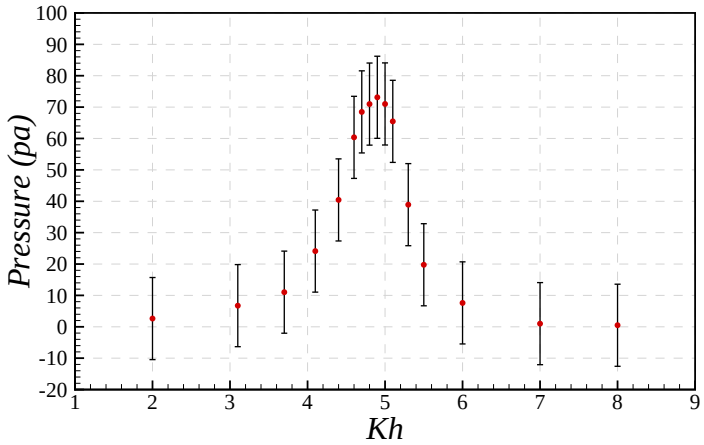

Figure 4.26: Pressure of four orifice FSCOWC with 95% level of confidence expanded uncertainty.

Since the fitted first order harmonic term of the pressure amplitude is smaller than the actual pressure, the mean power calculated in the time domain and the frequency domain (using Equation 4.16 and Equation 4.19 respectively) are first investigated. Results are shown in Figure 4.27.

Obviously, the mean power calculated by two different method yields almost identical mean power even the fitted first order harmonic pressure is smaller than the actual pressure. To explain this, instantaneous power are studied for $Kh = 4.9$ as shown in Figure 4.28.

As indicated, the power calculated by time domain method (power calculated by Equation 4.16) has higher instant peak power while at the same time has a wider zero power duration. These higher and lower power compensate each other leads

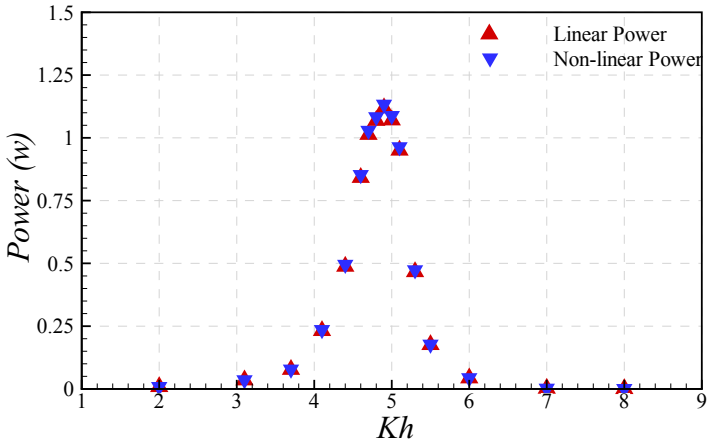

Figure 4.27: Comparison between the power calculated in time domain (non-linear power) and frequency domain (linear power)

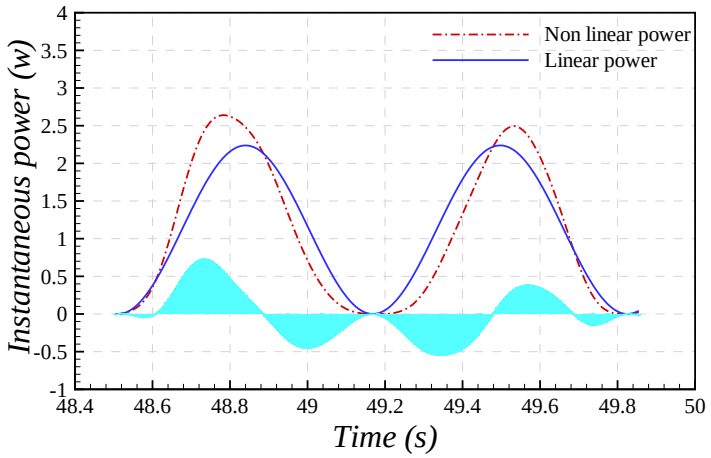

Figure 4.28: One typical period of instantaneous power for $Kh = 4.9$. The cyan area shows the power difference between the two different power calculated by different methods

to a almost same total power as the power calculate by frequency domain method (calculated by Equation 4.19) which is illustrated by the difference between two power as shown in cyan.

So far the suitability of estimating the mean power by using the frequency domain method has been proved. Therefore it is reasonable to estimate the uncertainty in the power by method proposed previously. The mean power for four orifice FSCOWC with expanded uncertainty are presented in Figure 4.29.

Inspection of the uncertainty in the mean power at 95% confidence level suggest that the absolute uncertainty in the mean power is about $\pm 0.2W$ around the resonant point (Figure 4.30) corresponding to a relative uncertainty about $\pm 18\%$ (see Figure 4.31). One shall notice that the relatively small absolute uncertainty at lower and higher frequency is a result of uncertainty propagation instead of reduction in the absolute uncertainty in the measurements.

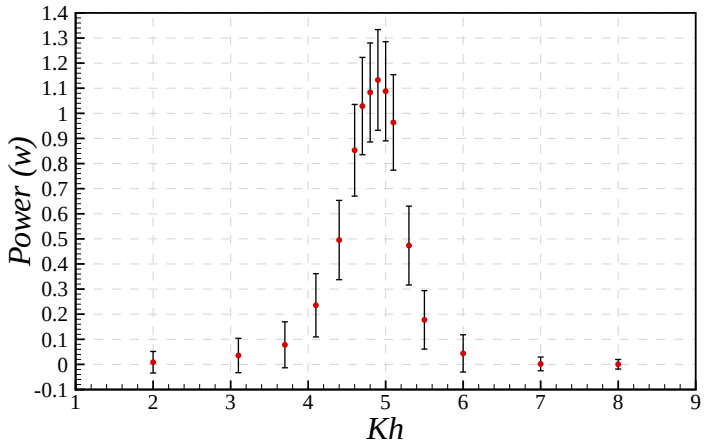

Figure 4.29: Mean power captured of four orifice FSCOWC with 95% level of confidence expanded uncertainty

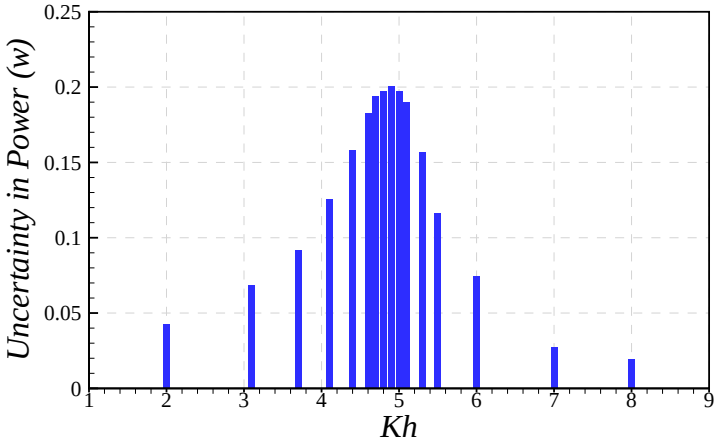

Figure 4.30: Absolute uncertainty in the captured power.

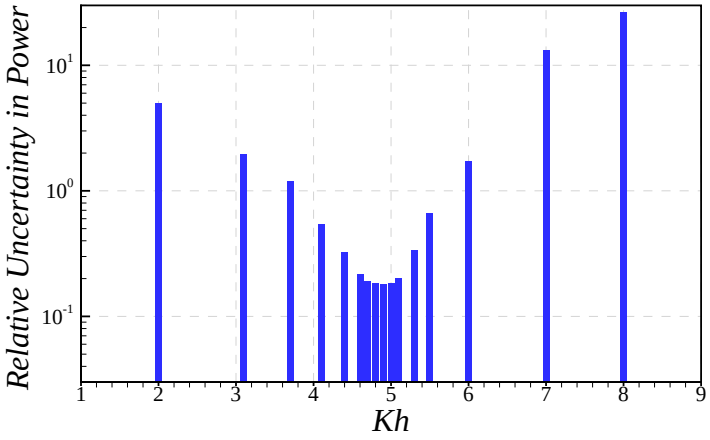

Figure 4.31: Relative uncertainty in the captured power, where the Y axis is in log scale and 1 equals to 100%.

±18% relative uncertainty in the power is certainly not good enough for assessing the performance of a model scale device. To reduce the uncertainty in the power,

contribution of each uncertainty component (as stated in Equation 4.20) to the total uncertainty is investigated. The total uncertainty in the power is dominated by the uncertainty in the pressure amplitude (almost 100%). Clearly, a reduction in the uncertainty in the pressure measurement required in order to minimize the uncertainty in the power.

To minimize the total uncertainty in the pressure, a methodology of calibrating the pressure transducer was developed and the uncertainty was estimated based on the new calibration results. Due to a new calibration factor was adopted, the pressure signal was re-processed. For detailed information on calibration of the pressure transducer, see Appendix A. The new pressure amplitude with uncertainty estimated based on the calibration is shown in Figure 4.32. Clearly, the new uncertainty is much more reasonable than the uncertainty provided by the manufacture.

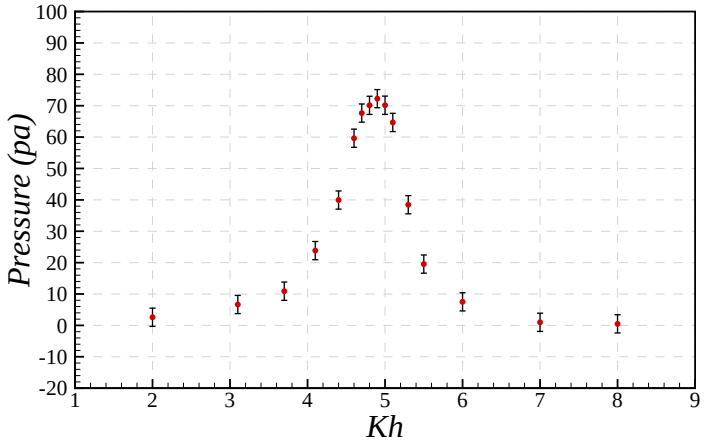

Figure 4.32: Pressure amplitude for four orifices case with 95% uncertainty estimated based on new calibration.

With the new uncertainty estimated for the pressure, the total uncertainty in the power is just about $0.045w$ as shown in Figure 4.33. The relative uncertainty is about 4.2% around the resonance frequency.

The uncertainty in the capture width (Figure 4.34) around the resonance is about $0.011m$ giving a relative uncertainty about 4.4%.

The uncertainty in the capture factor (Figure 4.35) around the resonance is about 0.037 giving a relative uncertainty about 4.6%. The increase in the relative uncertainty from power to capture width and then to capture factor exhibits the nature of uncertainty propagation.

Although the uncertainty in the pressure reduced dramatically after calibration,

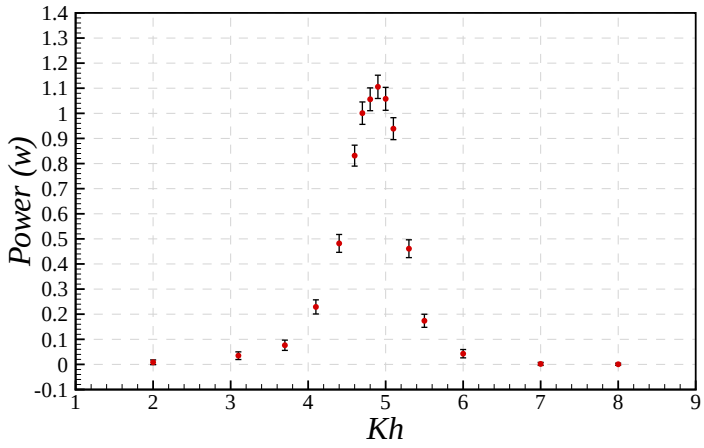

Figure 4.33: Mean power captured of four orifice FSCOWC with 95% level of confidence expanded uncertaintycalculated based on new pressure amplitude.

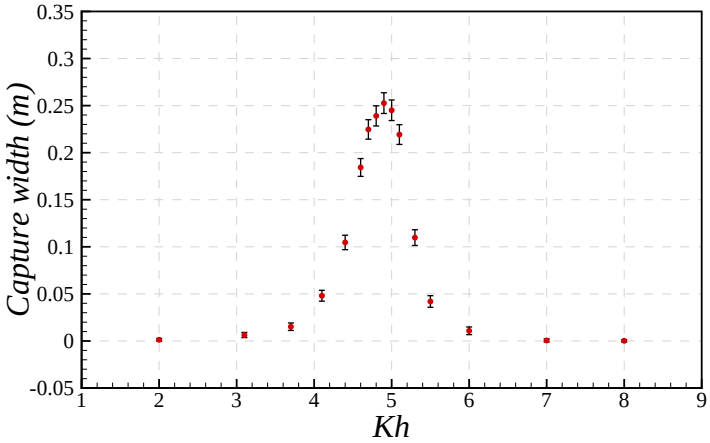

Figure 4.34: Capture width of four orifice FSCOWC with 95% level of confidence expanded uncertaintycalculated based on new pressure amplitude.

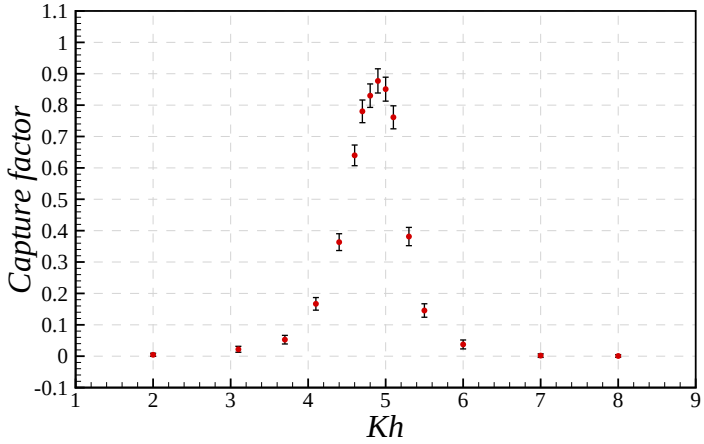

Figure 4.35: Capture factor of four orifice FSCOWC with 95% level of confidence expanded uncertainty calculated based on new pressure amplitude.

the uncertainty in the pressure measurement still contributes the largest part of the total uncertainty in the power as shown in Figure 4.36.

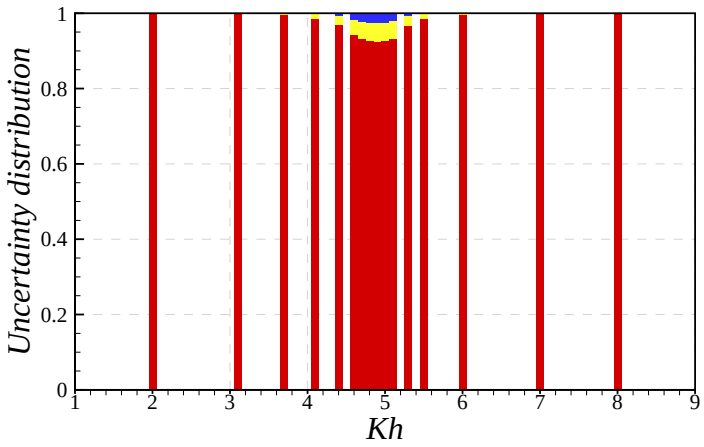

Figure 4.36: Uncertainty distribution, where the red, blue and yellow bar denotes the uncertainty contribution of the uncertainty in the pressure amplitude, in the OWC elevation amplitude and in the cross-section area, respectively.

4.9.3.2 Single orifice FSCOWC

Results of the single orifice FSCOWC are shown from Figure 4.37 to 4.41 illustrating the RAO, the pressure amplitude, the mean power, the capture width and the capture factor, respectively.

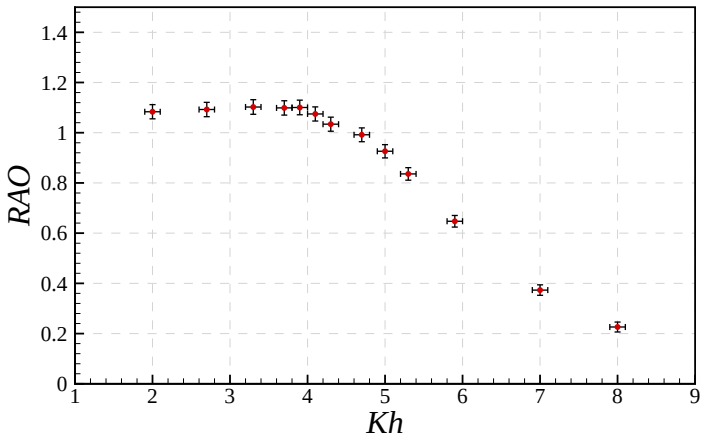

Figure 4.37: RAO of single orifice FSCOWC with 95% level of confidence expanded uncertainty.

Due to the strong damping effect introduced by the single orifice plate, the OWC motion is much smaller than the cases without orifice and with four orifices. The resonate peak is less obvious in the RAO plot. On the other hand, the peak pressure amplitude is larger than that of the four orifices case. Clearly, the pressure amplitude exhibits a obvious peak at $Kh = 4.1$ (Figure 4.38).

The maximum mean power captured by the single orifice case (Figure 4.39) is less than half of the maximum mean power captured by the four orifice case, however, it has a wider bandwidth and extract more power at lower and higher frequency.

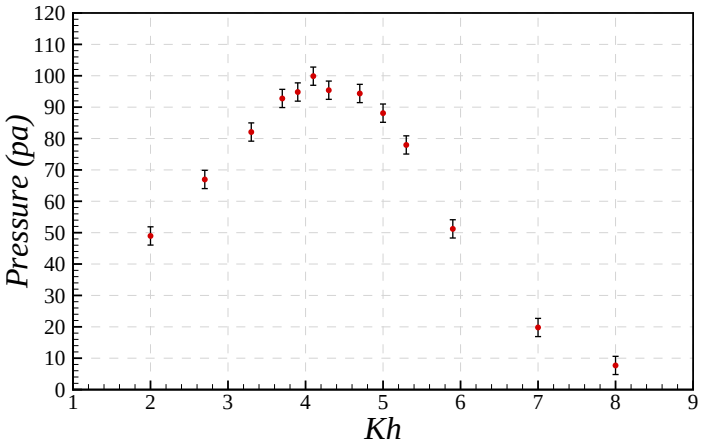

Figure 4.38: Pressure of single orifice FSCOWC with uncertainty at 95% level of confidence.

It is noted that the power captured around $Kh = 4.1$ and $Kh = 4.3$ are not 'smooth' forming a 'bump'. Although the uncertainty in the measurement may explain this phenomenon. It is in fact a result of tank width effect and will be discussed in detail later.

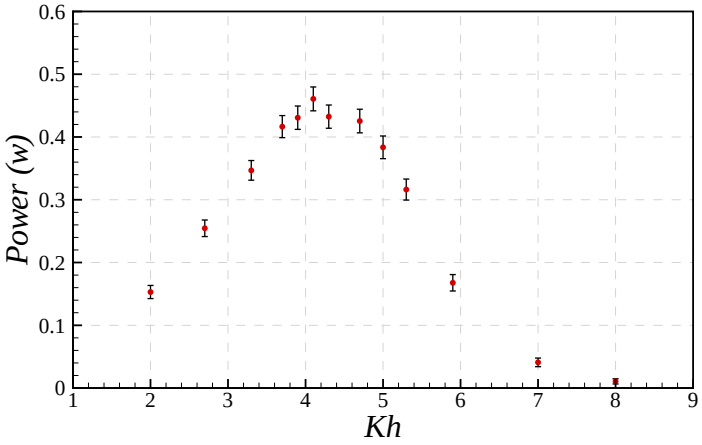

Figure 4.39: Mean power of single orifice FSCOWC with uncertainty at 95% level of confidence.

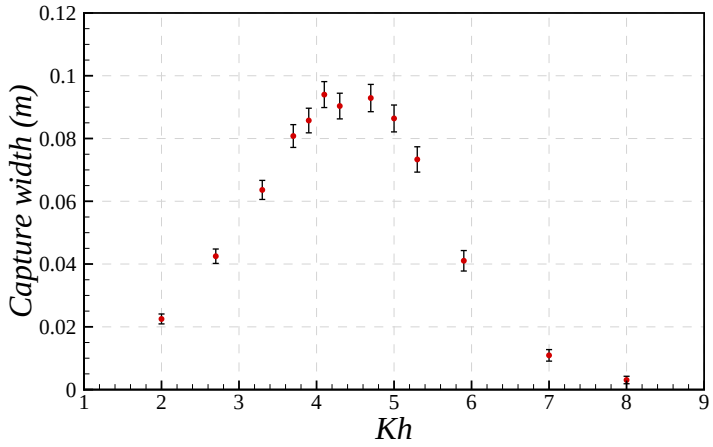

Figure 4.40: Capture width of single orifice FSCOWC with uncertainty at 95% level of confidence.

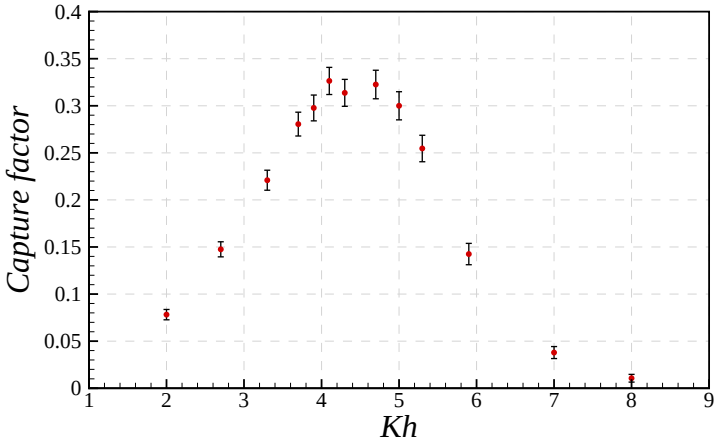

Figure 4.41: Capture factor of four orifices and single orifice cases compared with the numerical

The capture factor of the four orifices and single orifice cases are compared with the numerical solution of the analytical model as shown in Figure 4.42. It is clear that the four orifices case matches the analytical model better around the resonance frequency while the single orifice case agrees with the analytical result well at high and low frequencies. This indicates that to optimise the performance of the device, smaller damping of the PTO can provide higher power output around resonance frequency while higher PTO damping perform better at off resonance frequencies.

4.10 Chapter summary

In this chapter, a procedure for testing a 1:50 scaled FSCOWC device was developed. The RAO, the pressure amplitude inside the FSCOWC device, the mean power, the capture width and the capture factor were investigated for three

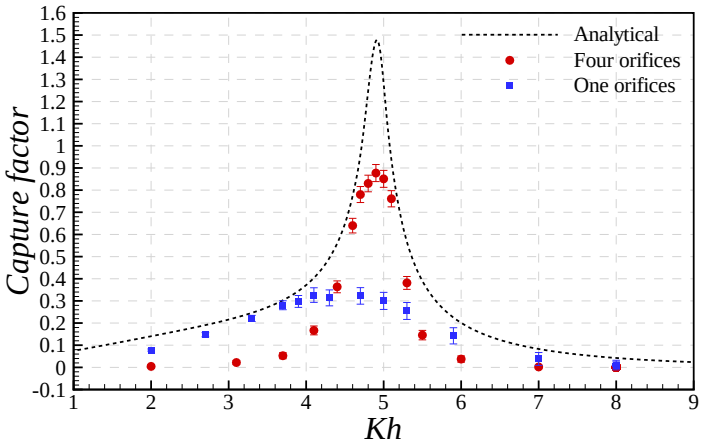

Figure 4.42: Capture factor of four orifices and single orifice cases compared with the numerical solution of the analytical modelling

different PTO damping level.

Comparison between the result obtained based on traditional method of estimating the incident wave (monitoring the incident wave by a reference wave probe) and pre-calibrated incident wave indicated that results obtained by traditional method will introduce non negligible error due to wave decay along wave propagation direction and tank spatial variation, especially in the estimation of the available incident wave power.

Comparison between the OWC elevation measured by the resistance wave probe and the ultra sonic wave probe suggested that the calibration factor of the resistance wave probe may be affected by the appearance of the inner solid wall of the device. Therefore, it is suggest to avoid putting the wave probe close to the device itself when monitoring the OWC elevation or calibrate the probe together with the device so that the effect will be included in the calibration.

Methodology and procedures of estimating the uncertainty in the measurement was developed. The uncertainty in the pressure measurement dominated the total uncertainty in the power and the relative uncertainty in the power was about $\pm 18\%$. With the new uncertainty estimation in the pressure measurement from the pressure transducer calibration, the total relative uncertainty in the power reduced to about $\pm 4\%$ at 95% level of confidence around the resonance frequency. The reason why the uncertainty in the pressure transducer estimated by calibration is smaller than that provided by the manufacture is that the calibration was done for the range of pressure measured in the test rather than the full scale of the pressure transducer. This suggests that to reduce the uncertainty in the measurement, one can calibrate the instruments in such a way so that the calibrated range is close

to the maximum quantity will be measured in the test.

Different level of PTO effect results show that weaker PTO damping (the orifice control parameter) leads to a higher peak mean power while stronger PTO damping provides a wider capture bandwidth. Based on this finding, it is recommend to use a low damping effect PTO system when the device will be deployed at a site where the sea state is relatively constant. So that maximum power can be captured. While on the other hand, if a device is going to be installed on a site where the sea state varied substantially, a higher damping PTO system is preferred so that the device can absorb power most of the time.

So far, the findings and conclusion are drawn based on the assumption that the spatial variation inside the FSCOWC device is negligible. It is extremely difficult to investigate the spatial variation of the OWC simply because of lack of effective method to measure the elevation of the entire OWC without affecting the OWC motion too much. Therefore, the spatial variation effect should be studied by numerical method.

Chapter 5

Experiment on a small scale FSCOWC

5.1 Chapter overview

To study the scale effect in tank testing of a FSCOWC device, an one third of the moderate FSCOWC scaled FSCOWC device is proposed in this chapter. In addition, two artificial walls are adopted to mimic the tank side walls and investigate the tank blockage effect on the performance of the FSCOWC.

5.2 Scaling law

It is well known that for wave-structure interactions, Froude scaling law (Sarpkaya and Isaacson, 1981) are well adopted to achieve similitude between the prototype and reduced scale model. Which means that the gravity is considered to be dominant over the other forces acting on the structure. Therefore, the Froude scaling law is selected to scale the environment and the device. Detailed scale information is listed in Table 5.1. Among those item listed in the table, according to Froude scaling, the length should be scaled with the scale factor which will scale the air volume by S^3. This, however, will scale the air compressibility incorrectly since the volume of air needs to be scaled by S^2 in order to scale the air compressibility correctly (see Sheng et al. (2014)). Therefore, to achieve the correct air compressibility, the length of the air chamber was kept the same as that of the moderate scale FSCOWC so that the volume of the air in the chamber

is scaled by S^2.

*Table 5.1: Scaling table. * it shall be noted that the air chamber length does not obey the Froude scaling law and the length of the air chamber should be the same as the moderate scale test.*

Parameter	Unit	Scale factor
*Length**	[m]	S
Stiffness	[N/m]	s^2
Area	$[m^2]$	S^2
Volume	$[m^3]$	S^3
Time	[s]	$S^{0.5}$
Frequency	$[s^{-1}]$	$S^{-0.5}$
Force	[N]	S^3
Mass	[kg]	S^3
Velocity	[m s^{-1}]	$S^{0.5}$
Acceleration	[m s^{-2}]	1
Power	[watt]	$S^{3.5}$
Capture width	[m]	S
Capture factor	non dimensional	1

5.3 Facilities

The experiment was carried out in the Henry Dyer Hydrodynamic Laboratory of the University of Strathclyde. The tank is equipped with a highly repeatable flap type wave maker. (The wave maker is not absorbing type as that in the Kelvin Hydrodynamic Laboratory, which introduced additional difficulty of reflection from the wave maker.) The tank has a dimension of $21.5m \times 1.53m \times 0.8m$. The width of the tank is almost one third of the width of the Kelvin Hydrodynamic Laboratory. This offered the opportunity to exclude the effect induced by different tank width. To keep the experiment similar to that done in the Kelvin tank, all the other equipment (e.g. the data acquisition interface.) were the same as used in the moderate scale test.

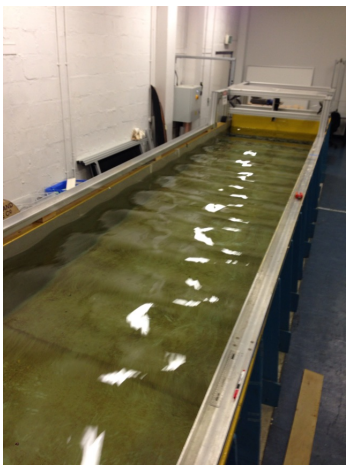

Figure 5.1: Henry Dyer Hydrodynamic Lab

5.4 FSCOWC models and configuration

Due to the use of standard material, not all dimensions of the device were exactly one third scaled, for instance, the thickness of the orifice plate is $4.0 \pm 0.2mm$ instead of $4.17mm$. Detailed geometry information of the one third scale FSCOWC can be found in Table 5.2, geometry information of the moderate scale device is included for comparison.

Table 5.2: Geometry details of the Two FSCOWC device

Component	Parameters (mm)	Large scale	Small scale
OWC model	total length	1045.0±0.5	706.7±0.5
	draft	350.0±10.0	11.7±3.0
Orifice plate	Plate Diameter	299.0±0.5	100.0±0.5
	Thickness	12.5±0.2	4.0±0.2
	Orifices Diameter	35.0±0.2	11.6±0.2
	Orifices position (PCD)	170±0.2	56.6±0.2
Tube	Outer Diameter	299.0±0.5	100.0±0.5
	Inner Diameter	287.0±0.5	96.0±0.5
Ring	Inner Diameter	299.3±0.5	96.3±0.5
	Outer Diameter	390.0±0.5	130±0.5
	Thickness	45.3±0.2	15.1±0.2
	Fillet radius	22.0±0.2	7.6±0.2

The FSCOWC device was fixed in position by attaching the device to the calibration system as illustrated in Figure 5.2. This configuration allows the

device to move with the calibration frame, so that the resistance wave probe can be calibrated together with the device. Therefore in this case the influence of appearance of the solid inner wall on the probe calibration factor will be included in the calibration process as discussed in previous chapter.

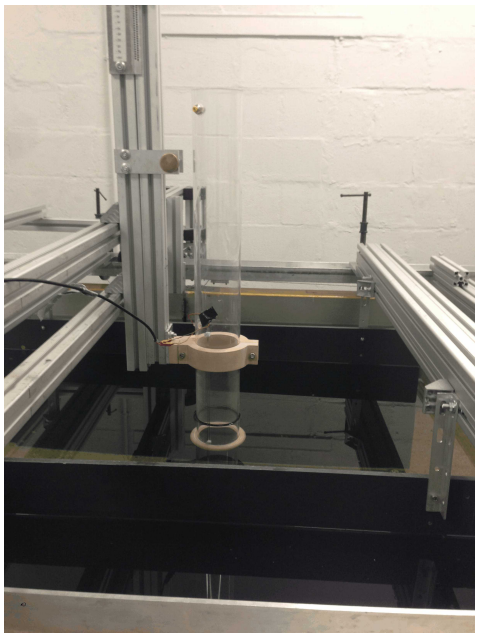

Figure 5.2: Configuration of the one third scaled FSCOWC experiment with two artificial walls

5.5 Instruments

According to the scaling law, the frequency is enlarged around 1.7 times. This makes the Ultrasonic wave probe (The Ultrasonic wave probe has a sampling rate at $50Hz$.) not suitable to capture the details of the OWC and incident wave information. Hence, in this test, only the resistance wave probe was adopted to measure the incident wave and the OWC motion. In order to make sure the presence of the resistance wave probe will not affect the OWC too much, the resistance wave probe was also scaled accordingly. This is because the presence of the wave probe will affect the volume of the OWC, the resistance wave probe used in the moderate scale has two metal rod with diameter equals 3mm which has a negligible impact on the volume of the moderate OWC (the diameter of the moderate OWC is 287±0.5mm while the small scale OWC has a diameter of 96±0.5mm, therefore the diameter of the wave probe used in the small scale test was scaled to 1mm.

Since the pressure range in current test is much smaller than that of the moderate

scale test, the pressure transducer used in the moderate scale test did not suit the small scale test since the noise signal is almost the same order as the pressure data signal. A smaller range ($\pm 62pa$) differential pressure sensor was therefore adopted to measure the pressure. Details of the SENSIRION SDP1000-L025 low differential pressure sensor can be found in Sensirion (2014). Although the SDP1000-L025 pressure sensor has a higher accuracy (1.5% of the span.) than the Honeywell pressure sensor (2% of the span), the SDP1000-L025 has a 40ms response time lag and has additional error over temperature about 0.03% measure value per degree. Both of the response time and temperature affects the final power estimating and hence introduced additional uncertainty to the results.

In order to minimise the temperature effect on both of the resistance wave probe and the pressure sensor, a digital thermometer was employed to measure the water and air temperature during the test.

5.6 Testing procedures

A simple test of the temperature effect on the wave probe reading was carried out prior to the formal testing to determine when the wave probe needs to be recalibrated. This was simply done by putting the calibrated resistance wave probe into a bucket of warm water(around $36°C$) and waiting for the water to cool down to the room temperature as shown in Figure 5.3. The readings from the wave probe and the thermometer were then recorded. Although the relationship between the temperature and the wave probe reading was weakly non-linear, $1°C$ change in temperature gave roughly $0.5mm$ difference in the wave probe reading. Assuming a linear relationship between the probe reading and the temperature, it is not difficult to conclude that $0.2°C$ will lead to $0.1mm$ difference in the probe reading. Therefore, the wave probe was recalibrated every time when the temperature changes $0.2°C$.

To minimise the uncertainty introduced by different testing procedures, the procedures of current test was kept the same as the moderate scale test. Calibrated the incident wave field of any tested frequency first (Modification of input wave amplitude to the wave maker is carried out (if necessary) so that the generated wave will have a wave amplitude with maximum 1.5% difference compared with the desired wave amplitude.). Regular wave tests were then carried out. During each test, the temperature was recorded for the air and water respectively.

Figure 5.3: Testing of the temperature effect on the resistance wave probe

After the tests using the full tank width, two artificial walls were installed in the tank to modify the tank width (Figure 5.2). Gaps between the two artificial walls equal to $730 \pm 1mm$ and $370mm \pm 1mm$ were tested to simulate the half tank width and the quarter tank width situation. Waves of the full tank width were repeated to investigate the effect of the appearance of the artificial walls. To make sure the two artificial wall do not behave like a harbour that will collect wave, the incident wave was rechecked before testing and essential modification was implemented when necessary.

Repeatability tests were carried out randomly during the tests.

5.7 Data processing

The data processing was largely the same as for the moderate scale test except for the correction of the response time latency of the pressure transducer. The additional error in the pressure sensor induced by temperature the temperature is about 0.1% of the measured data which corresponding to $0.02pa$ when the

pressure reached its maxima.

Since the wave probe was recalibrated several times, although the standard uncertainty did not varied a lot, the standard uncertainty was chosen to be the largest one among all the calibrations.

Phase lag in the pressure sensor was corrected simply by shifting the time 40ms ahead.

5.8 Results presentation

5.8.1 Uncertainty in the RAO

Although much care was put on scaling the device and the environment loading, it is almost impossible to scale the uncertainty in the instruments according to the designed scale. For example, the uncertainty in the resistance wave probe of the moderate scale was 0.46mm which is pretty much the limitation of this type of wave probes. The effect of failure scale the uncertainty in the instruments makes the final uncertainty very large. For instance, if we consider the combined uncertainty in the RAO (Equation 4.20), assuming the uncertainty in the wave probes are the same for both scale tests. If we omit the small covariance and divide the equation with RAO (η_{owc}/a) on both side of the equation, we have the relative uncertainty as

$$\frac{u_c(RAO)}{RAO} = \sqrt{\left(\frac{u(\eta_{owc})}{\eta_{owc}}\right)^2 + \left(\frac{u(a)}{a}\right)^2} \tag{5.1}$$

Now if we assume that no scaling effect exists, namely the RAO from the one third scaled test equals to that of the moderate scale test, it is not difficult to deduce that the combined uncertainty in the RAO for the one third scaled test is 3 times larger than that of the moderate scale test since the η_{owc} and a are 1/3 of the moderate scale.

In fact, the relative large uncertainty is the most severe challenge for small scale experiment. Especially for those experiments whose aim are to compare the difference between different conditions. Because in most of the case, the difference between different conditions are probably in the same order of the uncertainty and may be even much smaller than the uncertainty if expanded uncertainty with

large coverage factor is considered. This will be illustrated by the RAO of the open tube case.

Calibration of the resistance wave probe used in the FSCOWC device indicated a mean standard uncertainty of $\pm 0.547mm$ and $\pm 0.342mm$ in the probe that used to calibrate the incident wave field.

5.8.2 Open tube: Scale effect

The comparison of the moderate scale and one the small scale RAO of the open tube case are shown in Figure 5.4 with their uncertainty at 95% level of confidence.

Despite the relative large uncertainty in the small scale test, it is clear that the RAO of the small scale is smaller than that of the moderate scale test around the resonance frequency. This is because of the fact that the fluid property were not scaled, the viscosity was kept the same as the moderate scale test. Therefore, the viscous force which oppose the motion of the OWC is larger. As well as smaller RAO magnitude, it can be seen that the resonant point of the small scale case is shifted to a lower frequency.

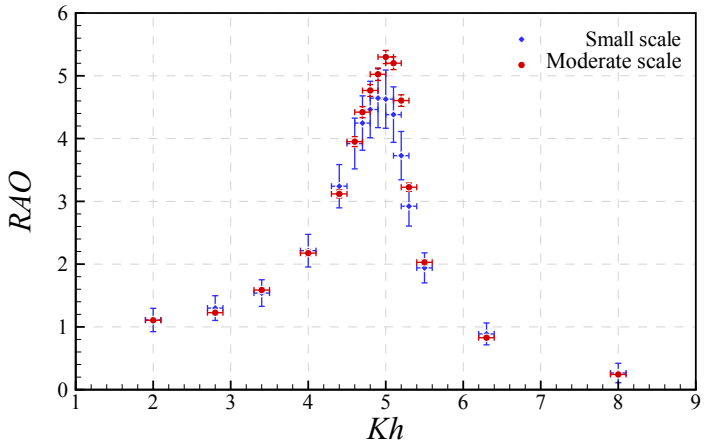

Figure 5.4: Comparison of the open tube RAO for the moderate scale and the one third scaled FSCOWC with 95% level of confidence

To explain that, hydrodynamic coefficients such as added mass coefficient would be helpful. However, frequency independent empirical hydrodynamic coefficients will fail to tell any difference between the moderate scale and small scale experiment due to the reason that the frequency independent empirical hydrodynamic coefficients do not account for the viscous effect. On the other hand, to obtain frequency dependant hydrodynamic coefficients, force oscillation test at different frequency is

required which is difficult to perform especially for the open tube case. Therefore, in this study, equivalent frequency independent linear hydrodynamic coefficients that will lead to similar results are investigated. The equivalent frequency independent linear hydrodynamic coefficients were obtained by an iterative procedure based on the Dynamic Magnification Factor (DMF). For details of calculation of the hydrodynamic coefficients, see Appendix B. The equivalent frequency independent linear hydrodynamic coefficients obtained by the proposed method is shown in Table 5.3. As can be seen, the added mass coefficient and damping ratio for the moderate scale test are both smaller than that of the small scale result. This explained the smaller RAO and the shift of the resonance peak.

Table 5.3: Equivalent frequency independent added mass coefficient and linear damping ratio for moderate scale and small scale open tube case.

Open tube case	Added mass coefficient	Damping ratio
Moderate scale	0.205	0.0617
Small scale	0.218	0.0704

5.8.3 Open tube: tank width effect

When talking about the difference between different tank width, the difference between each tank width is covered by the large uncertainty and it is hard to tell any difference between different tank widths as shown in Figure 5.4.

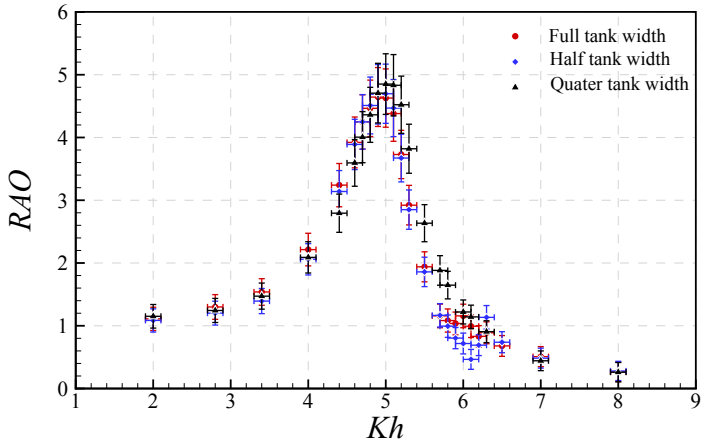

Figure 5.5: RAO with 95% level of confidence for full tank, half tank and quarter tank width

Neglect the uncertainty, as indicated by Figure 5.6, the result between the half tank and full tank are almost identical except for those around $Kh = 6$. The second resonance like phenomenon is most obvious at half tank and disappeared at quarter tank.

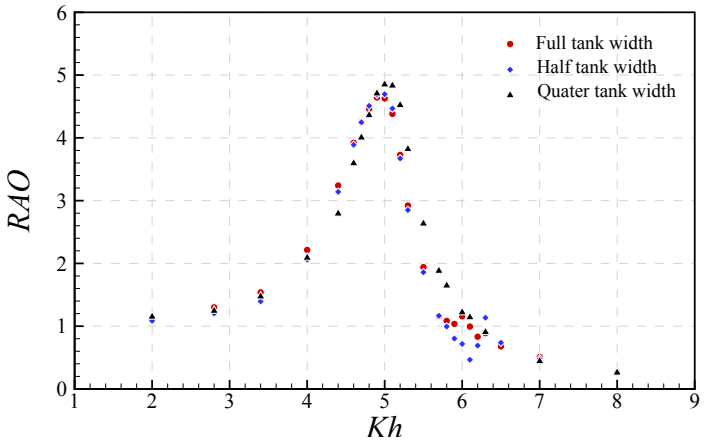

Figure 5.6: RAO for full tank, half tank and quarter tank width without uncertainty

Using the same DMF method as discussed above, the equivalent frequency independent linear damping ratio and added mass coefficient are plotted along with the DMF and fitted DMF from Figure 5.7 to 5.9. As can be seen, from full tank to quarter tank, the added mass coefficients increased slightly from 0.218 to 0.220 and reduced to 0.19 while the damping ratio decreases when the tank width reduces.

The second peak like phenomenon is not of particular interest in this case since it happened at low frequency where the performance of the device is poor. The three different tank width results suggest that this may be related to the tank width and hence may significantly bias the assessment of the performance of the device if the peak power output is around those frequencies. Therefore, the tank width ratio (defined as the ratio between the wavelength and the tank width w_T) is investigated. The tank width ratio is plotted along with the DMF.

Checking the width ratio at where the peak like phenomenon happens suggests that the phenomenon happened at width ratio equals to 0.5 for full tank and 1 for half tank. It is found that those frequencies matches the tank sloshing frequency which happens when

$$\frac{\lambda}{w_T} = \frac{2}{M} \tag{5.2}$$

where, the M is the mode of slosh with 1 standing for the first sloshing mode, 2 standing for the second sloshing mode, etc. The λ is the wavelength of the incident wave.

This, explained the 'bump' like power capturing for the moderate scale with one orifice since $Kh = 4.2$ corresponding to the third mode of tank sloshing.

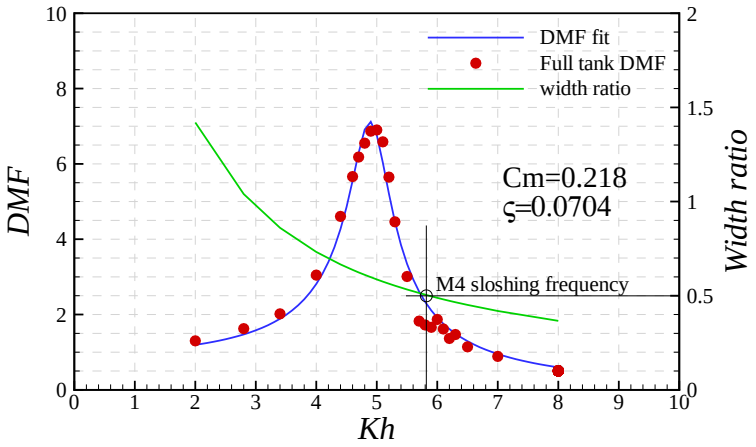

Figure 5.7: DMF, fitted DMF and tank width ratio for open tube case at full tank width.

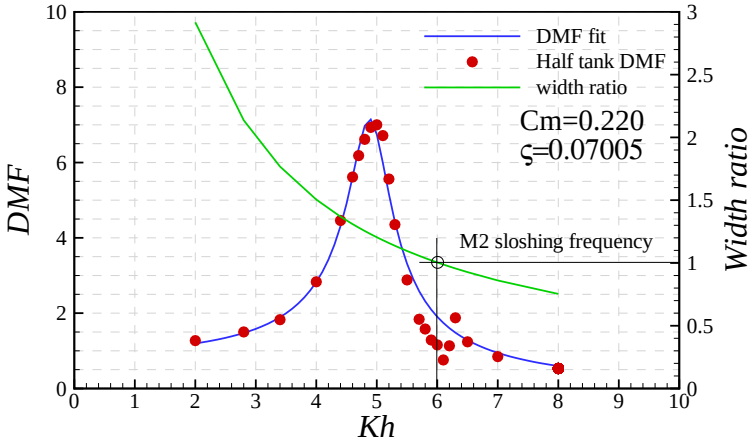

Figure 5.8: DMF, fitted DMF and tank width ratio for open tube case at half tank width.

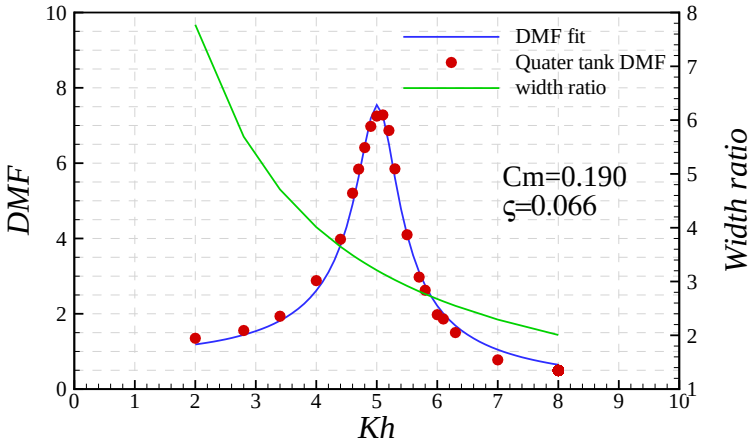

Figure 5.9: DMF, fitted DMF and tank width ratio for open tube case at quarter tank width.

5.8.4 OWC With PTO: tank width effect

Due to the fact that the relative uncertainty in the OWC response is too large for the one orifice case which has a maximum RAO near 1 as indicated by the

moderate scale test, therefore the small scale test with PTO was only carried out for the four orifice case.

The RAO for the four orifice case is shown in Figure 5.10, again, due to the large uncertainty it is difficult to get any information.

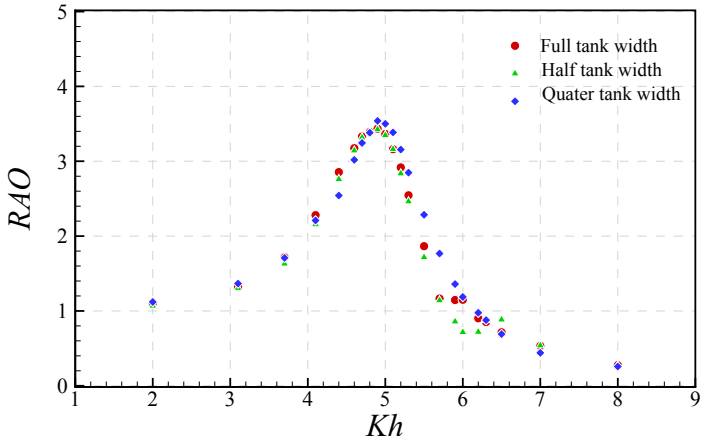

Figure 5.10: RAO for full tank, half tank and quarter tank width for four orifices case

The pressure amplitude as illustrated by Figure 5.11 does indicate that the maximum pressure amplitude increased when the wall approached the device even considering the 95% confident interval. It can be seen that the pressure amplitude also experienced the second peak like phenomenon around Kh=6.

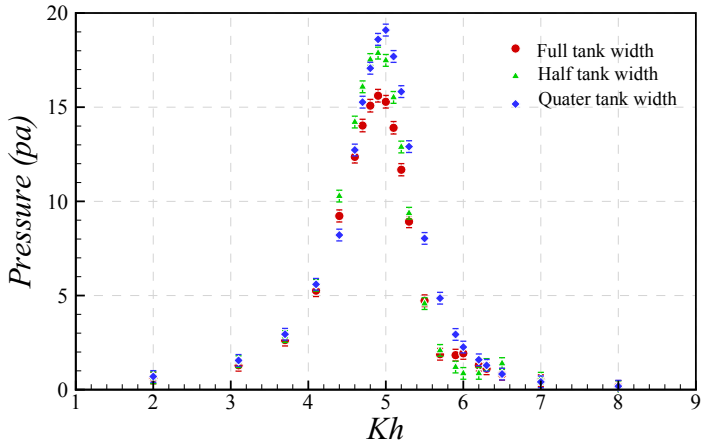

Figure 5.11: Pressure for full tank, half tank and quarter tank width for four orifices case with uncertainty at 95% confidence level

The uncertainty in the power, capture width and capture factor (Figure 5.12, 5.13 and 5.14, respectively) are all about 5.5% of the value at the resonate point at the 95% level of confidence.

Clearly, the maxima of the power captured increased with the approaching of the two side walls. This is because of that the tank wall behave similar as the

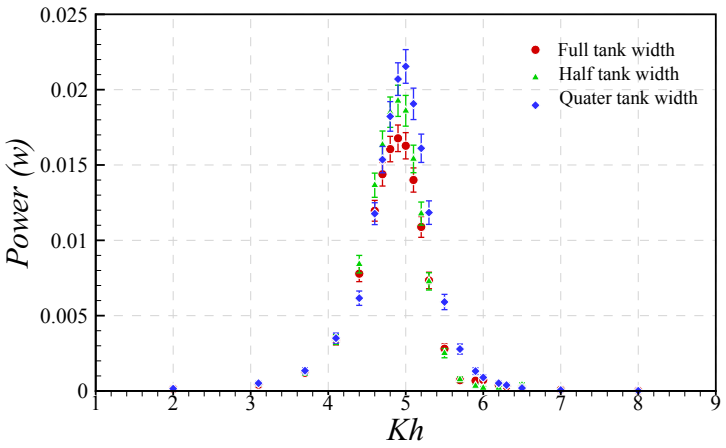

Figure 5.12: Power for full tank, half tank and quarter tank width for four orifices case

back wall of the asymmetry device that prevent lose of energy due to radiation (Sarmento (1992)). Although the resonance like phenomenon at tank sloshing frequency is obvious when looking at the RAO, it is almost negligible when talk about the captured power.

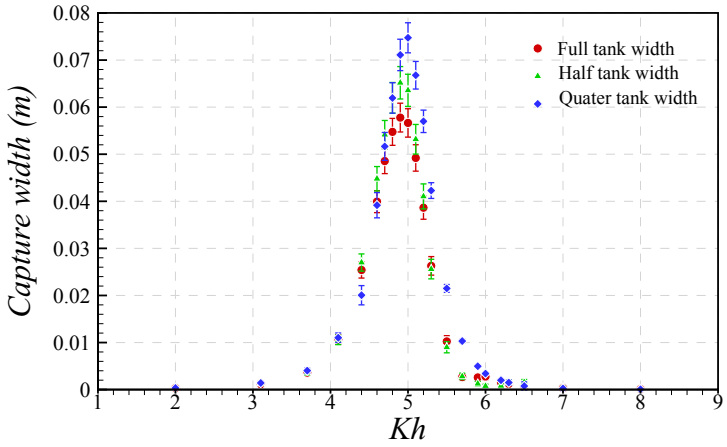

Figure 5.13: Capture width for full tank, half tank and quarter tank width for four orifices case

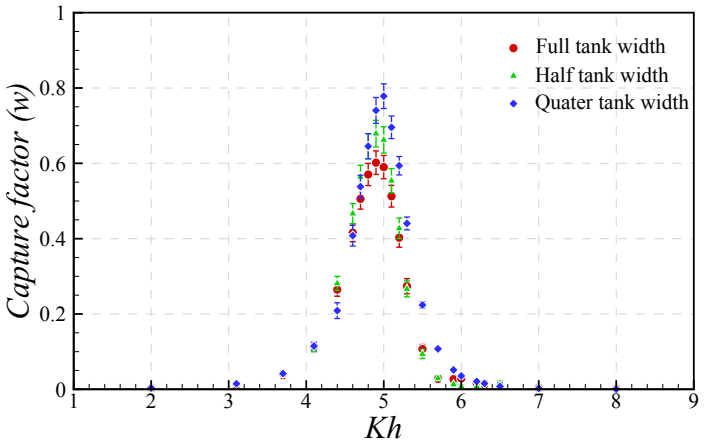

Figure 5.14: Capture factor for full tank, half tank and quarter tank width for four orifices case

As indicated by Figure 5.14, the maximum capture factor of the quarter tank case increased almost 20% compared with the full tank case. This suggests that proper allocation of each single unit can enhance the performance when array is considered. For example, the tank blockage effect in this study can be treated as there are extra two FSCOWC devices spacing w_T away from the tested device as discussed in Ersdal and Moe (2013).

5.8.5 OWC with PTO: scale effect

Due to the inability to scale the viscosity of the water, the small scale experiment experienced extra viscous effects and thus has a smaller response is expected as suggested by the open tube RAO. However, Figure 5.15 indicated a larger response of the OWC for four orifice case even the difference is in fact covered by uncertainty. This might be cased by failure of scaling the PTO system correctly since the PTO behaviour is quite sensitive to the geometry of the orifice and the orifice is not exactly scaled as mentioned before. The PTO character will be studied in detail later.

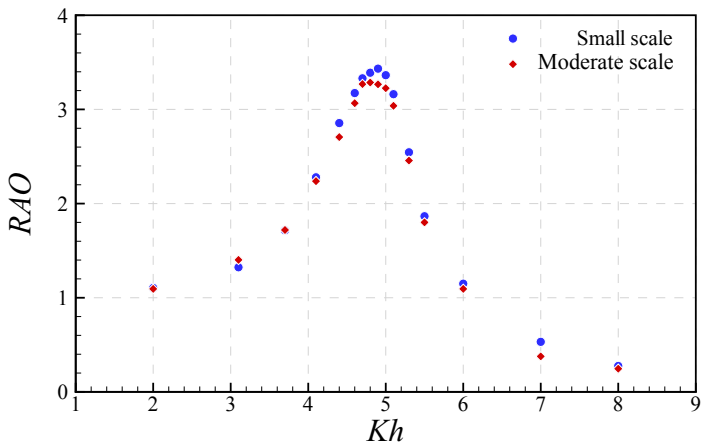

Figure 5.15: Comparison of the moderate scale RAO and the small scale RAO for four orifices case

On the other hand, the comparison between the pressure amplitude suggests that the pressure at small scale is much smaller than the moderate scale result (The small scale pressure is scaled up by a factor of 3.) This leads to a much smaller capture factor (see Figure 5.17).

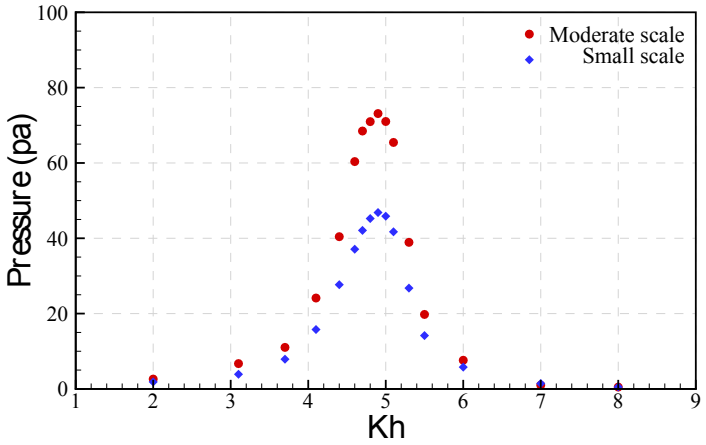

Figure 5.16: Pressure amplitude comparison between the small scale and moderate scale, where the small scale pressure is scaled up by a factor of 3.

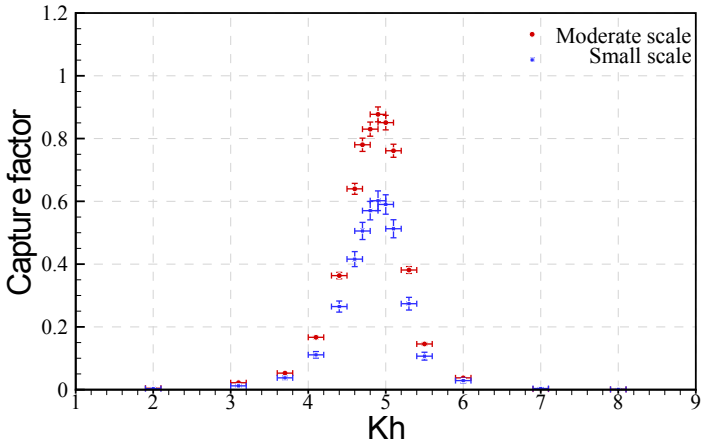

Figure 5.17: Comparison of the moderate scale capture factor and the small scale capture factor for four orifice case

5.9 Chapter summary

In this chapter, a further $1:3^{rd}$ scaled FSCOWC test were carried out to study the scale effect and tank blockage effect by means of tank testing.

Although the uncertainty in the pressure measurement is excellent by using a proper pressure sensor, however, small scale test encountered large uncertainty in the OWC elevation RAO calculation due to the nature of uncertainty propagation. This illustrate a big challenge of small scale model testing.

Using the DMF fitting technique, it is found that the smaller scale test experience a larger damping ratio due to viscosity. The added mass coefficient is also slightly large than that of the moderate scale test leading a shift in the resonance frequency. This shift in the resonance frequency is, however, not significant since it equals to about 0.0933 seconds difference in full scale period ($1:150^{th}$ scale.)

The results of the three different tank width effect tests suggest that there exists spike like phenomenon around the tank sloshing frequency. Although this does not affect the assessment of the performance for the four orifices case since that spike like phenomenon happened at where the power capture performance is not of great interest. However, in other cases, this could affect the performance of the device around resonance peak as suggested by the bump like captured power for the one orifice case at moderate scale test.

The comparison of the RAO at different tank width failed to give any useful information due to the large uncertainty in the measurement. However, clearly, the pressure amplitude and the power captured do increase when the width of the tank reduces even considering the uncertainty. Hence, care must be paid on reporting the results of tests done in narrow tank to prevent over estimate the performance at full scale.

Comparison between the small scale and moderate scale result suggest the small scale model gave a smaller capture factor. The power loss due to viscosity is one of the major reason. Comparison of the RAO for four orifice case at two different scale suggesting that the RAO at small scale seems to be larger than that of the moderate scale. On the other hand, open tube RAO at two different scale did suggest the RAO at small scale is smaller than that of the moderate scale. This finding implies the PTO behaviour was probably not scaled accurately. Numerical simulation may help to answer this since in numerical simulation the uncertainty in constructing the orifice plate would be negligible.

Chapter 6

Reflection-free Numerical Wave Tank

6.1 Chapter overview

As already mentioned in previous chapters, tank testing encounters uncertainties in scaling and measurement which makes the result less reliable especially in those tests whose main purpose is to compare small difference (e.g. tank blockage effect.). On the other hand, numerical simulations usually do not have the above disadvantage. Therefore, from this chapter, numerical simulations are carried out to assess the performance of the two different scaled FSCOWC devices, investigate the scaling effect and also the tank blockage effect. To accurately simulate the FSCOWC problem, numerical wave tank (NWT) construction is critical, hence, this chapter studies the NWT. The mesh effect and time step size effect on the result is investigated in detail.

6.2 Methodology

It is well known that all of fluid dynamics is based on three physical principles:

- Mass is conserved
- Newton's second law
- Energy is conserved

These physical principles are developed into the fundamental governing equations of fluid dynamics. They are the continuity equation, the momentum equations and the energy equation. The continuity equation for compressible fluid is expressed by Equation 6.1 as

$$\frac{\partial \bar{\rho}}{\partial t} + \mathrm{div}(\bar{\rho}\tilde{\mathbf{U}}) = S_m \tag{6.1}$$

Where, The S_m on the right hand side is the mass source term. The $\mathbf{U}$ is the velocity vector includes x,y and z components represented by u, v and w, respectively. The velocity components are consist of a mean part $(\tilde{U}, \tilde{V}, \tilde{W})$ and fluctuating part $(u^{'}, v^{'}, w^{'})$ if turbulence is considered. Therefore u, v, w can be expressed by:

$$\begin{aligned} u &= \tilde{U} + u^{'} \\ v &= \tilde{V} + v^{'} \\ w &= \tilde{W} + w^{'} \end{aligned} \tag{6.2}$$

The overbar in Equation 6.1 and 6.2 means time averaging while the tilde bar indicates a Favre averaging (density weighted average.). Since the maximum velocity in current study is far less than the sound speed and result in a Mach number (the ratio of flow velocity past a boundary to the local speed of sound.) far smaller than 1, therefore the turbulent fluctuations will not lead to any significant fluctuations in density (Bradshaw et al., 1981). Hence, the Favre averaging can be replaced by Reynolds averaging. That is $\tilde{U} = \bar{U}$.et.al.

The x, y and z momentum equations are give by Equation 6.3 for compressible turbulent flow. Where the S_{Mx}, S_{My} and S_{Mz} are the momentum source term for x, y and z momentum equations, respectively.

$$
\begin{aligned}
\frac{\partial(\bar{\rho}\tilde{U})}{\partial t} + \operatorname{div}(\bar{\rho}\tilde{U}\tilde{\mathbf{U}}) = &-\frac{\partial \bar{p}}{\partial x} + \operatorname{div}(\mu \operatorname{grad}\tilde{U}) \\
&+ [-\frac{\partial \overline{\bar{\rho}u'^2}}{\partial x} - \frac{\partial \overline{\bar{\rho}u'v'}}{\partial y} - \frac{\partial \overline{\bar{\rho}u'w'}}{\partial y}] + S_{Mx} \\
\frac{\partial(\bar{\rho}\tilde{V})}{\partial t} + \operatorname{div}(\bar{\rho}\tilde{V}\tilde{\mathbf{U}}) = &-\frac{\partial \bar{p}}{\partial y} + \operatorname{div}(\mu \operatorname{grad}\tilde{V}) \\
&+ [-\frac{\partial \overline{\bar{\rho}u'v'}}{\partial x} - \frac{\partial \overline{\bar{\rho}v'^2}}{\partial y} - \frac{\partial \overline{\bar{\rho}v'w'}}{\partial y}] + S_{My} \\
\frac{\partial(\bar{\rho}\tilde{W})}{\partial t} + \operatorname{div}(\bar{\rho}\tilde{W}\tilde{\mathbf{U}}) = &-\frac{\partial \bar{p}}{\partial y} + \operatorname{div}(\mu \operatorname{grad}\tilde{W}) \\
&+ [-\frac{\partial \overline{\bar{\rho}u'w'}}{\partial x} - \frac{\partial \overline{\bar{\rho}v'w'}}{\partial y} - \frac{\partial \overline{\bar{\rho}w'^2}}{\partial y}] + S_{Mz}
\end{aligned}
\tag{6.3}
$$

Considering the complexity of current simulation, the air compressibility is modelled by assuming the air is isothermal prefect gas and thus there's no need to solve the energy equation, therefore neglected here. The equation of state for prefect gas is given by Equation 6.4.

$$
p = \rho R T \tag{6.4}
$$

Here, R is the universal gas constant and T is the temperature.

Clearly, there are commonalities between Equation 6.1 and 6.3. If we introduce a general turbulent variable ϕ ($\phi = \bar{\Phi} + \phi'$), we can get the well known transport equation

$$
\begin{aligned}
\frac{\partial(\bar{\rho}\tilde{\Phi})}{\partial t} + \operatorname{div}(\bar{\rho}\tilde{\Phi}\tilde{\mathbf{U}}) = &\operatorname{div}(\Gamma_\phi \operatorname{grad}\tilde{\Phi}) \\
&+ [-\frac{\partial \overline{\bar{\rho}u'w'}}{\partial x} - \frac{\partial \overline{\bar{\rho}v'w'}}{\partial y} - \frac{\partial \overline{\bar{\rho}w'^2}}{\partial y}] + S
\end{aligned}
\tag{6.5}
$$

Where the first term on the left hand side is the transient term, the second term is the convection term and the first term on the right hand side is the diffusion term. The term in the brackets is the Reynolds stress term caused by the fluctuation term of ϕ. The last term is the source term. Equation 6.1, 6.3 and 6.4 formed the so called Reynolds-averaged Navier-Stokes (RANS) equations.

To compute turbulent flows with the RANS equations, a turbulence models is needed to predict the Reynolds stresses and the scalar transport term and close the system. Menter (1992)'s two equation $K-\omega$ sst model is employed in current study for its better performance in boundary layers.

When free surface flow is considered, the simple multiphase model Volume of Fraction (VOF) (Gueyffier et al., 1999) is usually adopted to solve the interface between the immiscible air and water on numerical grids.

The commercial Finite Volume Method (FVM) package STAR-CCM+ is selected to solve the problem. The numerical method used in STAR-CCM+ starts from integrating the governing equations of fluid flow over all the control volumes of the domain and leads to an algebraic equation system solvable on a computer by means of a number of discrete approximations.

The solution of the RANS equations is accomplished by using a segregated iterative method Which is the well known Semi Implicit Method for Pressure-Linked Equations (SIMPLE).

Since the objectives of the current study as listed in Chapter 2 is to develop a CFD procedure to accurately assess the performance of the FSCOWC device rather than develop a CFD methodology, the methodology is only simply described. Detailed information about CFD methodologies and basic background theory can be found in Versteeg and Malalasekera (2007) and Ferziger and Peric (2012).

6.3 Wave generation and absorption in CFD approaches

To accurately assess the performance of the FSCOWC device by CFD methods, it is critical to construct an accurate Numerical Wave Tank (NWT). Therefore, this section will study the NWT and validate the generated wave against wave theory.

6.3.1 wave generation

Several methods of wave generation in CFD have been developed during the past years. Generally, they can be sorted into two categories:

The first type of method is to directly simulate physical processes such as piston

wave maker which are directly analogy to hydrodynamic wave tank facilities, for instance, Anbarsooz et al. (2013). Since this method is reproducing the physics of the wave maker, therefore, it has the drawbacks of the real wave maker such as the evanescent wave in front of the wave maker Mei et al. (2005). This requires sufficient distance from the wave maker to the testing object in order to avoid the influence of the evanescent wave and hence will increase the total mesh number especially for 3D simulation. Furthermore, it usually involves use of moving mesh . This is a problem computer resource which again will increase the computation time.

The second type f approach employs numerical methods such as source term wave making. For instance, Lin and Liu (1999) developed a wave generator based on the concept of underwater explosion. By applying a periodic varying mass source term (derived from wave theory) into the continuity equation, the wave is thus generated. Although this method is quite simple and efficient, the quality of generated wave is quite dependent on the position of the source term. Thus great effort is needed on determining the source position even with some rules of thumb. An alternative source term wave generating method uses a momentum source term. Similar to mass source term method, this method realize wave making by adding a momentum source term derived from wave theory into N-S equation. To accomplish this, a source length of at least one wavelength is required which increases the calculation domain size.

As well as the source term methods, another numerical method sets the velocity profile over the water depth of wave on the inlet boundary, this is called boundary velocity input method. The theory behind this method is the same as physical mimic methods. However, by setting the velocity profile directly to the boundary there will be no evanescent wave. Unlike the mass source term method, the velocity at the boundary is updated according to the wave elevation directly at the boundary withthe velocity above the free surface equals to zero, therefore, no additional effort is needed on designing the boundary. based on it's simplicity and advantages over the other wave generation methods, the boundary inlet method is adopted in the present CFD simulation.

In order to reduce the computation time, the preliminary of the NWT is carried out in 2D simulation. Fenton's (1985) fifth-order wave theory is adopted to simulate the wave in order to include the non-linear effect. The water particle velocity is assigned to the velocity inlet boundary to define the velocity and the static pressure distribution is achieved implicitly by defining the volume fraction

of water along the water depth.

6.3.2 Domain and boundary conditions

The length of the NWT is declared by wavelength to avoid unnecessary increment of mesh number. (To accurately capture a wave, there must be enough mesh in the wave propagation direction, hence, for a constant length NWT tank, more mesh is needed to accurately capture a shorter wave.). The Detailed size of the domain and boundary conditions are shown in Figure 6.1. Since in starccm+ the 2D simulation is achieved by using a 3D simulation with only one cell thickness, the lateral boundaries are set to be symmetry.

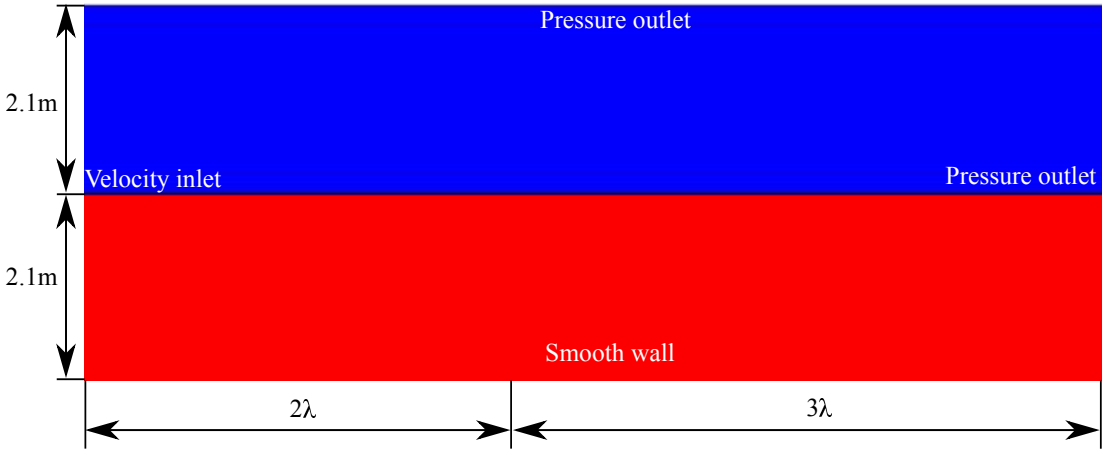

Figure 6.1: Domain size and boundary conditions. Left boundary is velocity inlet, right hand side and top boundaries are both set to pressure outlet, the tank bottom is set to be smooth wall and symmetry boundaries are set to be the lateral boundaries conditions.

6.3.3 Mesh topology

As point out by several researchers (e.g. Higuera et al. (2015), the quality of the NWT tank is quite sensitive to the mesh distribution. A dense mesh is usually preferred in FVM simulation in order to achieve an accurate result, however, for wave structure interaction a dense mesh is often not affordable since except for dense mesh around the structure, a similar order mesh is needed to accurately capture the wave while at the same time the domain needs to be large enough to avoid 'cut off' of the wave structure interaction.

To develop a proper mesh topology, the nature of the water wave is first investigated. As can been seen from the volume fraction of water for a fifth order wave ($\lambda =$

$2.69m$ $a = 30mm$) illustrated by Figure 6.2, the volume fraction of water under the wave is constant since it is all water. Therefore, it only require dense mesh around the wave region (wave crest to wave trough) to accurately capture the wave and the mesh beyond that region can be coarser.

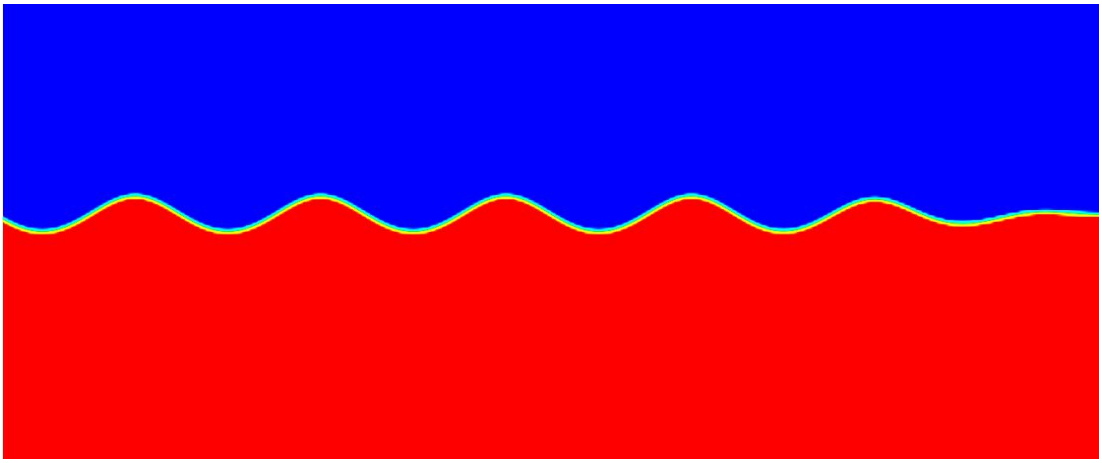

Figure 6.2: Volume fraction of water distribution for a fifth order wave. Where red is water while blue denotes air. For visualization purpose, this figure is scaled 10 times in gravity direction and only part of the whole domain is demonstrated.

As well as the wave elevation which determines the static pressure, it is necessary to capture the dynamic pressure to accurately calculate the total pressure induced by the wave. This requires accurate capture of the water particle velocity. As suggested by Figure 6.3, the velocity magnitude reduces with water depth. In this case the velocity magnitude tends towards zero. Therefore, the mesh topology is designed as shown in Figure 6.4 and Figure 6.5. The mesh is dense at wave region and gradually coarsen along water depth direction so that it is capable of capturing both the wave elevation and velocity accurately and at the same time minimizing the mesh needed.

The coarsening of the mesh along the water depth direction is decided by the water particle velocity magnitude. For example, in Figure 6.3, the red color region is the maximum water particle velocity magnitude region and the green part shows the velocity magnitude reduced by about 50% of the maximum velocity magnitude. Besides, the variation of velocity magnitude in the green and blue part is relatively small. Hence the mesh around the green and blue part can be coarser than that used at the red region. In the present simulation, as can be seen from Figure 6.2, the coarsening of the mesh is done in such a way so that the size of the mesh is related to the velocity magnitude, i.g. the mesh size of the green part is twice of that in the red region and when the mesh size is further enlarged 2 times when the velocity reduced to 25% of the velocity magnitude in the red

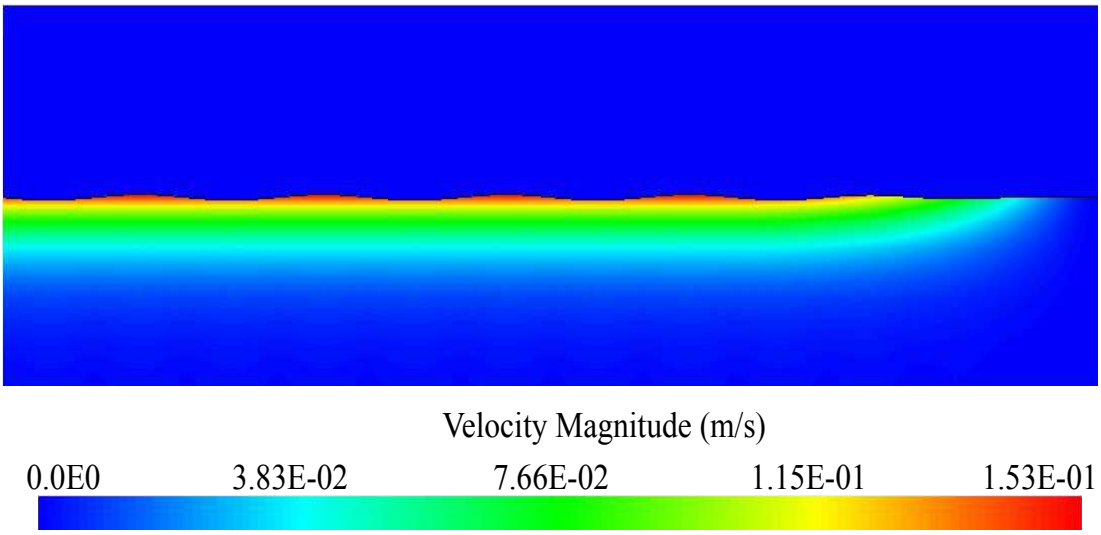

Figure 6.3: Theoretical water wave particle velocity magnitude distribution.

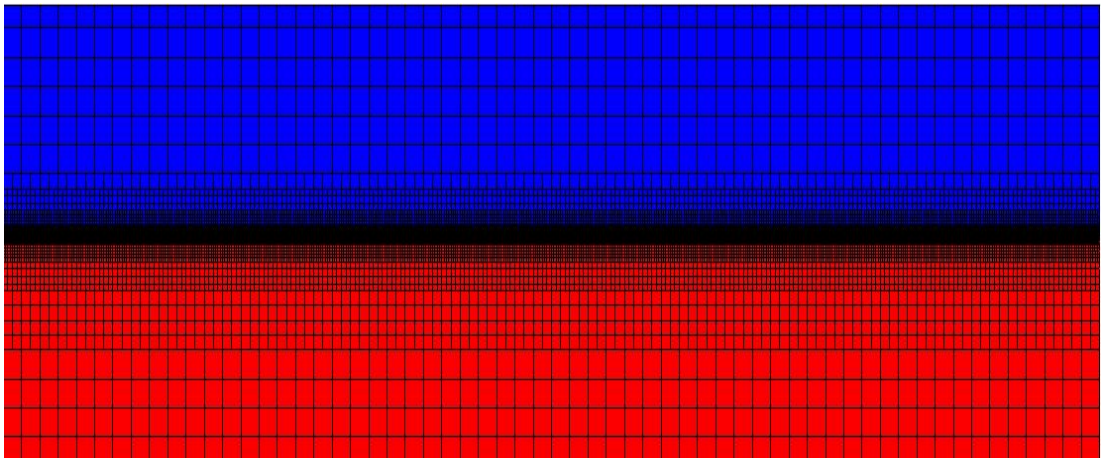

Figure 6.4: Mesh topology for the entire domain.

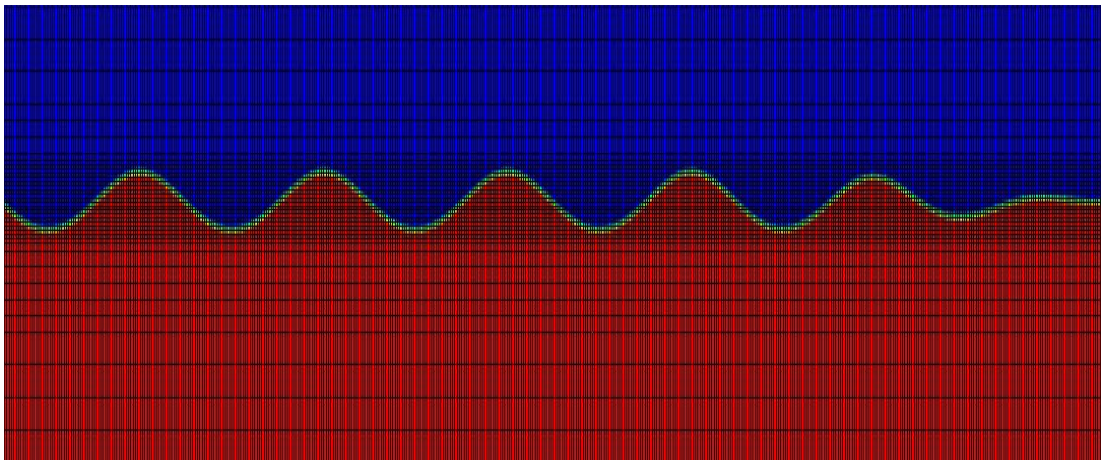

Figure 6.5: A close look at the mesh in the wave region. For visualization purpose, this figure is scaled 10 times in gravity direction and only part of the whole domain is demonstrated.

region and so forth.

Detailed mesh sensitivity study will be discussed after numerical solver.

6.3.4 Wave absorbing

Although the pressure outlet (right hand side) of the wave tank is designed to let the wave pass without reflection, wave reflection usually happens at specified boundaries (e.g. pressure outlet boundary). This is because the boundary condition (in the present study) is specified as the hydrostatic pressure of the incident wave at the location of the pressure outlet, numerical dissipation etc. lead to a slight different hydrostatic pressure of the wave when the wave arrive at the boundary and hence reflection happened.. This requires a wave absorbing technique to absorb the wave travelling from the inlet at the end of the NWT tank to avoid interaction between the FSCOWC and the reflected wave from the end of the NWT which is the pressure outlet in this case.

6.3.4.1 Wave absorbing at the end of the tank

By analogy to the wave beach used in experiment testing, a porous media-like technology is used in present study. This is accomplished by adding a momentum source into the z component of Equation 6.3 with the form of

$$S_{Mz} = \rho(f_1 + f_2|w|)\frac{e^{WT} - 1}{e - 1}w \tag{6.6}$$

Where the WT in the equation is a distance-weight damping strength function values varying from 0 to 1 represents 0% to 100% of designed damping strength:

$$WT = (\frac{x - x_{st}}{x_{ed} - x_{st}})^{nd} \tag{6.7}$$

Here x is the x axis location of a single control volume (cell) within the absorbing region, the x_{st} denotes the start point of the absorbing region while x_{ed} is the end point of the absorbing region. The f_1, f_2 and nd are damping strength control parameter and they are set to 10,10 and 2 in current study, respectively.

The distance weighted damping strength function is employed to absorb the wave smoothly since abrupt absorbing will also cause reflection. The length of the absorbing region is selected based on real tank testing experience that the

performance of the beach reached its optimum when the length of the beach is longer than 2 times of the wave length (Cruz, 2007). The distance weighted damping strength variation against tank length is illustrated in Figure 6.6.

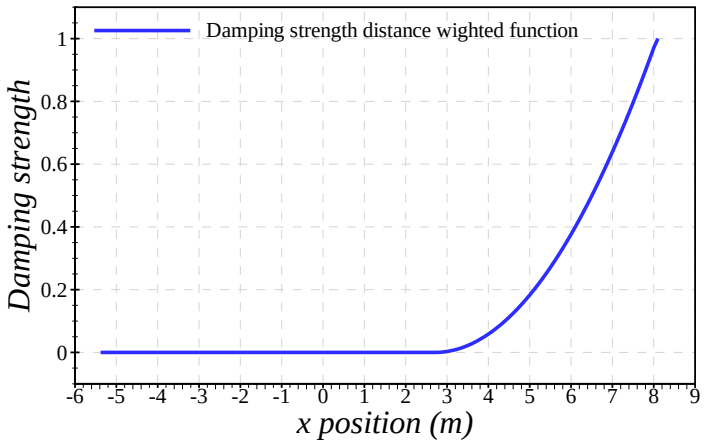

Figure 6.6: Distance weighted damping strength variation against tank length.

The effect of the wave absorbing technique is shown in Figure 6.7.

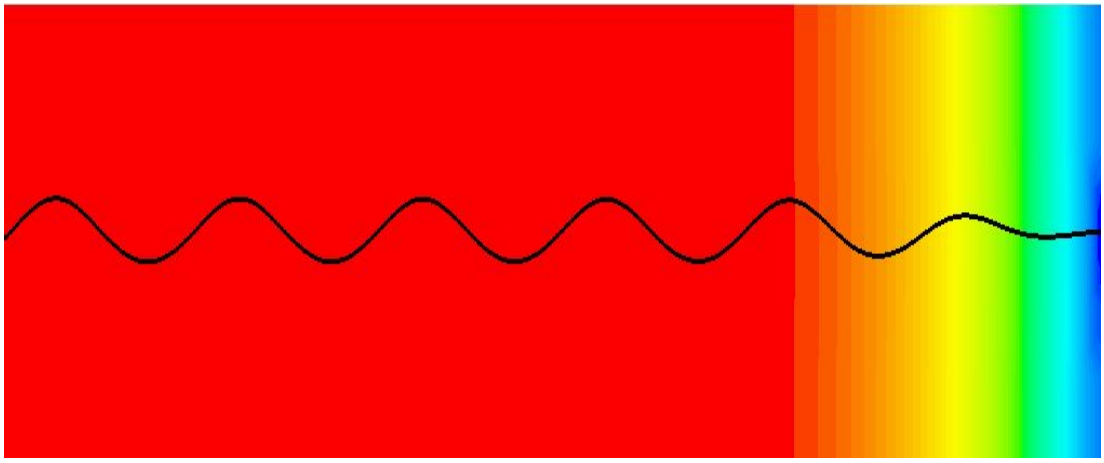

Figure 6.7: Wave elevation decay within wave absorbing region. Where the black line is the wave elevation, the red region is without wave absorbing and blue region corresponding to damping strength equals to 1.

6.3.4.2 Wave reflection absorbing at the inlet of the tank

For NWT without a structure inside the tank, wave absorbing at the end of the tank is enough to avoid reflection. However for wave-structure interaction case, due to the reflection, the diffraction and the radiation wave resulting from wave structure interaction, part of the wave will travel towards the inlet boundary

and will be reflected back into the tank from the inlet. This kind of reflection from the inlet does not affect the result extensively for sea-keeping cases since the ship usually has a faster speed than the reflected wave and hence the wave will not affect the result. On the other hand, to accurately access the performance of a WEC device, accurate determination of the incident wave energy is crucial. Conventional wave damping method can not absorb the reflected wave while at the same time allow the incident wave to pass the absorbing region.

To absorb the reflected wave from the inlet while at the same time allow the incident wave pass to the structure, the Euler Overlay Method (EOM) is employed. The EOM method is first used in Finite element method (Kim et al., 2006) and later FVM (Kim et al., 2012) to minimize the computation domain. The main theory behind the EOM is to merge the Euler equation and the N-S equation by specifying a smooth transfer function between them so that the problem can be solved by solving the Euler equation in the far field and using the N-S equation to solve the problem in the near filed as illustrated by Figure 6.8.

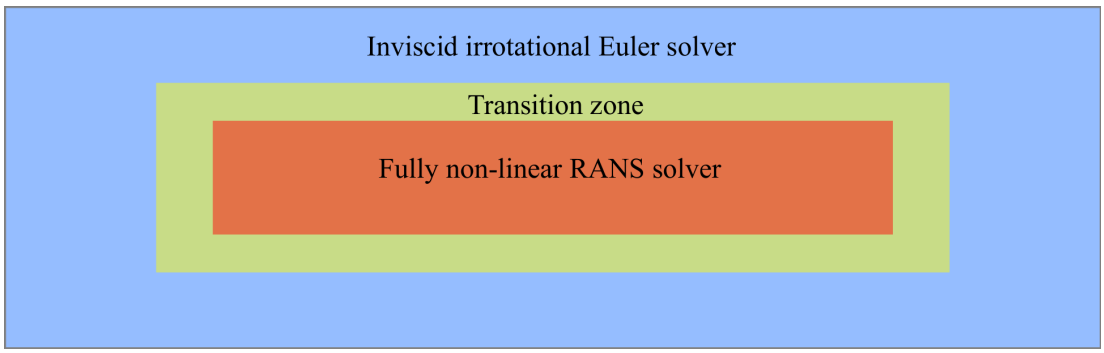

Figure 6.8: Illustration of Euler Overlay Method.

The EOM is accomplished by utilising the source term (S) in the transport equation in the present study. Assume that the discretized transport equation at a given cell takes the following form:

$$a'\phi + b' = S(\phi) \tag{6.8}$$

Assuming a' and b' are constant and ϕ is a general physical quantity we are interested in.

Let's further assume that the source term $S(\phi)$ takes the form of

$$S(\phi) = c(\phi - \phi^*) \tag{6.9}$$

Where c and ϕ^* are constant.

Then, the solution of ϕ has the form of

$$\phi = \frac{-b' - c\phi*}{a' - c} \tag{6.10}$$

Clearly, ϕ tends to ϕ^* when $|c|$ approaching infinity

$$\lim_{|c|\to\infty} \phi = \phi^* \tag{6.11}$$

Due to $dS(\phi)/d\phi = c$, positive c will make the system unstable (the system will repel any attempt to reach $\phi = \phi^*$) while a negative c makes the system stable (it will attract any attempt to reach $\phi = \phi^*$). Hence when $c \to -\infty$, $\phi = \phi^*$ and the source term (Equation|6.9) becomes

$$S(\phi) = -c(\phi - \phi^*) \tag{6.12}$$

Now if we construct the source term in such a way that ϕ stands for the numerical solution of the physical quantity and replace ϕ^* with analytical solution, we can force the numerical solution to be equal to the analytical solution. By construction and applying a phase (water) source term and a velocity source term into the continuity and momentum equations respectively, the pressure and velocity of the generated wave can be thus be forced to be equal to that of the target wave.

For the same reason as discussed for the wave absorption at the end of the tank, the absorbing of the reflection at the inlet also needs a distance weighted transfer function to avoid wave reflection cased by abrupt absorption. The following form of the forcing coefficient c was suggested by Kim et al. (2006)

$$c = c_0 cos^2(\pi x^*/2) \tag{6.13}$$

Here the c_0 is the maximum value of the forcing coefficient and the x^* is the relative coordinate within the forcing zone (zero at the beginning and 1 at the end).

The optimal value of the c (the forcing coefficient.) is problem dependent (Enger et al., 2014). 100 is found to be sufficient and efficient in present study.

Due to at present stage, there's no structure inside the NWT and hence no

reflection from the inlet, the effect of the wave absorbing from the inlet will be examined and discussed later.

6.3.5 Numerical solver and computation

In order to minimize the dissipation induced by numerical truncation error (so that wave decay along the propagation direction will be minimized), all the numerical iteration schemes were carried out in a higher order manner. That is, using a second order upwind scheme for convection fluxes, central-differencing scheme for diffusion fluxes, and quadratic backward scheme for time derivative (all being second-order approximations).

6.3.5.1 Determination of time step size

In the equation for volume fraction of water, the convection flux was discretized using a special high-resolution interface-capturing (HRIC)(Wacławczyk and Koronowicz, 2008) scheme which is designed to keep the interface sharp. The HRIC scheme can be divided into three steps. Firstly, the normalised cell face value will be estimated from a scheme that continuously connects the upwind and downwind schemes on the Normalized Variable Diagram (NVD) diagram Leonard (1991). Secondly, since the Downwind Differential scheme (DDS) can cause alignment of the interface with the mesh, another scheme is needed. To switch smoothly between the schemes, another modification based on the angle between the interface normal and the cell face normal is introduced, using introduced a control parameter named the angle factor (AF). The final modification is based on the local Courant number defined as:

$$C_u = \frac{u \cdot A_f}{V_{pc}} \delta t \tag{6.14}$$

Here u denotes the velocity perpendicular to a cell face which has an area of A_f. V_{pc} is the volume of that cell and δt is simply the time step size. Equation 6.14 states the amount of fluid convected across a cell face during a time step. When the C_u is smaller than the lower limit of the local Courant number C_{u_l} the HRIC scheme is used. For C_u larger than the upper limit of the local Courant number C_{u_u}, the upwind (UD) scheme is adopted to solve the cell face value. While $C_{ul} < C_u < C_{u_u}$, a blend of HRIC and UD is used. Obviously, a local

Courant number which is smaller than the low limit of the Courant number triers more accurate interface capturing scheme. For detailed explanation about the HRIC scheme and the AF, one can refer to Wacławczyk and Koronowicz (2008). Moreover, when second order time discretization is used for unsteady simulation, it is recommended to set the mesh size and time step size in such a way so that the local Courant number is smaller than 0.5. This is because a second order temporal scheme discretization of the unsteady term requires two previous time steps as well as the current time steps. A Courant number smaller than 0.5 essentially ensures that there are 3 time steps' information in one cell. To achieve a C_u that is smaller than 0.5, one can use the following equation can be used to design the time step size:

$$\delta t = \frac{C_u \cdot \delta x}{u} \tag{6.15}$$

Here the δx is the length of a single cell in the wave propagation direction. The value of u can be estimated as the phase velocity of the target wave defined as the wavelength divided by the period.

By setting the C_u equals to 0.5, one can get the corresponding time step size. Giving a safety factor to the C_u is always preferred. The C_u is set to 0.25 in present study.

If we examine Equation 6.15, it is obvious that use of larger cells can lead to larger times step size. To optimise the computation time and at the same time keep an acceptable level of accuracy, mesh size and time step size effect are examined. The results will be presented in next section.

6.3.5.2 Determination of number of inner iterations

The value of the normalised residuals of transport equation is the key criteria for judging whether the convergence has been achieved or not for steady state CFD simulation. However, small normalised residuals for unsteady state simulation does not essentially guarantee a converged results. Therefore, it is critical to select a proper cycles of inner iterations to ensure the solution converged in each time step and at the same time keep the computation time as short as possible.

The determination of number of inner iterations in the present study is accomplished by monitoring the variation of physical quantities against number of inner iteration. In this case, the wave elevation is monitored as shown in

Figure 6.9. Clearly, after 5 inner iteration steps, the solution tends to convergence. Hence, 5 inner iterations is selected to be the number of inner iterations.

The current number of iteration is selected based on the optimised under relaxation factor (URF). The optimisation of the URF is accomplished by the method provided by Satish et al.. The URFs are set to be 0.9, 0.5, 0.8 for velocity, pressure and volume fraction, respectively, in current study.

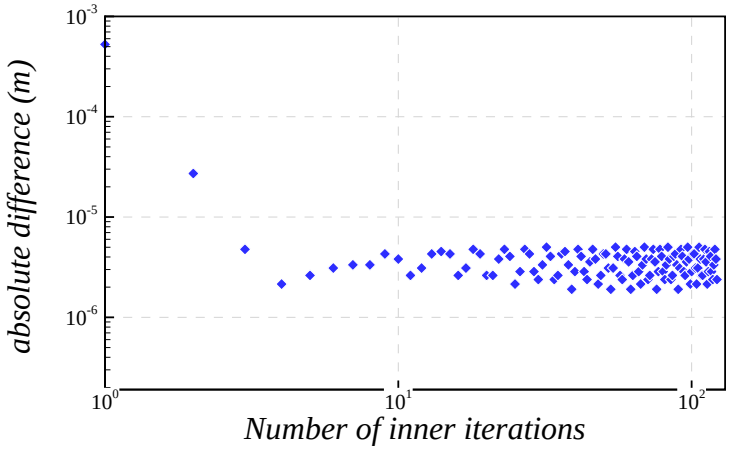

Figure 6.9: Determination of number of inner iterations. The relative difference between the iterated result and the theory is less than 0.001%.

6.4 Results presentation

Results of the NWT calculation including mesh convergence and time step size effect are presented in this section.

To find the balance between the computation resource and accuracy, a systematic mesh effect study on the result is carried out. The wave parameters for mesh effect test is listed in Table 6.1 which corresponding to the resonant case for the moderate scale model simulation. Different mesh settings are listed from Table 6.2 to 6.7. These tests are carried out to investigate the impact of mesh density and aspect ratio on the quality of the generated wave. Cases are split into 5 groups based on the number of cells in one wavelength to study the effect of mesh number in the wave propagation direction. Further three cases with different number of cells in wave height direction are tested to investigate the effect of mesh number in the wave height direction. Results are presented in follwoing sections

Table 6.1: Wave parameters for mesh testing

KH	Frequency (Hz)	Period (s)	water depth (m)	wave length (m)	wave height (m)
4.9	0.761	1.313	2.1	2.69	0.06

Table 6.2: Test matrix-Total

mesh effect	δx size	base size	base size (m)	percentage of base size	δx size(m)
Group 1	$1/60\lambda$	$1/15\lambda$	0.179	25%	0.044
Group 2	$1/80\lambda$	$1/20\lambda$	0.134	25%	0.033
Group 3	$1/100\lambda$	$1/25\lambda$	0.107	25%	0.026
Group 4	$1/120\lambda$	$1/30\lambda$	0.089	25%	0.022
Group 5	$1/140\lambda$	$1/35\lambda$	0.076	25%	0.019

Table 6.3: Test matrix-Group 1

Group 1	δ Z(m)	H/δZ	aspect ratio ($\delta z/\delta x$)	total cells
case1	0.011	5.348	1/4	9405
case2	0.006	10.69	1/8	13005
case3	0.003	21.39	1/16	18045

Table 6.4: Test matrix-Group 2

Group 2	δ Z(m)	H/δZ	aspect ratio	total cells
case4	0.0084	7.131	1/4	15840
case5	0.0042	14.262	1/8	20640
case6	0.0021	28.523	1/16	29280

Table 6.5: Test matrix-Group 3

Group 3	δZ(m)	H/δZ	aspect ratio	total cells
case7	0.0067	8.914	1/4	23775
case8	0.0034	17.827	1/8	32175
case9	0.0017	35.655	1/16	45375

Table 6.6: Test matrix-Group 4

Group 4	δZ(m)	H/δZ	aspect ratio	total cells
case10	0.0112	5.348	1/2	29790
case11	0.0056	10.696	1/4	35500
case12	0.0028	21.393	1/8	45630

Table 6.7: Test matrix-Group 5

Group 5	δZ(m)	H/δZ	aspect ratio	total cells
case13	0.0096	6.239	1/2	40320
case14	0.0048	12.479	1/4	47040
case15	0.0024	24.958	1/8	62160

6.4.1 Angle factor effect

As mentioned in Section 6.3.5.1, the AF is introduced for better interface capturing. To find the AF effect on the simulation, different simulations based on different AF are carried out. Figure 6.10 illustrated different wave elevations under different AF value in spatial domain based on case2. Clearly, the wave elevation decays faster with a larger AF value (Here, the wave elevation decay is caused mainly by numerical artificial diffusion instead of physical decay.). However, as indicated by Figure 6.11, small AF trends to wrinkle the wave profile.

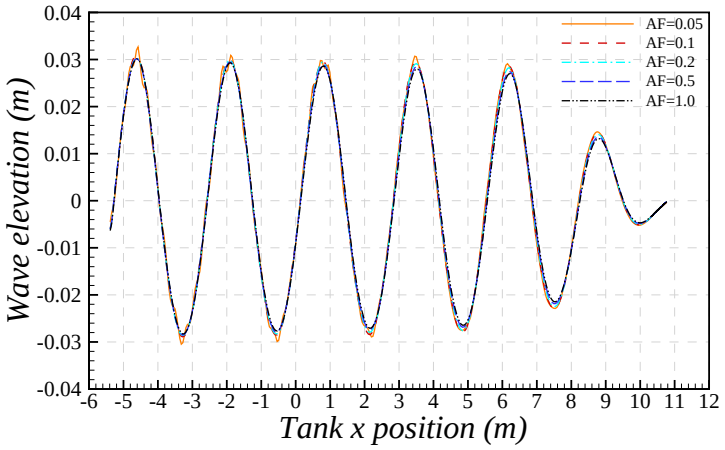

Figure 6.10: Angle factor effect on the wave profile along with the tank length direction.

Clearly, AF equals to 0.2 can provide a moderate wave decay while at the same time keep the interface sharp and smooth. Hence, all the simulation carried out later are based on AF equals to 0.2.

6.4.2 Mesh aspect ratio effect

As shown by Figure 6.12, when the mesh aspect ratio (defined as the ratio between the length of a single cell and the height of a single cell.) equals to 1/4, the wrinkling effect still exist even with the AF equals to 0.2.

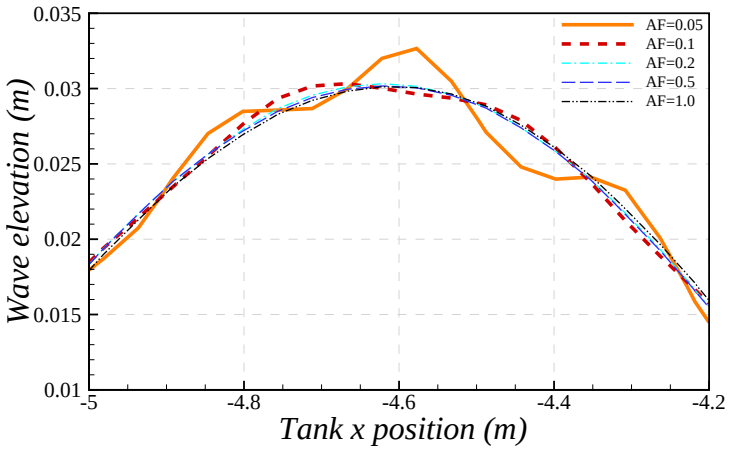

Figure 6.11: Enlarge angle factor effect on the wave profile along the tank length direction.

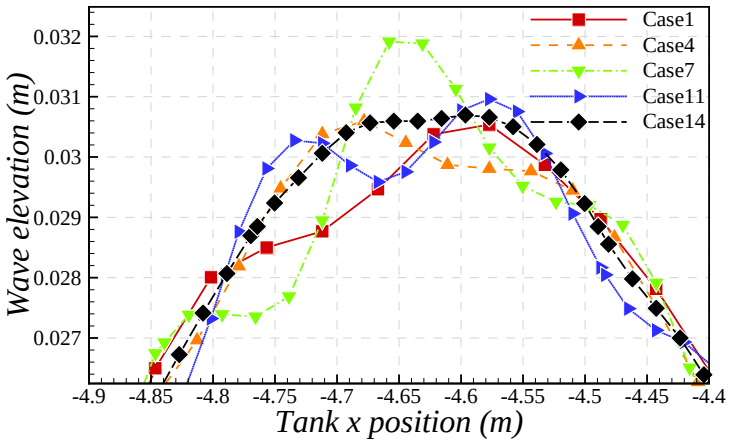

Figure 6.12: Wave profile along the tank length direction When mesh aspect ratio equals to 1/4.

All the simulations are free of the wrinkling effect when the mesh aspect ratio equals to 1/8 and 1/16 as indicated by Figure 6.13 and 6.14.

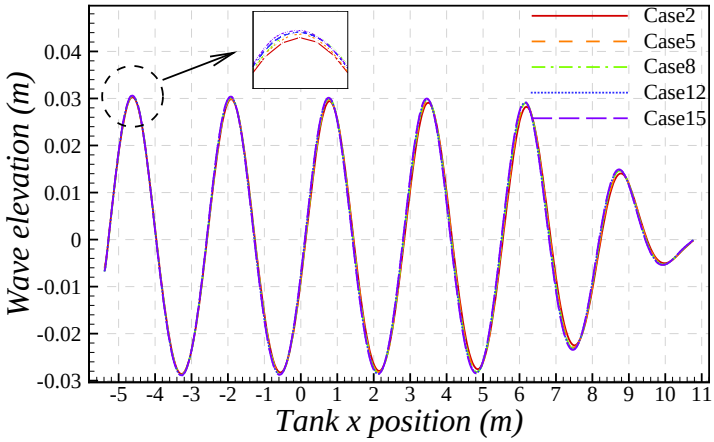

Figure 6.13: Wave profile along the tank length When mesh aspect ratio equals to 1/8.

Special cases are founded when the aspect ratio equals to 1/2 as illustrated by

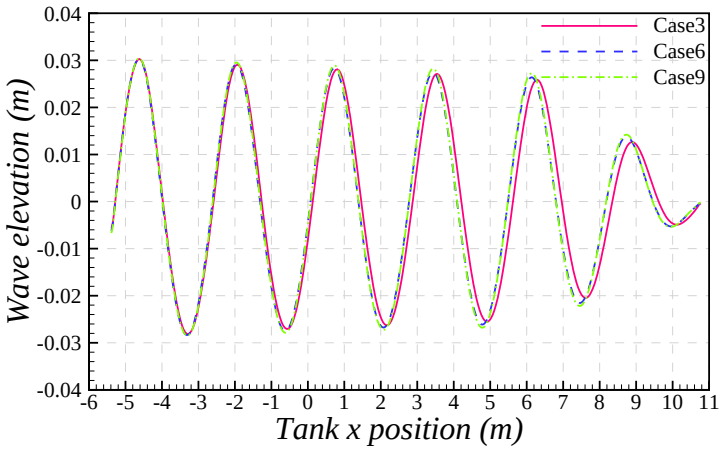

Figure 6.14: Wave profile along the tank length When mesh aspect ratio equals to 1/16.

Figure 6.15. Case 10 experienced significant wrinkling effect while case 13 provide a smoother wave profile. Compare the two cases, the only difference is the total number of cells. As indicated by Figure 6.2, when the total number of cells increased, the wrinkling effect is reduced. This suggests that dense mesh can solve this wrinkling problem. However, it is obviously not computer resource friendly, especially since to keep the time step size in a reasonable range, A denser mesh requires even smaller time step size.

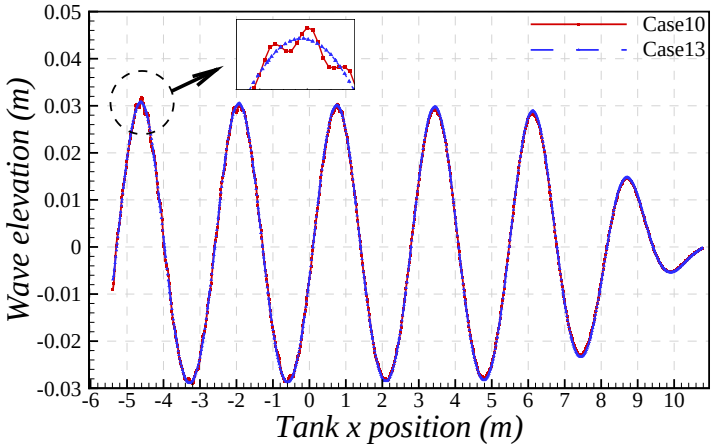

Figure 6.15: Wave profile along the tank length When mesh aspect ratio equals to 1/2.

Another solution to this wrinkling problem is to further increase the AF, however, as suggested by Figure 6.10, larger AF leads to more severe artificial wave decay along the propagating direction.

Among all the tests carried out so far, the cases with mesh aspect ratio equal to 1/8 and 1/16 cases provide the most satisfactory results. Hence, the result of mesh aspect ratio equals to 1/8 and 1/16 are compared in Figure 6.16. Note that the case 9 has almost 5 times more cells than case 2, even though Case 9 decayed

more than case 2. Therefore, it is fair to conclude that mesh aspect equals to 1/8 is the most economic mesh topology.

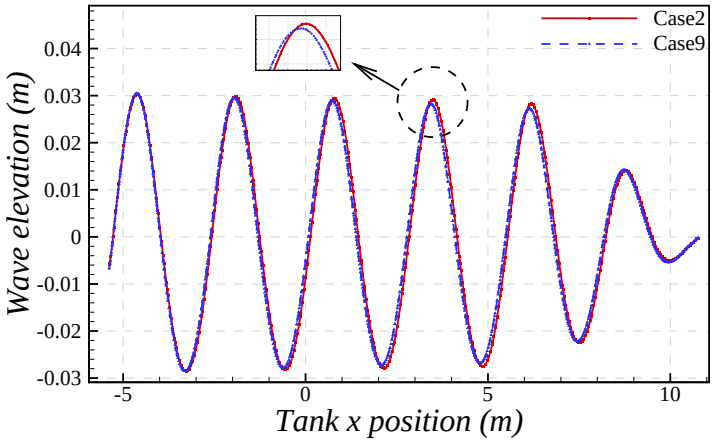

*Figure 6.16: Comparison of wave profile along the tank length between mesh aspect ratio=*1/8 *and* 1/16.

Table 6.8 tabulates the wave heights obtained at 2 wavelength away from the inlet after 40 seconds physical simulation (more than 20 wave periods.) for mesh aspect ratio equal to 1/8. Clearly, the wave height difference between the numerical result and the fifth order stokes wave theory decrease with the increment of total cell numbers. It should be noted that potential theory does not involve any viscosity and turbulent effect. Hence, as well as numerical difference, the results presented here also include the difference introduced by physical decay. Considering this, 3% difference in the wave height at 2 wavelength away from the inlet boundary would be a satisfied result. The computation time of the case 15 which provide the best result is about 5 times more than that of the case 5 while the result only improved about 1.3%. Case 12 and case 8 take about 2 and 3 times more computation time while the result only improved about 0.7%. Considering all the above, the mesh topology of the case 5 is selected to be the most appropriate mesh setting for further study.

Table 6.8: Wave height obtained at 2 wavelength away from the inlet after 40 seconds physical simulation for mesh aspect ratio equals to 1/8*. The simulation is carried out by using a PC with 32G RAM and 4 core Intel i7-2600 processor. Simulation is done by Star-CCM+ version 9.02.005.*

Case ID	Through (m)	Crest (m)	Wave height difference between wave theory (%)	Computation time (hours)
case2	0.02960	0.02816	-3.727%	2h12m
case5	0.02983	0.02838	-2.975%	3h08m
case8	0.03012	0.02838	-2.225%	5h53m
case12	0.03012	0.02854	-2.217%	9h46m
case15	0.03024	0.02872	-1.733%	16h50m

6.4.3 Time step size effect

The effect of time step size on the generated wave is investigated and results are illustrated by Figure 6.17. As indicated when time step size is smaller than 0.005 seconds, almost no difference is observed. When time step size is larger than 0.005, obvious numerical wave decay happened and the wavelength is slightly different.

Time step size calculated by Equation 6.15 yields to a time step size equals to 0.004 suggesting the validity of the proposed time step size calculation.

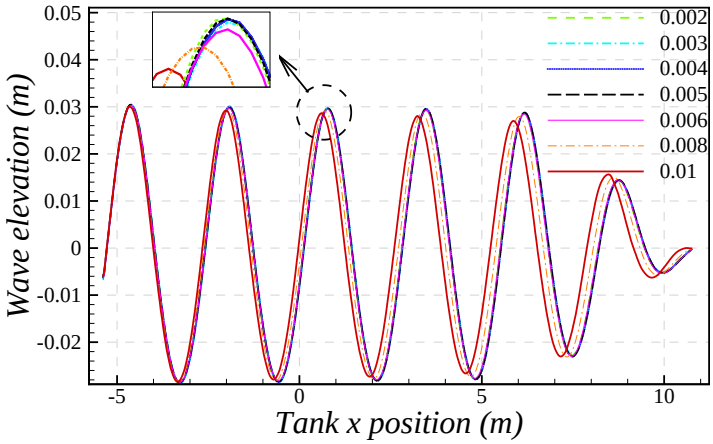

Figure 6.17: Wave profile along the tank length for case 5 at different time step size.

6.5 Chapter summary

A reflection free NWT is developed in this chapter. Different aspects that will affect the result have been examined. Results indicate that angle factor, mesh aspect ratio and time step size will affect the generated wave. Hence, it is recommended to examine the NWT before simulating the device.

Although fifth order stokes wave theory is adopted in current simulation, the available wave energy in the wave is simply estimated by using linear wave theory (Equation 3.23) which is not a decent way to calculate the available energy accurately since that does not account for any non-linearity of the wave. A better way to estimate the available energy in the wave is monitor the energy flux at where the device will be located (Luo et al., 2014) in the absence of the device. This requires additional simulation for each wave frequency that is going to be tested. For 3D cases, it is not economic. Therefore, linear wave theory is adopted to estimate the available wave energy.

Chapter 7

RANS simulation of the moderate scale FSCOWC

7.1 Chapter overview

Base on the NWT study in previous chapter, the moderate scale FSCOWC device is simulated in this chapter and results are compared with experiment.

7.2 Geometry of the FSCOWC device

Geometry details used in the CFD simulation are listed in Table 7.1. Comparison between the physical model and the CFD model is illustrated in Figure 7.1.

Clearly, the dimensions specified in the CFD simulation involve less measurement uncertainty (the uncertainty in the geometry modelling due to mesh size can not be assessed, however, dense mesh is used in the present simulation to minimize this effect). This indicated the possibility of geometry modelling difference between the physical modelling and the CFD modelling.

Because of the symmetry of the FSCOWC device and the symmetry of the wave structure interaction problem (radiation and diffraction), it is reasonable to assume that the problem can be simulated by using symmetry condition. That is the simulation can be performed in a symmetric manner so that only half of the domain need to be simulated by utilising the symmetry boundary condition.

Table 7.1: OWC geometry details where PCD is pitch circle diameter. The relative large uncertainty in the geometry is due to the uncertainty in the measurement instead of the uncertainty in the manufacturing.

Component	Parameters (mm)	EFD	CFD
OWC model	total length	1045.0 ± 0.5	1045.0
	draft	350.0 ± 10.0	350.0
Orifice plate	Plate Diameter	299.0 ± 0.5	299.0
	Thickness	12.5 ± 0.2	12.5
	Orifices Diameter	35.0 ± 0.2	35.0
	Orifices position (PCD)	170 ± 0.2	170.0
Tube	Outer Diameter	299.0 ± 0.5	299.0
	Inner Diameter	287.0 ± 0.5	287.0
Ring	Inner Diameter	299.3 ± 0.5	299.0
	Outer Diameter	390.0 ± 0.5	399.0
	Thickness	45.3 ± 0.2	45.3
	Fillet radius	22.0 ± 0.2	22.0

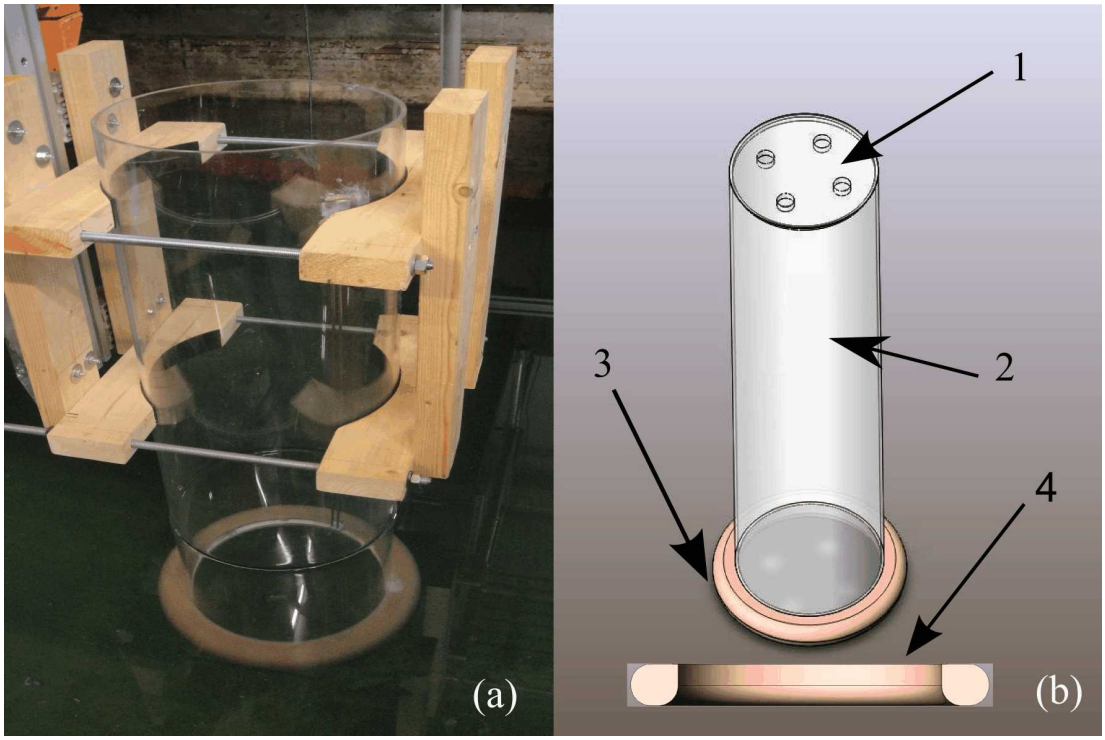

Figure 7.1: Comparison between the physical model and the CFD model. Where 1 is the orifice rig, 2 is the tube, 3 is the ring and 4 is the sectional view of the ring.

7.3 Domain and boundary conditions

The details of the CFD domain, coordinate system and boundary conditions are illustrated in Figure 7.2. Where the water depth is set to be $2.1m$, the width of the tank is set to be half of the Kelvin tank ($2.3m$ due to symmetry condition).

The transparent face is set to be symmetry boundary. The gray face is set to be a smooth wall to simulate the tank wall. The origin of the coordinate system located at the center of the FSCOWC 2.5λ away from the velocity inlet and 3.5λ away from the pressure outlet.

The EOM region is set to be one wavelength from the velocity inlet and the damping region is set to be twice the length of the wavelength from the pressure oulet.

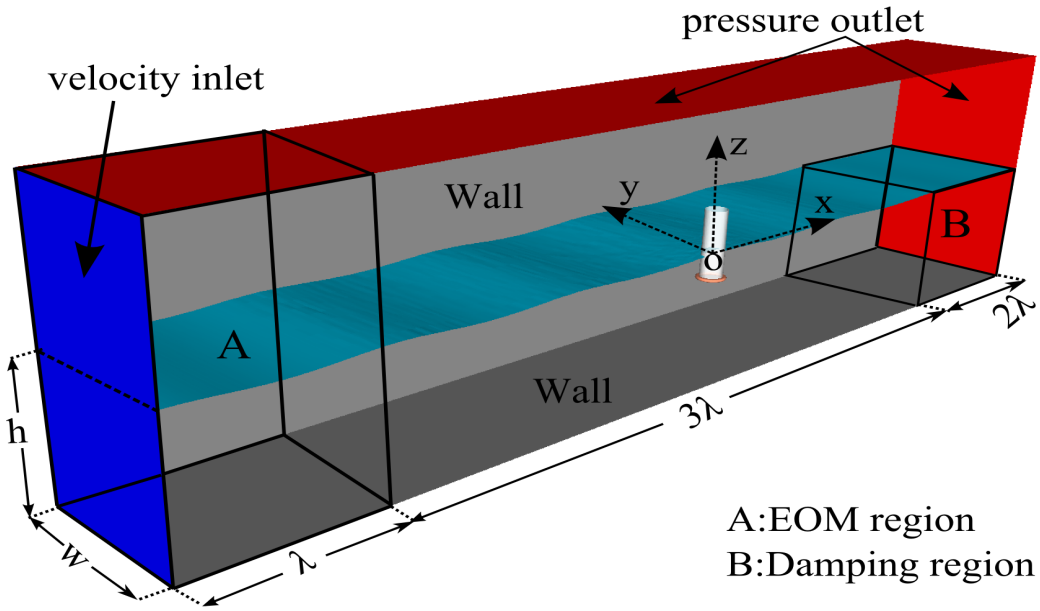

Figure 7.2: CFD domain and boundary conditions. Here, the OWC device located 2.5λ away from the inlet.

7.4 Mesh distribution

The overall mesh distribution is illustrated in Figure 7.3 (a). The mesh around the FSCOWC is refined to capture the wave structure interaction as shown in Figure 7.3 (b) (The mesh showing here is mirrored for visualization purpose, only half of the mesh is created in simulation.). In order to capture the shear force within the boundary layers around the structure, boundary layers are generated in such a way so that the $Y+$ value is smaller than 1 for the maximum response case and use the same boundary layer parameters for other cases. Figure 7.4 illustrated the Y+ value for the four orifice simulation when the flow inside the device reached its maxima at Kh=4.8. The Kh=4.8 is the peak response for four orifice case and hence Y+ value for the other frequencies will be smaller then current Y+. The

boundary layer around the ring and the orifice are shown in Figure 7.3 (d) and (c). As indicated by Figure 7.3 (e), the mesh inside the FSCOWC is much denser for the purpose of accurately capturing the spatial variation of the OWC surface. Meshing of the wave tank is based on the optimized mesh setting determined in the previous chapter (Figure 7.3 (f)).

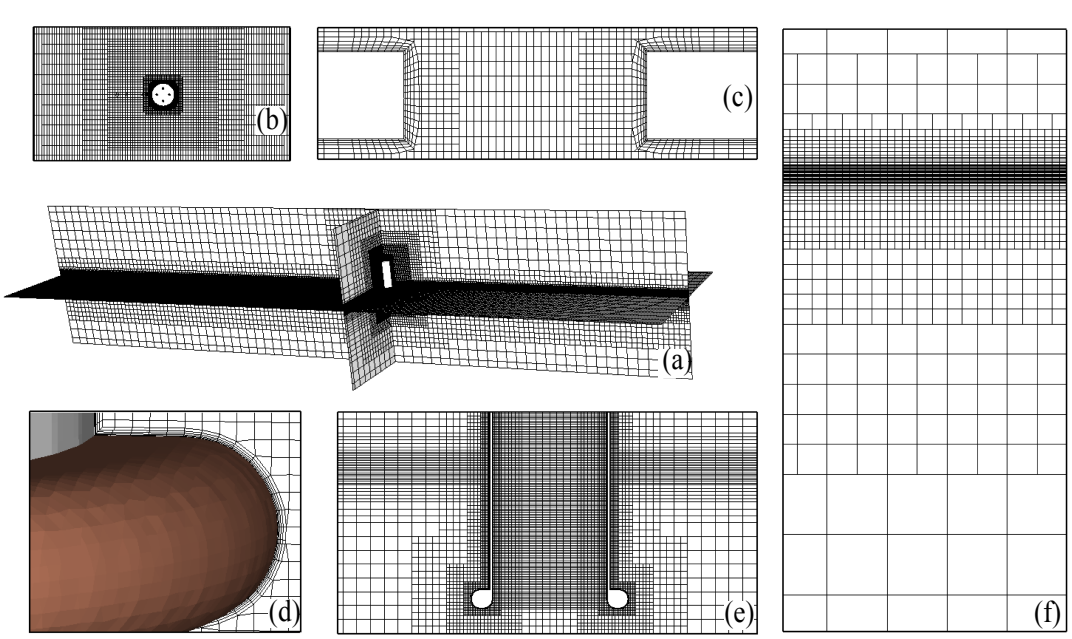

Figure 7.3: Mesh distribution. a) Overall view. b)Mesh refinement around the device. c) Mesh around orifice. d)Mesh around the ring. e) Mesh around inside the tube. f) Mesh around free surface.

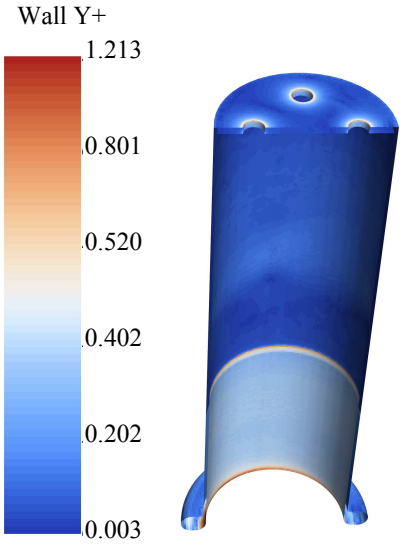

Figure 7.4: Wall Y+ plot for the four orifice case when the volume flow rate reached its maxima at Kh=4.8.

7.5 Results presentation

Results including the spatial variation effect of the OWC inside the device and inlet reflection effect (EOM effect) will be presented and discussed in this section. Results are compared with EFD.

7.5.1 Mesh dependence tests

As well as experiment, RANS simulation has uncertainties introduced by numerical modelling which can be classified mainly as below:

- Physical modelling: Turbulence, geometry, etc.
- Discretization and solution errors: mesh, time step size etc.
- Computer round-off error.
- Programming errors.

Among those uncertainties listed above, the most significant source would be that induced by the mesh size. Therefore, mesh dependency test were carried out to make sure the uncertainty introduced by the mesh size is acceptable. This is done by calculating the same case with three different mesh density level. The mesh was refined based on the cell volume with a factor of $2^{\frac{3}{2}}$. Ideally, the mesh dependency tests should be carried out for each test simulated, however, since it requires three different simulations which is obviously not economic, the mesh dependency test was only carried out for the four orifice case at the resonance frequency $Kh = 4.8$ and assuming that the uncertainty at other frequency will be comparable. Results are listed in Table 7.2. The OWC response was monitored at the center of the OWC in order to be consistent with the tank testing.

Table 7.2: Mesh dependency test

Mesh density level	cell number	owc elevation (mm)	pressure (pa)	power (watts)
Fine	1410298	89.71	62.12	0.87
Medium	660683	89.37	60.12	0.81
Coarse	329271	88.61	59.81	0.79

As can be seen, all the results are very close to each other. Based on the results obtained from the mesh dependency test, the grid convergence index (GCI) was calculated for the power capture to represent the uncertainty in the power at the fine mesh. All the simulations were then carried out at fine mesh level. The GCI

at the fine level indicated an uncertainty about 4.1% in the power captured, 0.73% in the pressure amplitude and 2.4% in the OWC elevation. It is important that each grid level yield solutions that are in the asymptotic range of convergence for the computed solution. This can be checked observing two GCI value calculated for the fine and coarse grid using $GCI_{32}/(r^{P_a}GCI_{21})$, here GCI_{32} is the GCI in the coarse grid, r is the grid refine ratio and the P_a is the apparent order of the solution. In this study, the GCI_{32} equals 8.6%, giving a value of 1.035 by using the above equation. The value is close to 1 indicating the solution is in the asymptotic range of convergence and the refinement is acceptable. For details information on how to calculate the GCI, see Appendix D and John W (2008).

7.5.2 EOM effect

As stated previously, the reflection from the inlet will have an effect on the final result and it is not clear when running NWT since there's almost no reflection happened at the inlet. Therefore, the effect of reflection from the inlet is first examined based on the Open tube case at an incident wave frequency equal to $Kh = 5.0$. As can be seen from Figure 7.5, when the response of the OWC is developing ,there is almost no difference between the case with and without EOM. However, after the OWC response is developed, it is clearly that the reflection from the inlet has an effect on the OWC repose. In this case, the reflection from the inlet introduced a minor phase shift and increased the response slightly.

It should be noted that although in this case, the reflection from the inlet is notvery significant due to the nature of 3D radiation (radiation due to the motion of the OWC.) and reflection (from the front wall of the device.). On the other hand, the reflection may be considerable when simulating a 2D case. Hence, absorbing the reflection from the inlet is necessary when simulating a 2D case, which is often neglected by researchers.

7.5.3 Open tube

The open tube RAO of the OWC is plotted in Figure 7.6 along with the result from moderate scale experiment. The incident wave amplitude is calculated based on the mesh dependency and time step size effect tests, i.e. the device is located at 1.5 wavelength away from the EOM region and hence the wave will have decayed 2.23% of the desired incident wave amplitude. A typical 80 seconds physical

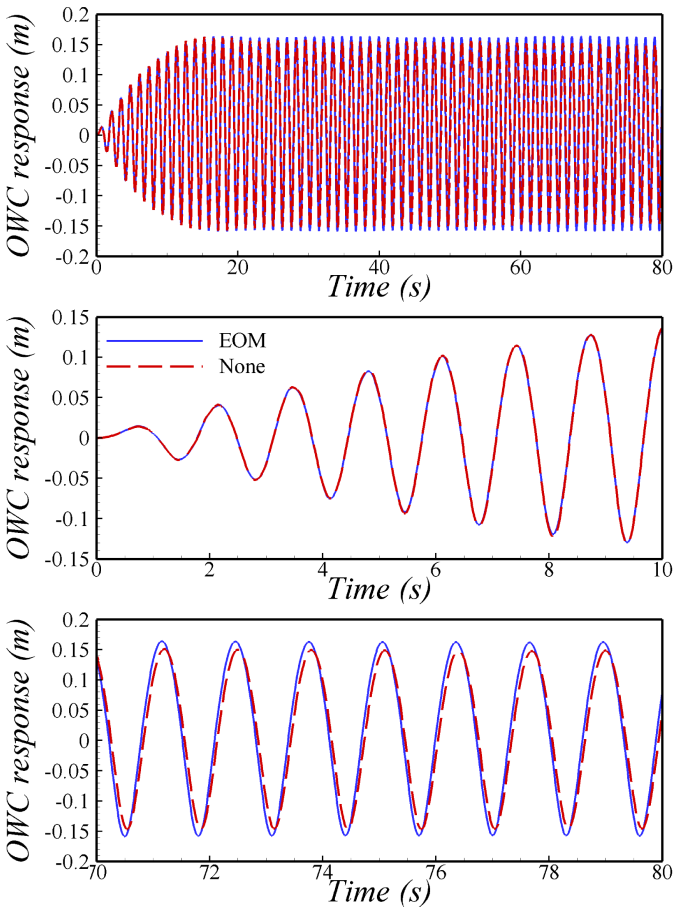

Figure 7.5: EOM effec, with and without velocity inlet reflection absorbing.

time simulation takes 7 days on a 72 cores High Performance Computer (HPC with Dual Intel Xenon X5650 2.66Ghz CPUs (6cores each) and 48GB RAM)). As indicated, the resonance frequency is slightly lower than $Kh = 5$ while the resonance in the experiment is about $Kh = 5$. Although this can be explained by the uncertainty lies in the measurement of the testing, there's another possibility that will lead to a minor difference in the resonance frequency. As discussed in the NWT construction part, the mesh has a dissipation effect on the incident wave. This effect will also apply to the radiated wave from the device. Hence, it will affect the hydrodynamics resulting a different added mass coefficient.

Except for the slightly shift in the resonance frequency, it is noticed that the RAO of CFD at the resonance frequency is slightly higher than that of the experiment. This may be caused by the reasons that the turbulence and viscosity is not modelled accurately enough. In addition, due to the wave decay along the wave propagation direction, the incident wave amplitude arriving at the device is smaller than that of the experiment. This leads to a slightly smaller response of the OWC inside and thus smaller damping resulting a larger RAO.

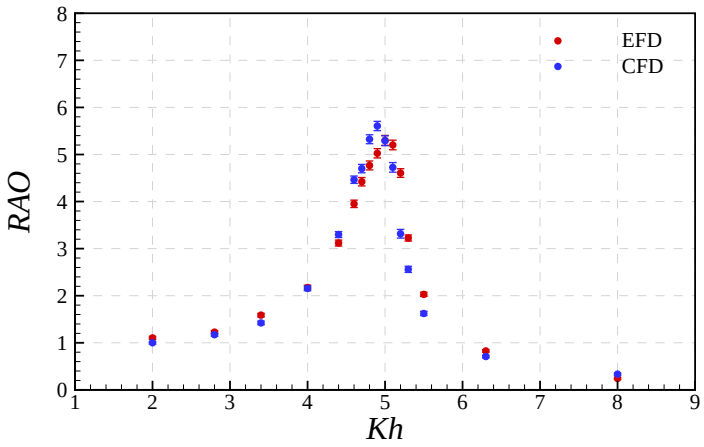

Figure 7.6: CFD RAO of the moderate scale FSCOWC for open tube.

Based on the DMF method, the equivalent frequency independent hydrodynamic coefficients are listed in Table 7.3. As can be seen, the added mass coefficient of the CFD tube is larger than that of the experiment while the damping coefficient is smaller than that of the experiment.

It should be noted here that when using the DMF method to fit the added mass coefficient for tank testing results, the fitted added mass coefficient is an equivalent added mas coefficient that will provide a similar response by a solid cylindrical tube with a draft equals to $0.35m$ (because the draft is set to be $0.35m$ in the DMF fit method), therefore, if the draft of the experiment is less than $0.35m$ (while the draft is set to be 0.35), the added mass coefficient of the experiment will be smaller than it should be so that the total mass is correct. Thus, the difference in the added mass coefficient between the CFD and EFD results is actually a sum of the difference in the mass and difference of added mass. For detailed hydrodynamic determination result, see Appendix B.

Table 7.3: Comparison between the equivalent frequency independent hydrodynamic coefficients for CFD and EFD.

Added mass	Open tube	Four orifices	one orifice
EFD	0.205	0.224	0.251
CFD	0.227	0.242	0.260
Damping			
EFD	0.062	0.097	0.344
CFD	0.057	0.102	0.376

Overall the simulation result matches the experiment well indicating the success in modelling the wave structure interaction problem. Although there is a small difference in the resonance frequency, the difference is less than $0.1s$ in period

when extrapolated into full scale period ($1:50^{th}$).

7.5.4 OWC with PTO

The RAO, pressure, mean power, capture width and capture factor are illustrated from Figure 7.7 to 7.14. (Note here that the power calculation is based on the surface integral method instead of calculate based on the OWC elevation. The surface integral method will be discussed in next section.)

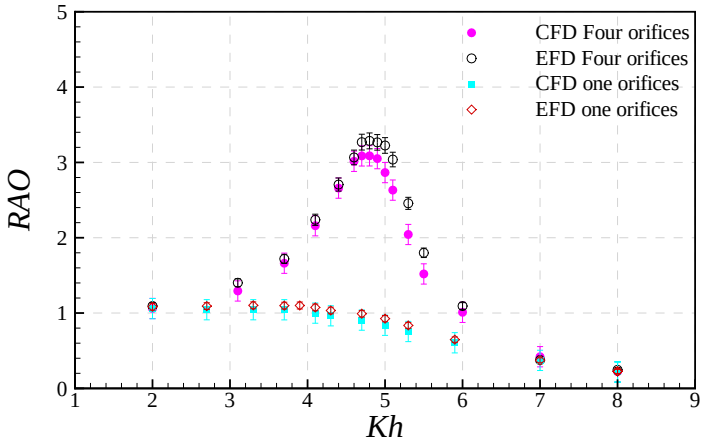

Figure 7.7: CFD RAO of the moderate scale FSCOWC for four and one orifices case.

As can be seen from the RAO comparison between the RANS simulation and experiment results, the RANS simulation results are smaller than that of the experiment while the RANS simulation open tube RAO is slightly larger than that of the experiment. One possible reason is that the damping effect introduced by the PTO may not be simulated accurately due to the uncertainty in the measurement of the orifice size. The damping coefficients in the simulation are larger than that of the experiment (see Table 7.3), this explains why the OWC response of the CFD simulation is smaller than that of the EFD.

The pressure amplitude obtained from CFD simulation is smaller than that of the experiment as suggested by Figure 7.9. This is expected because of the actual wave arrived at the device is smaller than that of the experiment.

The capture factor of the RANS simulation shows a good agreement with the experiment in the overall trend. However, generally speaking, the RANS simulation shows a smaller capture factor magnitude. This is mainly caused by the PTO character was not simulated accurately. Except for the size of the orifice which contributes to failure of simulating the PTO character accurately, there are several

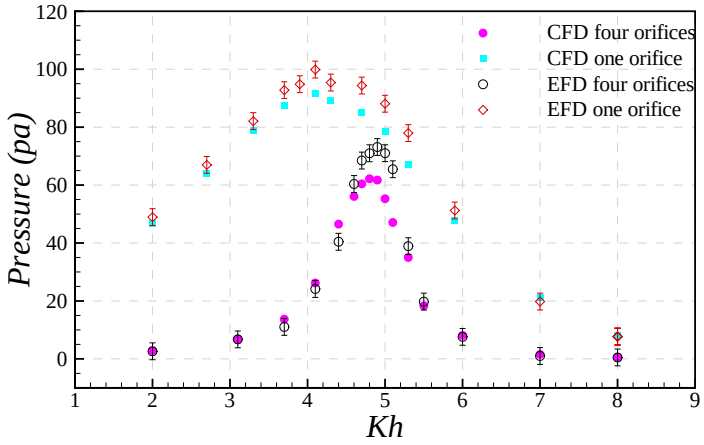

Figure 7.8: CFD pressure of the moderate scale FSCOWC for four and one orifices case.

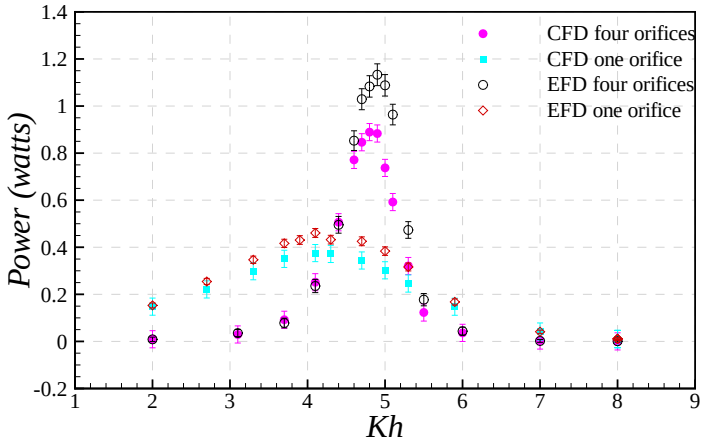

Figure 7.9: CFD mean power of the moderate scale FSCOWC for four and one orifices case.

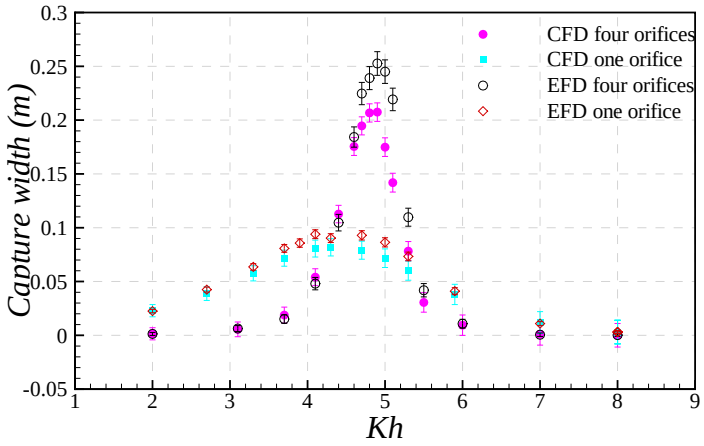

Figure 7.10: CFD capture width of the moderate scale FSCOWC for four and one orifices case.

other aspect that will affect the PTO character. For instance, the roughness of the orifice material which was not modelled in the CFD.

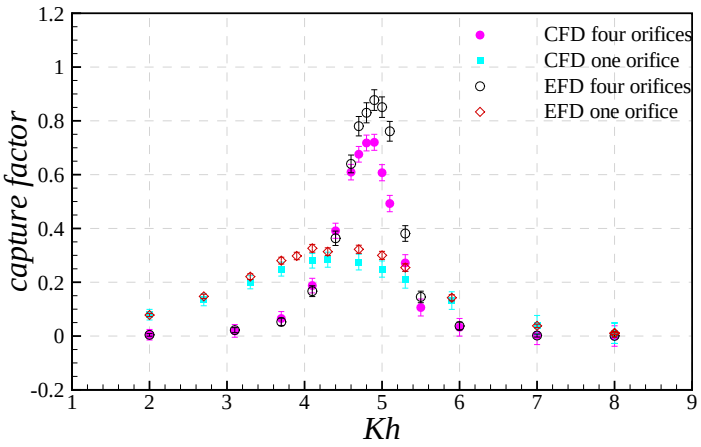

Figure 7.11: CFD capture factor of the moderate scale FSCOWC for four and one orifices case.

Spatial variation of the OWC

One of the assumption made in the experiment is that the OWC inside the device is assumed to be flat and level even when it is oscillating, and hence we can derive the volume flow rate simply by calculating the time derivative of the OWC response. However, the surface of the OWC is not flat and level in real case as shown in Figure 7.12.

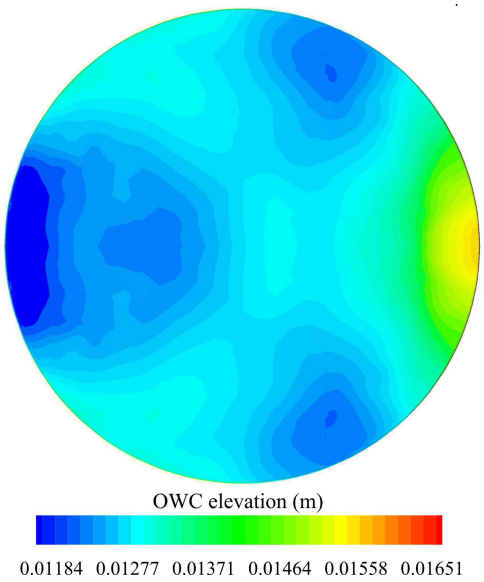

Figure 7.12: OWC surface position in gravity direction when encountered with wave in CFD simulation when Kh=5 for open tube case. Here, the contour is mirrored for visualization purpose.

It is not easy to investigate this spatial variation effect on the captured power by experimental method due to the difficulty in measuring the air flow rate driven by the OWC directly. On the other hand, this can be achieved by numerical methods.

Therefore, the power calculated by using the elevation of the OWC is compared with the power calculated directly from the air is compared to check the spatial variation effect. Three different plan sections are created to compute the power directly from the air flow at 0.4, 0.5 and 0.6m away from the initial free surface as shown in Figure 7.13. The power is computed by the follow equation:

$$Power = \int_{\delta A_s}^{A_s} w \cdot p \; dA_s \tag{7.1}$$

where the A_s is the area of the plane section.

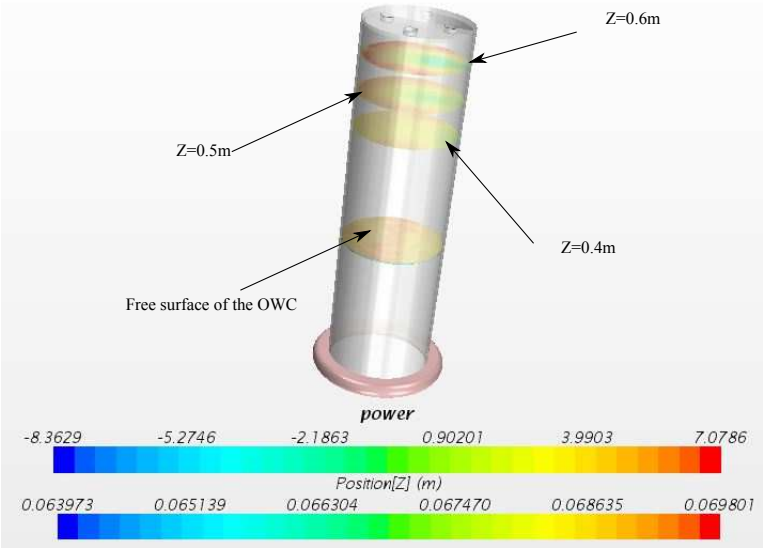

Figure 7.13: Illustration of calculating the power directly from the air flow.

The mean power obtained by different monitoring and calculation method is presented in Figure 7.14 for both four and one orifice cases. Generally speaking, different methods yields very similar power output.

A close inspection indicated there do exist discrepancy between different methods and different height of monitoring the power. For the four orifices case, the power measured at $0.4m$ and 0.5 are almost identical to each other while the power measured at $6m$ showed a discrepancy against the other two. This is because that $0.6m$ is too close to the orifice and much affected by the flow. As indicated by Figure 7.15, the flow in the chamber around the orifice is much affected by vorticity and therefore energy dissipated more around the orifice. When talking about the power calculated by the OWC elevation, the discrepancy is simply caused by sampling since the OWC surface is not flat. The relative difference between the power calculated by the OWC elevation and the power measured at

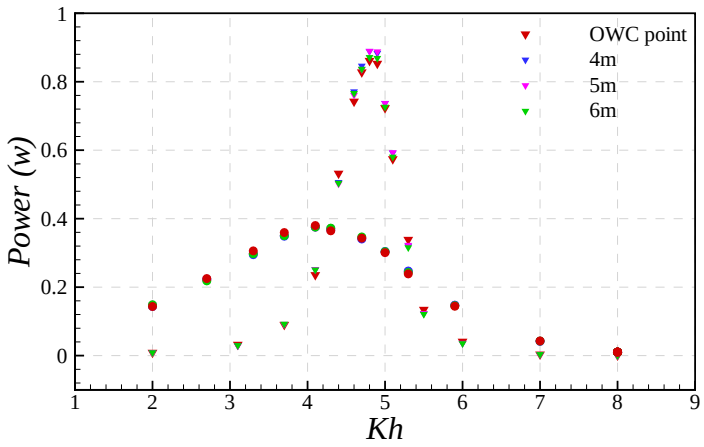

Figure 7.14: Comparison of the mean power captured monitored at different height in the chamber for four and one orifice case.

$0.4m$ at $Kh = 4.8$ is about 3.1%. The results for the one orifice case are almost identical to each other. This is because of that the strong damping introduced by the one orifice lead to a smaller and relatively flat OWC motion. In fact, for the four orifices case, those power captured by different methods are almost identical to each other when the RAO is less than about 2.

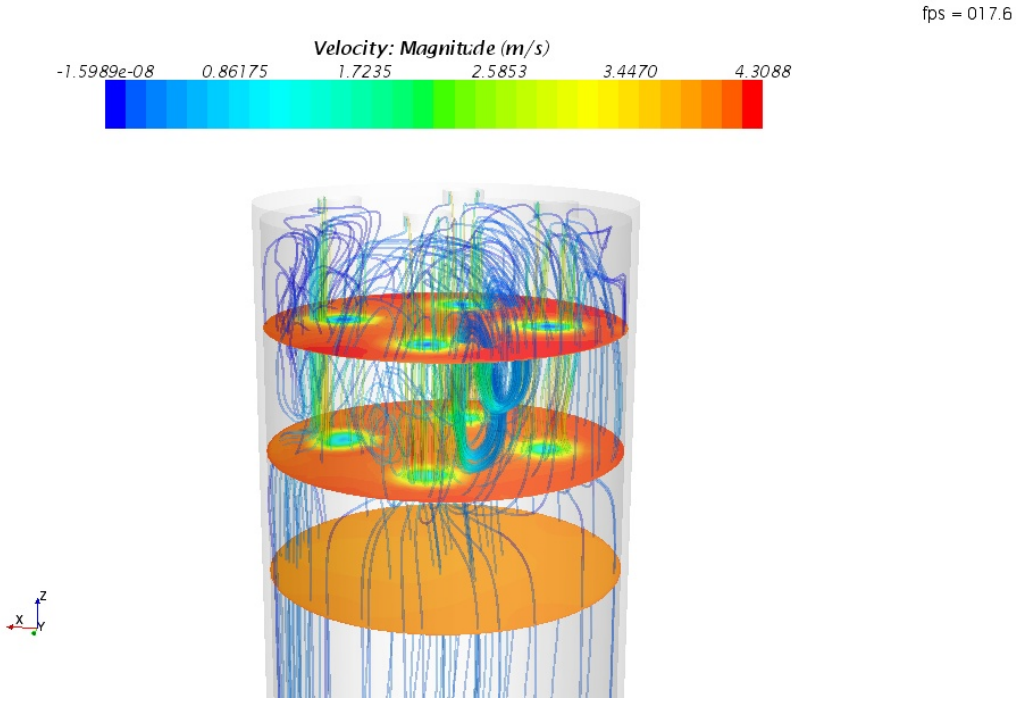

Figure 7.15: Stream line through the orifice for the four orifices case at $Kh = 4.8$.

7.6 Chapter summary

The moderate scale FSCOWC is simulated by using the reflection free NWT constructed in previous chapter, uncertainty induced by mesh was investigated. Results were compared with the experiment results.

The effect of reflection from the velocity inlet boundary was checked based on results from the NWT with and without EOM wave absorbing technique. Results indicate that the reflection from the velocity inlet boundary do influence the predicted performance of the device. Therefore, to accurately simulate the device, reflection absorbing at the inlet boundary is essential.

The influence of the spatial variation of the OWC on the power calculation was investigated and results suggested that the spatial variation of the OWC does affect the assessment of the power captured by the device for the large OWC motion case. The spatial variation effect trends to be negligible when the OWC elevation is small.

Comparison between the CFD and EFD results suggested the draft of the FSCOWC might not be modelled accurately due to the uncertainty in the measurement of the experiment. The resonance peak of the open tube happened at a lower frequency compared with the experiment. Indicating that the draft of the experiment may be smaller than the target draft. Except for the discrepancy in the resonance frequency, the open tube results from CFD simulation gave a slightly larger response while the cases with PTO exhibit smaller response. This suggests that the PTO character may not be simulated accurately due to uncertainty in the measurement. This may also be caused by the draft of the experiment is smaller than that of the CFD since the response is very sensitive around resonance frequency.

Overall, the results of the CFD and EFD agreed with each other well.

Chapter 8

RANS simulation of the small scale FSCOWC

8.1 Chapter overview

Based on the same methodology used in the moderate scale simulation, the small scale FSCOWC is simulated by RANS method in this chapter. The tank width effect is also investigated.

8.2 Scaling of the small scale simulation

As mentioned earlier in the experiment part, to scale the air stiffness correctly, the length of the chamber is kept the same as the moderate scale one. The details of the small scale FSCOWC device used in the simulation can be found in Table 8.1. Figure 8.1 compares the two different scale devices. Except for the geometry of the device, all the other relevant parameters are scaled according to Froude scaling law. For example, the water depth and incident wave frequency et.al.

Except for those physical parameters, most of the numerical simulation related parameters are treated in a way designed to minize the difference (between the moderate scale and small scale simulation) introduced by numerical simulation. For example, the mesh is scaled based on the wavelength so that the number of cells in pre wavelength is kept the same as the moderate scale simulation. The total physical simulation time and time step size are scaled according to Froude

Table 8.1: OWC geometry details of the small scale FSCOWC where PCD is pitch circle diameter

Component	Parameters (mm)	EFD	CFD
OWC model	total length	706.7±0.5	706.7
	draft	11.7±3.0	11.7
Orifice plate	Plate Diameter	100.0±0.5	100.0
	Thickness	4.0±0.2	4.0
	Orifices Diameter	11.6±0.2	11.6
	Orifices position (PCD)	56.6±0.2	56.6
Tube	Outer Diameter	100.0±0.5	100.0
	Inner Diameter	96.0±0.5	96.0
Ring	Inner Diameter	96.3±0.5	96.3
	Outer Diameter	130±0.5	130.0
	Thickness	15.1±0.2	15.1
	Fillet radius	11.0±0.2	11.0

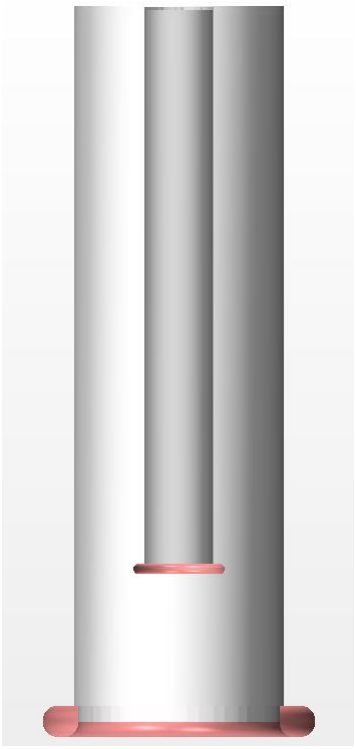

Figure 8.1: Comparison of the moderate scale and small scale FSCOWC geometry.

scaling law. Total number of inner iterations and under-relaxation factors are kept the same as the moderate scale simulation.

8.3 Results presentation

8.3.1 Open tube

The open tube RAO against different tank width for small scale simulation is plotted in Figure8.2. Clearly, the response for half tank and quarter tank is slightly larger than that of the full tank. Besides, it is obvious that the resonance of the quarter tank RAO shifted slightly to higher frequency compared with full tank and quarter tank. The resonance of the half tank has the trend of shifting to a higher frequency although it is not clearly due to resolution. This phenomenon agrees with the result obtained from the small scale experiment.

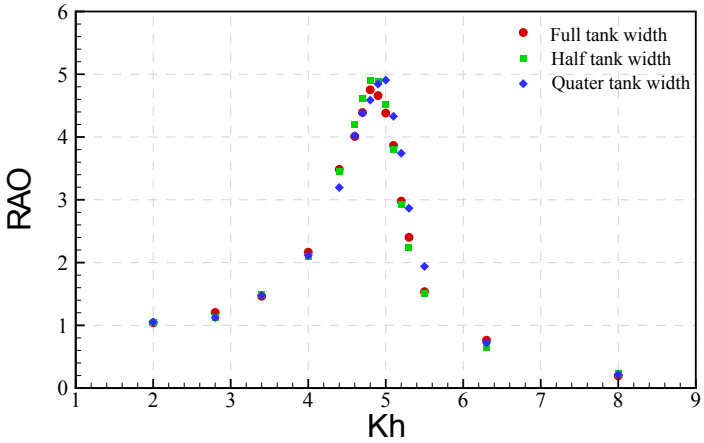

Figure 8.2: Open tube RAO for different tank width.

Compared with moderate scale RANS simulation (Figure 8.3), the response at the resonance is smaller than that of the moderate scale. This is caused by failure of scaling the fluid properties as explained in the experiment part. As mentioned in previously, the resonance of the small scale experiment shifted to a lower frequency compared with the moderate scale experiment. That finding was not ascertain due to the uncertainty in the measurement (especially the draft and diameter which will affect the resonance significantly.). However, by carefully scaling the model and mesh as discussed in above section, this issue is resolved by using RANS simulation. As indicated, the resonance peak shifted to a lower frequency due to larger damping introduced by the viscosity.

On the other hand, the CFD RAO of the open tube case matches that of the EFD well if uncertainty is considered as shown in Figure 8.4. However, similar as the moderate scale problem, a small discrepancy is observed in the resonance

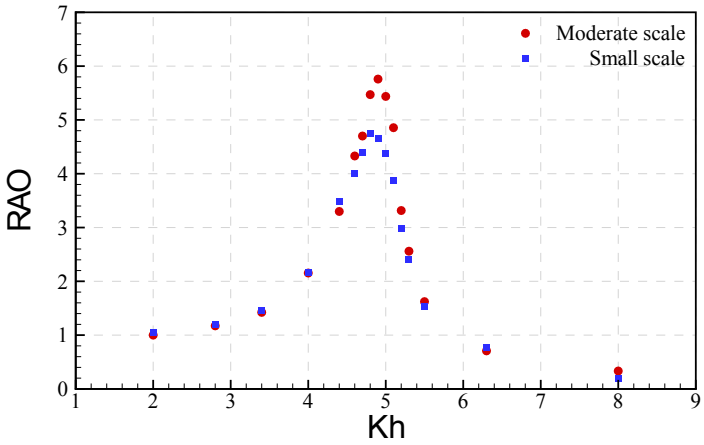

Figure 8.3: Open tube RAO compared with moderate scale RANS simulation.

frequency. This still can be explained by the uncertainty in measuring the draft since same method was adopted to align the draft line and the water surface.

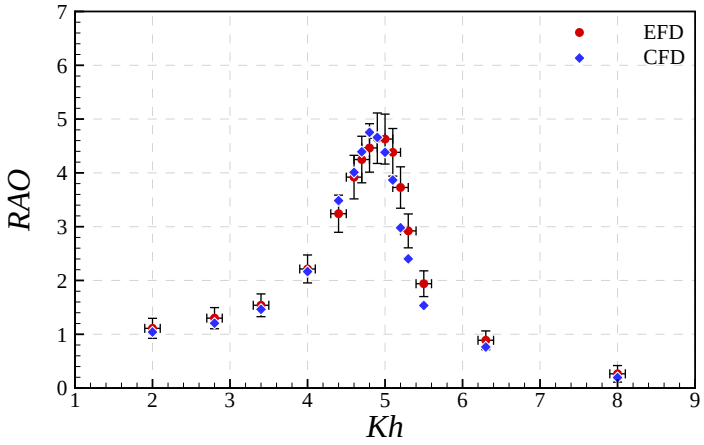

Figure 8.4: Open tube RAO compared with EFD result for full tank condition.

8.3.2 With PTO

Results for the four orifices case at different tank width are plotted from Figure 8.5 to 8.9. As can be seen, except for higher power captured at narrower tank width, CFD simulation also captured the spike like phenomenon around $Kh = 6$. Although CFD simulation does have uncertainties introduced by numerical discritization, it is reasonable to assume that the uncertainty is uni-directional due to the methodology adopted. Hence, the uncertainty is omitted when comparing CFD results against CFD results.

As indicated by the RAO, the pressure and the power, quantities at lower and higher frequency are not affected by the tank width significantly. The major

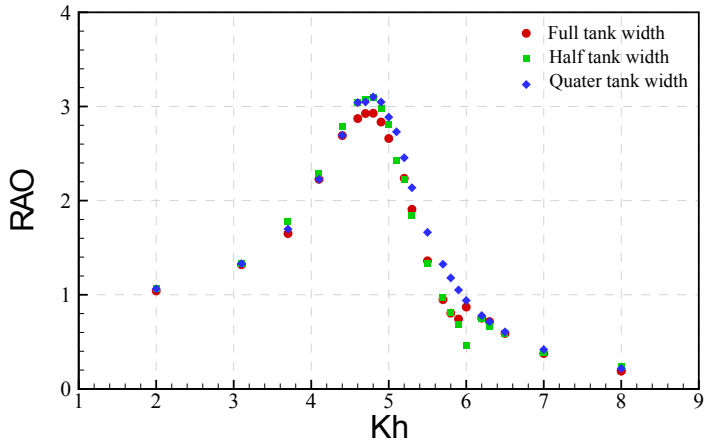

Figure 8.5: Four orifice RAO for different tank width.

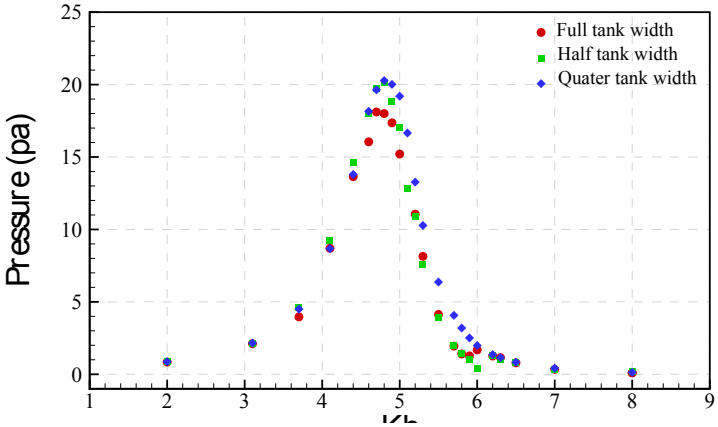

Figure 8.6: Four orifice pressure amplitude for different tank width.

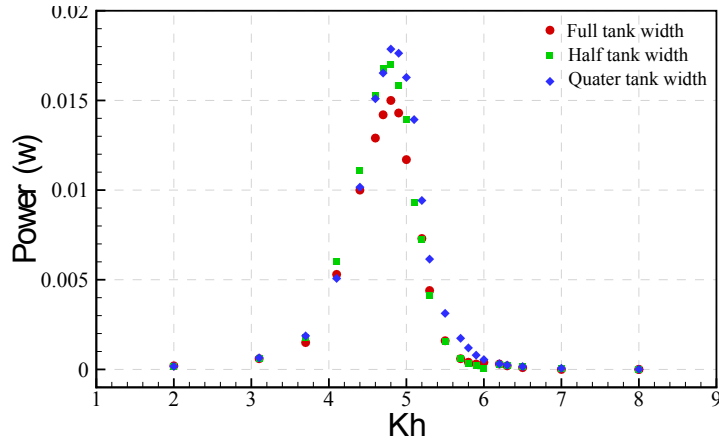

Figure 8.7: Four orifice mean power captured for different tank width.

change took place around the resonance frequency indicating that the tank width effect is OWC response dependent. This is because that larger motion radiate much wave to the tank wall and hence much reflected wave from the tank wall.

Taking the advantage of numerical simulation, open sea condition was simulated

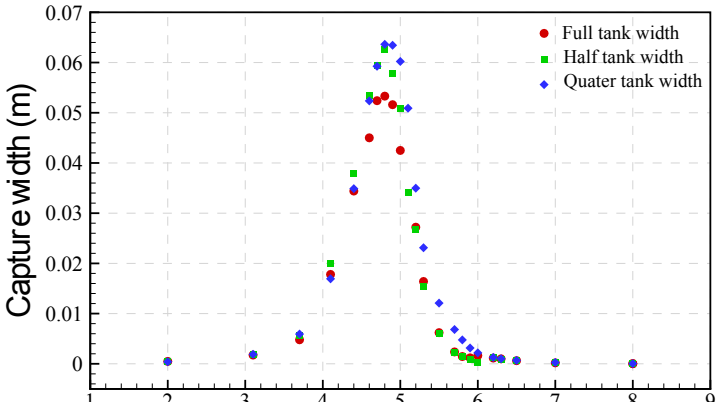

Figure 8.8: Four orifice capture width for different tank width.

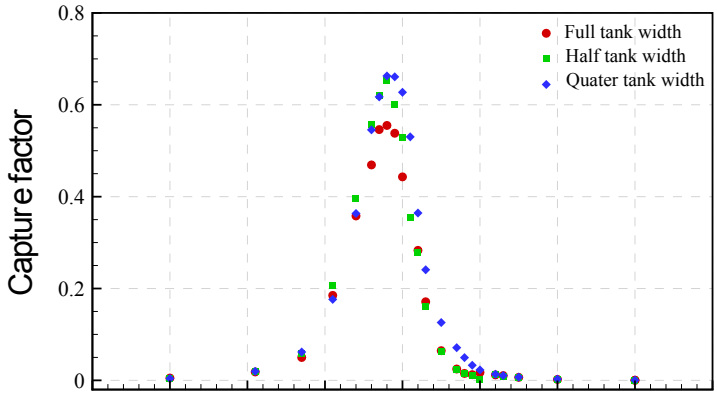

Figure 8.9: Four orifice capture factor for different tank width.

around the resonance frequency to investigate the wall effect on the full tank case. The mean power captured are shown in Figure 8.10.

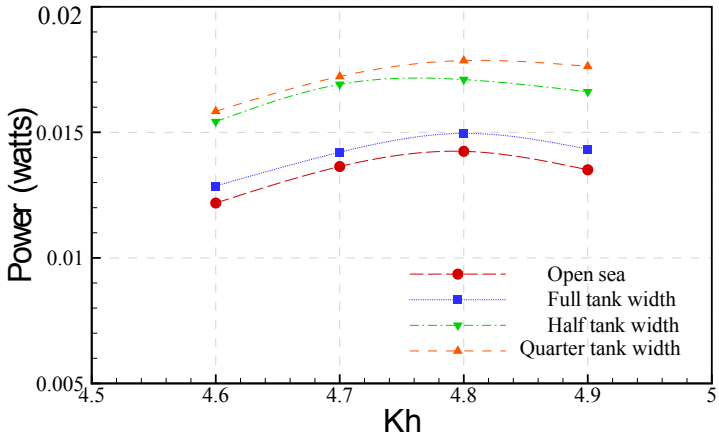

Figure 8.10: Comparison of mean power captured at different tank width around the resonance frequency for four orifices case.

As can be seen, the power captured approaches the open sea condition when the tank width increases. The relative increment of the peak power captured is about 5%, 23% and 28% for the full tank, half tank and quarter tank, respectively.

Clearly, the increment in the mean power captured from full tank to half tank is larger than that from half tank to quarter tank.

Comparison between the moderate scale and small scale simulation for four orifices cases are shown from Figure 8.11 to 8.15. Since to the pressure, power and capture width are dimensional properties, extrapolated values (extrapolated to moderate scale based on Froude scale law.) are plotted along with the small scale results for comparison.

As expected, due to viscosity effect, the response of the small scale result is smaller than that of the moderate scale and thus the pressure amplitude.

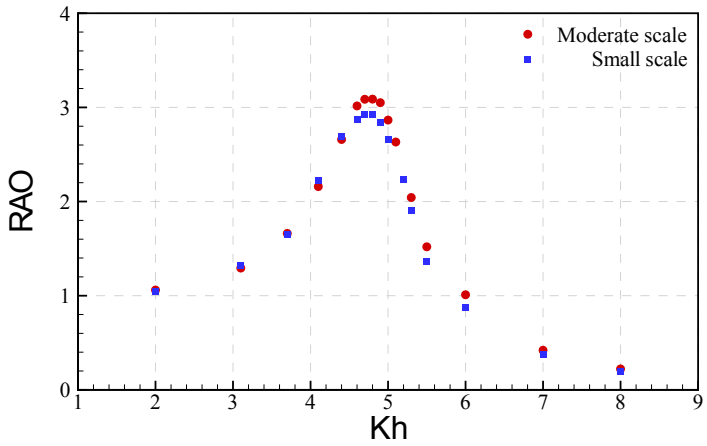

Figure 8.11: Comparison between the moderate scale and small scale RAO for four orifices case.

Comparing the RAO of the four orifice case and the open tube case, it is obvious that the difference between the moderate scale and small scale in the RAO of the four orifices case is much smaller than that of the open tube case. This indicates that the damping effect introduced by the orifice dominates the total damping effect.

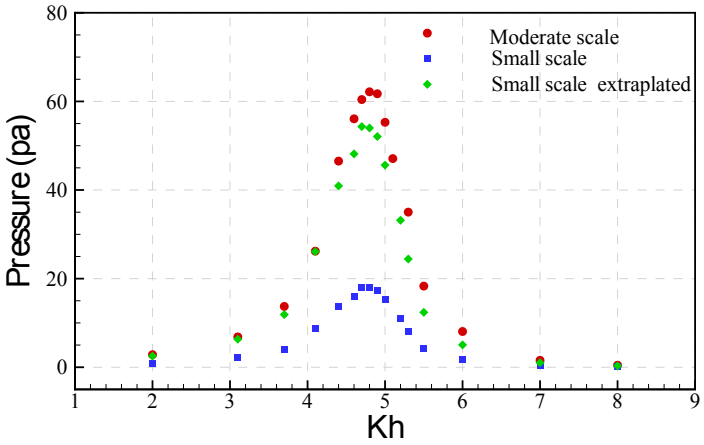

Figure 8.12: Comparison between the moderate scale and small scale pressure amplitude for the four orifices case.

The relative difference in the power is about 21% as suggested by Figure 8.13.

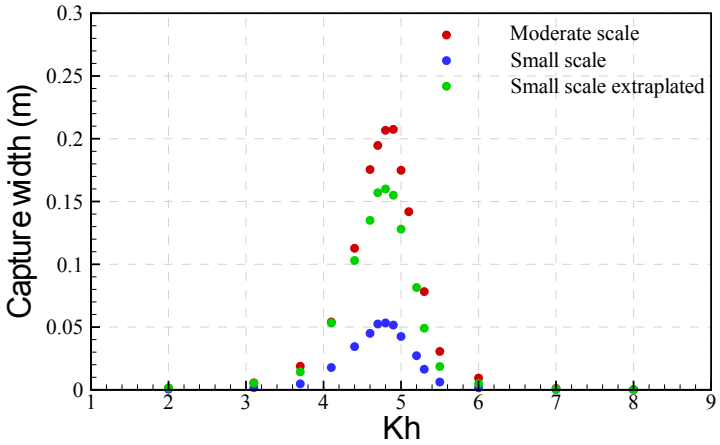

Figure 8.13: Comparison between the moderate scale and small scale mean power captured for the four orifices case.

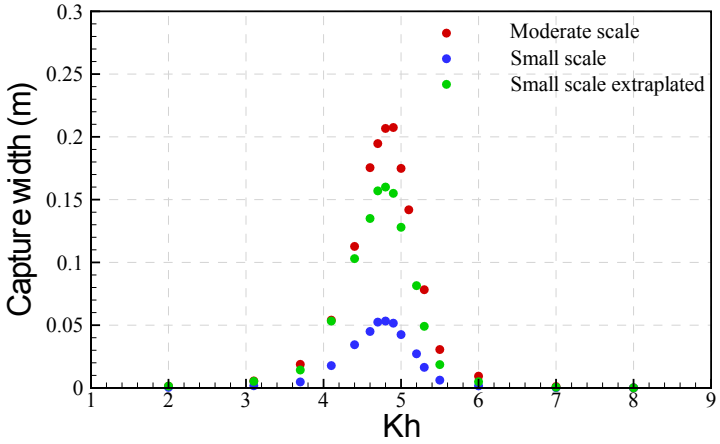

Figure 8.14: Comparison between the moderate scale and small scale mean capture width for the four orifices case.

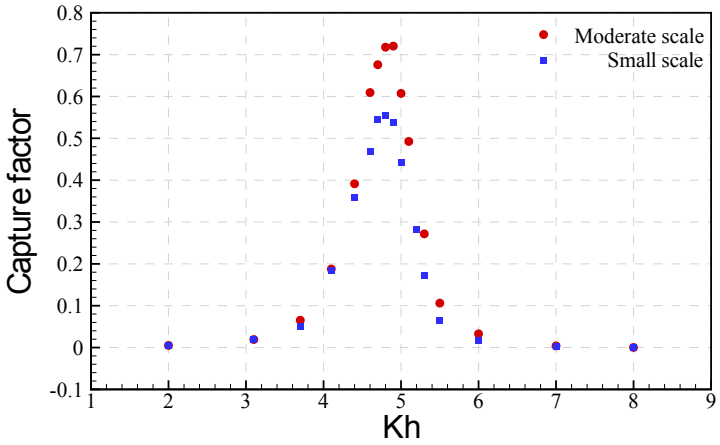

Figure 8.15: Comparison between the moderate scale and small scale mean capture factor for the four orifices case.

A further three times larger scale (about $1:16.7^{th}$ scale of the full scale device and referred as the large scale simulation hereafter (of the moderate scale device) simulations were carried out around the resonance frequency to investigate the scale effect. The mean power captured is shown in Figure 8.16 (where the small scale and moderate scale power were extrapolated to the large scale according Froude scale). The average relative difference in the mean power captured is about 6.6% in the moderate scale and 34.6% in the small scale compared the the large scale case. Clearly the difference between the moderate scale and the large scale case is much smaller than that in the small scale case. This is because that the moderate scale and large scale cases may have reached the critical Reynolds number while the small scale case stayed below the critical Reynolds number and hence much affected by the viscosity effect.

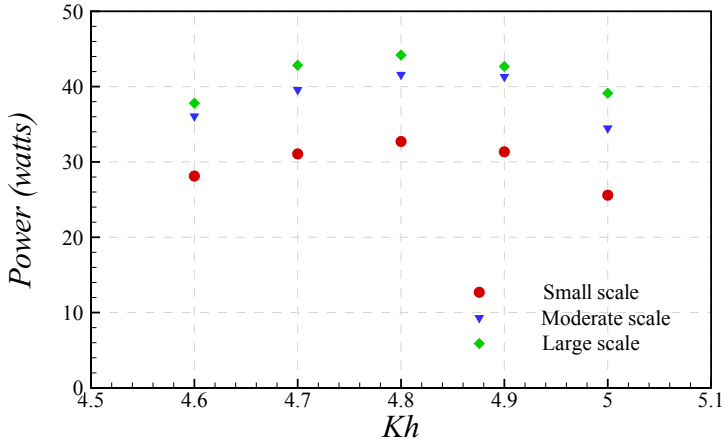

Figure 8.16: Comparison between the power captured for four orifices case at different scale, where the power are all extrapolated to the largest scale.

Due to the experiment failed to scale the orifice correctly while the CFD simulation

scaled the orifice exactly one third time of the moderate scale orifice, the comparison between the CFD and EFD is not satisfied as can be seen from Figure 8.17.

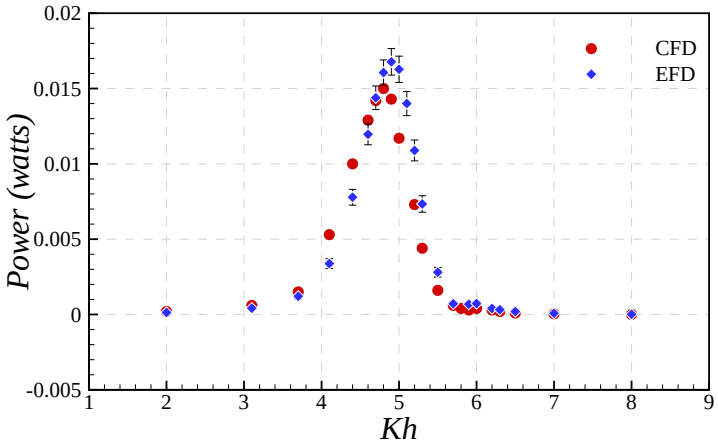

Figure 8.17: Mean power captured comparison between the CFD and EFD for four orifices case.

8.4 Chapter summary

In this chapter, RANS simulation of the small scale device at different tank width is carried out.

Results from different tank width agree with the experiment that narrower tank width will lead to higher power capturing performance even the comparison between the CFD and EFD result was not good due to failure of simulating the PTO accurately.

Overall, the power output increased with reduction of tank width around the peak power output frequencies. The full tank width simulation over predicted the device's performance at open sea condition by about 5% while the quarter tank over predicted the devices' performance at open sea condition by about 28%.

Spiky phenomenon was successfully captured around the tank sloshing frequency by RANS simulation as well. Although in this case, the spike like phenomenon is not of particular interest since it happened at those frequencies where the power output is low. The relative difference in the power out put between the three different tank width around the sloshing frequency is more than 80% at $Kh = 6$. The spike like phenomenon will significantly affect the assessment if the peak response frequency is near the tank sloshing frequency.

Comparison between different scale results indicated that the small scale simulation experienced significant scale effect compared with the moderate scale simulation. Compared with the large scale case, the smaller scale under predicted the mean power captured by about 34.6% while the moderate scale only under predicted the mean power captured by about 6.6%.

It is obvious that the major aspect that bias the assessment of the performance of the device at the small scale is the scale effect. Although the quarter tank width simulation over predicated the performance by about 28%, the tank width is quite critical.

Chapter 9

CFD study of simulated PTO characteristics

9.1 Chapter overview

As discussed in previous chapter it was suggested that the PTO system was not scaled correctly which leads to the unsatisfactory comparison between the small scale and moderate scale experiment. The PTO character, namely the orifice character will be studied in more detail in this chapter.

9.2 Characteristics of the PTO system

It is well know that the relationship between the flow rate and the pressure drop across a Wells Turbine is approximately linear while the pressure drop approximately equal to square of the volume flow rate for a non-linear turbine such as Darrieus turbine (Sheng et al., 2013). The relationship between the flow rate and the pressure drop can be modelled by

for linear PTO

$$p = \wedge q \tag{9.1}$$

for non-linear PTO

$$p = \wedge q^2 \tag{9.2}$$

where, the $\wedge$ is a real constant.

The constant $\wedge$ is determined by plotting the squared volume flow rate against the pressure drop and fitted using least square regression. The gradient is then the $\wedge$. An example is shown in Figure 9.1 for the four orifices case at $Kh = 4.9$.

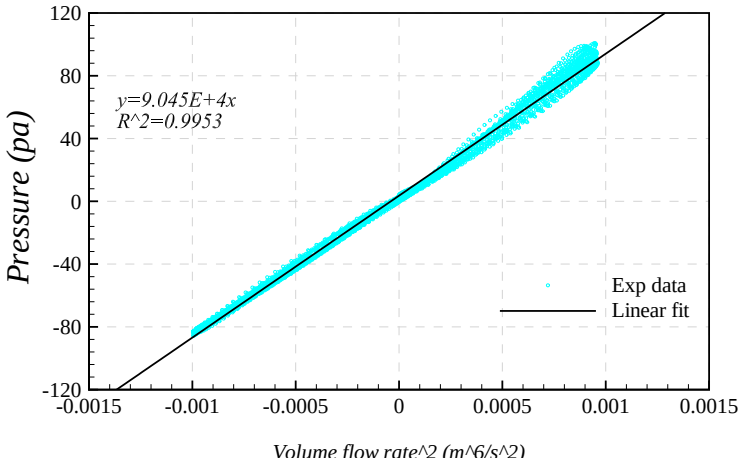

Figure 9.1: Square of Volume flow rate against pressure drop for the four orifices case at $Kh = 4.9$.

Figure 9.2 shows the comparison between the $\wedge$ from RANS simulation and tank testing against the Reynolds number (calculated based on the diameter of the air chamber and velocity in the air chamber) for the four orifices case.

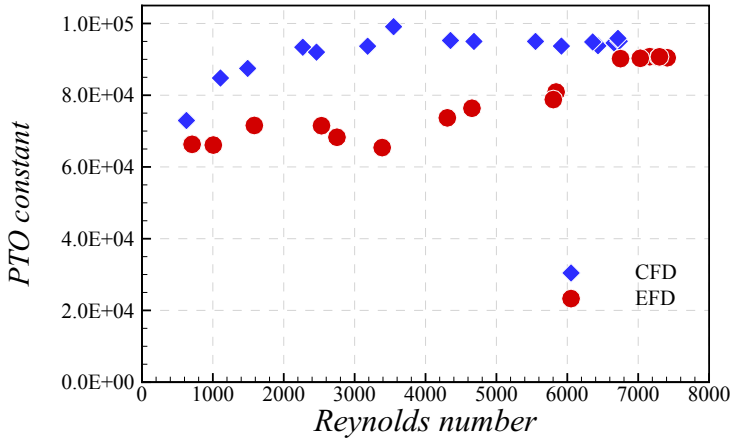

Figure 9.2: Comparison of $\wedge$ against Reynolds number for the moderate scale four orifices case simulation and tank testing.

It is obvious that the PTO constant is different between the RANS simulation and the tank testing which accounts for the different output power obtained in the RANS simulation and tank testing (Note here that the uncertainty in the PTO constant for the experiment around the at the highest Reynolds number is about 3237 $pa \cdot s/m^3$. The comparison between the RANS simulation and tank testing for the one orifice case is shown in Figure 9.3.

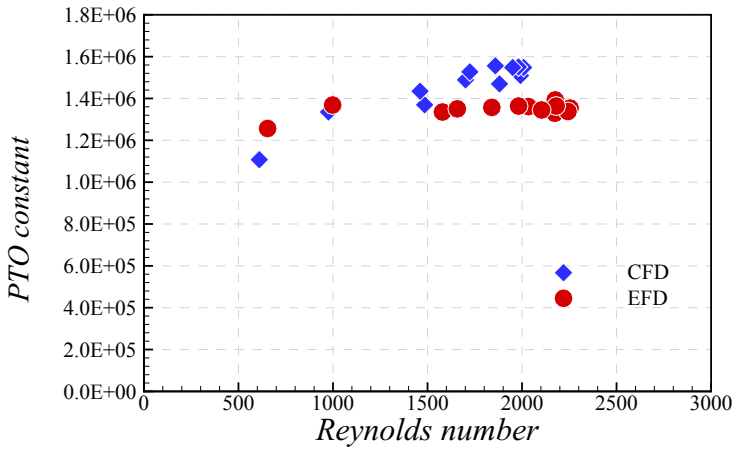

Figure 9.3: Comparison of the simulation and tank testing $\wedge$ against Reynolds number for the moderate scale one orifices case .

Comparison of the PTO constant for the four orifices case between the moderate scale and small scale tank testing result is shown in Figure 9.4, where the small scale PTO constant was extrapolated to the moderate scale according to Froude scaling and the Reynolds number was kept the same. The small scale PTO constant is much smaller than that of the moderate scale, suggesting the failure of scaling the PTO.

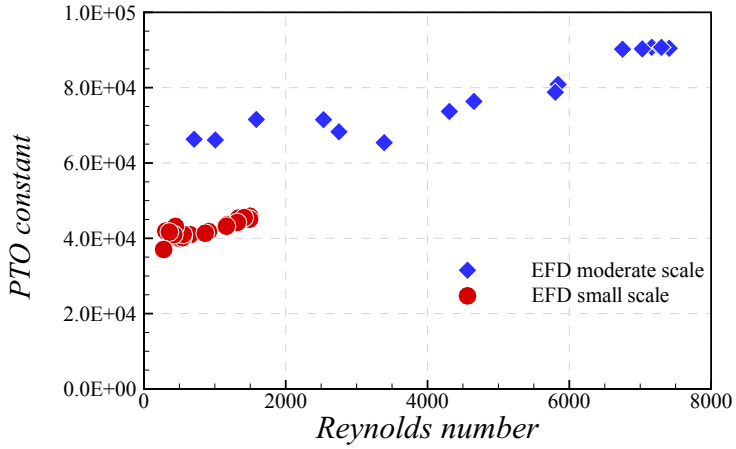

Figure 9.4: Comparison of the tank testing $\wedge$ against Reynolds number for the moderate scale and small scale one orifices case.

On the other hand, comparison of the PTO constant for the four orifices case between the moderate scale and small scale RANS simulation is shown in Figure 9.5. It is clear that the small scale PTO constant shows a similar trend of the moderate scale test. The PTO constant of the small scale simulation falls into a region that is Reynolds number dependent. The PTO constant of the moderate scale simulation suggests that the PTO constant tends to be constant when the Reynolds number is around 3000 which is slightly larger than the critical Reynolds number of pipe

flow.

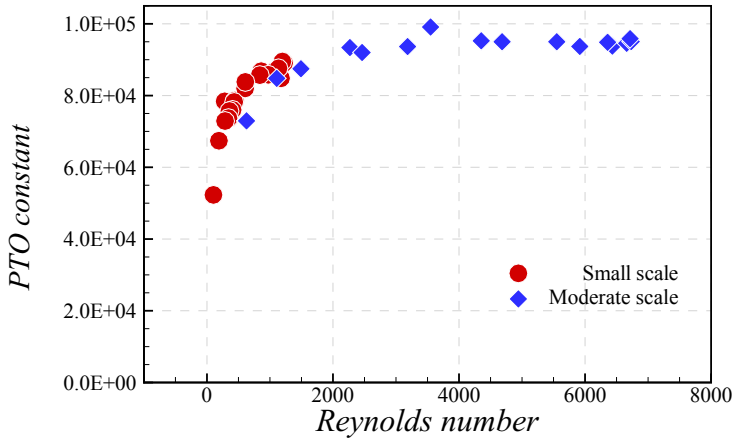

Figure 9.5: Comparison of the simulation $\wedge$ against Reynolds number for the moderate scale and small scale four orifices case

The large scaled case exhibits a larger PTO constant than the moderate scale simulation as indicated by Figure 9.6, where the PTO constant of the large scale case was electroplated to the moderate scale according to Froude scaling.

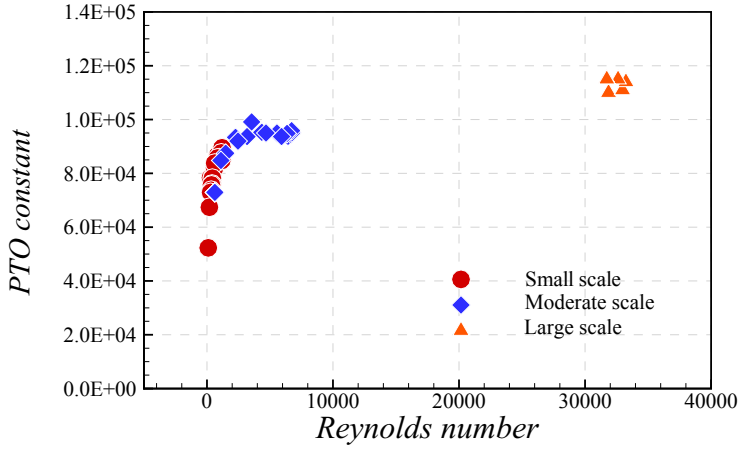

Figure 9.6: Comparison of the simulation PTO constant $\wedge$ against Reynolds number for three different scale four orifices case.

To further investigate whether the larger PTO constant of the large scaled simulation is caused by Reynolds sensitivity or other reasons, further simulation was carried out. For details of orifice plate simulation see Appendix E.

As can be seen from Figure 9.7, the small scale and moderate scale results match the $\wedge$ obtained from the orifice simulation well while there exists discrepancy between the orifice simulation and the large scale simulation.

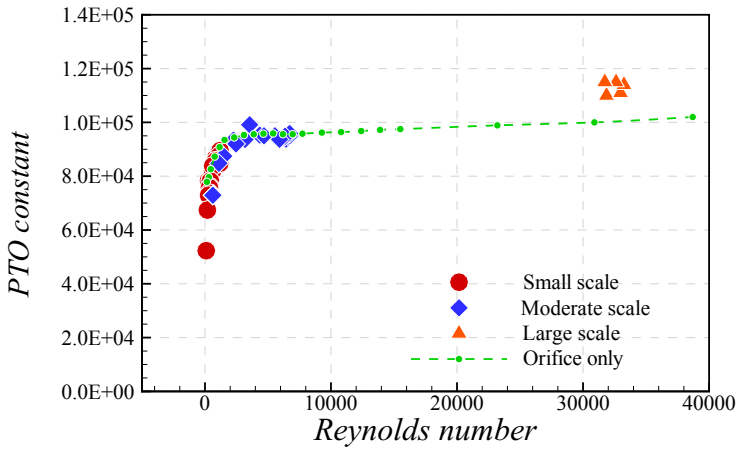

Figure 9.7: Comparison of the simulation ∧ against result from orifice simulation.

Figure 9.8 illustrated the PTO constant of the moderate scale orifice simulated by compressible and incompressible condition. As can be seen, the PTO constant of the compressible simulation grows with the increment of Reynolds number while the incompressible simulation tends to convergence when the Reynolds number is larger than 20000. The PTO constant of the compressible simulation is close to that of the incompressible simulation when the density of the two simulation is close to each other. At lower Reynolds number, when the density of the incompressible simulation is larger than that of the compressible simulation, the PTO constant of the compressible simulation is slightly smaller than that of the incompressible simulation.

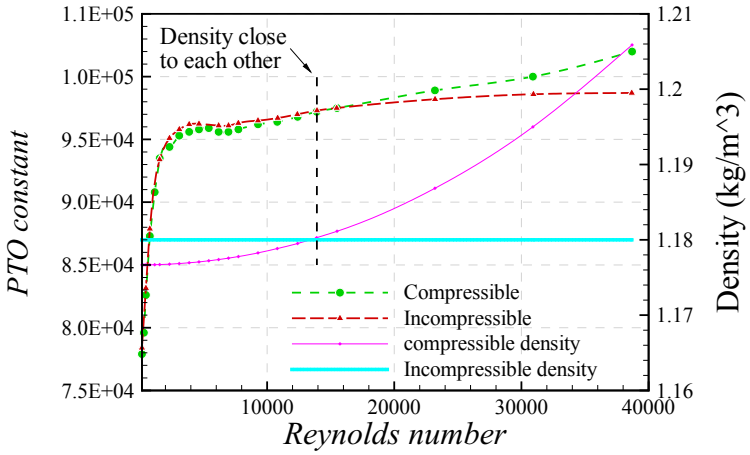

Figure 9.8: Comparison of the simulation ∧ against result from orifice simulation.

The close value of the PTO constant between the compressible and incompressible simulation at low Reynolds number suggest that the air compressibility can be regard as negligible at model scale.

Having the above observation in mind, the large discrepancy between the large scale

simulation and the orifice simulation can be explained by the air compressibility as following

As point out by several researchers (e.g. Sheng et al. (2014),Sarmento (1992)), in order to keep the spring like air compressibility effect at model scale the same as the full scale device, the height of the chamber should be kept the same as the full scale device to scale the mean air volume inside the chamber by a scale factor of s^2. Formulated by Sarmento (1992), the linearised relation of the flow rate through the PTO can be calculated by

$$q_{PTO} = q_{owc} - \frac{V_0}{\gamma p_0}\frac{dp}{dt} = q_{owc} - \frac{A_{w_{air}} H}{\gamma p_0}\frac{dp}{dt} \tag{9.3}$$

where the q_{PTO} is the volume flow rate through the PTO system and the q_{owc} is the volume flow rate driven by the OWC. The γ is the specific heat ratio for air, the V_0 is the mean air volume in the chamber and the P_0 is the atmosphere pressure while p is the pressure drop. The $A_{w_{air}}$ denotes the cross section area of the air chamber and H stands for the height of the air chamber.

Since it is not easy to scale the atmosphere pressure, to keep the q_{PTO} scaled according to Froude scale, the V_0 has to be scaled by a scale factor of s^2 instead of traditional scale for volume s^3. Keeping the height the same as the full scale resolved this scaling issue.

For the above reason, the height of the chamber was kept the same for all the three different scale simulations and the individual orifice simulation.

However, the air volume in the chamber is in fact dynamically changing with the OWC response (reaching the minima when the owc response reaches the maxima and vice versa.). The instantaneous air stiffness of the air should be calculated from the remaining air volume in the chamber (thus the remaining chamber height.). The stiffness induced by the air can be can be calculated by (Bayoumi, 2013)

$$k_{stiffness_{air}} = \frac{\gamma p_0 A_{w_{air}}^2}{V_0} = \frac{\gamma p_0 A_{w_{air}}}{H} \tag{9.4}$$

Keeping the average chamber height the same leads to different maximum and minimum chamber height during the OWC operation time when the model is scaled and hence resulting a different air stiffness. In fact, larger motion leads to a larger air stiffness (Bayoumi (2013)). This larger air stiffness leads to a smaller

OWC response as can be seen from the comparison of the RAO for the three different scale shown by Figure 9.9.

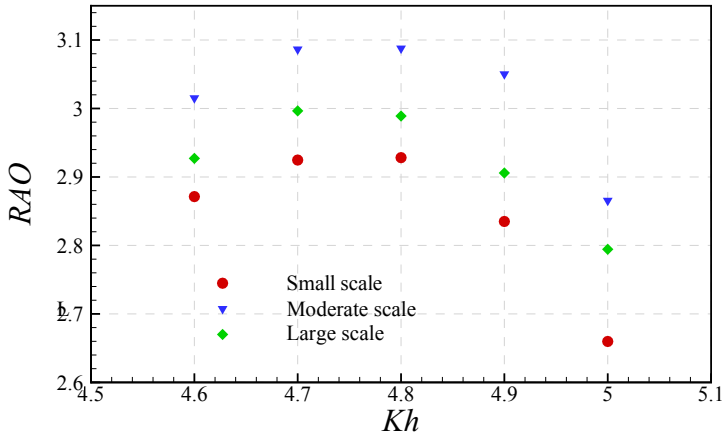

Figure 9.9: Comparison of the four orifices case RAO for different scales' simulations.

On the other hand, according to the ideal gas isothermal law, less volume would lead to a larger pressure. Hence, the pressure is larger as shown by Figure 9.10. The individual simulation of the orifice plate did not include the changing of the air volume in the chamber, thus leading a different PTO constant.

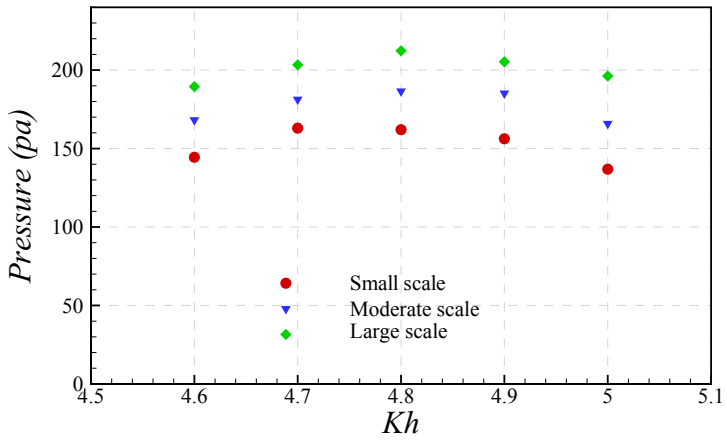

Figure 9.10: Comparison of the four orifices case Pressure for different scales' simulations.

9.3 Chapter summary

The PTO behavior was studied in this chapter. The PTO constant was not simulated accurately (by CFD simulation as indicated by the comparison between the RANS simulation and tank testing, one possible reason would be due to the uncertainty in the size of the orifice and hence the orifice wasn't modelled accurately enough.

Scaling of the PTO for the tank testing was not a success as suggested by the comparison of the PTO constant of the tank testing. On the other hand, the comparison of the PTO constant between the large and small scale RANS simulation shows the scaling of the PTO in the RANS simulation was reasonable.

Additional individual PTO simulation suggest that the air compressibility is negligible at model scale.

Results from the large scale simulation indicate that RANS simulation is capable of correctly simulate the scaling effect due to air compressibility by using ideal gas model. The compressibility of air at the further third moderate scale lead to a smaller OWC response and a slightly larger pressure resulting a larger PTO constant.

Chapter 10

Conclusion and future works

10.1 Conclusion

This thesis investigated several aspects related to assessing the performance of the proposed cost effective FSCOWC WEC by tank testing and RANS simulation. The main conclusion are drawn as below

Scale effect

Scale effect may be the aspect that most bias the assessment of the performance of the FSCOWC. As suggested by the RANS simulation result, the small scale simulation under predict the power output at the resonance peak about 34% compared with the large scale case.

The scaling effect can be mainly divided into 2 parts as following

The first scaling effect is the by the conflict between scaling the device according to Froude scaling and Reynolds number. Due to the Reynolds number at model scale is normally smaller than that at larger scale and full scale, power loss due to viscosity at small model scale will under predict the performance of the full scale device.

The second scaling effect is caused by the air compressibility. As suggested by the orifice simulation, the PTO constant tends to converge when the Reynolds number increasesfor incompressible condition while for the compressible simulation the PTO constant still increase with increasing Reynolds number.

Although the large scale case showed a slightly larger power output compared with the other two scale's results, the power output might be smaller than the result extrapolated from the moderate scale simulation when the scale further goes up (if the mean volume of air in the change is kept the same). This may be one of the reason that some full scale devices' performance is lower than the results extrapolated from model test.

Scaling of air compressibility

The assumption that keeping the mean height of the air chamber as the same as that of the full scale will lead to a correctly scaled air stiffness is only valid if the motion of the OWC is small compared with the height of the chamber at full scale. This would not be always satisfied simply because that will not be economic, for instance, the response of the four orifice case is about $0.1m$ for the moderate scale $(1:50^{th})$ test which corresponding to about $5m$ at full scale, the height of the chamber would be $50m$ even assuming that 10% is so called 'small'.

To keep the stiffness of the model scale induced by the air compressibility close to that of the full scale device, a more practical way would be keeping the minimum air chamber height at model scale the same as that of the full scale, and connect the air chamber with a air reservoir equipped with a control valve that allows the air reservoir open to the air chamber only during the inhalation process. The volume of the air contained in the air reservoir should be designed in such a way so that it will produce air chamber height the same as the maximum air chamber height as the full scale. This requires the volume of air in the reservoir equals to the volume as represented by grey shade in Figure 10.1. By doing this, the maximum and minimum air stiffness will be scaled properly according to Froude scaling law.

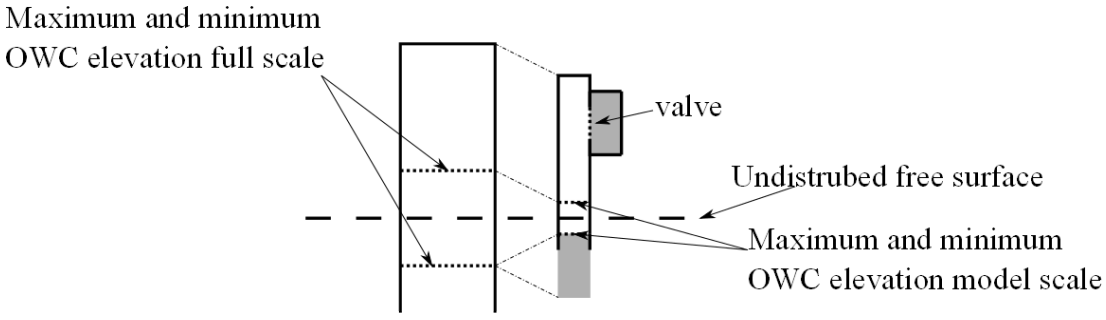

Figure 10.1: Illustration of using valve to scale the air compressibility.

Tank width effect

Both experiment and RANS simulation suggested that spike like phenomenon will take place when the incident wave frequency equals to the tank sloshing frequency. Besides, the power output will increase when the tank width reduces.

It is noted that the increment in the power output is not linear against tank width. In fact, the difference in the half tank case and quarter tank width results is small compared with the increment from full tank to quarter tank. This indicates that the power output may not increase when the tank width further reduces. Theoretically, the power output should drop at some point when the tank width is close to the diameter of the device. This is because when the tank width equals to the diameter of the device, the problem can be regards as a two dimensional case where the capture factor would not exceed 1.

The growth in the power output due to tank width to some point suggests that there exists an optimised configuration for an array of device since the tank width effect on the device can be treated as three devices spacing tank width to each other.

Comparison of the RANS simulation between the full tank width and open sea condition suggest that the power output is still slightly affected by the tank width effect.

Tank testing VS RANS simulation

Large uncertainty in the measurement is one of the drawbacks of testing a small scale device (below 1:100 scale), for instance, the uncertainty in the power measurement for the small scale four orifices case around the resonance peak is about 5.5% at 95% level of confidence. To minimize the uncertainty in the measurement at such a scale, expensive high accuracy instruments are essentials. Even neglecting the uncertainty, such a scale experiences significant scale effect (Mainly due to Reynolds number sensitivity.). Therefore, tests under 1:100 scale is only recommended for concept validation purpose.

A moderate scale test can provide a reasonable representation of a full scale device at a reasonable cost. Although the uncertainty reduced a little bit due to larger scale. The uncertainty in the power measurement in this thesis is still about 4% around the peak power output. Besides, due to testing in a wall bounded tank will

introduce some unwanted effect such as the spike like phenomenon around tank sloshing frequency. Based on the simulation results, it seems that the moderate scale test in current thesis still over estimated the power output for a full scale device at open sea condition due to the appearance of the tank walls.

On the other hand, RANS simulation successfully simulated the tank width effect and provided an open sea condition by using the non-reflecting numerical wave tank established . The scale effect was reasonably reproduced and provided a further scaled up data. However, due to the RANS simulation failed to model the experiment condition exactly (mainly due to the uncertainty in the measurement of experiment and assumption made in the simulation, for instance, turbulence model et.al), the agreement between the RANS simulation and tank testing results is not perfect. However, the situation can be improved. For example, the determination of the draft can be improved with the assist of accurate instrument (See Appendix for detail.). The difference introduced by the modelling of the orifice plate can also be improved. One possible solution is to calibrate the orifice plate during experiment stage and introduce the PTO constant to the simulation (See Şentürk and Özdamar (2013) for example.).

RANS simulation in 3D is still expensive regarding the computation time, especially for wave structure interaction simulation since large amount of mesh is needed to simulate the wave accurately. One simulation around the resonance peak take roughly 7 days with 72 cpu cores due to large amount mesh and small time step size required. Compared with small scale tank test, RANS simulation is still not economic. The cost of small scale tank testing probably is less than the small scale RANS simulation. However, when the scale goes up, the advantage of RANS simulation take over the tank testing regarding the cost since the cost of tank testing increase dramatically with scale while the simulating time remains almost constant for RANS simulation regardless of scale.

Summary

As indicated by the present study that assessment of the performance of a (certain) type of WECs device during tank testing stage may be biased by the scale of the model and tank width. Results suggests that small scale testing (without considering the tank width effect.) will generally under estimate the performance of a device mainly due to difficulty in scaling the device and environment in a way that will follow Froude scaling and Reynolds scaling at the same time (e.g.

power loss cased by viscosity.). On the other hand, narrower tank tends to over predict the power output of the device.

Since tank testing and RANS simulation all have their own merits and drawbacks, it is recommended to assess the performance of the device by both tank testing and RANS simulation. Good practice would be validate the RANS simulation with a moderate scale tank testing result and use RANS simulation to investigate the scale effect and tank width effect.

10.2 Future works

- The scale effect experiment in fact failed in current study due to large uncertainty. Therefore, further scale tank testing should be carried out. For instance, a large scale device ($1 : 16.7^{th}$ of the full scale).
- Current study investigated the effect of tank width on the performance of the proposed device. Future work will focus on investigating the correction methods.
- Methodology of calibrating the orifice by testing needed to be developed.
- RANS simulation of the orifice will be performed in 3D unsteady state so that the variation of the volume of the air in the chamber can be included in the simulation.
- Future work will also investigate the interaction between the proposed device and a fixed wind turbine tower as proposed to check the feasibility of the concept of combining wind and wave power to reduce the total cost.

References

Anaconda, 2014. Sea energy anaconda URL: http://www.checkmateukseaenergy.com/.

Anbarsooz, M., Passandideh-Fard, M., Moghiman, M., 2013. Fully nonlinear viscous wave generation in numerical wave tanks. Ocean Engineering 59, 73–85.

Antonio, F.d.O., 2010. Wave energy utilization: A review of the technologies. Renewable and sustainable energy reviews 14, 899–918.

Bayoumi, A.S.E.M., 2013. Development of numerical wave power prediction tool offshore oscillating water column wave energy converter. Thesis.

Bradshaw, P., Cebeci, T., Whitelaw, J.H., 1981. Engineering calculation methods for turbulent flow. NASA STI/Recon Technical Report A 82, 20300.

Celik, I.B., Ghia, U., Roache, P.J., 2008. Procedure for estimation and reporting of uncertainty due to discretization in cfd applications. Journal of fluids Engineering-Transactions of the ASME 130.

Clément, A., McCullen, P., Falcão, A., Fiorentino, A., Gardner, F., Hammarlund, K., Lemonis, G., Lewis, T., Nielsen, K., Petroncini, S., Pontes, M.T., Schild, P., Sjöström, B.O., Sørensen, H.C., Thorpe, T., 2002. Wave energy in europe: current status and perspectives. Renewable and Sustainable Energy Reviews 6, 405–431. doi:http://dx.doi.org/10.1016/S1364-0321(02)00009-6.

Cruz, J., 2007. Ocean wave energy: current status and future prespectives. Springer Science & Business Media.

Dalrymple, R.A., Dean, R.G., 1991. Water wave mechanics for engineers and scientists. Prentice-Hall.

Day.A.H., 1987. An intergrated approach to the design of moonpools for subsea operations. Ph.D. thesis. University of Strathclyde.

Dieck, R., Steele, W., Osolsobe, G., 2005. Test uncertainty. American Society of Mechanical Engineers, New York, ASME PTC , 19.1–2005.

Drew, B., Plummer, A., Sahinkaya, M.N., 2009. A review of wave energy converter technology, in: Proceedings of the Institution of Mechanical Engineers, Part A: Journal of Power and Energy, pp. 887–902.

El Marjani, A., Ruiz, F.C., Rodriguez, M., Santos, M.P., 2008. Numerical modelling in wave energy conversion systems. Energy 33, 1246–1253.

EMEC, 2013. European marine energy centre(emec). URL: http://www.emec.org.uk/blog-max-carcas-discusses-the-cost-of-developing-marine\-renewables/.

Enger, S., Perić, M., Monteiro, H., 2014. Coupling of 3d numerical solution method based on navier-stokes equations with solutions based on simpler theories.

Şentürk, U., Özdamar, A., 2013. An alternative approach to estimate the hydrodynamic efficiency of an oscillating water column using computational fluid dynamics. Progress in Computational Fluid Dynamics, an International Journal 13, 120–129.

Şentürk, U., Özdamar, A., Bornova, I., 2011. Modelling the interaction between water waves and the oscillating water column wave energy device. Mathematical and computational applications 16, 630.

Ersdal, S., Moe, A.M., 2013. Model test of the aker wave energy converter concept, in: ASME 2013 32nd International Conference on Ocean, Offshore and Arctic Engineering, American Society of Mechanical Engineers. pp. V008T09A030–V008T09A030.

Evans, D., 1982. Wave-power absorption by systems of oscillating surface pressure distributions. Journal of Fluid Mechanics 114, 481–499.

Evans, D.V., 1978. The oscillating water column wave-energy device. IMA Journal of Applied Mathematics 22, 423–433. doi:10.1093/imamat/22.4.423.

Evans, D.V., Porter, R., 1995. Hydrodynamic characteristics of an oscillating water column device. Applied Ocean Research 17, 155–164. doi:Doi10.1016/0141-1187(95)00008-9.

Evans, D.V., Porter, R., 1997. Efficient calculation of hydrodynamic properties of owc-type devices. Journal of Offshore Mechanics and Arctic Engineering 119, 210–218.

Falcão, A.F., Henriques, J.C., 2014. Model-prototype similarity of oscillating-water-column wave energy converters. International Journal of Marine Energy 6, 18–34.

Falcão, A.F., Henriques, J.C., 2016. Oscillating-water-column wave energy converters and air turbines: A review. Renewable Energy 85, 1391 – 1424. URL: http://www.sciencedirect.com/science/article/pii/S0960148115301828, doi:http://dx.doi.org/10.1016/j.renene.2015.07.086.

Falnes, J., 1994. Small is beautiful: How to make wave energy economic, in: 1993 European wave energy symposium, Edinburgh, Scotland, pp. 367–372.

Falnes, J., 2002. Ocean waves and oscillating systems: linear interactions including wave-energy extraction. Cambridge university press.

Falnes, J., 2007. A review of wave-energy extraction. Marine Structures 20, 185–201.

Fenton, J.D., 1985. A fifth-order stokes theory for steady waves. Journal of waterway, port, coastal, and ocean engineering 111, 216–234.

Ferziger, J.H., Peric, M., 2012. Computational methods for fluid dynamics. Springer Science & Business Media.

Folley, M., Whittaker, T., 2009. Analysis of the nearshore wave energy resource. Renewable Energy 34, 1709–1715.

Forestier, J., Holmes, B., Barrett, S., Lewis, A., 2007. Value and validation of small scale physical model tests of floating wave energy converters, European Wave and Tidal Energy Conference.

GeneralAcoustics, 2014. Ultralab® uls sensing of water level and waves. URL: http://www.generalacoustics.com/downloads/UltraLab_ULS_small.pdf.

Gomes, R., Henriques, J., Gato, L., Falcão, A., 2015. Testing of a small-scale model of a heaving floating owc in a wave channel and comparison with numerical results. Renewable Energies Offshore , 445.

Gueyffier, D., Li, J., Nadim, A., Scardovelli, R., Zaleski, S., 1999. Volume-of-fluid interface tracking with smoothed surface stress methods for three-dimensional flows. Journal of Computational Physics 152, 423–456.

GUM, I., 2008. Guide to the expression of uncertainty in measurement, (1995), with supplement 1, evaluation of measurement data, jcgm 101: 2008. Organization for Standardization, Geneva, Switzerland .

Gunn, K., Stock-Williams, C., 2012. Quantifying the global wave power resource. Renewable Energy 44, 296–304.

He, F., Huang, Z., 2014. Hydrodynamic performance of pile-supported owc-type structures as breakwaters: An experimental study. Ocean Engineering 88, 618–626. doi:http://dx.doi.org/10.1016/j.oceaneng.2014.04.023.

Heath, T., 2012. A review of oscillating water columns. Philosophical Transactions of the Royal Society A: Mathematical, Physical and Engineering Sciences 370, 235–245.

Heath, T., Whittaker, T., Boake, C., 2000. The design, construction and operation of the limpet wave energy converter (islay, scotland), in: 4th European wave energy conference, pp. 4–6.

Higuera, P., Losada, I.J., Lara, J.L., 2015. Three-dimensional numerical wave generation with moving boundaries. Coastal Engineering 101, 35–47. doi:http://dx.doi.org/10.1016/j.coastaleng.2015.04.003.

Honeywell, 2014. 160pc series pressure sensors datasheets. URL: http://www.farnell.com/datasheets/103022.pdf.

Ikoma, T., Masuda, K., Omori, H., Osawa, H., Maeda, H., 2013. Improvement of wave power take-off performance due to the projecting walls for owc type wec, in: ASME 2013 32nd International Conference on Ocean, Offshore and Arctic Engineering, American Society of Mechanical Engineers. pp. V008T09A022–V008T09A022.

ITTC, 2008a. Guide to the expression of uncertainty in experimental hydrodyanmics, in: ITTC procedure 7.5-02-01-01.

ITTC, 2008b. Uncertainty analysis instrument calibration, in: ITTC procedure 7.5-01-03-01.

Jin, J., Liu, Z., Hyun, B.S., Hong, K., 2012. Effects of wave direction on performance of oscillating water column type wave energy convertor, in: The Twenty-second International Offshore and Polar Engineering Conference, International Society of Offshore and Polar Engineers.

John W, S., 2008. Examining spatial (grid) convergence. https://www.grc.nasa.gov/WWW/wind/valid/tutorial/spatconv.html.

Kamath, A., Bihs, H., Arntsen, i.A., 2014. Comparison of 2d and 3d simulations of an owc device in different configurations. Coastal Engineering Proceedings 1, structures. 66.

Kamath, A., Bihs, H., Arntsen, i.A., 2015. Numerical modeling of power take-off damping in an oscillating water column device. International Journal of Marine Energy 10, 1–16. doi:http://dx.doi.org/10.1016/j.ijome.2015.01.001.

Kim, J., Kyoung, J., Ertekin, R., Bai, K., 2006. Finite-element computation of wave-structure interaction between steep stokes waves and vertical cylinders. Journal of waterway, port, coastal, and ocean engineering 132, 337–347.

Kim, J., O'Sullivan, J., Read, A., 2012. Ringing analysis of a vertical cylinder by euler overlay method, in: ASME 2012 31st International Conference on Ocean, Offshore and Arctic Engineering, American Society of Mechanical Engineers. pp. 855–866.

Knott, G., Flower, J., 1979. Wave-tank experiments on an immersed parallel-plate duct. Journal of Fluid Mechanics 90, 327–336.

Koola, P.M., Ravindran, M., Narayana, P.A., 1995. Model studies of oscillating water column wave-energy device. Journal of energy engineering 121, 14–27.

Lamont-Kane, P., Folley, M., Whittaker, T., 2013. Investigating uncertainties in physical testing of wave energy converter arrays, in: Proceedings, 10th European Wave and Tidal Energy Conference (EWTEC 2013), Aalborg, Denmark.

Larsen, J., Dancy, H., 1983. Open boundaries in short wave simulations—a new approach. Coastal Engineering 7, 285–297.

Leonard, B., 1991. The ultimate conservative difference scheme applied to unsteady one-dimensional advection. Computer methods in applied mechanics and engineering 88, 17–74.

Li, Y., Yu, Y.H., 2012. A synthesis of numerical methods for modeling wave energy converter-point absorbers. Renewable and Sustainable Energy Reviews 16, 4352–4364.

Lin, P., Liu, P.L.F., 1999. Internal wave-maker for navier-stokes equations models. Journal of waterway, port, coastal, and ocean engineering 125, 207–215.

López, I., Pereiras, B., Castro, F., Iglesias, G., 2014. Optimisation of turbine-induced damping for an owc wave energy converter using a rans–vof numerical model. Applied Energy 127, 105–114. doi:http://dx.doi.org/10.1016/j.apenergy.2014.04.020.

Luo, Y., Nader, J.R., Cooper, P., Zhu, S.P., 2014. Nonlinear 2d analysis of the efficiency of fixed oscillating water column wave energy converters. Renewable Energy 64, 255–265. doi:http://dx.doi.org/10.1016/j.renene.2013.11.007.

Masuda, Y., 1971. Wave-activated generator. Int. Coll. on the Expositions of the Oceans (Trans.), Bordeaux, France .

Mei, C.C., Stiassnie, M., Yue, D.K.P., 2005. Theory and applications of ocean surface waves: linear aspects. volume 23. World Scientific.

Menter, F.R., 1992. Improved two-equation k-omega turbulence models for aerodynamic flows. NASA STI/Recon Technical Report N 93, 22809.

Morris-Thomas, M.T., Irvin, R.J., Thiagarajan, K.P., 2007. An investigation into the hydrodynamic efficiency of an oscillating water column. Journal of Offshore Mechanics and Arctic Engineering 129, 273–278.

OceanEnergy, 2014. Development. URL: http://oceanenergy.ie/development-history/.

OffshoreWind.biz, 2012. Uk: Ocean energy plans to deploy oe buoy wave energy converter at wave hub. https://www.offshorewind.biz/2012/10/29/uk-ocean-energy-plans-to-deploy-oe-buoy-wave-energy-converter-at-wave-hub/.

Ohneda, H., Igarashi, S., Shinbo, O., Sekihara, S., Suzuki, K., Kubota, H., Ogino, H., Morita, H., 1991. Construction procedure of a wave power extracting caisson breakwater, in: Proceedings of the 3rd Symposium on Ocean Energy Utilization, Tokyo, pp. 171–179.

Poullikkas, A., 2014. Technology prospects of wave power systems. Electronic Journal of Energy & Environment 2, 47–69.

Pérez-Collazo, C., Greaves, D., Iglesias, G., 2015. A review of combined wave and offshore wind energy. Renewable and Sustainable Energy Reviews 42, 141–153.

Raghunathan, S., 1995. The wells air turbine for wave energy conversion. Progress in Aerospace Sciences 31, 335–386. doi:http://dx.doi.org/10.1016/0376-0421(95)00001-F.

Richard, B., 2012. Carbon Trust UK wave enegy resource. Technical Report. AMEC Environment & Infrastructure UK Limited.

Salter, S.H., 1974. Wave power. Nature 249, 720–724.

Sarmento, A., 1992. Wave flume experiments on two-dimensional oscillating water column wave energy devices. Experiments in fluids 12, 286–292.

Sarmento, A.J.N.A., Falcao, A.F.D., 1985. Wave generation by an oscillating surface-pressure and its application in wave-energy extraction. Journal of Fluid Mechanics 150, 467–485. doi:Doi10.1017/S0022112085000234.

Sarpkaya, T., Isaacson, M., 1981. Mechanics of wave forces on offshore structures. Van Nostrand Reinhold Company.

Satish, S., Prithiviraj, M., Hari, S., . Optimization of under-relaxation factors and courant numbers for the simulation of sloshing in the oil pan of an automobile. URL: http://www.cd-adapco.co.kr/sites/default/files/technical_document/pdf/Swathi%20Satish_NITKarnataka.pdf.

Sensirion, 2014. Sdp1000 / sdp2000 low range differential pressure sensor for air and non-aggressive gases .

Sheng, W., Alcorn, R., Lewis, T.A.A.B.I.A.B.A.A.A.A.I.A.A.A.A.A.B.A.M.B.A.A., 2014. Physical modelling of wave energy converters. Ocean Engineering 84, 29–36.

Sheng, W., Lewis, A., Alcorn, R., 2012. On wave energy extraction of oscillating water column device, in: 4th International Conference on Ocean Energy.

Sheng, W., Thiebaut, F., Babuchon, M., Brooks, J., Lewis, A., Alcorn, R., 2013. Investigation to air compressibility of oscillating water column wave energy converters, in: ASME 2013 32nd International Conference on Ocean,

Offshore and Arctic Engineering, American Society of Mechanical Engineers. pp. V008T09A005–V008T09A005.

Stoker, J., 1957. Water waves. Interscience, New York .

Sykes, R.K., Lewis, A.W., Thomas, G., 2008. A numerical and physical comparison of a geometrically simple fixed and floating oscillating water column, in: ASME 2008 27th International Conference on Offshore Mechanics and Arctic Engineering, American Society of Mechanical Engineers. pp. 659–668.

power technologies, O., 2014. Ocean power technologies. URL: http://www.oceanpowertechnologies.com/.

TETHYS, 2012. URL: http://mhk.pnnl.gov/wiki/index.php/Mutriku_Wave_Power_Plant.

Thorpe, T.W., 1999. A brief review of wave energy. Harwell Laboratory, Energy Technology Support Unit London, UK.

Twidell, J., Weir, A.D., 2006. Renewable energy resources. Taylor & Francis.

Versteeg, H.K., Malalasekera, W., 2007. An introduction to computational fluid dynamics: the finite volume method. Pearson Education.

Wacławczyk, T., Koronowicz, T., 2008. Comparison of cicsam and hric high-resolution schemes for interface capturing. Journal of theoretical and applied mechanics 46, 325–345.

Wang, D.J., Katory, M., Li, Y.S., 2002. Analytical and experimental investigation on the hydrodynamic performance of onshore wave-power devices. Ocean Engineering 29, 871–885. doi:http://dx.doi.org/10.1016/S0029-8018(01)00058-0.

Washio, Y., Osawa, H., Nagata, Y., Fujii, F., Furuyama, H., Fujita, T., 2000. The offshore floating type wave power device 'mighty whale'open sea tests, in: Proceedings of the 10th international offshore and polar engineering conference, pp. 373–380.

Whittaker, T., McIwaine, S., Raghunathan, S., 1993. A review of the islay shoreline wave power station, in: Proceedings of (First) European Wave Energy Symposium, pp. 283–6.

Whittaker, T., Stewart, T., 1993. An experimental study of nearshore and shoreline oscillating water columns with harbours, in: European Wave Energy Symposium, pp. 21–24.

Zaoui, L., Bouali, B., Larbi, S., Benchatti, A., 2014. Performance analysis of a 3d axisymmetric oscillating water column. Energy Procedia 50, 246–254. doi:http://dx.doi.org/10.1016/j.egypro.2014.06.030.

Zhang, Y., Zou, Q.P., Greaves, D., 2012. Air–water two-phase flow modelling of hydrodynamic performance of an oscillating water column device. Renewable Energy 41, 159–170. doi:http://dx.doi.org/10.1016/j.renene.2011.10.011.

Abbreviations

BBDB	Backward Bent Duct Buoy
CFD	Computational Fluid Dynamics
DAQ	Data Aquasition
DMF	Dynamic Magnification Factor
EFD	Experimental Fluid Dynamics
FIR	Finite Impluse Response
FSCOWC	Fixed Symmetrical Cylinerdical OWC
MOWC	Multi OWC
NVD	Normalized Variable Diagram
NWT	Numerical Wave Tank
OWC	Oscillating Water Column
PCD	Pitch Circle Diameter
PTO	Power Take Off
RANS	Reynolds Average Narvier Stokes
WEC	Wave Energy Converter
MG	MegaWatts
ITTC	International Towing Tank Coference
RAO	Response Amplitude Operator
SEE	Standard Error Estimator
HRIC	High Resolution Interface Capturing
UD	Upwind scheme
DDS	Downwind Differential Scheme
AF	Angle Factor
URF	Under Relaxation Factor

Nomenclature

A_w	water plane area (m^2)
a	wave amplitude (m)
c_i	sensitivity coefficient
C_u	Courant number
Cf	capture factor
Cm	added mass coefficient
D	diameter (m)
d	draft (m)
FS_{in}	internal free surface
FS_{out}	external free surface
g	gravity acceleration ($9.81 m/s^2$)
h	water depth (m)
k	wave number
k	coverage factor (In chapter 4 where uncertainty is discussed)
l	capture width (m)
M	mode of sloshing equals (0,1,2,3.....)
p	time independent pressure (pa)
$P(t)$	time dependent pressure (pa)
P_w	incident wave power (watts)
P_a	atmosphere pressure (pa)
$Q(t)$	time dependent volume flux (m^3/s)
$q(t)$	time independent volume flux (m^3/s)
R	universal gas constant
$r(x_i, x_j)$	correlation coefficient between x_i and x_j
$S^2(y_k)$	variance of observation
T	wave period (s)
U	expanded uncertainty
u	standard uncertainty (In chapter 4 where uncertainty is discussed)
u, v, w	velocity in x,y,z direction, respectively (m/s)

u_c	combined uncertainty
V_g	wave group velocity (m/s)
W	mean power $(watts)$
w_T	tank width (m)
Y	measurand
$y^{`bar}$	arithmetic mean of y
η	free surface elevation (m)
ω	cicular wave frequency $(radians/s)$
ω_n	natural frequency in radians $(radians/s)$
ϕ	time independent velocity potential
$\Phi(x, y, z, t)$	velocity potential
ϕ^R	radiation potential
ϕ^s	scattering potential
Φ_n	normal component of velocity potential
ρ	density (kg/m^3)
$\wedge$	PTO constant
ζ	damping coefficient

Appendix A

Pressure transducer calibration

To minimize the uncertainty in the pressure transducer, it is worthwhile to examine the calibration factor and how the uncertainty is quantified by the manufacturer. As shown in Figure A1, the black curve line is the actual input-output curve of a pressure transducer. The calibration factor is defined as the slope of the best linear fit. The linearity of the pressure transducer is the maximum deviation from the actual output and the fitted straight line. The linearity is the most significant source of uncertainty. Due to the reason that the maximum deviation may not happen at the measurement range, the maximum deviation calculated for the full scale range may over predict the deviation for the actual measurement range. This might be the case for current study since the full scale of the pressure transducer is $\pm 692pa$ while the maximum pressure measured during the tests was about $110pa$. Therefore, recalibrating the transducer in the measurement range may help to reduce the maximum deviation between the actual output and the fitted line, and thus reduce the uncertainty.

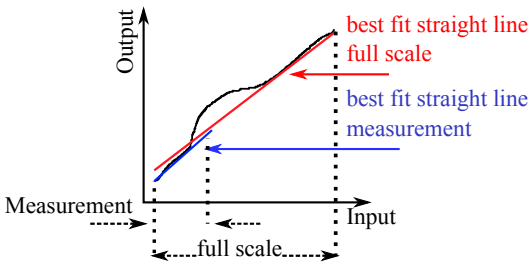

Figure A1: Pressure transducer calibration.

The calibration of the pressure transducer was achieved by connecting the transducer and an accurate digital pressure transducer to an sealed tube at the same time as shown in Figure A2. The tube is open to water at the other end

and it was partially submerged in water. It was clamped to a beam so that it can hold its position. It is not necessarily required to be perpendicular to the water surface as long as the tube does not move during the calibration.

During the calibration, water was adding into the container (loading condition) so that a pressure difference was created inside the tube. Water was taking out of the container to create pressure difference as well in order to produce the off-loading condition. By considering the loading and off-loading condition, the uncertainty introduced by the hysteresis effect can also be included in the calibration.

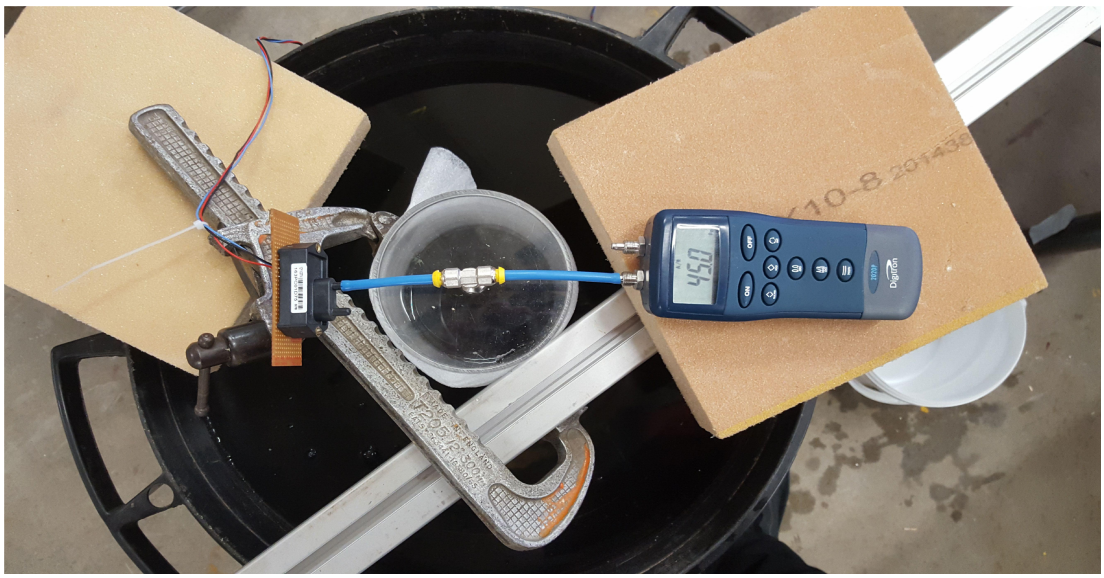

Figure A2: Pressure transducer calibration.

The comparison between the pressure measured by the digital pressure sensor and the pressure measured by the pressure transducer is shown in Figure A3.

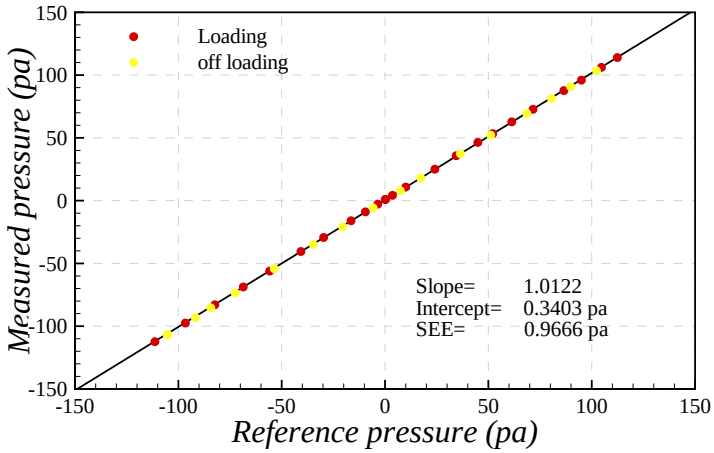

Figure A3: Comparison between the pressure measured by the digital pressure sensor and the pressure transducer, where the pressure transducer used the manufacture specified calibration factor.

As suggested by the SEE, the standard uncertainty in the linear fit is about 0.97 *pa* giving 2.9 *pa* at 95% level of confidence. The uncertainty lies in the digital pressure sensor at 95% level of confidence is about 2.71*pa*. Therefore the total uncertainty in the pressure transducer is about 4.0*pa* which is about 1/3 of the uncertainty specified by the manufacture.

It can be deduced from the slope that there was linear difference between the pressure measured by two different pressure sensors. This become more evident when looking at the residuals as shown in Figure A4. The residuals increased nearly linearly when the pressure changes. This suggests that the calibration factor may be not good enough. Therefore, a new calibration factor was calculated and results are shown in Figure A5. As can be seen, the SEE calculated from the new calibration factor is only 0.348*pa* yielding 1.044*pa* at 95% level of confidence.

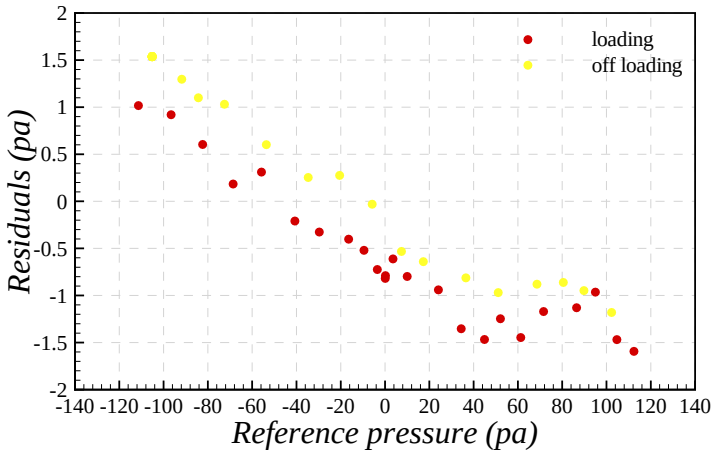

Figure A4: Residuals between the pressure measured by the digital pressure sensor and the pressure transducer.

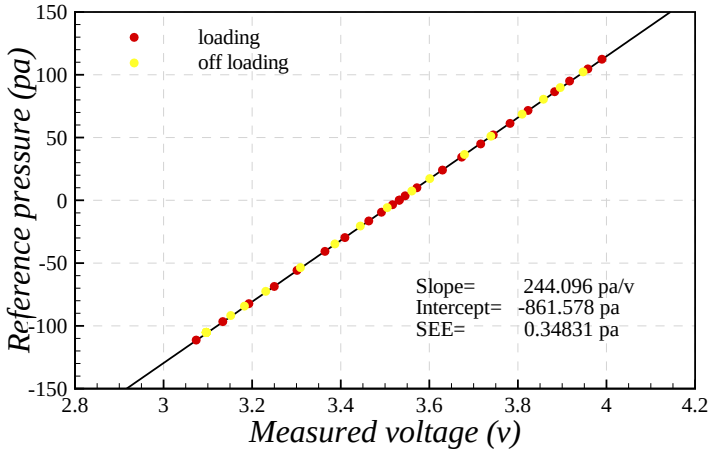

Figure A5: New calibration for the measurement range.

The residuals shown in Figure A6 exhibits no linear dependency on the pressure with the new calibration factor. All the residuals are within the uncertainty region.

From the residuals plot, the pressure transducer exhibits an obvious hysteresis effect between loading and off loading and the hysteresis effect was taken into account when calculate the uncertainty.

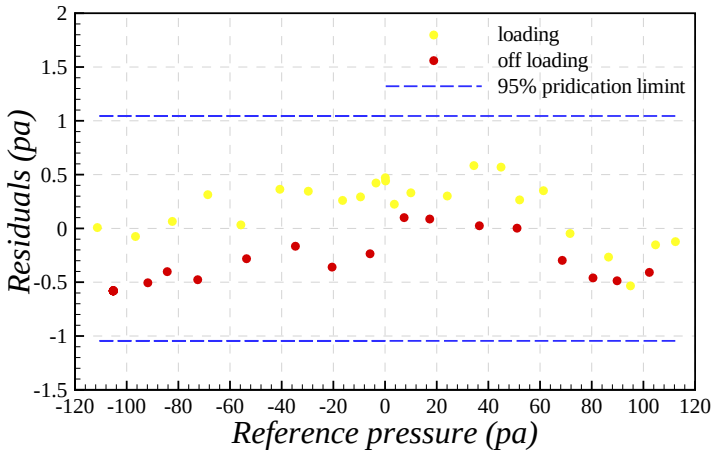

Figure A6: Residuals for the new calibration, where the 95% prediction limit is calculated based on linear regression theory.

Combining the uncertainty in the digital pressure sensor, the total uncertainty in the pressure transducer at 95% level of confidence is only $2.094pa$ which is about quarter of the uncertainty specified by the manufacture.

Since the calibration was carried out after the test and the manufacture specified calibration factor was used during the test, correction to the pressure measured was made. This is simply done by converting the measured pressure signal to a voltage signal and apply the new calibration factor to the voltage signal.

Appendix B

Determination of hydrodynamic coefficients

As explained previously, frequency independent empirical hydrodynamic coefficients will fail to tell any difference between the moderate scale and small scale experiment due to the reason that the frequency independent empirical hydrodynamic coefficients does not include the viscous effect. On the other hand, to obtain frequency dependant hydrodynamic coefficients experimentally, force oscillation test at different frequency is required which is difficult to perform especially for the open tube case. Therefore, in this study, equivalent frequency independent linear hydrodynamic coefficients that will lead to similar results are investigated. The equivalent frequency independent linear hydrodynamic coefficients are obtained by using the Dynamic Magnification factor (DMF).

The DMF is defined as the ratio of the dynamic system response amplitude to the equivalent static response Day.A.H. (1987). The expression of the DMF is given by Equation B1

$$DMF = \frac{1}{\sqrt{(1-\gamma^2)^2 + (2\varsigma\gamma)^2}} \tag{B1}$$

where, the γ is the the frequency ratio defined as the ratio between the response frequency ω and the undamped natural frequency ω_n while the ς is the damping ratio defined as the ratio between the damping B and the critical damping $B_c = 2m\omega_n = 2\sqrt{(mk_s)}$. The k_s is simply the stiffness of the system.

Figure B1 illustrate the typical DMF under different damping ratio, which tends

to 1 at low frequency and approach 0 at high frequency.

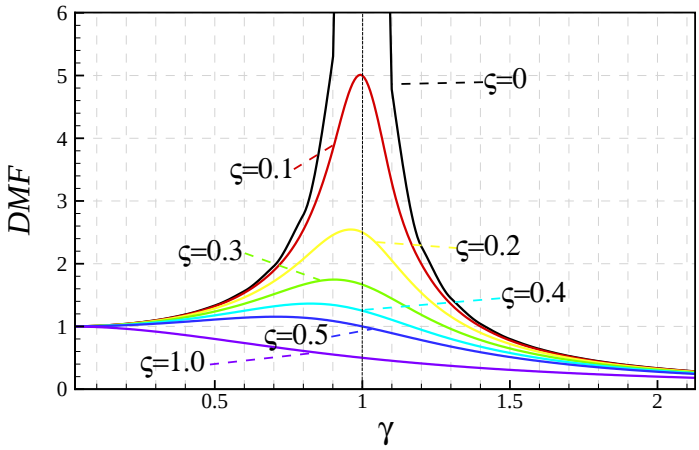

Figure B1: Illustration of DMF under different damping ratio.

The analytical expression, DMF can also be calculated directly from the dynamic response (in this case, the response of the OWC). Assuming the OWC is a single mass-spring-damper problem and the one degree freedom motion of the OWC in heave direction can be modelled by Equation B2

$$m\ddot{z} + B\dot{z} + k_s z = F \tag{B2}$$

where the m and F are the mass, and the total force acting on the OWC. The z is the displacement of the OWC and $\ddot{z}$ and $\dot{z}$ stands for the acceleration and velocity, respectively. It should be noted here, the B in the equation does not include the hydrodynamic damping induced by radiation. It is all the other damping exclude the radiation damping, for instance, the viscous damping.

It is well know that for a floating body experience a wave, the total force acting on the body can be expressed by

$$F = F_I + F_D + F_R \tag{B3}$$

where F_I, F_D and F_R are the incident wave force , the diffraction force and the radiation force, respectively.

In current study, the diffraction parameter (D/λ) is always smaller than 0.2 and thus the diffraction force is negligible (Sarpkaya and Isaacson, 1981). The radiation force is usually decomposed into a function of added mass m_a and

radiation damping coefficient B_R as

$$F_R = -m_a\ddot{z} - B_R\dot{z} \tag{B4}$$

Substitute Equation B3 and B4 into Equation B2 we have

$$(m + m_a)\ddot{z} + (B)\dot{z} + k_s z = F \tag{B5}$$

Note here, the F is eventually equals to F_I due to the F_D is negligible. To let the damping coefficient account for the total damping that the system is experienced, the B_R is combined with the other damping and the B in the Equation B5 stands for the total damping coefficient hereafter.

Due to the appearance of the added mass, the undamped natural frequency is now calculated by

$$\omega_n = \sqrt{\frac{k_s}{m + m_a}} \tag{B6}$$

where the $k_s = \rho g A_w$.

Defining the added mass coefficient C_m to be the ratio between the actual mass and added mass, the nature frequency can be rewritten as

$$\omega_n = \sqrt{\frac{g}{d(1 + c_m)}} \tag{B7}$$

According to linear wave theory, the incident wave force is actually the dynamic pressure integrated over the body and can be write in the form

$$F = F_0 cos(\omega t) \tag{B8}$$

where the F_0 is the incident wave force amplitude and can be calculated by integrating the dynamic pressure over the wetted body surface s as

$$F_0 = \int_S \rho g a \frac{cosh(k(h + T))}{cosh(kh)} ds \tag{B9}$$

The T in the equation is the vertical position of the body at where the pressure is calculated.

Assuming the particular response is harmonic and have the form of

$$z = Z_0 cos(\omega t + \phi) \tag{B10}$$

where the Z_0 is the harmonic response amplitude and the ϕ is the phase.

Substitute Equation B9 and B10 into B5 leads to an expression for the Z_0 as

$$Z_0 = \frac{F_0}{\sqrt{(k_s - (m + m_a)\omega^2)^2 + (B^2\omega^2)}} \tag{B11}$$

Equation B11 can be expressed in the following form by replacing the ω and B by γ and ς

$$Z_0 = \frac{F_0}{k_s} \frac{1}{\sqrt{(1 - \gamma^2)^2 + (2\varsigma\gamma)^2}} \tag{B12}$$

Clearly, the second fraction term of the Equation B5 is the DMF. Recall the definition of the RAO which is simply the response amplitude divided by the incident wave amplitude a. Therefore, the RAO can be converted to DMF by

$$DMF = RAO \frac{k_s a}{F_0} \tag{B13}$$

The damping ratio and added mass coefficient can then be determined by comparing the theoretical DMF calculated by Equation B1 with the actual DMF obtained by Equation B13 through an iterative procedures: an initial guess was made to the damping ratio and added mass coefficient and then optimised by using a Generalized Reduction Gradient Algorithm so that the difference between the actual DMF and the theoretical DMF is a minima.

The comparison of the DMF calculated from the experiment and the fitted DMF are shown from Figure B2 to for different conditions. It can be seen that that the fitted DMF agrees with the actual DMF well. The discrepancy between the fitted and actual DMF is caused by the fact that the damping and added mass is in fact frequency dependent while DMF treated the added mass and damping as a frequency independent quantities.

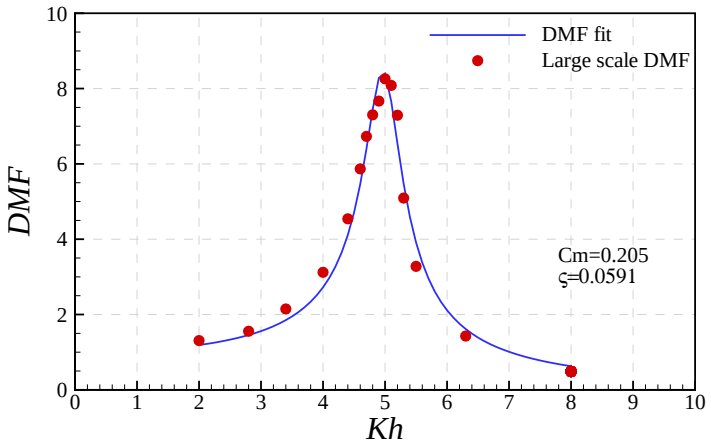

Figure B2: Comparison between the actual DMF and the fitted DMF for the moderate scale open tube case.

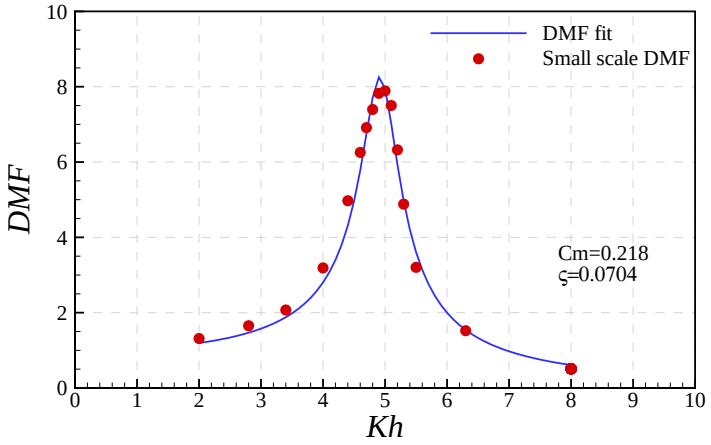

Figure B3: Comparison between the actual DMF and the fitted DMF for the small scale open tube case.

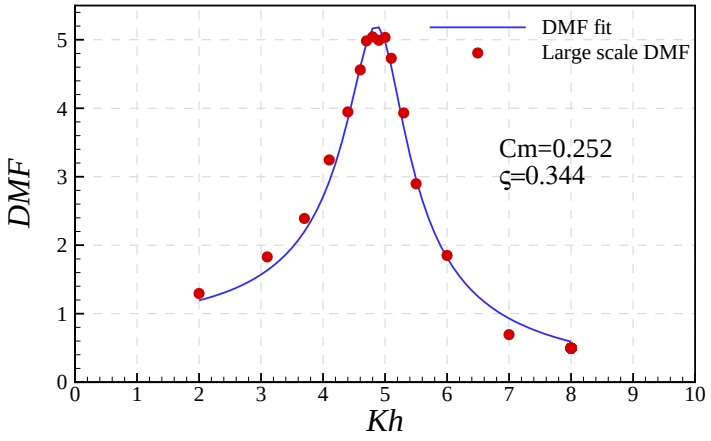

Figure B4: Comparison between the actual DMF and the fitted DMF for the lareg scale four orifices case.

The difference between the actual and fitted DMF for the for orifice case is caused by the reason that for the one orifice case, the damping become strongly non-linear

and hence linear fit does not provide a good result. This can be proved by the free decay test for different conditions.

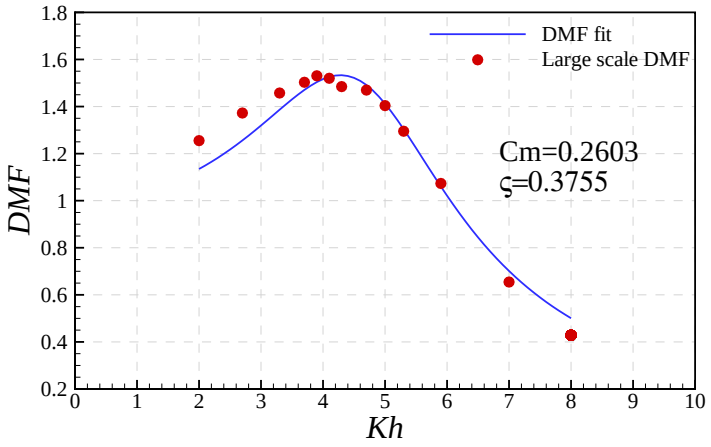

Figure B5: Comparison between the actual DMF and the fitted DMF for the moderate scale one orifice case.

As can be seen from Figure B6 and B7, free decay of the open tube and four orifices case match the linear damping fit well. On the other hand, the one orifice case (Figure B8) match the non-linear fit better than linear fit.

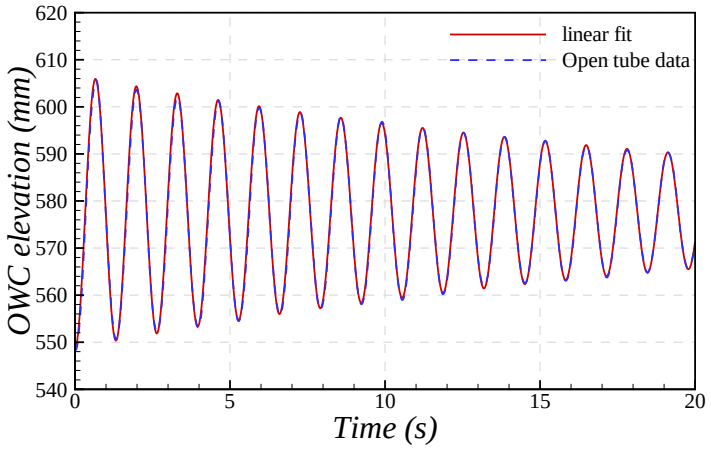

Figure B6: Comparison between the experiment free decay test and linear fitted free decay for open tube case.

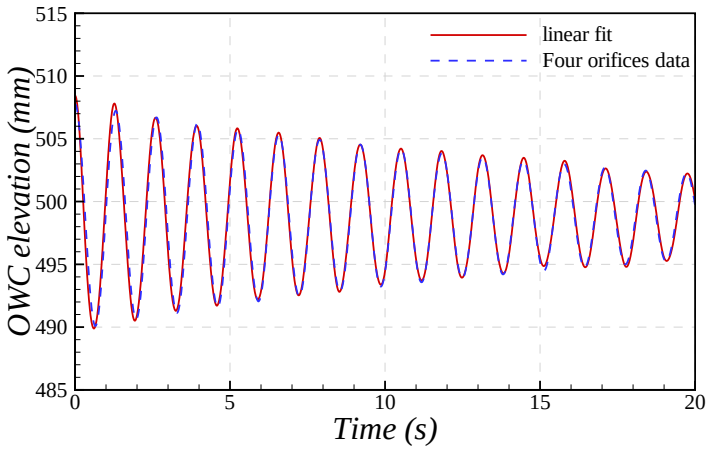

Figure B7: Comparison between the experiment free decay test and linear fitted free decay for open tube case.

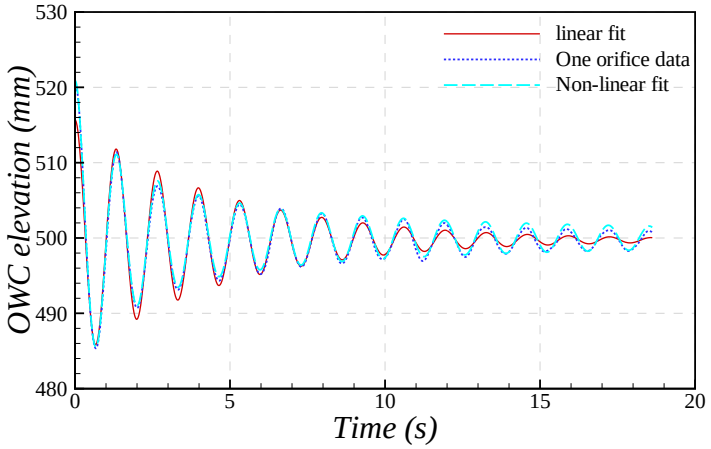

Figure B8: Comparison between the experiment free decay test and fitted free decay for open tube case.

DMF fit of the RANS simulations of the large and small scale open tube cases are illustrated below.

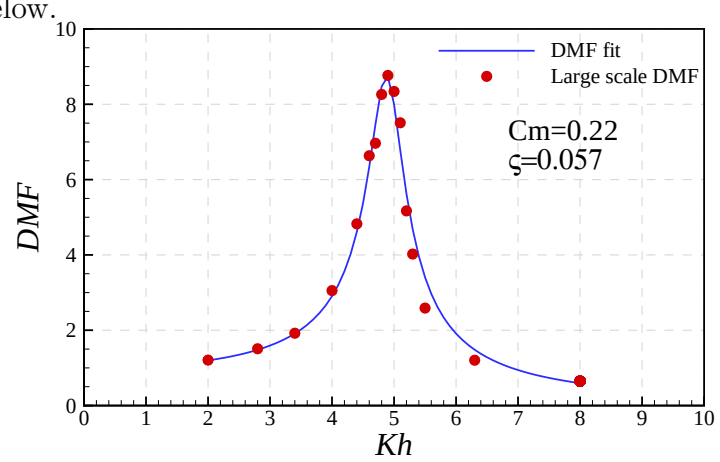

Figure B9: Comparison between the calculated DMF and fitted DMF for RANS simulation of the moderate scale open tube case.

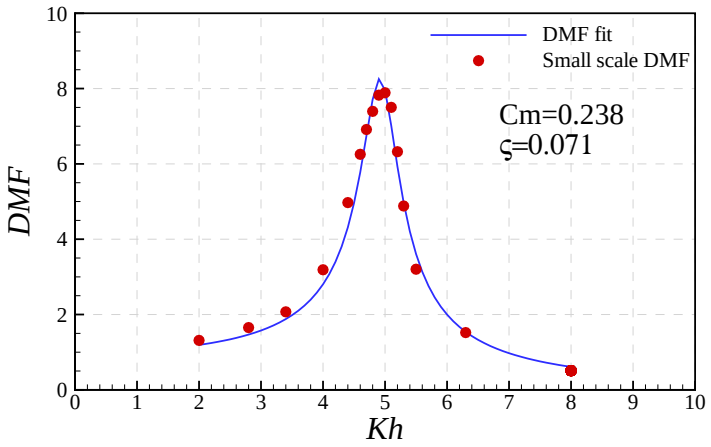

Figure B10: Comparison between the calculated DMF and fitted DMF for RANS simulation of the small scale open tube case.

DMF fit of the RANS simulations of the moderate scale four and one orifice cases are illustrated below.

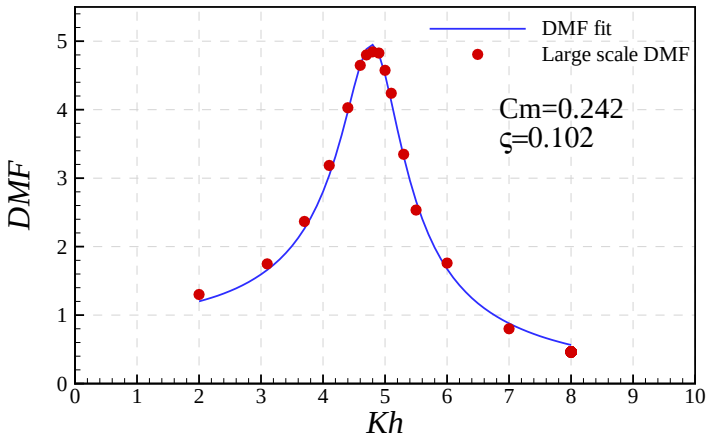

Figure B11: Comparison between the calculated DMF and fitted DMF for RANS simulation of the moderate scale four orifices case.

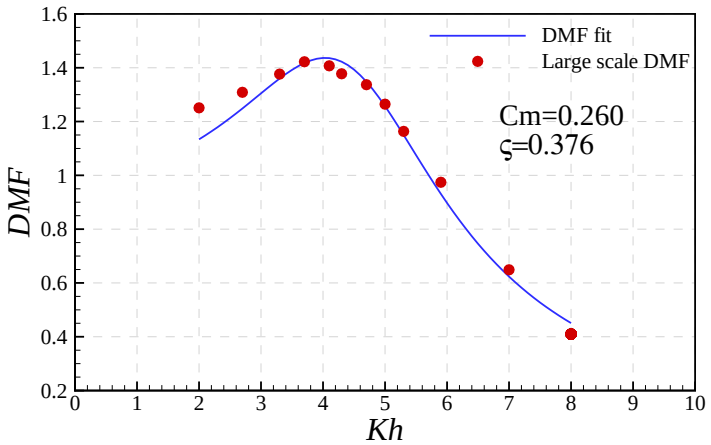

Figure B12: Comparison between the calculated DMF and fitted DMF for RANS simulation of the moderate scale one orifice case.

Appendix C

Further results for tank width effect

Further results for the tank width effect are presented in this appendix. Tank testing DMF plot against tank width ratio for the four orifices case are illustrated below.

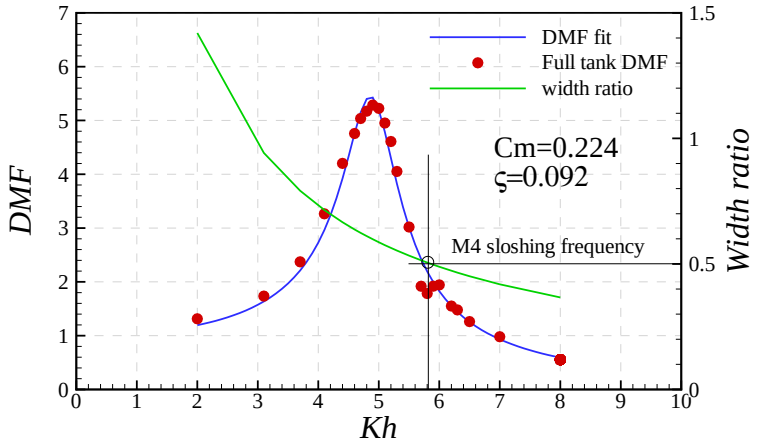

Figure C1: DMF, fitted DMF and tank width ratio for tank testing of four orifices case at full tank width.

As can be seen, the spike like phenomenon happened at the same frequency as those of the open tube case.

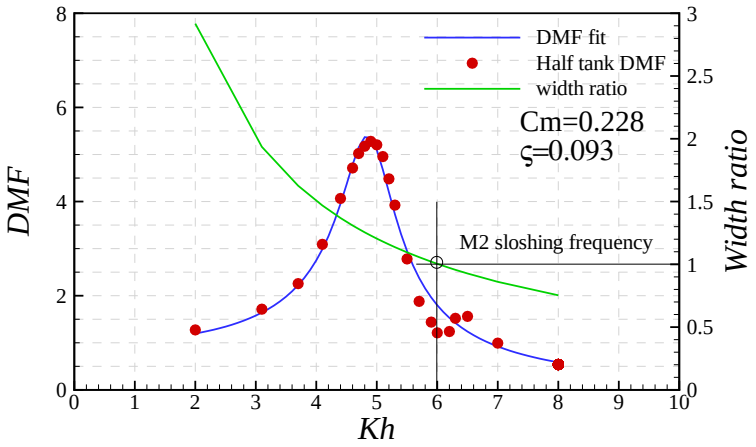

Figure C2: DMF, fitted DMF and tank width ratio for tank testing of four orifices case at half tank width.

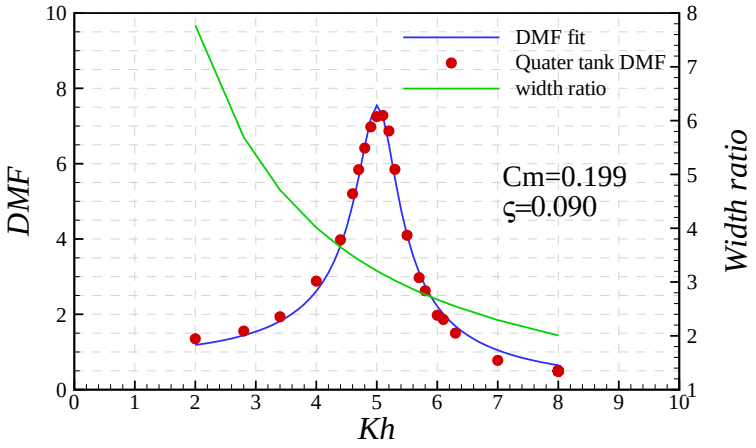

Figure C3: DMF, fitted DMF and tank width ratio for tank testing of four orifices case at quarter tank width.

Similarly, the results for the RANS simulation are illustrated below.

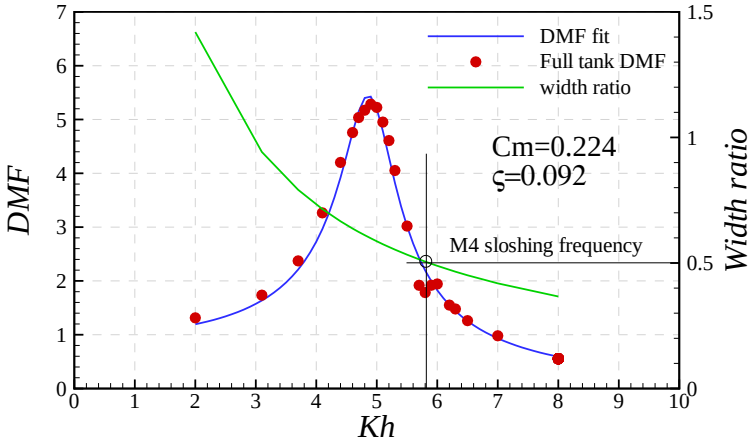

Figure C4: DMF, fitted DMF and tank width ratio for RANS simulation of four orifices case at full tank width.

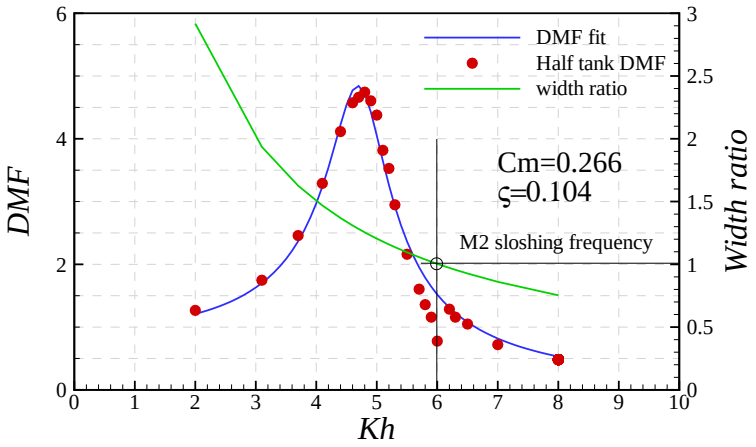

Figure C5: DMF, fitted DMF and tank width ratio for RANS simulation of four orifices case at half tank width.

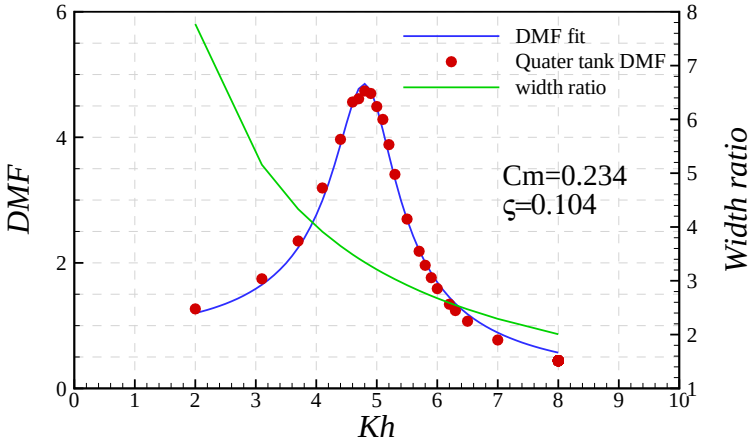

Figure C6: DMF, fitted DMF and tank width ratio for RANS simulation of four orifices case at quarter tank width.

Both the RANS simulation and tank testing showed the same spike like phenomenon at the same incident wave frequency. As suggested by the peak response of the Open tube tank testing and RANS simulation, the nature frequency of the simulation and tank testing are different. However, the spike like phenomenon happened at the same incident frequency. This suggests that the spike like phenomenon will take place regardless of the device.

Appendix D

RANS simulation uncertainty

The calculation of the Uncertainty in the power captured is based on the procedure for estimation due to discretization in CFD application given by Celik et al. (2008). It can be summarized in following steps

The first step is to define a representative cell, mesh or grid size h_{size}. For instance, for two-dimensional simulation the h_{size} can be calculated by

$$h_{size} = [\frac{1}{N}\sum_{i=1}^{N}(\delta A_i)]^{1/2}] \tag{D1}$$

For three-dimensional case it can be calculated by

$$h_{size} = [\frac{1}{N}\sum_{i=1}^{N}(\delta V_i)]^{1/3}] \tag{D2}$$

whereδA_i and δV_i are the area or volume for the i^{th} cell.

In current test, the mesh was refined based on a base size that controls the mesh size globally. The topology of the mesh in the whole domain was kept the same, only the base size was changed to achieve different mesh density. The h_{size} was hence chosen to be cubic base size to stand for the volume of each cell.

The next step is to run three simulations based on significantly different set of grids to obtain the variables of interest. The refinement factor r defined to be the ratio between the different h_{size} is recommended to be larger than 1.3 based on experience. The base size was refined by a factor of $\sqrt{2}$, hence the h_{size} was refined by a factor of $sqrt(2)$.

Calculate $r_{21} = h_{size2}/h_{size1}$,$r_{32} = h_{size3}/h_{size2}$, where h_{size1},h_{size2} and h_{size3}

denotes the representative cell size for the fine, medium and coarse mesh, respectively. After that calculate the difference ϵ between each variable Φ obtained by different meshes, let $\epsilon_{21} = \Phi_2 - \Phi_1$ and $\epsilon_{32} = \Phi_3 - \Phi_2$, where Φ_1,Φ_2 and Φ_3 denotes the variable obtained from the fine, medium and coarse mesh, respectively.

Based on above information, the apparent order p_a can be calculated via

$$p_a = \frac{1}{Ln(r_{21})} |Ln(|\epsilon_{32}/\epsilon_{21}|) + q(p_a)| \tag{D3}$$

$$q(p_a) = Ln\left(\frac{r_{21}^{p_a} - sign}{r_{32}^{p_a} - sign}\right) \tag{D4}$$

$$sign = sgn(\epsilon_{32}/\epsilon_{21}) \tag{D5}$$

For $r_21 = r_32$, $q(p_a) = 0$. Otherwise, the p_a can be obtained by iteration method.

Step four will be calculate the extrapolated value by

$$\Phi_{ext}^{21} = \frac{r_{21}^{p_a}\Phi_{21} - \Phi_2}{r_{21}^{p_a} - 1} \tag{D6}$$

Finally, the approximate relative error, the relative error and the fine-grid GCI can be calculated by Equation D7,D8 and D9, respectively.

$$e_a^{21} = |\frac{\Phi_1 - \Phi_2}{\Phi_1}| \tag{D7}$$

$$e_{ext}^{21} = |\frac{\Phi_{ext}^{21} - \Phi_1}{\Phi_{ext}^{21}}| \tag{D8}$$

$$GCI_{fine}^{21} = \frac{1.25e_a^{21}}{r_{21}^{p_a} - 1} \tag{D9}$$

Complete mesh dependency test result can be found in Table D.1.

Table D.1: Mesh dependency test

Item	$\Phi = OWCelevation$	$\Phi = pressureamplitude$	$\Phi = meanpowercaptured$
$r_2 1$	$sqrt(2)$	$sqrt(2)$	$sqrt(2)$
$r_3 2$	$sqrt(2)$	$sqrt(2)$	$sqrt(2)$
Φ_1	0.090	62.119	0.877
Φ_2	0.088	60.118	0.847
Φ_3	0.088	59.809	0.788
p_a	1.659	1.798	2.038
Φ_{ext}^{21}	0.091	62.485	0.906
e_a^{21}	1.5%	3.2%	3.4%
e_{ext}^{21}	2.4%	0.73%	4.1%

Appendix E

Simulation of the orifice plate

The unsteady state time domain simulation of the orifice plate requires a huge amount of computation resource which is not suitable for large number of simulations. Therefore, the simulation of the orifice plate was carried out in steady state.

The domain and boundary conditions are illustrated in Figure E1. The volume of air inside the chamber was kept the same as the simulation of the wave-structure interaction case. Ideal gas law was used to solve the compressibility of the air for compressible case while the incompressible simulation was carried out with constant density model.

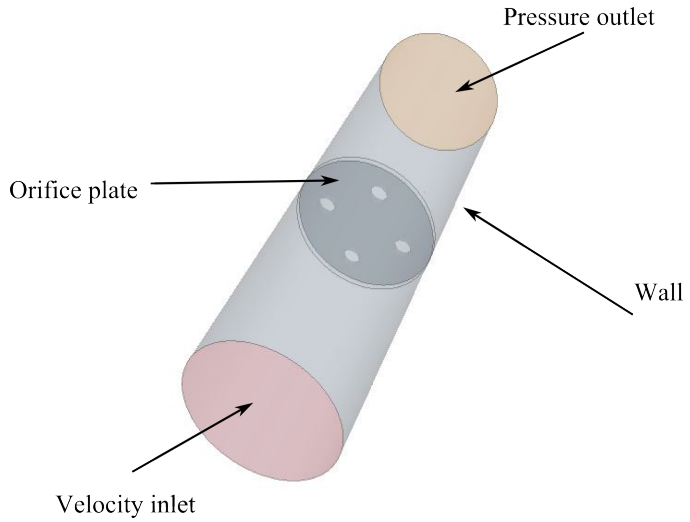

Figure E1: Boundary conditions of the orifice plate simulation.

1000 iterations were used for each simulation to make sure the result is converged. The convergence of the simulation is illustrated in Figure E2 for the compressible

case at velocity equals to $0.02m/s$. As can be seen the results do converged.

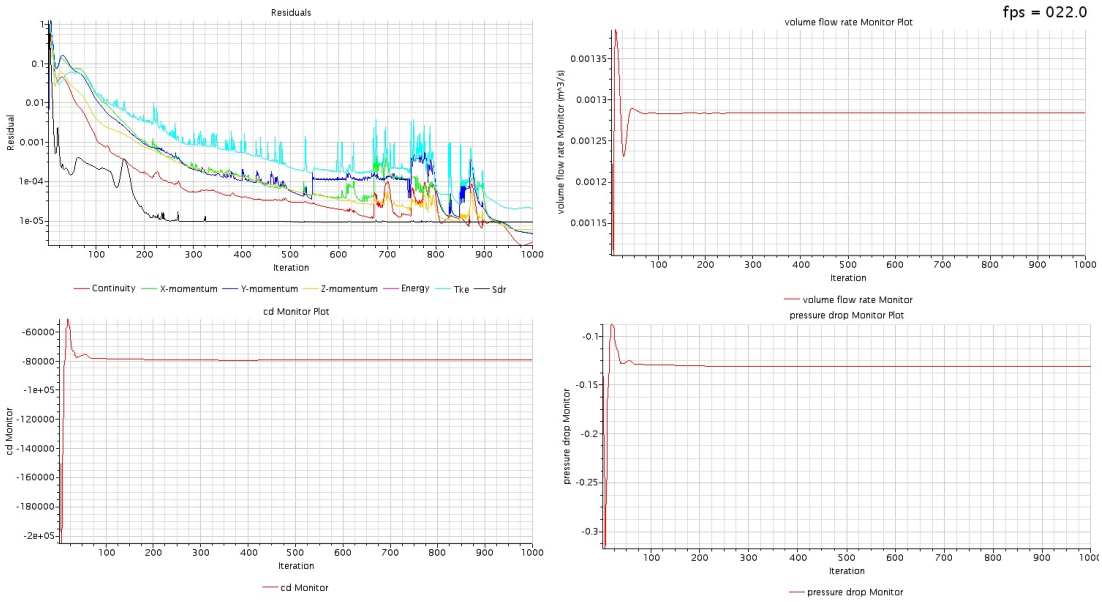

Figure E2: Illustration of the convergence of the simulation for velocity equals to $0.02m/s$.

The velocity contour and streamline was shown in Figure E3. The pressure and density contour for velocity equals to $0.02m/s$ is shown in Figure E4. Due to the small pressure, the change in the density is negligible. When the pressure increased, the density do changed as can be seen from Figure E5.

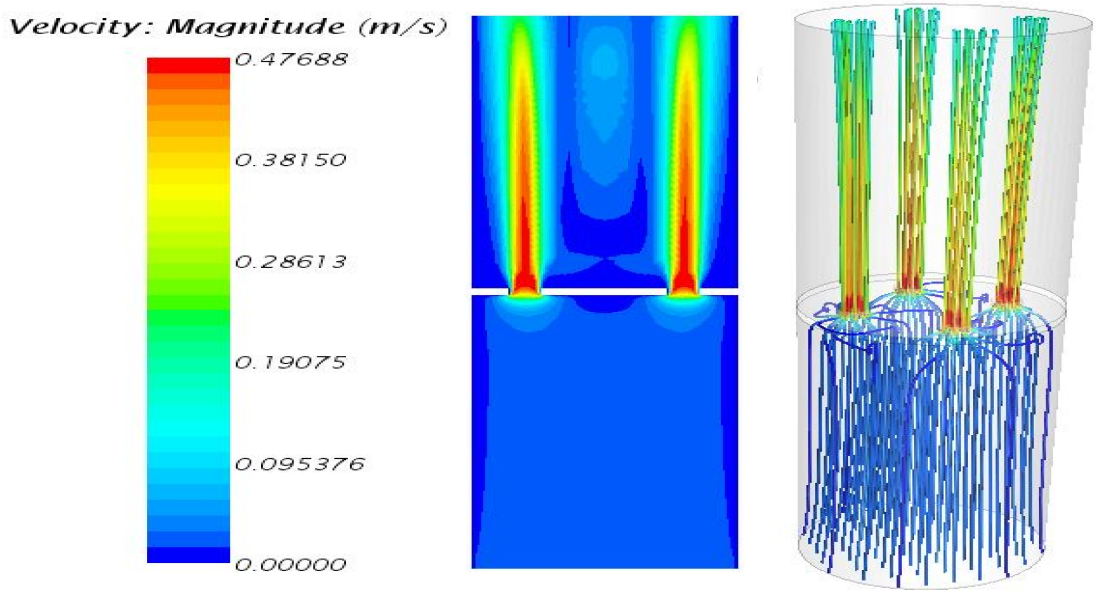

Figure E3: Velocity contour and streamline of compressible simulation at velocity equals to $0.02m/s$.

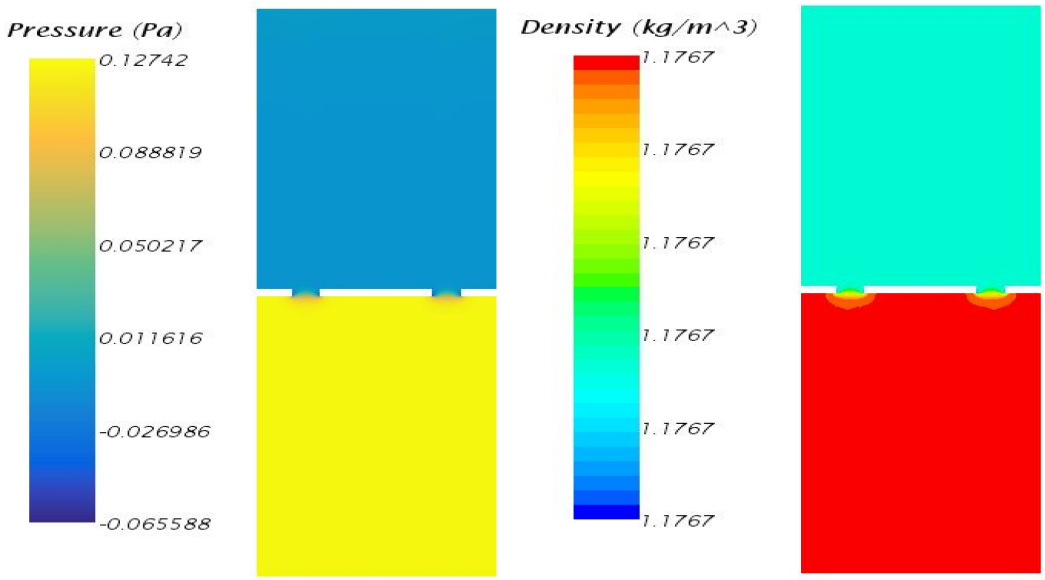

Figure E4: Pressure and density contour for compressible simulation at velocity equals to 0.02m/s.

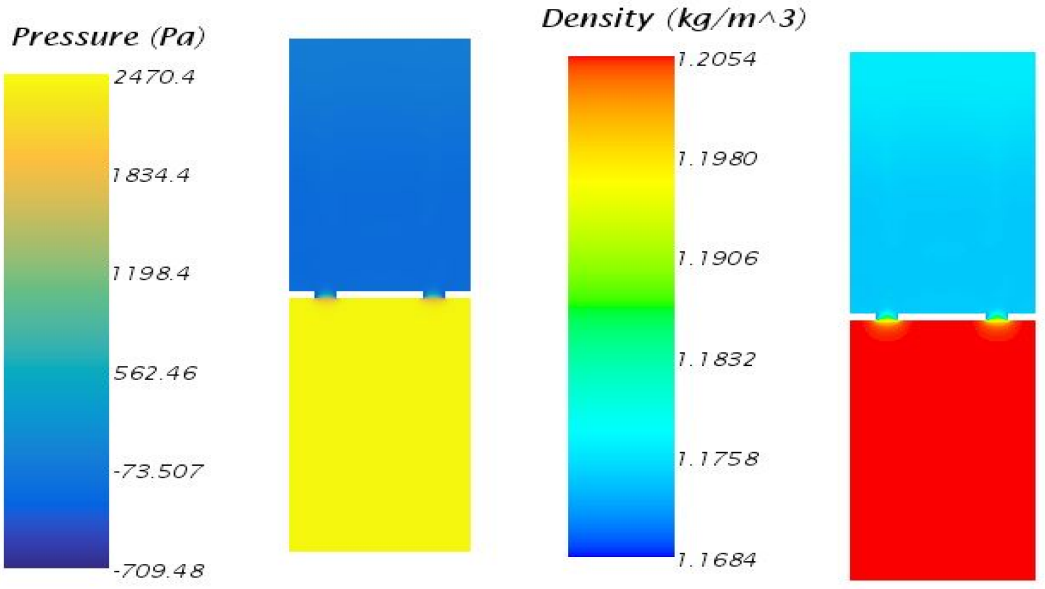

Figure E5: Pressure and density contour for compressible simulation at velocity equals to 2.5m/s.

Due to the simulation was carried out in steady state, the variation of the volume of the air inside the chamber due to motion of the OWC was not accounted.

Appendix F

Recommendation for tank testing

Design

1)When design the tank testing model, the size of the tank should be take into account as well. It is suggested to design the model in such a way so that the effect of scale and tank width effect will be minimized.

2)Design the wave amplitude based on the accuracy limit of the wave probe so that the uncertainty in the measurement of the incident wave amplitude is a minima. Typically, less than 3%.

3)Select proper instruments so that the full scale of the instrument is close to the range of the measurement in the tests.

Calibration

1) Calibrate all the instruments and calculate the uncertainty in the instruments. Ideally, the calibration should cover the range of measurement in the tests. At least 20 approximately equal spaced points should be included in the calibration. At least 100 sampled data should be taken for each data to minimize sampling effect.

Calibration of pressure transducer or load cells need to be done in both direction to identify whether the instruments have a hysteresis character. If so, the calculation of the uncertainty should include the hysteresis.

If the uncertainty in the instruments at full scale is too large compared with the measurement, non-linear calibration should be carried out. Alternatively, if the full scale of the instruments is far larger than that of the range of the measurement, a selected range of the instrument can be used instead of the full scale, for instance, the pressure transducer used in current study for the large scale test.

2) The wave at any frequency that is going to be tested should be calibrated at where the model is going to be allocated prior to any formal test to minimize the tank spatial variation effect on estimating the incident wave power. Another reference wave probe should be placed some where between the calibration point and the wave maker for referencing.

Installation

1) Normally, the uncertainty in the draft of ships and other floating structures (hence, the displacement and mass of the structure) are usually not a problem since the draft can be secured by the displacement. Current FSCOWC device's draft is determined purely by sight, hence care must be paid on aligning the draft line to the water surface. Instrument's aid is preferred is possible. For instance, the draft of the current device could have be determined by utilizing the ultrasonic wave probe. First mount the ultrasonic wave probe at somewhere above the draft line and put the device on a flat surface vertically, take the measurement from the flat surface to the wave probe. Then put the device into water and take the measurement from the water surface to the wave probe. Adjust the submergence of the device so that the difference between two measurement equals to the draft.

2) If resistance type wave probe is used to measure the OWC elevation, the probe should be placed away from the inner wall of the device to avoid the change of the performance of the wave probe due to appearance of a solid object.

3) The location of the device shall be in the middle of the tank in tank width direction. The location in the tank length direction should be optimised in such a way so that sufficient data would be obtained before reflection from the beach and the wave maker.

During the tests

1) The wave information obtained by the reference wave probe mentioned in the wave calibration part should be compared with the wave information obtained during the calibration stage to make sure the calibration is still valid.

2) Repeat tests should be carried out to assess the repeatability the test at different time scale.

3) Care must be paid on the wave frequencies that's around the tank sloshing frequencies as discussed in the tank width effect experiment.

4) If resistance type wave probe is involved in the testing, the temperature of the water should be monitored. The resistance wave probe should be re-calibrated once the temperature changed half a degree.

Data processing and reporting

1) When applying filter to minimize the noise, it is recommend to use a filter frequency that is at least 10 times higher (when using low pass filter. 10 times lower when using high pass filter) than the main frequency of the data so that the real data will not be filtered.

2) Latency in the instruments should be identified and corrected since the phase difference between the quantities may affect the final result. For example, in current study the phase lag between the pressure and volume flow rate.

3) To minimize the sampling effect on the results, sufficient data should be selected for further processing. For example, in current study at least 10 periods of data (after the response is stable.) was selected for data processing.

4) To minimize the effect of the reflection from the end of the tank , the window of the data should be selected before the reflected wave from the end of the tank reached the device. This can be simply done by estimate the time that the reflection wave needs to reach the device (divide the distance from the device to the end of the tank by the group velocity of the wave.)and select the data before that time.

5) Calculate the uncertainty for each quantity that is interested.

6) When extrapolate the results to full scale open sea condition, care must be

paid on the tank blockage effect and scale effect. The width of the tank and scale must be reported along with the final results.

List of Figures

1.1 Renewable energy resources, where Photosynthesis stands for biomass. Figure is taken from Twidell and Weir (2006). 2
1.2 Global annual mean wave power density and mean best direction (shown as arrows). Figure is taken from Gunn and Stock-Williams (2012). 3

2.1 Classification of WECs proposed by Antonio (2010). 9
2.2 Pelamis wave power machine. Figure is taken from Drew et al. (2009). 9
2.3 Anaconda WEC. Figure is taken from (Anaconda, 2014). 10
2.4 Salter's Duck. Figure is taken from Drew et al. (2009). 10
2.5 Floating absorber, the OPT buoy. Figure is taken from Drew et al. (2009). 11
2.6 submerged pressure differential device: the Archimedes Wave Swing. Figure is taken from Drew et al. (2009). 12
2.7 Blowhole at Quobba Western Australia. Figure is taken from Heath (2012). 12
2.8 Shoreline OWC. Figure is taken from Poullikkas (2014). 13
2.9 Sparbuoy OWC (left); Mutriku power plant during a storm (right). Figure is taken from TETHYS (2012) 13
2.10 Whistling buoy. Figure is taken from Heath (2012). 15
2.11 Navigation buoy in Tokyo Bay. Figure is taken from Heath (2012). 15
2.12 Queen's University Belfast $75kW$ demonstrator on Islay. Figure is taken from Heath (2012). 16
2.13 Wavegen LIMPET OWC plant. Figure is taken from Heath (2012). 17
2.14 Backward Bent Duct Buoy (BBDB). Figure is taken from OffshoreWind.biz (2012). 17
2.15 Illustration of symmetrical and Asymmetrical OWC devices: (a) symmetrical device,(b) asymmetrical device. Where FS_{in} and FS_{out} is free surface inside and outside the chamber respectively . 19

2.16 Shoaling of a 10s energy period wave propagating orthogonal to depth contours for different seabed slopes. Figure is taken from Folley and Whittaker (2009). 23
2.17 Reinforced concrete Greenwave device under construction 24
2.18 Sketch of a combined wind and wave power system 25
2.19 Two different scale models used in Forestier's experiment. (1:15 left and 1:50 scale right.) Figure is taken from Forestier et al. (2007). 29
2.20 Kamath's reflection free numerical wave tank configuration. 31

3.1 Sketch of the proposed OWC device 35
3.2 Maximum capture factor for the proposed OWC device 39

4.1 The Kelvin Hydrodynamic Lab 42
4.2 The absorbing wave maker 42
4.3 FSOWC model fixed in the middle of the tank by a wooden rack . 43
4.4 Scale drawing of the designed moderate scale FSCOWC. 44
4.5 Wave probes: A)resistance type wave probe B)Ultra sonic wave probe 46
4.6 *Honeywell*® 163PC0D75 pressure sensor 47
4.7 data acquisition system: left) the power supplier, amplifier and data acquisition interface, right) Spike software collecting data. . . 48
4.8 Uncertainty Analysis flow chart 51
4.9 Wave probe calibration system 52
4.10 Connection between the FSCOWC device and instruments 54
4.11 Typical raw data obtained from tests (Four orifices case when $Kh = 5.1$). Where from top to bottom are the FSCOWC elevation measured by the ultrasonic wave probe, the pressure difference and the FSCOWC elevation measured by the resistance wave probe, respectively. Data in right hand side is an enlarge view for time equals to 70 seconds to 80 seconds. 55
4.12 Raw pressure and pressure with low pass filter 56
4.13 OWC elevation for four orifice when $Kh = 2$ and $Kh = 8$. 57
4.14 Comparison between the filtered and the fitted pressure 58
4.15 Calibration result of the ultrasonic wave probe 62
4.16 Residuals and 95% confidence predication limit for the ultrasonic wave probe calculated based on linear regression theory (dashed line) and calibration theory (solid line). where the small error bar is the uncertainty with 95% confidence in the reference scale . . . 63
4.17 Calibration of wave field 64

4.18 wave field repeatability of the KHL tank 64
4.19 Comparison between the wave amplitude measured by the wave probe located at the place the FSCOWC device will be and that measured by the wave probe located at the reference point. . . . 65
4.20 Response Amplitude Operator for open tube case calculated based on the data obtained by different wave probes where the error bars indicate the 95% uncertainty with vertical error representing the uncertainty in RAO and horizontal error bar indicating the uncertainty in Kh. 66
4.21 Comparison between the corrected RAO obtained by resistance wave probe and the RAO obtained by the ultrasonic wave probe . 67
4.22 RAO calculated based on the calibrated incident wave amplitude and based on the wave amplitude measured by the reference wave probe, where RAO (calibrated) denotes the RAO calculated based on the the wave amplitude measured by the reference probe during the test. 67
4.23 Incident wave amplitude measured by the reference wave probe during calibration and during testing. 68
4.24 Percentage difference of incident wave power estimation based on wave amplitude measured from calibration and wave amplitude from reference probe. 68
4.25 RAO of four orifice FSCOWC with uncertainty at 95% level of confidence expanded uncertainty. 69
4.26 Pressure of four orifice FSCOWC with 95% level of confidence expanded uncertainty. 69
4.27 Comparison between the power calculated in time domain (non-linear power) and frequency domain (linear power) 70
4.28 One typical period of instantaneous power for $Kh = 4.9$. The cyan area shows the power difference between the two different power calculated by different methods 70
4.29 Mean power captured of four orifice FSCOWC with 95% level of confidence expanded uncertainty 71
4.30 Absolute uncertainty in the captured power. 71
4.31 Relative uncertainty in the captured power, where the Y axis is in log scale and 1 equals to 100%. 71
4.32 Pressure amplitude for four orifices case with 95% uncertainty estimated based on new calibration. 72

4.33 Mean power captured of four orifice FSCOWC with 95% level of confidence expanded uncertaintycalculated based on new pressure amplitude. 73
4.34 Capture width of four orifice FSCOWC with 95% level of confidence expanded uncertaintycalculated based on new pressure amplitude. 73
4.35 Capture factor of four orifice FSCOWC with 95% level of confidence expanded uncertainty calculated based on new pressure amplitude. 73
4.36 Uncertainty distribution, where the red, blue and yellow bar denotes the uncertainty contribution of the uncertainty in the pressure amplitude, in the OWC elevation amplitude and in the cross-section area, respectively. 74
4.37 RAO of single orifice FSCOWC with 95% level of confidence expanded uncertainty. 74
4.38 Pressure of single orifice FSCOWC with uncertainty at 95% level of confidence. 75
4.39 Mean power of single orifice FSCOWC with uncertainty at 95% level of confidence. 75
4.40 Capture width of single orifice FSCOWC with uncertainty at 95% level of confidence. 76
4.41 Capture factor of four orifices and single orifice cases compared with the numerical 76
4.42 Capture factor of four orifices and single orifice cases compared with the numerical solution of the analytical modelling 77

5.1 Henry Dyer Hydrodynamic Lab 81
5.2 Configuration of the one third scaled FSCOWC experiment with two artificial walls 82
5.3 Testing of the temperature effect on the resistance wave probe . . 84
5.4 Comparison of the open tube RAO for the moderate scale and the one third scaled FSCOWC with 95% level of confidence 86
5.5 RAO with 95% level of confidence for full tank, half tank and quarter tank width 87
5.6 RAO for full tank, half tank and quarter tank width without uncertainty 88
5.7 DMF, fitted DMF and tank width ratio for open tube case at full tank width. 89
5.8 DMF, fitted DMF and tank width ratio for open tube case at half tank width. 89

5.9 DMF, fitted DMF and tank width ratio for open tube case at quarter tank width. 89
5.10 RAO for full tank, half tank and quarter tank width for four orifices case 90
5.11 Pressure for full tank, half tank and quarter tank width for four orifices case with uncertainty at 95% confidence level 90
5.12 Power for full tank, half tank and quarter tank width for four orifices case 91
5.13 Capture width for full tank, half tank and quarter tank width for four orifices case 91
5.14 Capture factor for full tank, half tank and quarter tank width for four orifices case 91
5.15 Comparison of the moderate scale RAO and the small scale RAO for four orifices case 92
5.16 Pressure amplitude comparison between the small scale and moderate scale, where the small scale pressure is scaled up by a factor of 3. 93
5.17 Comparison of the moderate scale capture factor and the small scale capture factor for four orifice case 93

6.1 Domain size and boundary conditions. Left boundary is velocity inlet, right hand side and top boundaries are both set to pressure outlet, the tank bottom is set to be smooth wall and symmetry boundaries are set to be the lateral boundaries conditions. 100
6.2 Volume fraction of water distribution for a fifth order wave. Where red is water while blue denotes air. For visualization purpose, this figure is scaled 10 times in gravity direction and only part of the whole domain is demonstrated. 101
6.3 Theoretical water wave particle velocity magnitude distribution. . 102
6.4 Mesh topology for the entire domain. 102
6.5 A close look at the mesh in the wave region. For visualization purpose, this figure is scaled 10 times in gravity direction and only part of the whole domain is demonstrated. 102
6.6 Distance weighted damping strength variation against tank length. 104
6.7 Wave elevation decay within wave absorbing region. Where the black line is the wave elevation, the red region is without wave absorbing and blue region corresponding to damping strength equals to 1. 104

6.8 Illustration of Euler Overlay Method. 105
6.9 Determination of number of inner iterations. The relative difference between the iterated result and the theory is less than 0.001%. . . 109
6.10 Angle factor effect on the wave profile along with the tank length direction. 111
6.11 Enlarge angle factor effect on the wave profile along the tank length direction. 112
6.12 Wave profile along the tank length direction When mesh aspect ratio equals to 1/4. 112
6.13 Wave profile along the tank length When mesh aspect ratio equals to 1/8. 112
6.14 Wave profile along the tank length When mesh aspect ratio equals to 1/16. 113
6.15 Wave profile along the tank length When mesh aspect ratio equals to 1/2. 113
6.16 Comparison of wave profile along the tank length between mesh aspect ratio=1/8 and 1/16. 114
6.17 Wave profile along the tank length for case 5 at different time step size. 115

7.1 Comparison between the physical model and the CFD model. Where 1 is the orifice rig, 2 is the tube, 3 is the ring and 4 is the sectional view of the ring. 117
7.2 CFD domain and boundary conditions. Here, the OWC device located 2.5λ away from the inlet. 118
7.3 Mesh distribution. a) Overall view. b)Mesh refinement around the device. c) Mesh around orifice. d)Mesh around the ring. e) Mesh around inside the tube. f) Mesh around free surface. 119
7.4 Wall Y+ plot for the four orifice case when the volume flow rate reached its maxima at Kh=4.8. 119
7.5 EOM effec, with and without velocity inlet reflection absorbing. . 122
7.6 CFD RAO of the moderate scale FSCOWC for open tube. 123
7.7 CFD RAO of the moderate scale FSCOWC for four and one orifices case. 124
7.8 CFD pressure of the moderate scale FSCOWC for four and one orifices case. 125
7.9 CFD mean power of the moderate scale FSCOWC for four and one orifices case. 125

7.10 CFD capture width of the moderate scale FSCOWC for four and one orifices case. 125
7.11 CFD capture factor of the moderate scale FSCOWC for four and one orifices case. 126
7.12 OWC surface position in gravity direction when encountered with wave in CFD simulation when Kh=5 for open tube case. Here, the contour is mirrored for visualization purpose. 126
7.13 Illustration of calculating the power directly from the air flow. . . 127
7.14 Comparison of the mean power captured monitored at different height in the chamber for four and one orifice case. 128
7.15 Stream line through the orifice for the four orifices case at $Kh = 4.8$. 128

8.1 Comparison of the moderate scale and small scale FSCOWC geometry. 131
8.2 Open tube RAO for different tank width. 132
8.3 Open tube RAO compared with moderate scale RANS simulation. 133
8.4 Open tube RAO compared with EFD result for full tank condition. 133
8.5 Four orifice RAO for different tank width. 134
8.6 Four orifice pressure amplitude for different tank width. 134
8.7 Four orifice mean power captured for different tank width. 134
8.8 Four orifice capture width for different tank width. 135
8.9 Four orifice capture factor for different tank width. 135
8.10 Comparison of mean power captured at different tank width around the resonance frequency for four orifices case. 135
8.11 Comparison between the moderate scale and small scale RAO for four orifices case. 136
8.12 Comparison between the moderate scale and small scale pressure amplitude for the four orifices case. 137
8.13 Comparison between the moderate scale and small scale mean power captured for the four orifices case. 137
8.14 Comparison between the moderate scale and small scale mean capture width for the four orifices case. 137
8.15 Comparison between the moderate scale and small scale mean capture factor for the four orifices case. 138
8.16 Comparison between the power captured for four orifices case at different scale, where the power are all extrapolated to the largest scale. 138
8.17 Mean power captured comparison between the CFD and EFD for four orifices case. 139

9.1 Square of Volume flow rate against pressure drop for the four orifices case at $Kh = 4.9$. 142
9.2 Comparison of $\wedge$ against Reynolds number for the moderate scale four orifices case simulation and tank testing. 142
9.3 Comparison of the simulation and tank testing $\wedge$ against Reynolds number for the moderate scale one orifices case 143
9.4 Comparison of the tank testing $\wedge$ against Reynolds number for the moderate scale and small scale one orifices case. 143
9.5 Comparison of the simulation $\wedge$ against Reynolds number for the moderate scale and small scale four orifices case 144
9.6 Comparison of the simulation PTO constant $\wedge$ against Reynolds number for three different scale four orifices case. 144
9.7 Comparison of the simulation $\wedge$ against result from orifice simulation. 145
9.8 Comparison of the simulation $\wedge$ against result from orifice simulation. 145
9.9 Comparison of the four orifices case RAO for different scales' simulations. 147
9.10 Comparison of the four orifices case Pressure for different scales' simulations. 147

10.1 Illustration of using valve to scale the air compressibility. 150

A1 Pressure transducer calibration. 166
A2 Pressure transducer calibration. 167
A3 Comparison between the pressure measured by the digital pressure sensor and the pressure transducer, where the pressure transducer used the manufacture specified calibration factor. 167
A4 Residuals between the pressure measured by the digital pressure sensor and the pressure transducer. 168
A5 New calibration for the measurement range. 168
A6 Residuals for the new calibration, where the 95% prediction limit is calculated based on linear regression theory. 169

B1 Illustration of DMF under different damping ratio. 171
B2 Comparison between the actual DMF and the fitted DMF for the moderate scale open tube case. 174
B3 Comparison between the actual DMF and the fitted DMF for the small scale open tube case. 174
B4 Comparison between the actual DMF and the fitted DMF for the lareg scale four orifices case. 174

B5 Comparison between the actual DMF and the fitted DMF for the moderate scale one orifice case. 175
B6 Comparison between the experiment free decay test and linear fitted free decay for open tube case. 175
B7 Comparison between the experiment free decay test and linear fitted free decay for open tube case. 176
B8 Comparison between the experiment free decay test and fitted free decay for open tube case. 176
B9 Comparison between the calculated DMF and fitted DMF for RANS simulation of the moderate scale open tube case. 176
B10 Comparison between the calculated DMF and fitted DMF for RANS simulation of the small scale open tube case. 177
B11 Comparison between the calculated DMF and fitted DMF for RANS simulation of the moderate scale four orifices case. 177
B12 Comparison between the calculated DMF and fitted DMF for RANS simulation of the moderate scale one orifice case. 177

C1 DMF, fitted DMF and tank width ratio for tank testing of four orifices case at full tank width. 178
C2 DMF, fitted DMF and tank width ratio for tank testing of four orifices case at half tank width. 179
C3 DMF, fitted DMF and tank width ratio for tank testing of four orifices case at quarter tank width. 179
C4 DMF, fitted DMF and tank width ratio for RANS simulation of four orifices case at full tank width. 179
C5 DMF, fitted DMF and tank width ratio for RANS simulation of four orifices case at half tank width. 180
C6 DMF, fitted DMF and tank width ratio for RANS simulation of four orifices case at quarter tank width. 180

E1 Boundary conditions of the orifice plate simulation. 184
E2 Illustration of the convergence of the simulation for velocity equals to $0.02m/s$. 185
E3 Velocity contour and streamline of compressible simulation at velocity equals to $0.02m/s$. 185
E4 Pressure and density contour for compressible simulation at velocity equals to $0.02m/s$. 186

E5 Pressure and density contour for compressible simulation at velocity equals to $2.5m/s$. 186

List of Tables

2.1 Some promising UK wave energy technology developers and their device. 8
2.2 Features for different numerical scheme 26

4.1 Geometry details of the FSOWC where PCD is pitch circle diameter. Here, the relative large uncertainty in the geometry origins from the measurement. It is not the uncertainty in the manufacturing. 44
4.2 Nature frequency for different draft calculated based on rigid body theory 61

5.1 Scaling table. * it shall be noted that the air chamber length does not obey the Froude scaling law and the length of the air chamber should be the same as the moderate scale test. 80
5.2 Geometry details of the Two FSCOWC device 81
5.3 Equivalent frequency independent added mass coefficient and linear damping ratio for moderate scale and small scale open tube case. 87

6.1 Wave parameters for mesh testing 110
6.2 Test matrix-Total 110
6.3 Test matrix-Group 1 110
6.4 Test matrix-Group 2 110
6.5 Test matrix-Group 3 110
6.6 Test matrix-Group 4 110
6.7 Test matrix-Group 5 111
6.8 Wave height obtained at 2 wavelength away from the inlet after 40 seconds physical simulation for mesh aspect ratio equals to 1/8. The simulation is carried out by using a PC with 32G RAM and 4 core Intel i7-2600 processor. Simulation is done by Star-CCM+ version 9.02.005. 114

7.1 OWC geometry details where PCD is pitch circle diameter. The relative large uncertainty in the geometry is due to the uncertainty in the measurement instead of the uncertainty in the manufacturing. 117
7.2 Mesh dependency test 120
7.3 Comparison between the equivalent frequency independent hydrodynamic coefficients for CFD and EFD. 123

8.1 OWC geometry details of the small scale FSCOWC where PCD is pitch circle diameter 131

D.1 Mesh dependency test 183

Acknowledgements

First of all, I'd like to acknowledge my sincere veneration and indebtedness to my lead supervisor Dr.Qing Xiao for her supervision, guidance through my PhD research. Her knowledge and kindness inspired me a lot.

I would like to acknowledge my sincere veneration and indebtedness to my second supervisor Prof Sandy Day, for his valuable guidance and suggestions throughout my PhD research.

I am deeply indebted to Mr.David Clelland, for his treasured and continuous help.

Help from the Kelvin Hydrodynamic staff is indeed acknowledged, they are Mr.Charles Keay, Mr.Grant Dunning, Mr. Bill McGuffie, Mr. Bill Wright. Special thank goes to my mentor and friend Mr.Edward Nixon, for his valuable discussion, guidance, and taking care of me.

Mrs. Thelma Will, department administrative staff, her kindness and help is greatly acknowledged from the very first day of my PhD.

I would like to show my appreciation to Prof Chengi Kuo, for sharing his life experience and advices.

Dr. Qiuxin Gao, Dr. Zhiming Yuan, Dr. Wei Jin, their help and discussion are greatly acknowledged.

I would also like to thank the University of Strathclyde Faculty of Engineering for provision of the ARCHIE-WeSt high performance computing facilities. The CFD results were obtained using the EPSRC funded ARCHIE-WeSt High Performance Computer (www.archie-west.ac.uk), EPSRC grant no. EP/K000586/1.

I would show my appreciation to all my colleagues and friends who have made my PhD life more interesting. They are but not limited to Dr.Xing Sun, Dr.Ning Zhu, Dr.Lin Lin, Dr. Yigit Kemal Deirel, Dr. Tashin Tezdogan and so on.

This thesis is dedicated to
My parents and my wife
for their endless love and support to me